5
RESULTS AND DISCUSSION

This chapter analyzes experimental results to offer comprehensive explanations through both quantitative and qualitative descriptions of all dissimilar weld joints.

5.1 DISSIMILAR METAL WELD OF SUPER DUPLEX STAINLESS STEEL AND INCONEL 625

This section thoroughly investigates the structure-property relationship for filler metal selection and weldment heat input parameters. It contains a comprehensive heat-affected zone, weld zone, and base metal metallurgical characterization. The structural integrity of the sDSS 2507/IN-625 dissimilar weld joints is evaluated using mechanical characterization, residual stress measurement, and wear and corrosion behavior analysis.

5.1.1 QUALITATIVE AND QUANTITATIVE WELD JOINT INSPECTION

X-ray radiography and macrostructure analysis using stereo zoom microscope confirmed a defect-free welded joint connection before mechanical and microstructural evaluation. In Figure 5.1(a and c), the capping pass, pass order, fusion width, and depth affect the passes underneath it. Welded joints were fully penetrating and visually flawless. Welded joint areas were measured using Image J software—115 ± 3 mm2 for ER2594 and 102 ± 4 mm2 for ERNiCrMo-3. The capping and backing passes for an ER2594 weldment were 12.85 mm and 9.50 mm, while those for ERNiCrMo-3 were 11.92 mm and 9.14 mm. Radiographic film quality was authorized by ASME Sec-IX (QW-191.1.2). The radiography scan shows high-quality sDSS 2507/IN-625 DWJs with both filler metals (Figure 5.1(b and d)). The liquid dye penetrant test, also known as liquid penetrant inspection (LPI), is a low-cost method for detecting surface defects. First, the specimen's surface is cleaned (Figure 5.1(e)), and a red penetrant liquid is applied. The penetrant seeps into any surface flaws through capillary action. After a dwell time of 8-10 minutes, the excess liquid is wiped off, and a developer is applied to bring the trapped penetrant to the surface (Figure 5.1(e)). Upon inspection, the welded joint was confirmed to be free of defects.

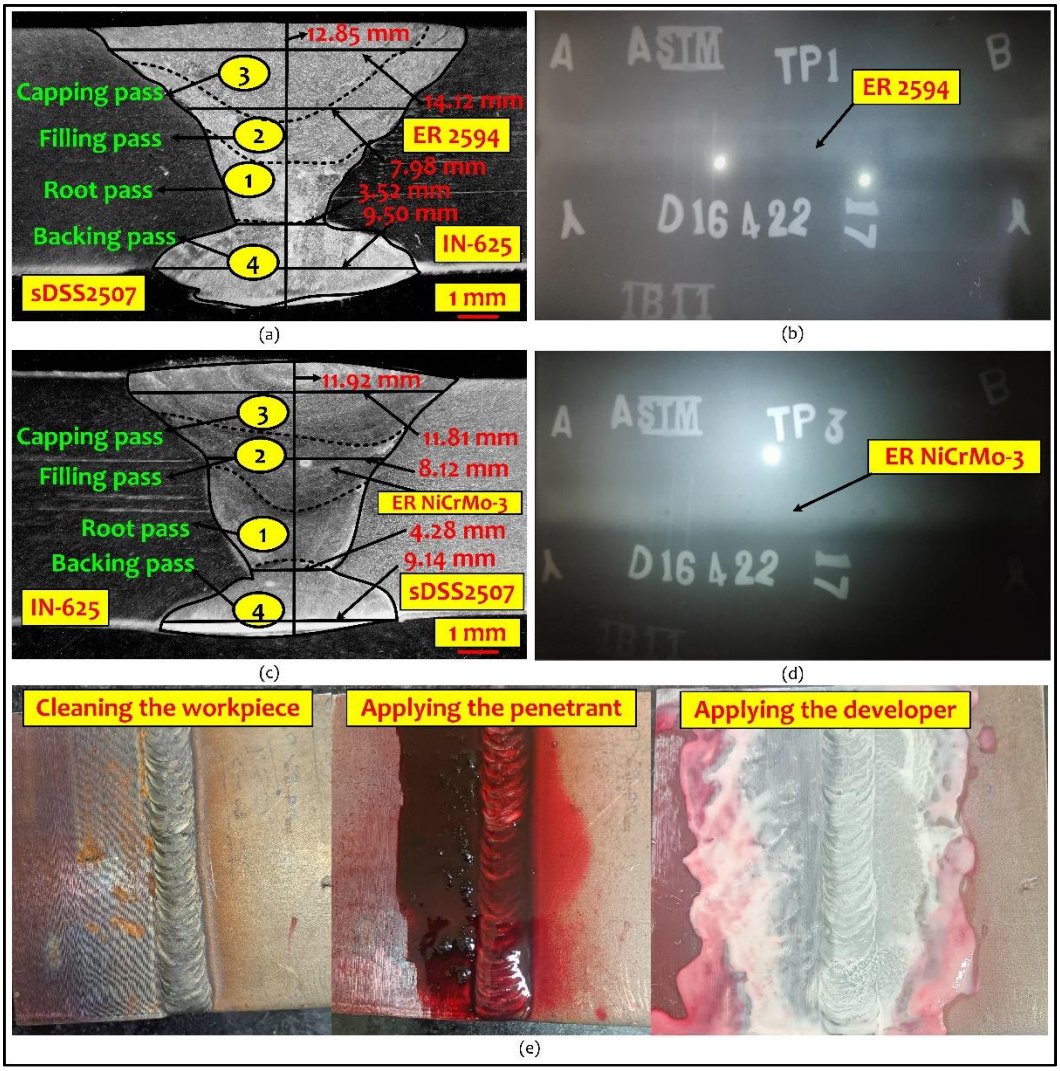

Figure 5.1 : Macrostructure, X-ray radiography and liquid dye penetration test of weldments showing its weld and passes with (a and b) ER2594 filler, (c and d) ERNiCrMo-3 filler, (e) Pre-cleaning, applying penetrant and applying developer, respectively.

5.1.2 MICROSTRUCTURAL CHARACTERIZATION

Microstructural characterization comprises microstructure study of the base metal, microstructure evolution investigation at the weld interface, and weld zone study of both filler metals and heat input effect using different characterization techniques for structure-property relationship assessment.

5.1.2.1 *BASE METAL*

The microstructure and mechanical properties of both base metals were studied. Figure 5.2 shows the optical microscopy (OM) and scanning electron microscopy (SEM) microstructures for both base metals (BM). The microstructure of the IN-625 is depicted in Figure 5.2(a and b). A Ni-rich elongated austenitic matrix with an average grain size of 25 ± 10 µm and annealing twin boundaries is evident. Energy-dispersive spectroscopy (EDS) measurements show Cr and Mo as the primary elements in intragranular precipitates, indicating $M_{23}C_6$ and M_6C carbides with greater Cr and Mo concentrations (Figure 5.2(c)). Figure 5.2(d and e) shows austenite grains rolling in sDSS 2507 BM's ferrite matrix. Grains of austenite exhibit linear extension and coaxial grains arranged in chains. Using Image J software, ferrite measurement revealed a dual-phase microstructure with 51.6% ferrite and 48.4% austenite at sDSS 2507. The EDS spectra of base metals for IN-625 and sDSS 2507 are shown in Figure 5.2(c and f). Figure 5.2(h) shows the base metals IN-625 and sDSS 2507 XRD to confirm phase presence and no intermetallic phase growth. Base metals had average tensile strengths of

930 MPa (IN-625) and 1002 MPa (sDSS 2507) (Figure 5.2(g)). Both IN-625 and sDSS 2507 had impact toughness values of 330 J and 310 J, respectively.

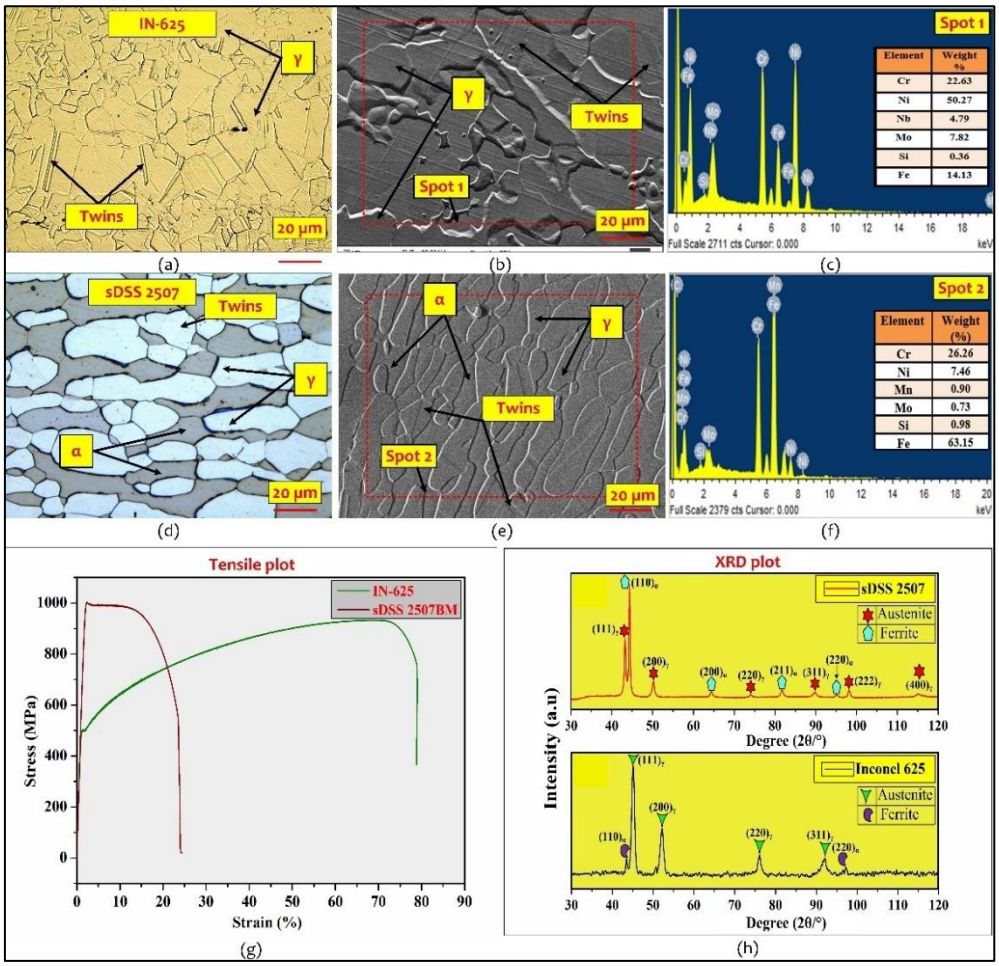

Figure 5.2 : The microstructure of base metal (a-b) IN-625 BM, (d-e) sDSS 2507 BM, respectively, The EDS analysis of the (c) sDSS 2507 BM, (f) IN-625 BM, respectively, and (g and h) The tensile and XRD plot of the sDSS 2507 and IN-625 base metal, respectively

5.1.2.2 *WELD INTERFACE*

Weld interface characterization affects joint strength and metal solidification. Weld interface formation is unpredictable despite V-groove and matching filler metal. Heating and cooling speeds affect interface nucleation and growth in multi-pass welding. Figure 5.3 depicts ER2594 filler weldment microstructure evolution at the sDSS 2507 weld interface. No macrosegregation appears at the sDSS 2507 weld interface. With matching ER2594 filler metal, interface weld metal is mixed and solidified properly. The heat-affected zone (HAZ) of sDSS 2507 can be divided into a high temperature (HT) and a low temperature (LT) HAZ or partially annealed zone. This uniformity and chemical composition resemblance to the sDSS 2507 BM/ER2594 weld interface led to epitaxial development around the fusion boundary. Maintain an elevated level and reduce cooling to prevent austenite precipitation. Partially transformed austenite (PTA), grain boundary austenite (GBA), inter-granular austenite (IGA), and Widmanstätten austenite (WA) may all be seen in SEM images of the sDSS2507 HAZ (Figure 5.3(a)). Multi-pass welding can cause secondary austenite (γ2) precipitation in thermally stable HAZ. In contrast, Figure 5.3(b) shows partial fusion in the ER2594 filler weldment IN-625 weld interface. The melting, solidification, chemical composition, and coefficient of thermal expansion (CTE) of ER2594 filler metal differs from IN-625 BM, preventing it from melting and fusing into the weld zone. Unmixed or partially mixed zones (UMZ/PMZ) result from insufficient BM-filler metal mixing. The IN-625 weld interface exhibits the formation of the PMZ. Filler-deficient features include the island and peninsula. Peninsulas and islands form

when the BM's liquidus temperature exceeds the weld zone (WZ's). PMZ's composition depends on the diffusion rate when crystal structures of different chemical compositions interact. PMZ concentration gradients cause significant segregation and deteriorate mechanical characteristics. Weld interface microstructure is influenced by the temperature gradient (G) (°C/m) and solidifying cell/dendrite growth rate (R) (μm/s) in the weld pool (Kumar, Yadav, et al., 2021). With a higher thermal conductivity of 15 W/mK compared to 9.8 W/mK, the sDSS 2507 HAZ is significantly larger than the IN-625 HAZ, respectively.

Microstructural analysis of WZ along the IN-625 interface revealed the presence of multi-directional grain growth, including cellular, columnar dendritic, and equiaxed grains (Figure 5.3(b)). Figure 5.3(c-e) shows the detailed characterization of the ERNiCrMo-3 weld interface with sDSS 2507 and IN-625 BMs, respectively. Interestingly, a well-defined fusion line has been observed at the sDSS 2507 BM/ERNiCrMo-3 weld interface, which could be attributable to the low compatibility between filler and BM. Furthermore, the PMZ can be seen in the optical image adjacent to the interface. Columnar and cellular dendritic growth is heterogeneously dispersed in the weld interface. In contrast, the IN-625 BM/ERNiCrMo-3 weld interface exhibits proper BM and filler mixing. Epitaxial growth has occurred at the IN-625 weld interface because both IN-625 BM and the ERNiCrMo-3 filler exhibit face-centered cubic (FCC) crystal order. At the weld interface, partially melted IN-625 grains commence epitaxial growth. Near the IN-625 equiaxed weld interface, cellular and columnar dendritic were randomly distributed, exhibiting multi-directional grain growth. One possible explanation is that slower welding speeds result in slower cooling rates. SEM investigation of the sDSS 2507 and IN-625 weld interface revealed secondary phases as interdendritic segregations. Nb and Mo-rich secondary phases form more densely at the IN-625 interface than the sDSS 2507 interface and depend on solidification microstructures. These phases in the weld metal or HAZ region reduce the weld metal's mechanical and corrosion properties due to the secondary phases' brittleness.

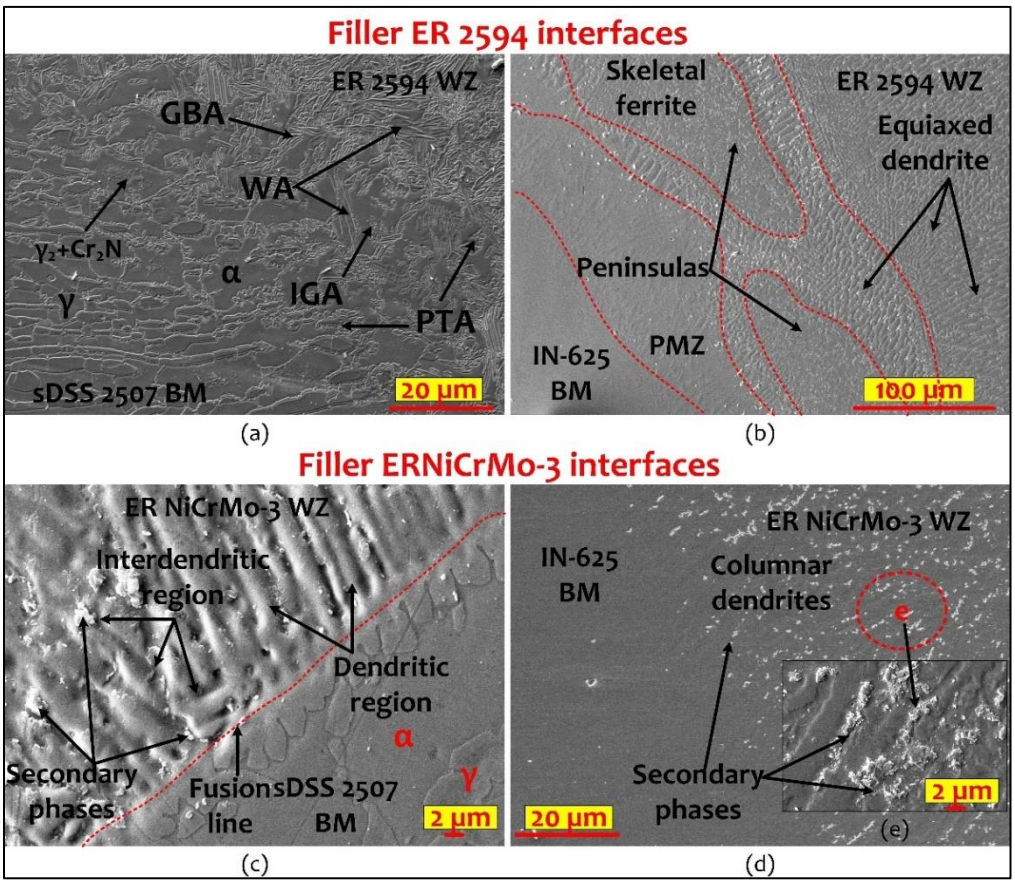

Figure 5.3 : Interface microstructure between the sDSS 2507BM/IN-625 BM and weld zone, respectively (a and b) for ER2594 filler; (c-e) for ERNiCrMo-3 filler

Line mapping and EDS spectra show chemical element mobility at both fillers' weld interfaces in Figures 5.4 and 5.5. Figure 5.4(a) depicts the EDS spectrum location and interface microstructural evolution for the sDSS 2507 BM to ER2594 WZ. Because sDSS 2507 BM and ER2594 filler have the same chemical composition and structure, Figure 5.4(b) revealed a uniform fluctuation of elements at the interface. Weld metal's EDS spectrum (spot 1) reveals Cr, Ni, Mo, and Nb as the filler's typical constituents, while IN 625's (spot 3) EDS spectrum reveals the base matrix's composition (Figure 5.4(c)). The results exhibit that Fe migrated from the ER2594 WZ to the IN-625 HAZ, but Ni, a gamagenic element, transferred from the IN-625 BM to the interface. As with spot 3 and spot 1, the EDS investigation of the UZ (spot 2) reveals varied results. A steady reduction in Fe content evidences Fe diffusion from the ER2594 WZ to the IN-625 BM. Compared to ER2594 WZ, IN-625 BM elements transported to the weld zone had a greater Ni concentration. Many peaks in the welded zone showed substantial heterogeneity and non-uniform distribution of Cr, Ni, Fe, Mo, and Nb. Figure 5.4(d) shows the interface and peninsula's elemental composition differences according to elemental line mapping. The peninsula had higher Ni, Mo, and Nb concentrations and lower Fe and Si. Figure 5.5(a) depicts the EDS spectra' location and the interface microstructure's evolution for the sDSS2507 BM to ERNiCrMo-3 WZ. EDS examination showed that the sDSS2507 BM had higher Cr, Mn, and Fe concentrations and lower Ni and Mo concentrations than the ERNiCrMo-3 WZ. Line mapping analysis shows considerable Ni, Fe, and Mo variation around the interface (Figure 5.5(b)). The EDS spectra results (Figure 5.5(c)) show that the element composition of the IN 625 weld interface varies along the weld joint's smooth and marginal regions. The chemical similarity of IN-625 and ERNiCrMo-3 filler metal prevents microsegregation and excessive diffusion across the weld interface. The weld zone and EDS analysis showed similar Cr, Ni, and Mo concentrations. Line mapping confirms this variation (Figure 5.5(d)). Fe's migration from sDSS 2507 BM is evidently demonstrated by its presence in the ERNiCrMo-3 WZ. The progressive loss of Fe from ERNiCrMo-3 WZ to IN-625 BM is evident.

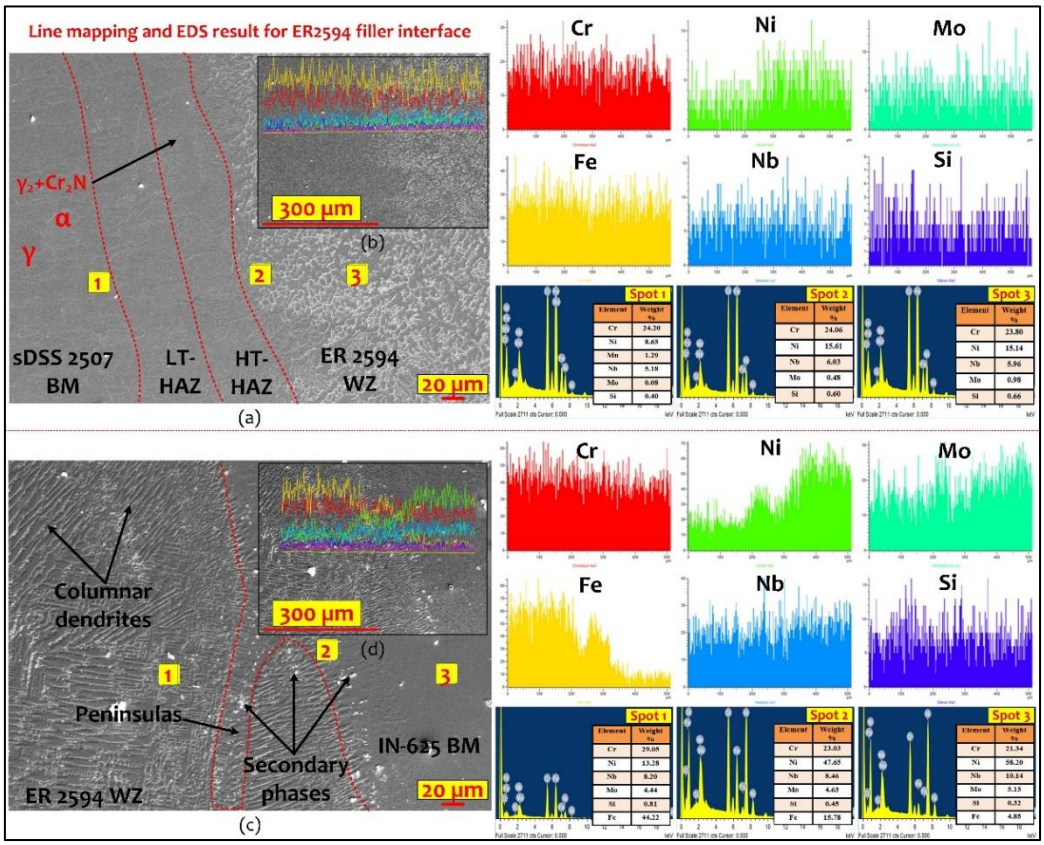

Figure 5.4 : *ER2594 filler EDS spectra location and line mapping analysis at the (a and b) sDSS 2507 and (c and d) IN-625 interface, respectively*

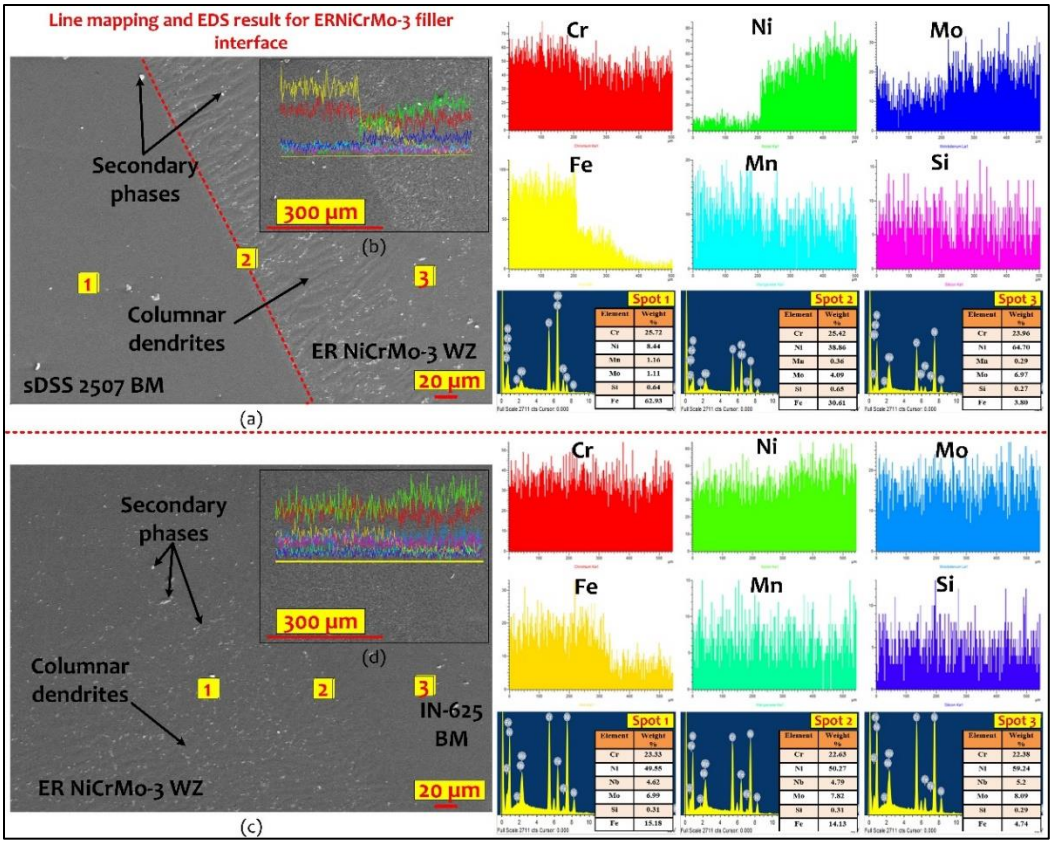

Figure 5.5 : ERNiCrMo-3 filler EDS spectra location and line mapping analysis at the (a and b) sDSS 2507 and (c and d) IN-625 interface, respectively

Both base metal interfaces underwent electron probe microanalyzer (EPMA) element mapping to investigate the relationship between microstructure anomaly and element distribution. The HAZ of both BMs clearly showed an unequal distribution of the elements. The EPMA results for C, Ni, Cr, Mo, and Nb diffusion at the IN-625 and sDSS 2507 interfaces with ER2594 filler are displayed in Figure 5.6(a and b), respectively. The EPMA findings demonstrate changes in elemental composition at the boundary between the peninsula and IN 625 BM (Figure 5.6(a)). However, Cr, Ni, Mo, and Nb diffusion variations near the weld interface are visible. Carbon segregation with a C-rich zone was seen at the interfaces of both ER2594 filler weldments. The distribution of C, Cr, Ni, Mo, and Nb throughout the sDSS 2507 BM interface is depicted in Figure 5.6(b). Elements like Cr and Mo do not display any discernible diffusion during solidification since they share the same chemical composition as the base metal. However, Ni and Nb show an evident variation across the weld interface. Peninsula formation can be seen in the backscattered electron image of the IN 625 interface. The EPMA results for C, Ni, Cr, Mo, and Nb diffusion at the IN-625 and sDSS 2507 interfaces with ERNiCrMo-3 filler are displayed in Figure 5.7(a and b), respectively. The distribution of C, Cr, Ni, Mo, and Nb throughout the IN-625 BM interface is depicted in Figure 5.7(a). Elements like Cr and Mo do not display any discernible diffusion during solidification since they share the same chemical composition as the base metal. However, Ni and Mo-Nb carbon-rich phases show an apparent variation across the weld interface. The EPMA findings demonstrate changes in elemental composition at the boundary between the peninsula and sDSS 2507 BM (Figure 5.7(b)). However, Cr, Ni, Mo, and Nb diffusion variations near the weld interface are visible. Carbon segregation with a C-rich zone was seen at the interfaces of both ER2594 filler weldments.

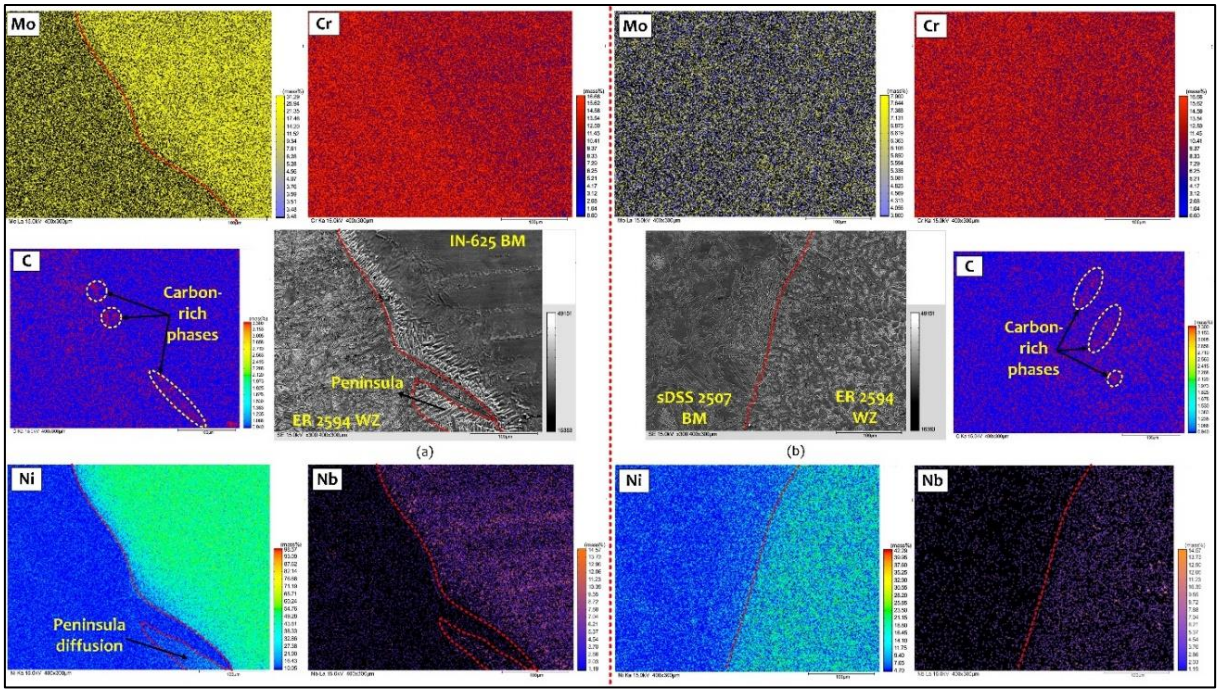

Figure 5.6 : EPMA analysis depicting the distribution of elements at the weld interface of (a) IN-625 BM and ER2594 filler, (b) sDSS 2507 BM and ER2594 filler

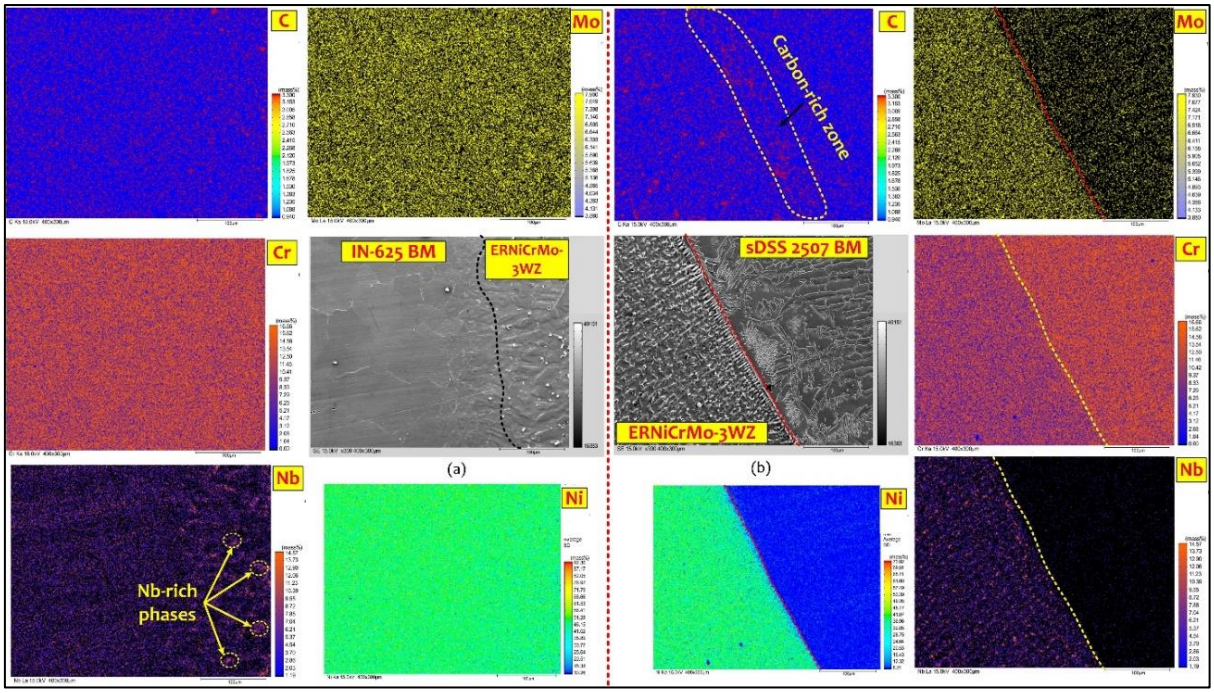

Figure 5.7 : EPMA analysis depicting the distribution of elements at the weld interface of (a) IN-625 BM and ERNiCrMo-3 filler, (b) sDSS 2507 BM and ERNiCrMo-3 filler

5.1.2.3 WELD ZONE

The Fe-Cr-Ni pseudobinary phase diagram and the Schaeffler diagram both show that the value of chromium equivalent (Cr_{eq})/ nickel equivalent (Ni_{eq}) in the weld zone affects the solidification mode and microstructural evolution (Figure 5.8(a and b)). Schaeffler constitution diagrams were also used to determine the weld microstructures produced by various filler metals, as presented in Figure 5.8(b). Table 4.1 shows the base and filler metals' Cr_{eq} and Ni_{eq}, and Table 5.1 lists the Cr_{eq} and Ni_{eq} of different passes for both filler weldments. The points associated with each filler metal's composition were found by projecting these results on the Schaeffler diagram to identify the weld metal microstructures. The weld compositions (circle

signs) for the ER2594 and ERNiCrMo-3 filler metals overlapped in the totally ferritic and fully austenitic regions, respectively, when the weld zone cross-section area was diluted by 30 percent. The first solid that forms during the solidification of ER2594 filler metals with high Cr_{eq}/Ni_{eq} ratios is ferrite, whereas the first solid that forms during the solidification of ERNiCrMo-3 filler metals with low Cr_{eq}/Ni_{eq} ratios is austenite, which is distinct as from sDSS 2507 base metal. While the ferritic-austenitic (FA) mode provides the highest resistance to solidification or hot cracking, the composition that contributes to primary austenite solidification (A and AF) is prone to cracking. In contrast to alloys that solidify as austenite, primary ferrite solidification in the FA mode is observed to offer better resistance to weld solidification cracking. The weld zone microstructure evolution for both filler metals is indicated to support the Schaeffler diagram evaluation. The XRD pattern was obtained from the WZ of both fillers' weldments (Figure 5.8(c)). The ER2594 filler WZ diffractogram pattern reveals the presence of mostly austenite (γ) and ferrite (α), with no further indication of the intermetallic phases (χ or σ phase) or precipitations (Cr_2N). The FCC and BCC crystals form with the least surface energy along their close-packed (111) γ and (110) α. PDF#52-0513 for FCC and PDF#06-0696 for BCC examined XRD patterns for content computation. The ERNiCrMo-3 weld zone predominately displays the presence of the austenite (γ) phase and may contain Ti and Nb-based nitrides and Cr-rich carbides. Diffraction patterns show a considerable difference between the ferrite peak intensities for ERNiCrMo-3 filler and ER2594 filler.

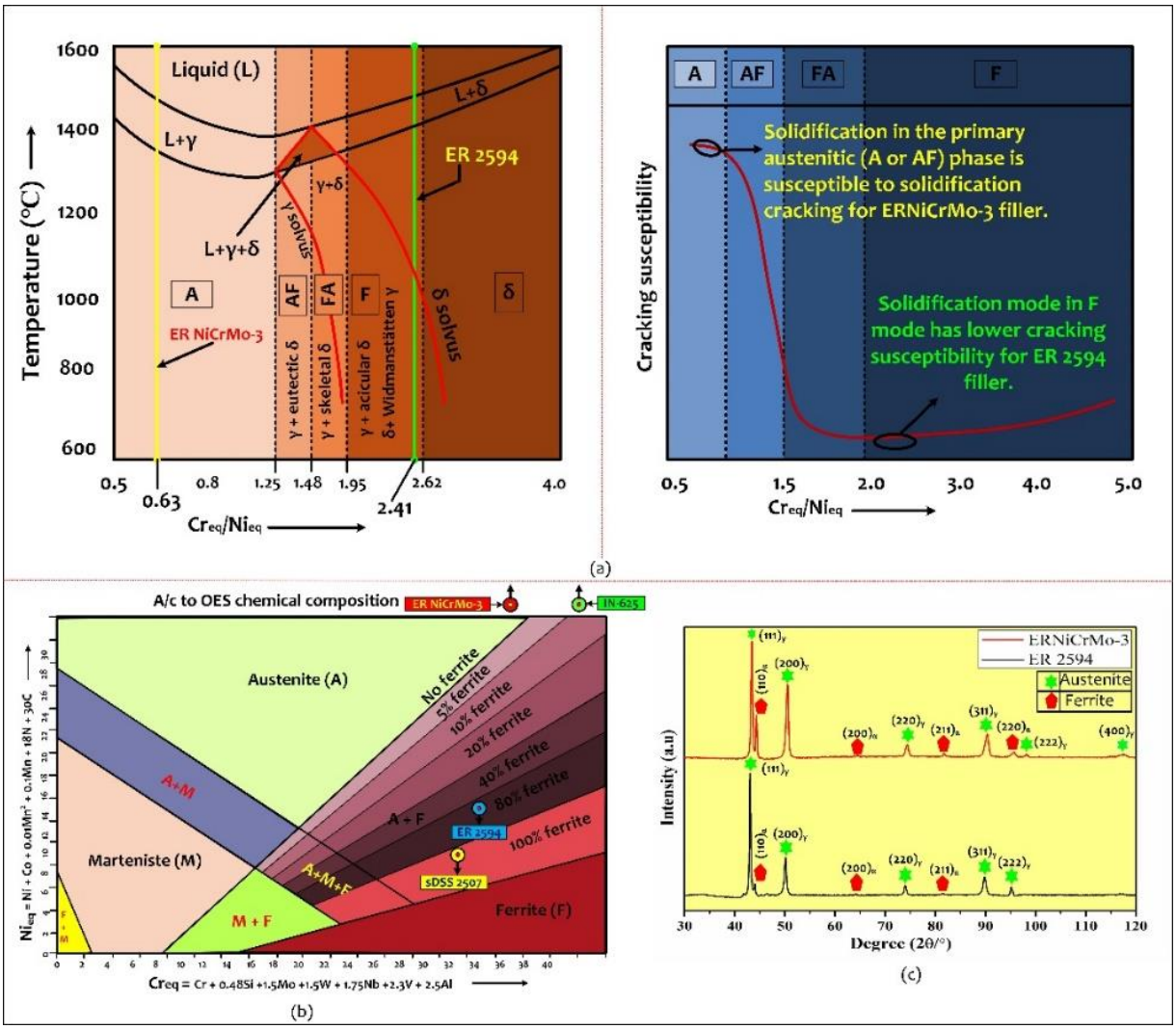

Figure 5.8 : The pseudo-binary diagram shows (a) the relative positions of the filler metals ER2594 and ERNiCrMo-3, (b) the Schaeffler diagram for predicting the solidification mode, and (c) both filler weldments' X-ray diffraction (XRD) patterns

Table 5.1 : Solidification mode as per Cr_{eq}/Ni_{eq} for both filler weldment

Filler	*Passes*	Cr_{eq}/Ni_{eq}	*Solidification mode reaction*
ER2594	Cap	2.71	F mode: L → L + δ → δ → δ + γ
	Filler	1.93	FA mode: L → L + δ → L + δ + $(\gamma + \delta)_{peritectic/eutectic}$ → δ + γ
	Root	2.83	F mode: L → L + δ → δ → δ + γ
	Backing	2.72	
ERNiCrMo-3	Cap	0.85	A mode: L → L + γ → L + γ + NbC → L + γ + Laves+ NbC → L + Laves + NbC
	Filler	0.91	
	Root	1.03	
	Backing	1.05	

Figure 5.9(a) and Figure 5.10(a-c) depict the microstructure evolution of the filler ER2594 WZ during several passes. At the weld cap fusion zone, WA, IGA, PTA, and GBA were frequently seen along with dark patches of inter-granular ferrite phases (Figure 5.10(a)). The skeletal ferrite structure evolved inside the austenite main matrix and became more apparent in the filler pass (Figure 5.10(b)), a transformation from the duplex microstructure in the cap WZ. Since ER2594 filler contains ferrite and austenite phases, and because these welding operations demonstrated a relatively slow cooling rate, skeletal ferrite morphology evolved in the weld zone. A closer look at the microstructure of the weld zone shows two distinct secondary phases. It was revealed that the intercellular and interdendritic spaces of the weld zone microstructure were particularly susceptible to exhibiting the first type of secondary phase. These lamellar precipitates display eutectic morphology (Figure 5.10(b)). EDS analysis of these phases showed Mo and Nb enrichment and increased Si concentrations. Such particles were labeled as Nb-rich Laves phase based on their chemical composition and shape. An additional secondary phase, this one rod-shaped within the ferrite matrix, forms during the weldment's filler pass (Figure 5.10(b)). The outcomes of the SEM/EDS study indicated that these segregates enriched in Nb and are of the Fe_2Nb type of laves phase. The backing and root passes of the weldments showed multi-directional grain development with columnar and cellular dendrites due to multi-pass welding. Additionally, it was seen that in the interdendritic region of the weld zone, small white secondary phases had precipitated (Figure 5.10(c)). As per EDS data (Table 5.2), the ER2594 weld zone has a higher weight % of Ni, Mo, and Nb than the filler metal. These elements were enriched in the fusion zone, proving that diffusion caused elemental changes during multi-pass welding. According to SEM/EDS analysis, Nb, Mo, and Si dominate all secondary phases. In Figure 5.10(c), columnar dendrites grow parallel to the borders, and sequential layer bands form perpendicular to the boundaries due to dynamic heat transfer. Instead of segregation, layer bands can be attributed to the subsequent deposition pass's partial remelting and complex thermal history. The weld zone may precipitate secondary austenite (γ_2) during multi-pass welding. The schematic illustration of secondary austenite (γ_2), formed either in association with Cr_2N or generated at the δ/γ interfaces during the transformation from reheat δ to γ in the weld center, is depicted in Figure 5.9(b).

Figure 5.10(d-f) displays the weld zone microstructure evolution of the ERNiCrMo-3 filler. A complete austenite microstructure was present in the ERNiCrMo-3 WZ, with columnar and cellular dendrites at the WZ's cap and equiaxed dendrites near the weld core (Figure 5.10(a)). SEM micrographs of precipitates and secondary phases that nucleate and develop in the weld zone's interdendritic region. Numerous morphologies, such as lamellar and rod-shaped, are clearly visible. In the columnar microstructure of the cap passes, the eutectic morphology of the laves phase is much more prevalent. This region had finer dendrites because it cooled faster than the filler and root pass's weld zone (Figure 5.10(b)). The root region of the weld zone exhibits cellular solidification structure and columnar dendrites (Figure 5.10(c)). The weld core and interface region showed multi-directional grain development. However, root and backing pass columnar microstructures have the most rod-shaped Laves phase form. The interdendritic area-extending eutectic Laves phases resemble chain particles, whereas the rod-shaped ones are smaller. Faster cooling generates a rod-shaped Laves phase, while slower

cooling generates a lamellar Laves phase (Schirra et al., 1991). The segregation of alloying elements like Nb, Mo, and Si produces all these precipitate morphologies. These alloying elements are abundant in interdendrites but scarce in dendrites. This will lead to an unstable and irregular distribution of the chemical alloying elements. After welding, the two base metals' thermal properties, such as specific heat and thermal conductivity, vary with temperature, causing a microstructure evolution. Equiaxed dendrites occur in the weld zone, notably in the filler and root passes, while columnar dendrites form at the fusion line. The temperature gradient (G)/growth rate (R) ratio causes dendritic morphological transformation. (Kou, 2003) state that higher heat input lowers the weld pool centreline temperature gradient. As a result, the G/R ratio would drop, and constitutional super-cooling would get worse right before the approaching solid-liquid interface. G/R inversely affects constitutional super-cooling, hence lowering it and changing the solidification mode from columnar to equiaxed dendritic. The solidification mode when utilizing ERNiCrMo-3 filler has changed from cellular to dendritic or equiaxed due to the constitutional super-cooling process becoming more intense (Dak & Pandey, 2021b). Interdendritic Nb-rich Laves phase segregation occurs in the weld zone. The Nb solubility of the groove is enhanced by the fact that its curved surface in Figure 14(c) has a smaller radius of curvature than the plane. As the groove Nb dissolves into the interdendritic, the Laves phase progressively changes from a long strip to a granular shape. Because Nb and Mo are poorly soluble in austenite, they separate from the liquid at the end of solidification. Thus, Mo and Nb are deficient in the first solid's dendritic cores but abundant in its interdendrites (Kumar, Yadav, et al., 2021). Mo and Ni were relatively dispersed and slightly concentrated in the ferrite, while C, Nb, and Cr were inter-dendritically concentrated. Nb changes in the weld zone may indicate Nb segregation and Nb-rich phases. Welds are more vulnerable to solidification cracks due to the high susceptibility of Nb to the observed segregation. Nb distribution patterns form as it segregate and solidify in interdendritic areas. Solute re-distribution behavior governed the solidification behavior of the weld zone. Nb's minimal equilibrium distribution coefficient ($k < 1$) causes it to re-distribute in inter-dendritic zones during solidification. If C_s and C_l are the respective solid and liquid compositions at the solid-liquid interface, then $k = C_s/C_l$ can be used to establish the equilibrium distribution coefficient. In the interdendritic areas, Nb and C combine to produce Nb-rich carbides. The EDS analysis revealed a more significant concentration of Nb elements when comparing the inter-dendritic to the dendritic region (Table 5.2). This is because Nb dissociates from the dendritic core during the solidification process and accumulates in the inter-dendritic regions. Figure 5.11(a and b) shows EPMA analysis with elemental mapping of ER2594 and ERNiCrMo-3 filler weld zone, respectively. ER2594 weld zone consistently showed slightly higher Ni, Nb, and Mo contents in EPMA analysis compared to the sDSS 2507 BM. In contrast to BM, Cr, in particular, displayed a slightly lower value. The elemental segregation in the ERNiCrMo-3 weld zone indicated considerable variations between the dendritic and inter-dendritic core. Concentrations of C, Nb, and Cr were found inter-dendritically, while Mo and Ni were more uniformly distributed and slightly concentrated in the ferrite. The segregation of Nb and the development of Nb-rich phases could be indicated by variations in Nb in the weld zone.

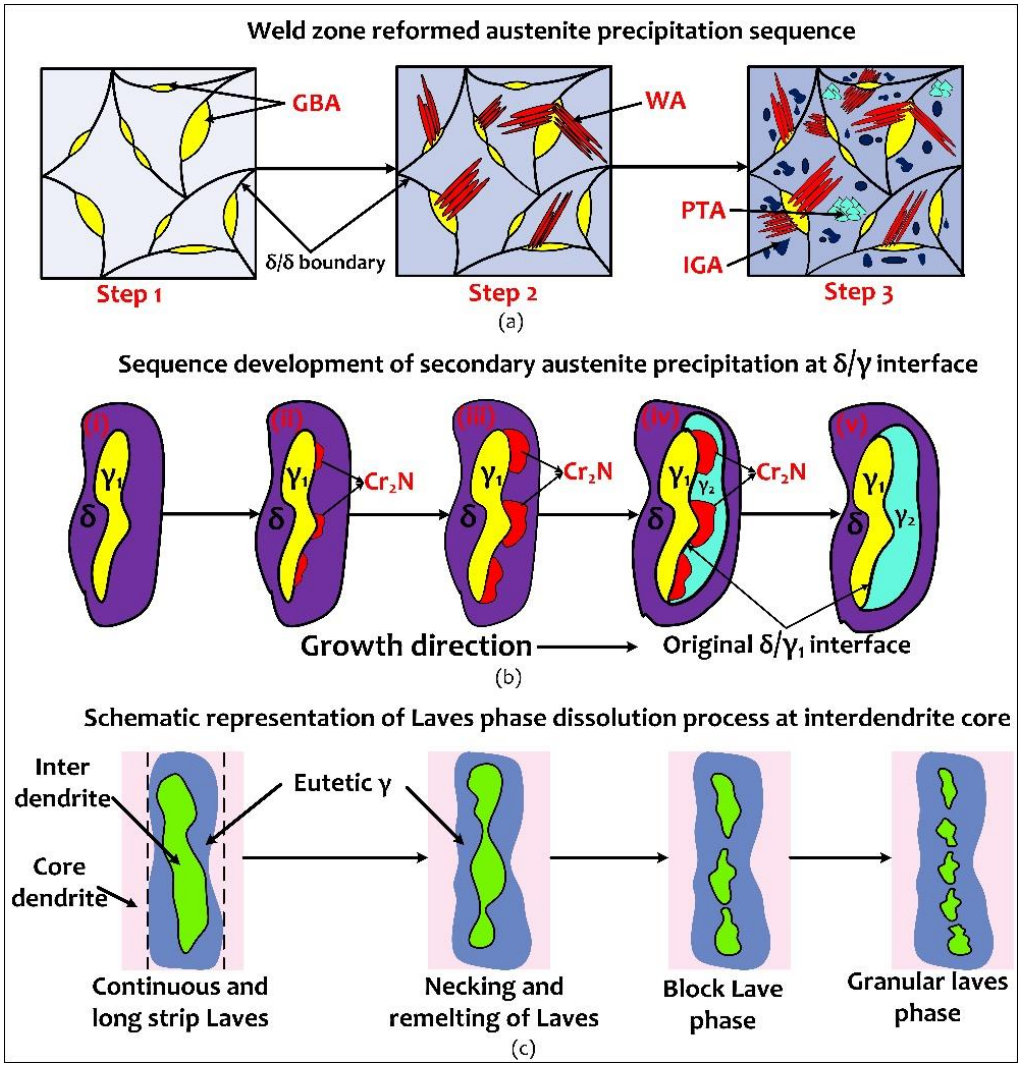

Figure 5.9 : Schematic illustration of the sequential development of (a and b) reformed austenite formation and secondary austenite at the δ/γ interface in ER2594 WZ (W. N. Khan et al., 2021) and (c) laves phase at the interdendritic core in ERNiCrMo-3 WZ (Liu et al., 2020)

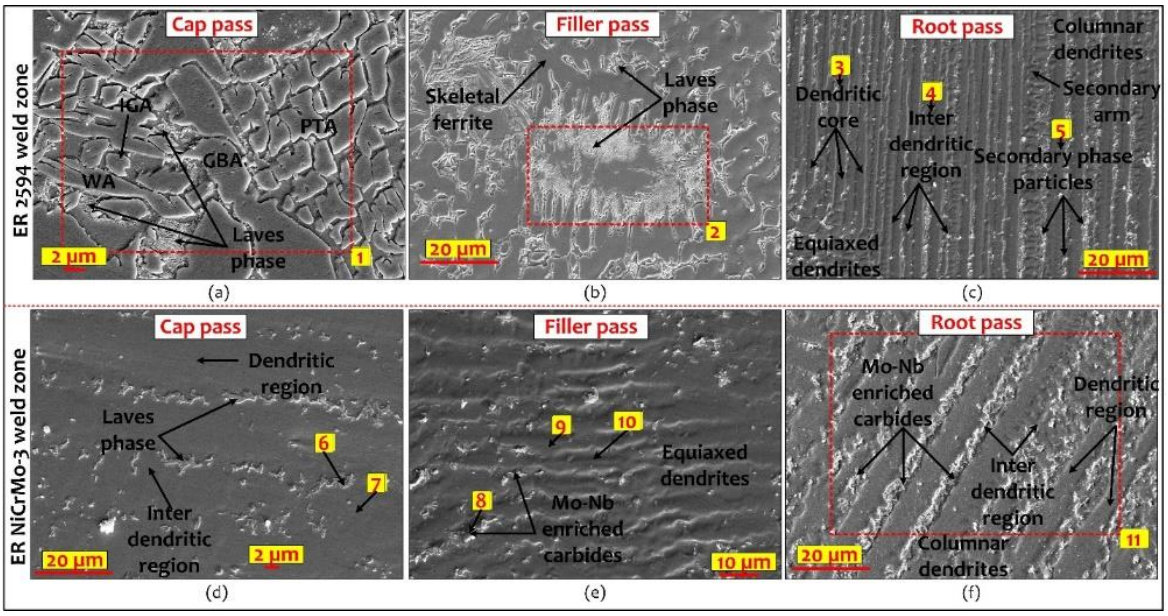

Figure 5.10 : SEM micrograph shows different pass, including cap pass, filler pass, and root pass for (a-c) ER2594 WZ, and (d-f) ERNiCrMo-3 WZ, respectively

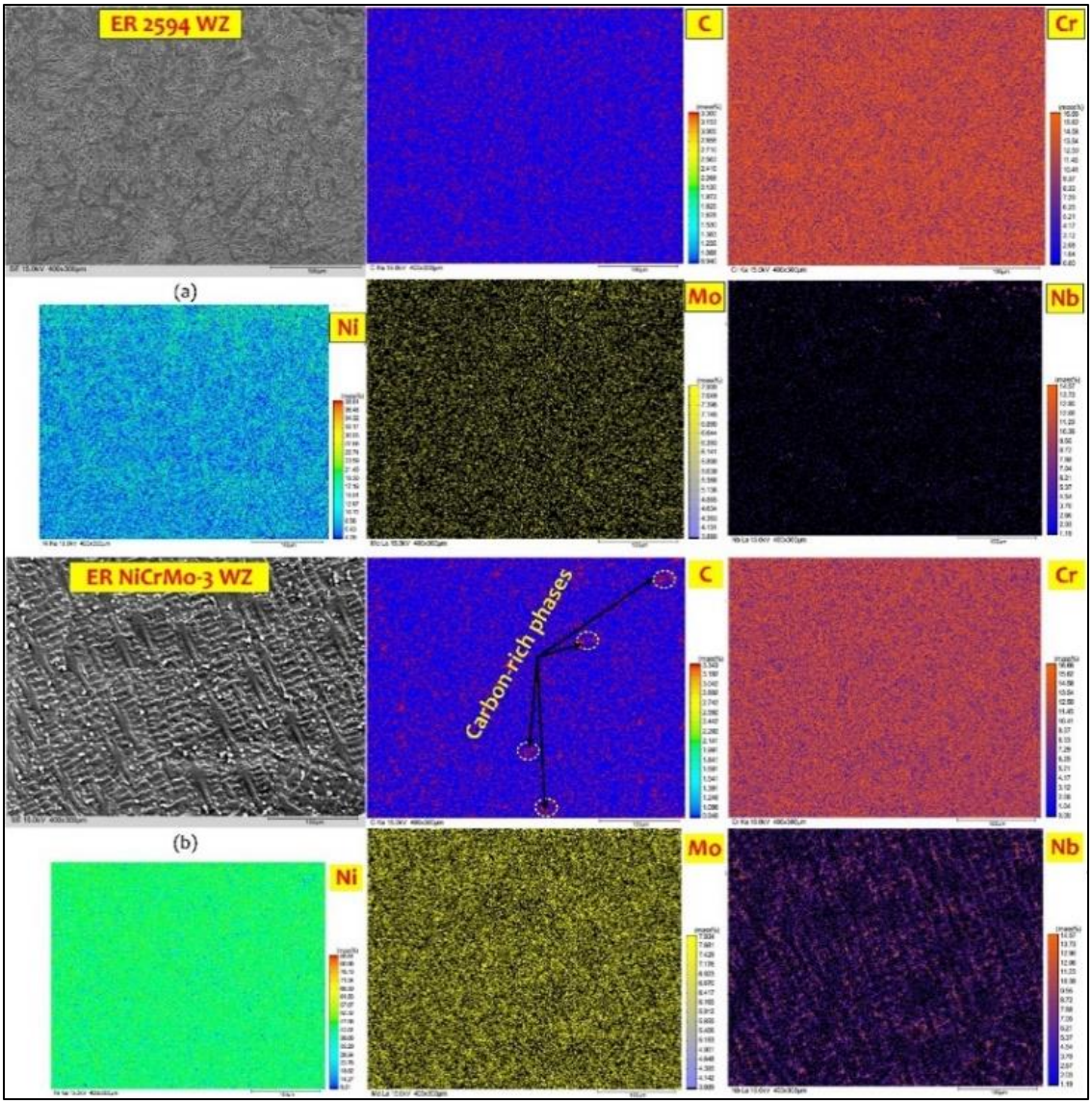

Figure 5.11 : EPMA analysis depicting the elemental distribution across the weld zone of (a) ER2594 filler, (b) ERNiCrMo-3 filler

Table 5.2 : EDS spectra of the indicated weld zone spot for ER2594/ERNiCrMo-3 filler metals

	ER2594 EDS spot spectra					*ERNiCrMo-3 EDS spot spectra*					
Elements (wt.%)	*1*	*2*	*3*	*4*	*5*	*6*	*7*	*8*	*9*	*10*	*11*
Cr	25.58	25.32	25.75	23.29	23.11	17.89	22.68	17.65	23.54	23.89	22.45
Ni	12.16	10.49	17.94	20.37	24.01	34.42	47.08	25.99	36.25	39.66	45.33
Nb	5.32	8.76	6.18	5.38	13.24	22.20	6.07	32.43	2.23	3.62	10.49
Mo	1.95	1.05	4.69	1.27	6.93	14.14	7.52	6.79	4.09	6.16	3.91
Si	0.73	0.62	0.70	0.63	1.28	0.84	0.65	0.71	0.41	0.43	0.46
Fe	54.25	53.33	44.74	49.07	31.42	10.51	16.01	16.43	33.39	26.24	17.34

5.1.2.4 EFFECT OF HEAT INPUT ON MICROSTRUCTURE EVOLUTION

The microstructure evolution of the weld zone and weld interface is significantly affected by heat input. The Cr_{eq} and Ni_{eq} have been calculated using an equation. 4.1 and 4.2 based on weld chemistry and OES chemical composition. The Cr_{eq}/Ni_{eq} ratios for weldments in the lower heat input (LHI) and higher heat input (HHI) states using ER2594 filler are 2.4 and 1.78, respectively. Interestingly, the HHI weldment solidifies in the ferritic-austenitic (F-A) mode, while the LHI weldment solidifies primarily in the ferritic (F) mode. For weldments employing ERNiCrMo-3 filler in both LHI and HHI conditions, the Cr_{eq}/Ni_{eq} ratios are 0.63 and 0.64, respectively. Weldments in both conditions using ERNiCrMo-3 filler solidify primarily in the austenitic (A) mode with 30% dilution.

Microstructural examinations of the welded joints reveal the effect of heat input on the ER2594 filler metal. Welding caused secondary phase production, reformed austenite, and ferrite grain growth in the sDSS 2507 HAZ. Higher welding heat inputs coarsened austenite grain and formed a partially melted zone on the IN-625 HAZ side. Due to the filler metal's higher liquidus temperature than the base metal, the IN-625 weld interface microstructure had peninsulas and islands. EDS and elemental line mapping confirmed the presence of unmixed zones (UMZ) on this interface, which revealed elemental variations along the peninsulas and islands. Furthermore, there were noticeable alterations in the weld metal's microstructure with different heat inputs. Due to faster cooling rates, higher heat inputs generated a multi-directional grain development pattern, whereas lower heat inputs resulted in finer cellular and columnar dendritic structures. An increase in heat input also led to an increase in base metal dilution, which changed the Ni content of the weld metal and affected its microstructure and solidification modes. Specifically, the austenite phase and various delta ferrites are generated from a partly duplex microstructure in the face pass. Further examination of the microstructure indicated the existence of unevenly dispersed Nb-rich Laves phases in the weld metal and IN-625 HAZ. Line mapping analysis showed Cr, Mo, and Nb enrichment and segregation at the weld interface. According to EDS, high heat input weldments had the highest weight % of Mo and Nb-rich phases in the inter-dendritic region. These results demonstrate the significant impact of heat input on the microstructural evolution and composition of both weldments.

An unmixed zone often forms because the base and filler metals have different chemical compositions and melting temperatures. Table 4.1 shows that the chemical composition of this study's ER2594 filler varied significantly from that of IN 625. Hydrodynamic mixing during welding produces a relatively homogenous chemical composition. When the base and filler metals differ significantly in chemical composition and melting range, only a tiny amount of the BM fully melts and re-solidifies without filler metal dilution, forming an unmixed zone. Under certain welding conditions, an unmixed zone can form due to inadequate fluid flow and mixing caused by convective currents (Dev et al., 2018). Because of the molten nickel alloy weld metal's sluggishness, Ni-based alloys are more likely to generate an unmixed zone than steel and stainless steel. (J. N. Dupont et al., 2011) reported incomplete welding mixing due to this. Process variables like viscosity also affect the formation of an unmixed zone. Figure 5.12 shows an island-like UMZ in the WZ's microstructure under both weldments. The peninsula is the BM away from the weld metal, whereas the island is in direct contact with it. Figure 5.12 also shows line mapping of the island and peninsula's microstructure to determine elemental migration. The island and peninsula showed significant migration of Cr, Ni, and Fe. It's noteworthy that neither weldment showed solidification or liquation cracking. Laves phase precipitation increases with heat input, reducing weldment ductility and toughness. This raises the risk of brittle fracture, particularly at lower temperatures. Nevertheless, LHI parameters can minimize laves phase precipitation, preserving the weld joint's ductility and toughness. Heat input affects laves phase precipitation differently depending on the alloy's welding circumstances and composition. The welded zone was heterogeneous, with chemical components like Cr, Ni, Fe, Mo, and Nb distributed unevenly.

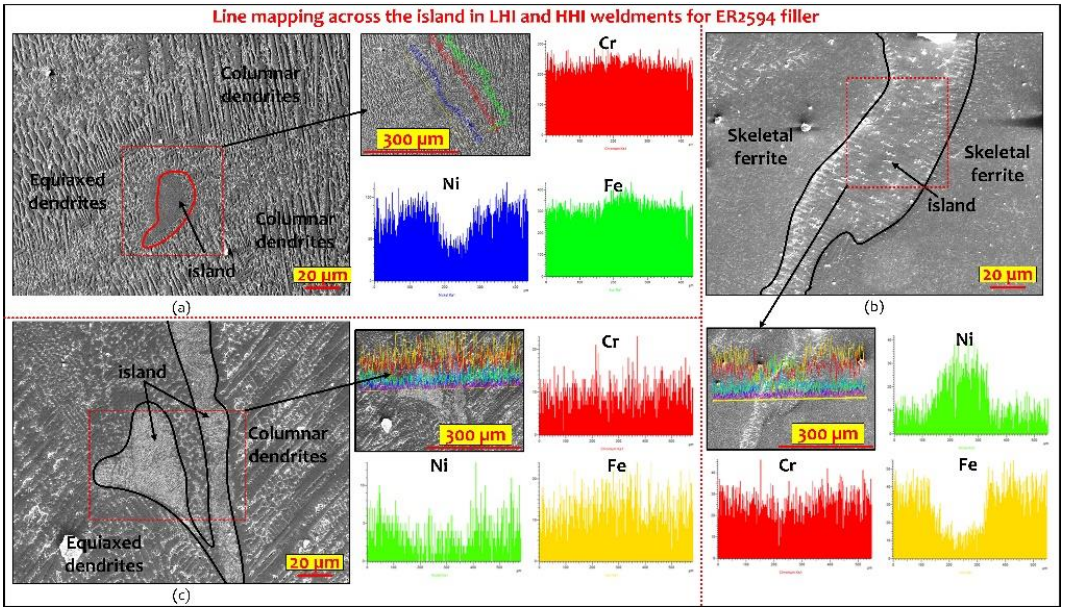

Figure 5.12 : Microstructure characterization and line mapping across the island in both weldments for ER2594 filler

Similarly, the microstructural differences observed clearly show the effect of heat input for ERNiCrMo-3 filler metal. The heating effect during welding passes caused variability in the LHI and HHI weldments' weld zones and the sDSS 2507 weld interface. The microstructure near the sDSS 2507 weld interface showed peninsulas and islands. EDS studies and elemental line mapping verified the elemental variation throughout the peninsula. Weld metal microstructure investigation showed an austenitic microstructure with columnar, equiaxed, and cellular dendrites. OM and SEM images of the weld fusion zone showed secondary phases rich in Nb and Mo around inter-dendritic zones, indicating solidification-induced Nb and Mo segregation. Both weldments had NbC and Laves phases with uneven morphologies in the interdendritic zones of cellular and columnar solidification. A study of the chemical composition revealed that the HHI weld zone was dominated by thick Laves phases with increased Mo concentration. The microstructure evolution also observed that the formation of islands and peninsulas resulted from variations in the mixing of components during welding. This island formation can be observed in the LHI and HHI weld zone's for ERNiCrMo-3 filler (Figures 5.13(a and b). It is significant to observe that no signs of solidification or liquation cracking have been seen in the ERNiCrMo-3 WZ. High heat input can lead to increased laves phase precipitation, which can reduce the ductility and toughness of the weldment. This can increase the risk of brittle fracture, particularly at low temperatures. On the other hand, LHI conditions can reduce laves phase precipitation, which can help maintain the weld joint's ductility and toughness. However, it is crucial to note that the exact effect of heat input on laves phase precipitation will depend on the alloy's specific welding conditions and composition. The welded zone was found to be significantly heterogeneous, with a non-uniform distribution of chemical elements like Cr, Ni, Fe, Mo, and Nb. The elemental line mapping in Figures 5.13(c and d) corroborates this finding by demonstrating that the weld zone and island have distinct elemental compositions. The island region showed higher concentrations of Fe, Cr, and Si and lower concentrations of Ni, Mo, and Nb. Further investigation through EDS mapping studies in Figure 5.13(e) reveals the occurrence of Nb and Mo-rich Laves phases in the welded zone. These precipitates increase the hardness of the welded zone but also accelerate crack initiation and propagation. These precipitates may alter the welded zone's mechanical properties; thus, more investigation is needed. The findings show that heat input affects microstructural evolution and secondary phase formation in dissimilar metal welds.

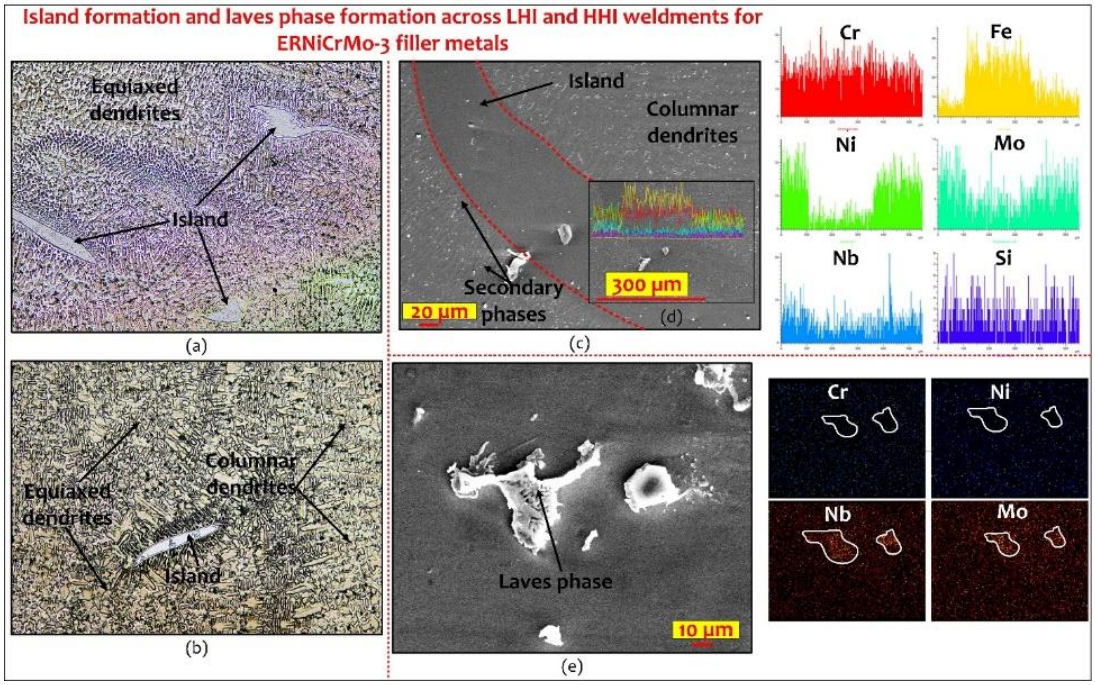

Figure 5.13 : Optical image shows island formation in weld zone of (a and b) LHI and HHI weldment, respectively (c-d) SEM micrograph and line mapping across the island, and (e) Area mapping of Laves phase

5.1.3 MECHANICAL CHARACTERIZATIONS

The microstructural characterization includes the effect of filler metal and heat input on the structural integrity of weld joints using microhardness, tensile, and impact test.

5.1.3.1 MICROHARDNESS

Microhardness results are shown in Figures 5.14 and 5.15 as a Matlab map and microhardness profile over the sDSS 2507/IN-625 weldment's cross-sectional area for filler metal. The position of the base metals, the HAZ region, and the weld zone were covered and evident through macrographs. In Figures 5.14(b) and 5.15(b), the matrix of measurement locations is displayed for ER2594 and ERNiCrMo-3 filler weldment, respectively. The sDSS 2507 BM and both filler weld metals were found to have a hardness value of more than the IN-625 BM. Microhardness measurements show that the IN-625 BM is typically about 265 ± 8 $HV_{0.5}$ on the scale, whereas the sDSS 2507 BM has an average hardness of 290 ± 10 $HV_{0.5}$. As a result, the IN-625 BM can be recognized as a weaker part in sDSS 2507/IN-625 DWJs. According to the microhardness map, sDSS 2507 BM shows superior hardness to IN-625 BM. (Ahmad et al., 2020) have also stated matching test results for both base metals. ER2594 and ERNiCrMo-3 weldments show microhardness variations of 304 ± 7 $HV_{0.5}$ and 290 ± 3 $HV_{0.5}$ in the sDSS HAZ and 282 ± 5 $HV_{0.5}$ and 280 ± 3 $HV_{0.5}$ in the IN-625 HAZ, respectively. Hardness has not been significantly reduced by grain growth in the HAZ of IN-625 for ERNiCrMo-3 or sDSS 2507 for ER2594 filler. The microhardness outlines demonstrate a distinct contrast between the weld zones of ER2594 and ERNiCrMo-3, with average hardness values of 310 ± 7 $HV_{0.5}$ and 270 ± 10 $HV_{0.5}$, respectively. The multipass welding process and heterogeneous microstructure, specifically the formation of reformed austenite and equiaxed dendritic microstructure for ER2594 filler, are the prime reasons for this heterogeneity. The weld zone microstructure is not homogeneous, which contributes to the variation in measured microhardness for ERNiCrMo-3 weldment. Low microhardness is due to the ERNiCrMo-3 weld zone's austenitic microstructure. Interdendritic element segregation promotes hard phases, but dendritic cores retain their nominal composition. Inconsistent constitutional cooling rates at the weld zone center and interface cause alloying element segregation, which defines the austenitic nature of the ERNiCrMo-3 filler WZ found in the current investigation. Referring to Figure 5.14(a), the middle of the cap pass of the ER2594 weldment has the highest hardness (i.e., 385.8 $HV_{0.5}$). The microhardness profile shows the weld zone hardness variation (from bottom to top) for both

filler weldments (Figure 5.14(a) and Figure 5.15(a)). The inhomogeneity of the ER2594 and ERNiCrMo-3 weld zones is shown by the higher microhardness of both filler welds at the top of the WZ than at the bottom. The microhardness value in the cap pass of ER2594 and ERNiCrMo-3 weldments shows a significant variation of 330 ± 6 $HV_{0.5}$ and 270 ± 5 $HV_{0.5}$, respectively. The WM's microstructural variability is corroborated by the cap pass regions of both weldments and the scattering of 60 $HV_{0.5}$. The microhardness value of the filler and backing pass of ER2594 and ERNiCrMo-3 weldments also shows a significant variation of 315 ± 4 $HV_{0.5}$ and 285 ± 6 $HV_{0.5}$, respectively, and 305 ± 8 $HV_{0.5}$ and 275 ± 6 $HV_{0.5}$, respectively. ERNiCrMo-3 weldments have comparable cap and root hardness values. In contrast, ER2594 weldments show a more significant variation in hardness values between passes. After the first pass, the root cools slowly, resulting in a more refined dendritic structure than the cap pass (J. N. Dupont et al., 1998). Evidence suggests that the cap-root temperature difference causes plastic deformation of the root (Sridhar et al., 2014).

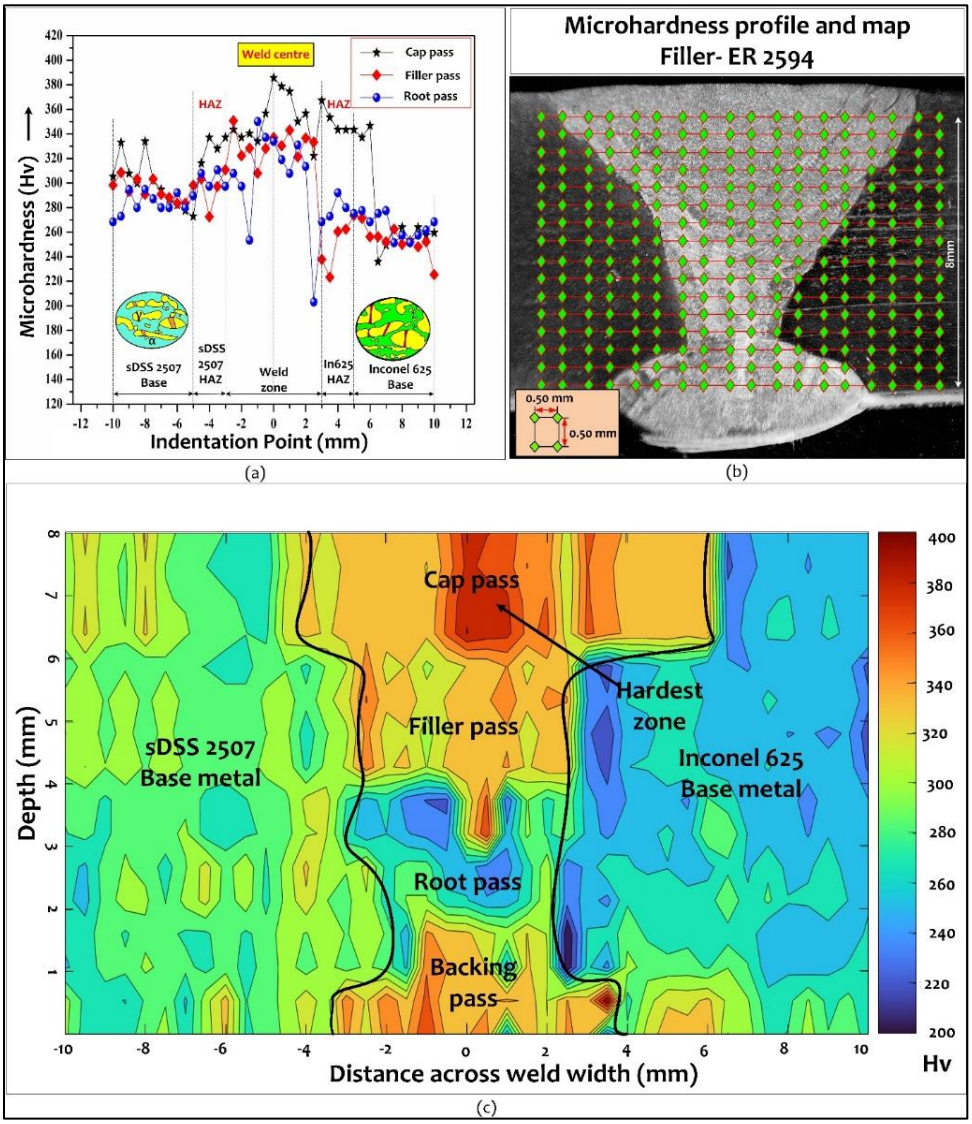

Figure 5.14 : (a) The microhardness profiles of ER2594 filler weldment's cap, filler, and backing pass, (b) Indentation measuring matrix for weldment of ER2594 filler, (c) Microhardness mapping shows the microhardness distribution across the ER2594 filler weldment

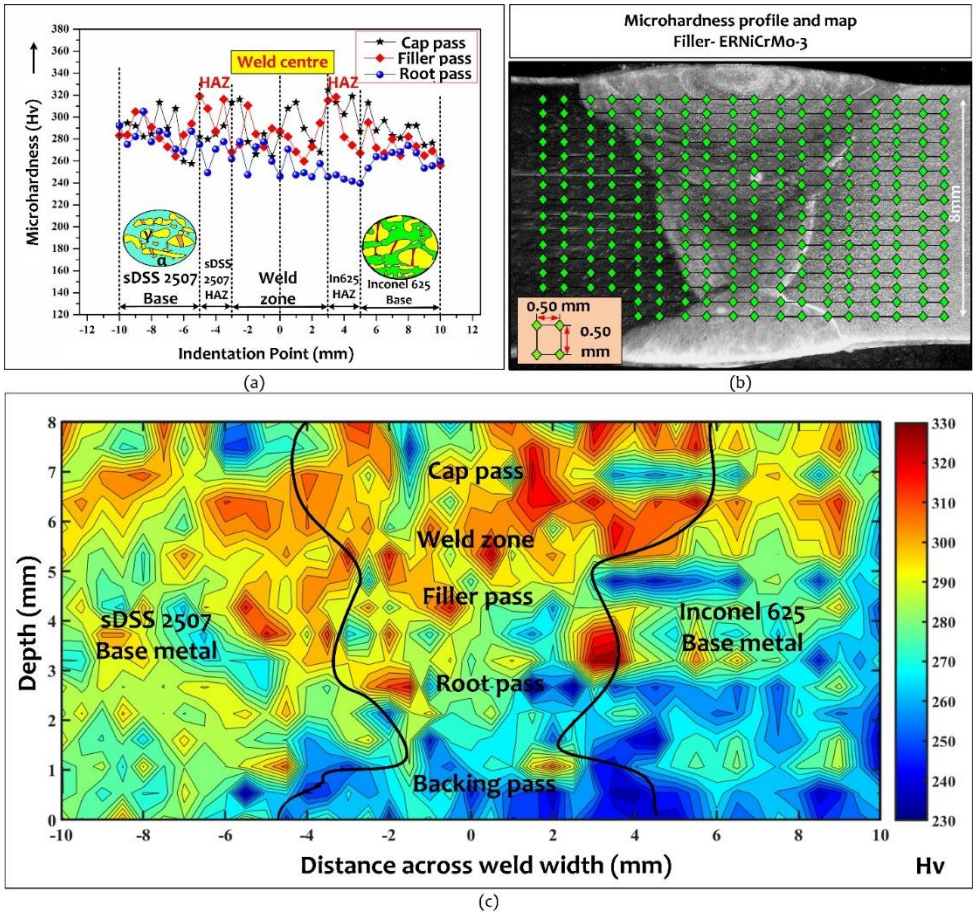

Figure 5.15 : (a) The microhardness profiles of ERNiCrMo-3 filler weldment's cap, filler, and backing pass, (b) Indentation measuring matrix for weldment of ERNiCrMo-3 filler, (c) Microhardness mapping shows the microhardness distribution across the ERNiCrMo-3 filler weldment

LHI and HHI weldments for ER2594 filler show microhardness variations of 310 ± 5 $HV_{0.5}$ and 290 ± 6 $HV_{0.5}$ in the sDSS HAZ and 280 ± 8 $HV_{0.5}$ and 295 ± 8 $HV_{0.5}$ in the IN-625 HAZ, respectively. A slight variance in HAZ microhardness depends on the microstructure of both weldments. Subsequently, the coarsening of grains and morphological changes in the HAZ account for most of the hardness value change. Hardness can be affected by the austenite to ferrite ratio, carbide distribution and shape variance, secondary phases formed in the WZ, and Cr content fluctuation in the sDSS 2507 HAZ and IN 625 HAZ. The weld zone hardness value ranged from 290–390 $HV_{0.5}$, averaging 310 ± 4 $HV_{0.5}$ for LHI and 300 ± 5 $HV_{0.5}$ for HHI. The microhardness investigation shows that weld zone hardness values for both heat input conditions show slight differences. The variation in microhardness typically reflects microstructural change during welding. The map clearly shows inhomogeneity in the microhardness of both weldments (Figure 5.16(a and b)). Table 5.3 summarises the variation in average microhardness values for both LHI and HHI in the cap pass, filling pass, and backing pass. LHI and HHI weldments show microhardness variations of 310 ± 5 $HV_{0.5}$ and 290 ± 6 $HV_{0.5}$ in the sDSS HAZ and 280 ± 8 $HV_{0.5}$ and 295 ± 8 $HV_{0.5}$ in the IN-625 HAZ, respectively. Table 5.3 also summarizes the variation in average microhardness values for both LHI and HHI in the cap pass, filling pass, and backing pass. In the cap pass (340 ± 5 $HV_{0.5}$ and 325 ± 6 $HV_{0.5}$) and backing pass (315 ± 6 $HV_{0.5}$ and 280 ± 10 $HV_{0.5}$) of LHI and HHI weldments, respectively, the microhardness value exhibits a substantial variation.

The microhardness variability in the WM is reflected in the scatter of 20–30 $HV_{0.5}$, which is also corroborated by the microstructural heterogeneity in the cap and backing pass region of both weldments. According to the microhardness profile, neither LHI nor HHI joints' base metal, HAZ, or weld zone exhibit any significant change in accordance with the hardness value. However, it is also clear that the hardness value decreases as the heat input increases. Several authors made a similar observation during their investigation (Kourdani & Derakhshandeh-

Haghighi, 2018b; Sadeghian et al., 2014; Vahman et al., 2020). The LHI weldment's cap pass measured a peak hardness of 385.8 $HV_{0.5}$, which was mostly caused by the formation of acicular and lathy delta-ferrite in the weld zone of the cap pass.

Table 5.3 : Average hardness value for both heat input weldments for ER 2594 filler

Hardness value ($HV_{0.5}$)	*Filler ER 2594 weldment*					
	Low heat input			*High heat input*		
	Cap Pass	*Filler Pass*	*Backing Pass*	*Cap Pass*	*Filler Pass*	*Backing Pass*
Average hardness of the weld zone	340±5	305±8	315±6	325±7	300±5	280±10
sDSS HAZ	315±4	285±5	280±6	325±6	290±8	285±5
IN-625 HAZ	345±6	265±7	270±4	310±5	300±7	280±6
Peak hardness at the weld zone	385.8	350.75	337.19	346.8	327.97	292.1

The sDSS 2507 HAZ indicates a minor change in hardness value for LHI and HHI weldment for ERNiCrMo-3 filler (i.e., 280 ± 8 $HV_{0.5}$ and 310 ± 4 $HV_{0.5}$, respectively). Similarly, the IN 625 HAZ exhibits minimal change in the hardness value of 285 ± 10 $HV_{0.5}$ for LHI weldment and 295 ± 7 $HV_{0.5}$ for HHI weldment. The variance in hardness is mainly attributable to HAZ's grain refinement and morphological growth. The hardness of the weld zone varied from 260–360 $HV_{0.5}$, with an average of 280 ± 6 $HV_{0.5}$ for LHI and 300±4 $HV_{0.5}$ for HHI. Microhardness testing demonstrates slight differences in weld zone hardness for both weldments. The heterogeneity in WZ microhardness could be attributed to several factors, including the welding process's multipass nature, the heterogeneous microstructure (dendritic, columnar, cellular), and the segregation of alloying elements. So, differences in WZ microhardness result from the anisotropy arrangement of solidification grain boundaries (SGBs), solidification subgrain boundaries (SSGBs), and interdendritic zones. The map demonstrates the heterogeneous microhardness distribution of the LHI and HHI weldment (Figure 5.16(c and d)). Average LHI and HHI microhardness values change across the cap, fill, and back passes listed in Table 5.4. The microhardness value varies significantly in the cap pass (270 ± 6 $HV_{0.5}$ and 315 ± 6 $HV_{0.5}$) and backing pass (275 ± 6 $HV_{0.5}$ and 310 ± 8 $HV_{0.5}$) of LHI and HHI weldments, respectively. The microstructural heterogeneity in both weldments' cap and backing pass supports the observation of a microhardness variation of 30-45 $HV_{0.5}$ in the WZ. Multi-pass welding and varied heat input may cause this scatter. The presence of more Nb produced more Nb-rich precipitates, which contributed to the cap pass's peak hardness of 356 $HV_{0.5}$ in the HHI weldment. The performance of the welded joint is unaffected by this hardness variation, maintaining the joint's structural integrity. It is also evident that the microhardness value increased with increased heat input.

Table 5.4 : Average hardness value for both heat input weldments for ERNiCrMo-3 filler

Hardness value ($HV_{0.5}$)	*ER NiCrMo-3 Filler weldment*					
	Low heat input			*High heat input*		
	Cap Pass	*Filler Pass*	*Backing Pass*	*Cap Pass*	*Filler Pass*	*Backing Pass*
Average hardness of the weld zone	270±6	285±8	275±6	315±6	300±5	310±8
sDSS HAZ	285±4	300±7	290±6	320±4	295±6	300±5
IN-625 HAZ	265±8	290±5	295±4	325±5	305±7	320±8
Peak hardness at the weld zone	310	319	313	356	324	356

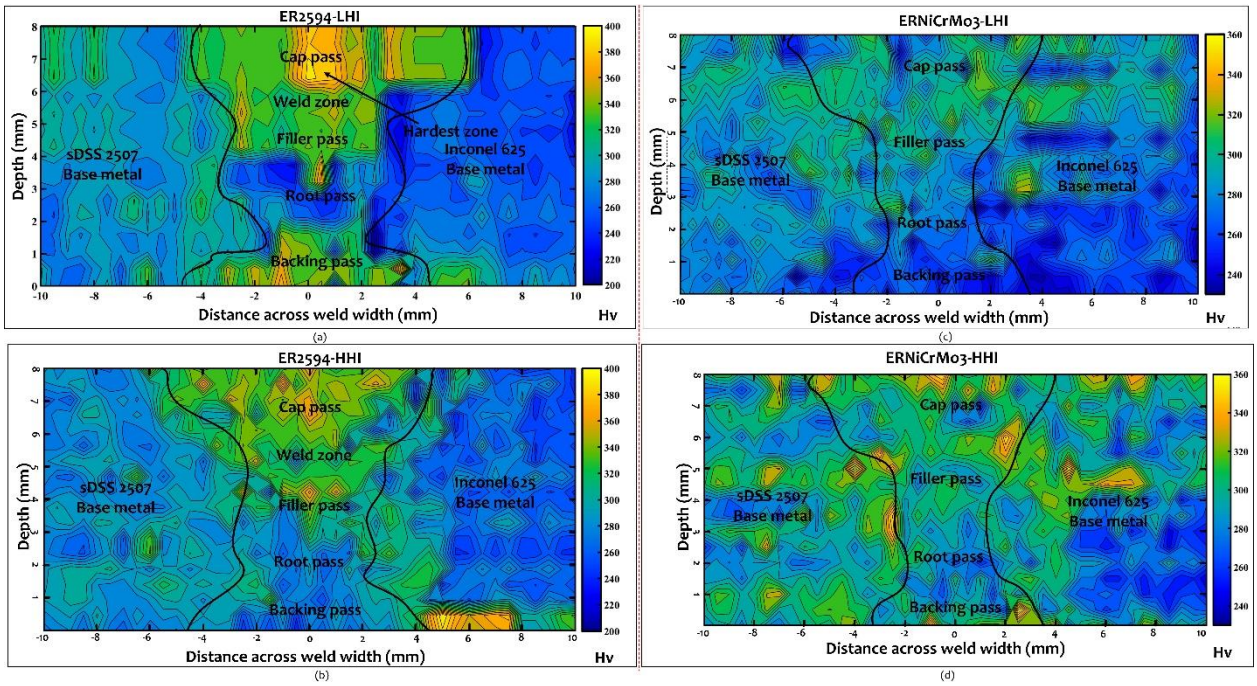

Figure 5.16 : The microhardness map of the weldment's cross-sectional area for (a and b) LHI and HHI weldment for ER2594 filler and (c and d) LHI and HHI weldment for ERNiCrMo-3 filler

5.1.3.2 *TENSILE TEST*

The sDSS2507/IN-625 DWJs' extracted coupons were put through a tensile test. Base metal ultimate tensile strengths (UTS) were measured to be 1000 ± 5 MPa for sDSS 2507 and 930 ± 7 MPa for IN-625 (Figure 5.17(a)). The UTS of ER2594 and ERNiCrMo-3 weldments were 750 ± 6 MPa and 790 ± 7 MPa, respectively. The welded joint's UTS and yield strength (YS) were found to be less than both BM. Mechanical properties of the sDSS 2507 and IN-625 BM exceeded the minimal requirements of ASTM A312/A790 and ASTM B829-19a, respectively. The welded joint mismatch was estimated using the WM to BM UTS ratio. Due to differences in chemical composition and solidification mode, the ERNiCrMo-3 filler welded joint has a higher UTS of 790.6 MPa, with a mismatch of 0.79 compared to sDSS and 0.848 compared to IN-625 BM. A mismatch of 0.75 with sDSS 2507 and 0.805 with IN-625 BM characterizes the welded joint made with filler ER2594, which has a tensile strength of 750.5 MPa (Table 5.5). ERNiCrMo-3 filler improves weld ductility over ER2594. The results for ER2594 weldment show that the weld breaks under conditions of local and uneven deformation without showing any obvious signs of ductility or plastic deformation (Figure 5.17(b)). The microhardness result, with its varying hardness value between zones, provides a similar characteristic. It provides a reasonable explanation for the location of the failure caused by the tensile load. Both filler weldment samples fractured from the weld zone, which featured a substantial concentration of macrosegregation and a noticeable PMZ presence. Figure 5.17(c and d) shows the typical stress-strain curve for sDSS2507/IN-625 DWJs with ER2594 and ERNiCrMo-3-ed coupons with their tensile properties, respectively. As per ASME Sec-IX BPVC, which regulates the acceptability of tensile test findings, "if the sample breaks from weld metal, the test shall be approved if the construction code approves the employment of weld with a weaker tensile strength at room temperature than BM." At the weld metal, both samples cracked during testing. Therefore, sDSS 2507/IN-625 DWJs can be used for both filler weldments, provided that the applicable construction standards permit this. SEM was used to evaluate the joints and base metal fractured tensile samples for fractography. The base metal and both weldments tensile tested specimens' SEM fractography (Figure 5.18). Figure 5.18(a and b) shows ductile and cleavage facets, dimples, macro and microvoids, and deep ductile tearing ridges in the fractured tensile specimen of both BM. Before fracture at different orientations, both base metals exhibited

adequate plastic deformation, indicating ductile fracture. According to the fractography results for the ER2594 filler-based DWJ in Figure 5.18(c), the hybrid failure mode is represented by the irregularly distributed dimples, cleavage facets, tear ridges, and voids. The presence of dimples, microvoids, and ductile tearing edges in Figure 5.18(d) suggest a dominant ductile failure mode, and the inclusion of Mo and Nb-rich phases in the ERNiCrMo-3 filler-based DWJ led to the higher UTS. The fracture surface is dominated by Mn, Ni, and Cr, according to the EDS data for both weldments, and their weight % match with the corresponding weld matrix (Figure 5.18(e and f). Therefore, it is possible to conclude that the filler composition significantly affects the tensile characteristics of the sDSS2507/IN-625 DWJs.

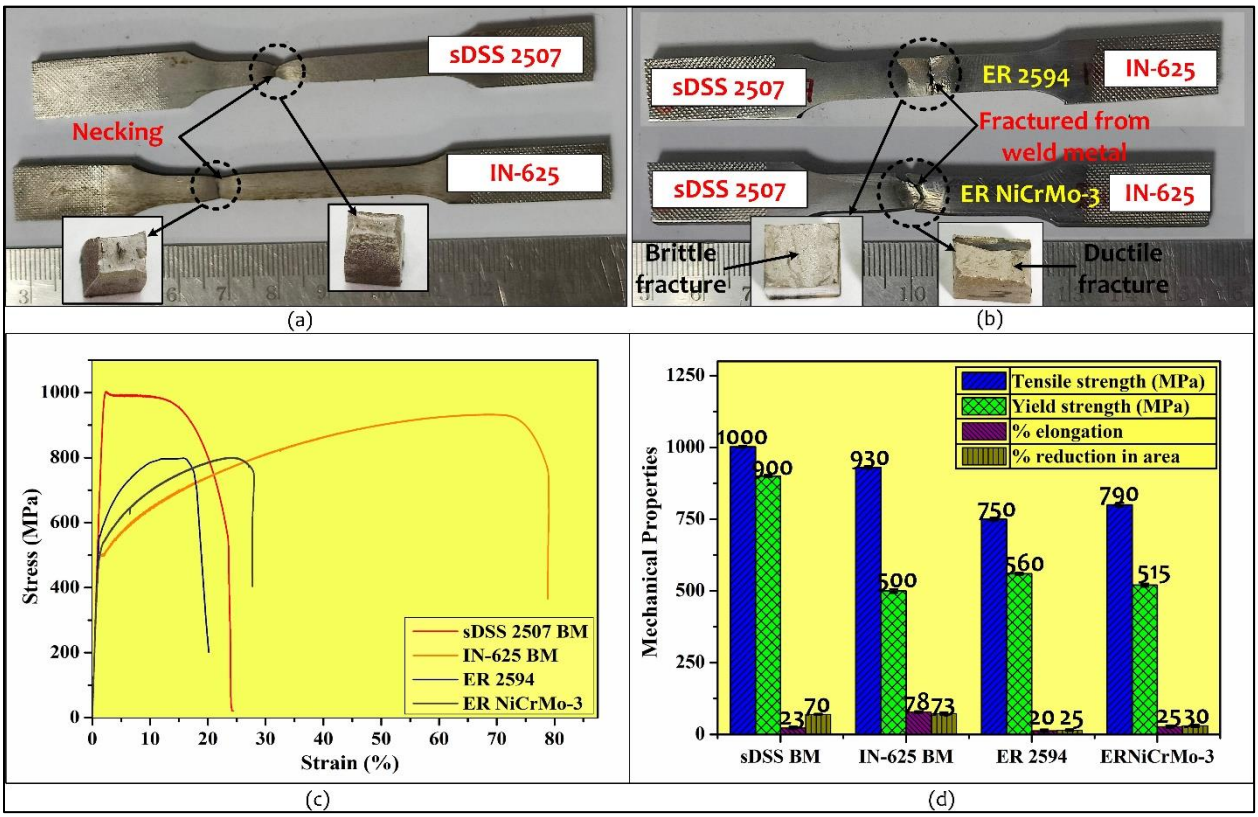

Figure 5.17 : (a and b) Tensile test specimens for base and weld metals before and after fracture, respectively (c and d) Engineering stress-strain curve and a comparison chart of the filler weldments as obtained by tensile testing, respectively

Table 5.5 : Detailed base and filler metal's tensile properties with weld mismatch

Samples	*Tensile Strength (MPa)*	*Elongation (%)*	*Weld mismatch with sDSS 2507 BM*	*Weld mismatch with IN-625 BM*	*Failure location*
sDSS 2507 BM	1002.5	27.8	--------	--------	--------
IN-625 BM	932.06	78.6	--------	--------	--------
ER2594 weldment	750.5	19.98	0.75	0.805	At weld center
ERNiCrMo-3 weldment	790.6	25.06	0.79	0.848	At weld center

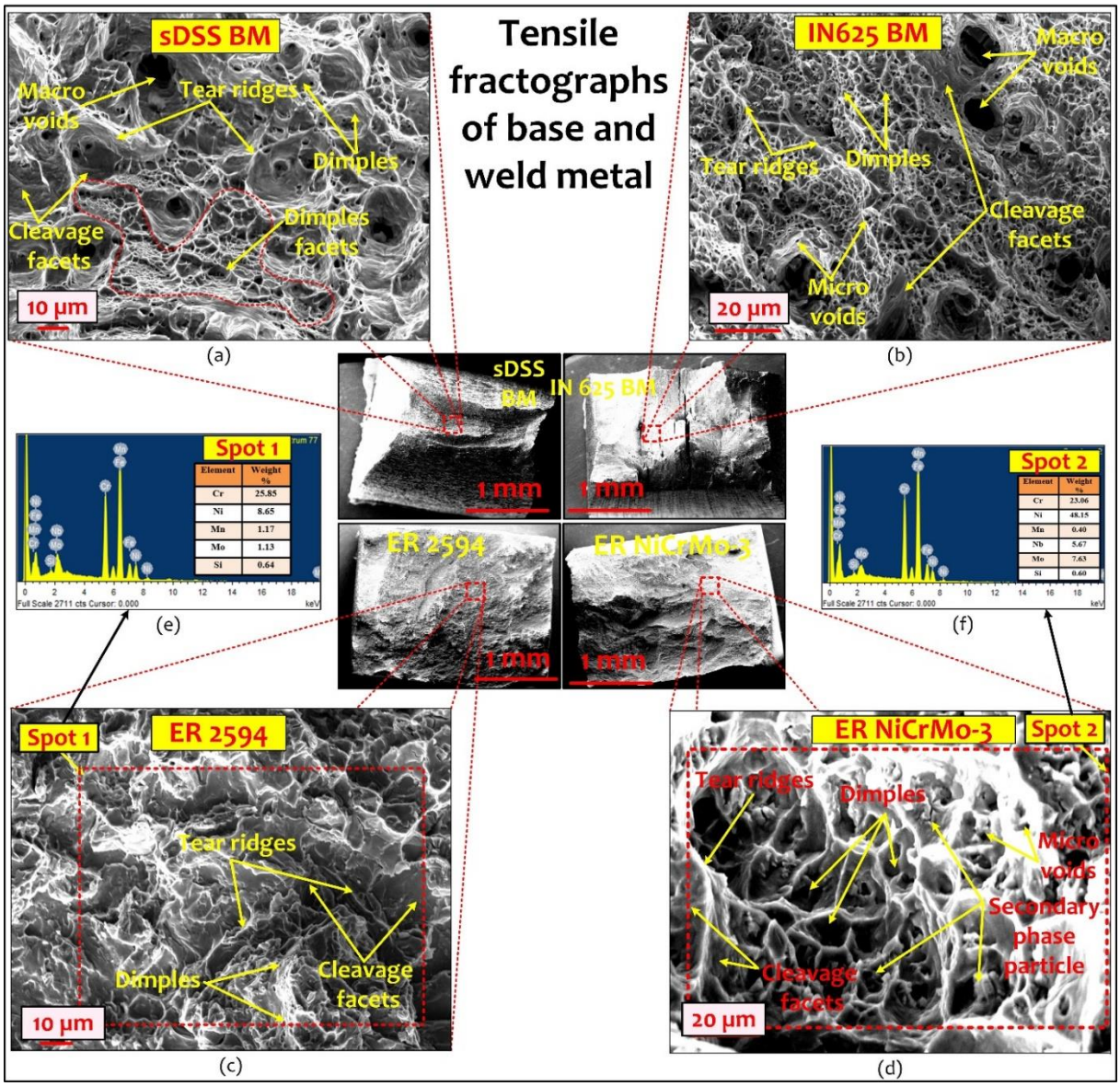

Figure 5.18 : SEM fractography image of the fractured tensile specimen for (a and b) sDSS 2507 and IN-625 BM, respectively, (c and d) ER2594 and ERNiCrMo-3 filler weldment, respectively, (e and f) LHI and HHI weldment fractured tensile sample's EDS spectra, respectively

Table 5.6 provides the strain (%), YS, and UTS, along with the weld mismatch for both LHI and HHI weldment for ER2594 filler. Weld mismatch values for sDSS 2507 and IN-625 are 0.79 and 0.86 for LHI and 0.73 and 0.79 for HHI, respectively, while the tensile strength of LHI weldment (798.5 MPa) is higher than HHI weldment (738.6 MPa). The ductility values for LHI and HHI samples were 20% and 18%, respectively. UTS and YS of tensile specimens decrease with increasing heat input. Slower cooling and increased heat input contribute to larger grain size in the weld zone. Hardness and cooling rate values are compatible with this. Figure 5.19(a) displays both weldments' after broken samples. Figure 5.19(c and d) displays the typical stress-strain curve, as well as a comparison chart of the filler weldments as obtained by tensile testing with LHI and HHI-ed coupons. The LHI and HHI specimens' UTS value was lower than the sDSS 2507 and IN-625 BM's. LHI and HHI weldments' average tensile strengths vary slightly. These findings demonstrate weld fracture under local and heterogeneous deformation circumstances without any noticeable signs of ductility or plastic deformation. The failure of both weldments also supports the results of the microhardness test. Figure 5.20(a-b) shows the fractography of the LHI and HHI weldment's fractured tensile surfaces. The failure mode seems to mix both ductile and brittle failures. Observation shows that failure happened on a nearly perpendicular plane. Shear ductility can be inferred from the presence of macro and microvoids and large dimples with a non-uniform distribution. Deep tear ridges and significant cleavage

facets indicate brittle failure, possibly due to abrupt crack propagation or insufficient weld interface bonding. Both weldments have substantially lower elongation than both BM, showing ductility decrease after welding. In the weld zone, the microstructure reveals γ_2 and precipitate particles and more WA. Secondary phases affect fracture behavior, whereas γ_2 and WA affect grain boundary migration and tensile strength. Secondary phases interact with huge dimples in the microstructure's arbitrary distribution. These subsequent phases promote fracture initiation. According to the EDS results for the LHI weldment, the fracture surface is dominated by the elements Cr, Ni, and Mn, and their weight percentages are identical to those of the weld matrix. However, the EDS of the fracture surface for the HHI weldment reveals the typical interface composition as described in the microstructural investigation. Therefore, it can be concluded that the heat input has minimal effect on the tensile characteristics of the sDSS2507/IN-625 DWJs.

Similarly, the LHI and HHI specimens for ERNiCrMo-3 filler broke from the weld metal. The LHI and HHI specimens' average UTS values were 800 ± 7 MPa and 857 ± 5 MPa, respectively. Values for average % elongation were found to be 27 ± 2% for LHI specimens and 29 ± 3% for HHI specimens. Tensile specimens' UTS and YS decrease as heat input increases. The weld region's grain size increases due to slower cooling and high heat input. This is compatible with cooling rate and hardness values. The WM's UTS ratio with the BM is used to compute the weld mismatch. For IN 625 BM, the mismatch values for LHI and HHI weldment are 0.85 and 0.91, while for sDSS 2507 BM, values are 0.80 and 0.86. The broken tensile specimens under LHI and HHI conditions are presented in Figure 5.19(b), demonstrating the sliding pattern in the LHI weld zone and the absence of necking and weld deformation. Figure 5.19(c and d) also shows typical stress-strain curves and a comparison chart of the filler weldments as obtained by tensile testing for the DWJs with LHI and HHI-ed coupons. The LHI and HHI specimens have lower UTS values than the sDSS 2507 and IN-625 BM. Both of the weldments' failures support the microhardness results. Due to Nb segregation and the creation of SGBs and MGBs, LHI weldments are weaker than HHI weldments. Fractography analysis was performed to ascertain the failure mode in broken tensile specimens. Figures 5.20(c and d) display the SEM fractography of the specimens used for both weldments' tensile tests. After investigation of the fractured LHI and HHI weldment specimens, the SEM fractograph can be seen to demonstrate the presence of dimples, cleavage facets, and microvoids with ductile tearing ridges, which indicate the primarily ductile failure mode. According to the LHI weldment's EDS data, the elements Cr, Ni, and Mn dominate the fracture surface, and their weight % matches the weldment matrix. However, the usual interface composition described in the microstructural investigation is confirmed by the EDS of the fracture surface for HHI weldment. Therefore, it can be said that the tensile properties of the sDSS2507/IN-625 DWJs are not significantly affected by the heat input.

Table 5.6 : Detailed LHI and HHI weldments for ER2594/ERNiCrMo-3 filler metal's tensile properties with weld mismatch

Specimen	*Tensile properties*				
	Tensile strength (MPa)	*Elongation (%)*	*Necking location*	*Weld mismatch with IN-625 BM*	*Weld mismatch with sDSS 2507 BM*
ER2594-LHI	798.5	2016	At weld center	0.86	0.79
ER2594-HHI	738.6	18.6	At sDSS 2507 HAZ side	0.79	0.73
ERNiCrMo3-LHI	798.6	27	At weld center	0.85	0.80
ERNiCrMo3-HHI	858.9	30	At weld center	0.91	0.85

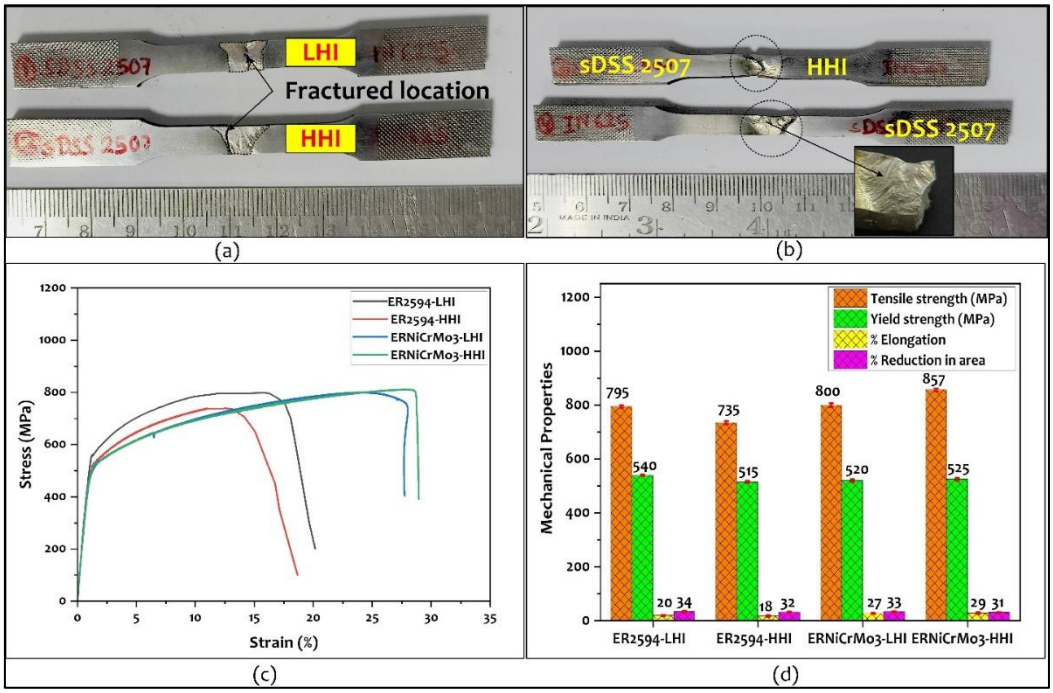

Figure 5.19 : (a and b) Tensile test specimens for LHI and HHI weld before and after fracture for ER2594 and ERNiCrMo-3 filler, respectively (c and d) Engineering stress-strain curve and a comparison chart of the filler weldments as obtained by tensile testing, respectively

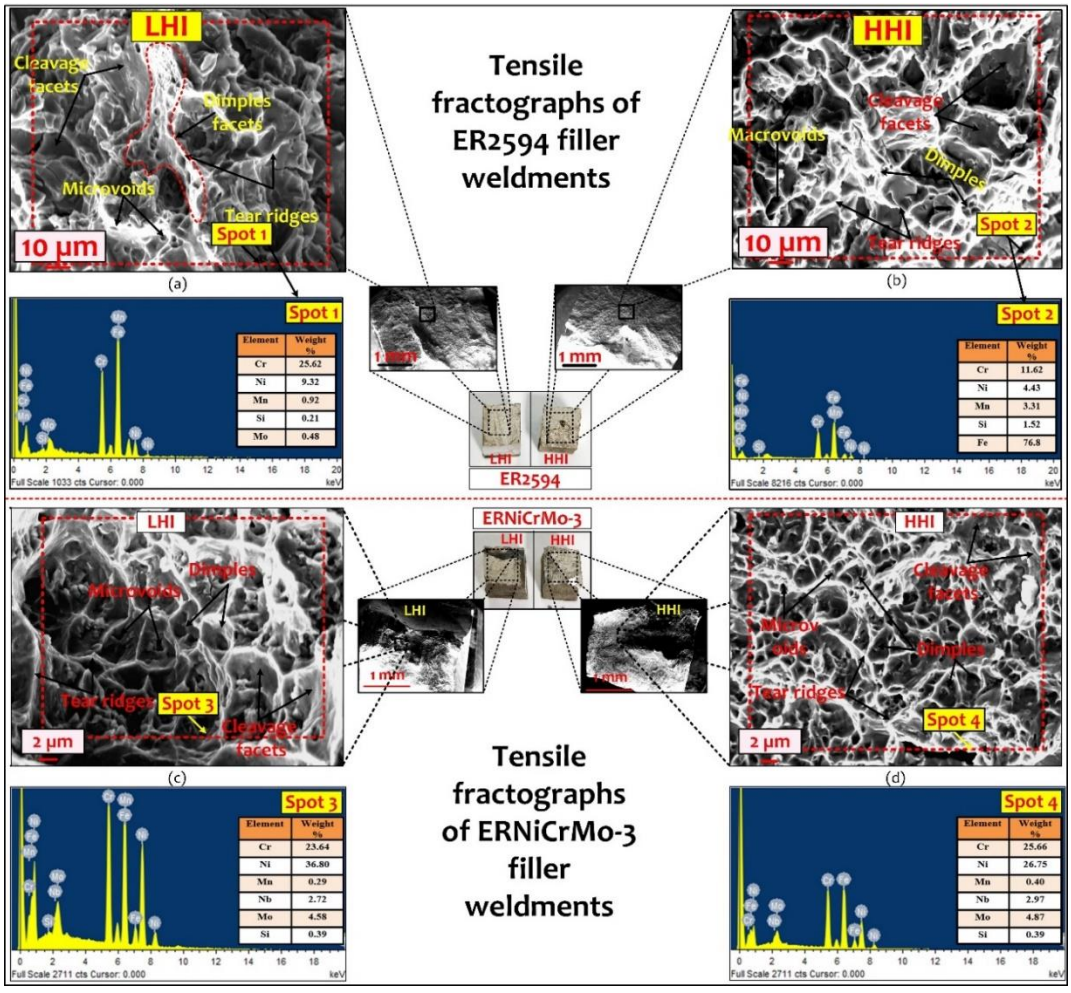

Figure 5.20 : SEM fractography image and fractured tensile sample's EDS spectra for LHI and HHI weldment for (a and b) ER2594 filler, (c and d) ERNiCrMo-3 filler, respectively

5.1.3.3 IMPACT TEST

At room temperature, an impact toughness test was performed to determine the impact toughness of the BMs and welded joints. The sDSS 2507 BM and IN-625 BM samples did not fracture completely, and only the notch deformation was detected. The impact toughnesses of the IN 625 and sDSS 2507 BM are 340 ± 3 J and 320 ± 5 J, respectively. Figure 5.20(a**)** shows the weld cap and root notch prior to the impact test. Figure 5.20(a) also includes an inset image depicting the fracture surfaces of all specimens after the impact test. ER2594 filler weldment's impact toughness for the V notch in the cap and root region was 100 ± 3 J and 110 ± 6 J, respectively, compared to ERNiCrMo-3's 165 ± 5 J and 180 ± 3 J. Results of the Charpy test were shown graphically in Figure 5.25(c)'s chart, showing variations in impact toughness along with the modes of failure for the two weldments. ER2594 WM's fractured specimen revealed a complete fracture with minimal plastic deformation, while ERNiCrMo-3 WM's lateral contraction in Figure 5.20(b) indicates the predominant ductile failure. The ER2594 WM was found to be the most susceptible to failure based on test findings since it had the lowest impact toughness. The Cr-rich ferrite phase and the imbalance from the required 50:50 δ/γ ratio appeared to be responsible. Diluting ER2594 filler metal with IN-625 BM produces WM with more Ni than sDSS 2507BM or the original filler metal. Ni's promotion of austenite alters the δ/γ ratio from 50:50. The Ni element enhances weld metal toughness; however, an uneven δ/γ ratio has deleterious effects. As a result, the specimens using ER2594 filler wire have lower impact resistance values. However, minimum impact toughness values of approximately 47 J ((EN ISO15614-1, 2017)) and 27 J ((DNVGL-OS-B101, 2015)) were suggested to meet the end application requirement for such a dissimilar joint for marine and offshore applications. Both filler weldments' resulting weld metal's impact toughness exceeds the 47 J criterion. SEM images of the typical fracture surfaces of a weld cap and weld root from a Charpy impact-tested specimen of ER2594 and ERNiCrMo-3 weld joint are displayed in Figure 5.20(c-f). The V-notch zone fracture lowers impact energy absorption in the notched samples at the weld cap and root for both filler weldments. Both filler weldments' impact toughness values fluctuate significantly due to the effect of filler composition on microstructure evolution. Fractography of the ER2594 fractured surface is shown in Figure 5.20(c and d), where microvoids and wedge cracks are present along with predominately brittle fracture with minimal area of ductile fracture. The fractographic features achieved in brittle fracture mode are cleavage facets and tearing ridge boundaries. However, the ERNiCrMo-3 weldments revealed dimples, the shear plane with dimples facets, micro- and macro voids with minimal cleavage plane, cracked boundaries, and layer debonding as fractographic features, indicating a predominant ductile failure (Figure 5.20(e and f)). The precipitation of intermetallic phases in the WZ, which acted as obstacles in the inter-dendritic zones, rendered the cracked boundaries unavoidable. The impact toughness of different weldments in Ni-based filler is influenced by the dendritic microstructure and alloying element segregation. (J. N. Dupont et al., 2011) also studied that the secondary phase precipitation lowers the weld joint's impact toughness in a Ni-based alloy. Also, (Sridhar et al., 2014) measured the low impact toughness for DSS/IN-625 DWJs.

Figure 5.22(a) includes an image depicting the fracture surfaces of all specimens after the impact test for ER2594 filler. Impact toughness for the weld cap and weld root specimen of LHI weldment was 95 ± 4 J and 105 ± 5 J, respectively, compared to 103 ± 5 J and 105 ± 3 J for HHI weldment of ER2594 filler. Test results showed that the WM of both heat input parameters was the most likely to fail due to reduced impact toughness compared to BMs **(**Figure 5.22(c)). The difference in impact toughness between the greatest (IN 625 BM) and lowest (LHI'weld cap) values is 245 J. The measurements reveal significant variations in impact toughness. The lower toughness value of sDSS 2507/IN-625 DWJs may be due to the formation of the Cr-rich ferrite phase and the imbalance from the ideal 50:50 ferrite to austenite ratio. IN-625 BM dilutes ER2594 filler metal to generate WM with a higher Ni content as sDSS 2507 BM or the ER 2594. The ratio of δ/γ is significantly different from 50:50 due to Ni's capacity to promote austenite. Although the Ni element increases the durability of the weld metal, the uneven δ/γ ratio has more significant detrimental consequences. The heat input variation slightly improves

impact toughness, while the chemical composition of the weld zone significantly affects toughness. Due to the intermetallic phases generated in the fusion line, the LHI weldment's impact toughness was lower than the HHI's. The presence of the Laves phase has been demonstrated to lower toughness. Long-striped phase shape and location near grain boundaries promote crack nucleation and propagation, lowering toughness. Impact toughness can be reduced due to a rise in matrix hardness brought on by grain refinement and Laves phase precipitation. Figures 5.22(d-g) display typical SEM images of the fracture surfaces of a Charpy impact-tested specimen's weld cap and weld root for LHI and HHI weldments, respectively. The fractured surface of the all-weld metal reveals brittle failure with cleavage facets, intragranular wedge cracks, and tearing ridges. However, the mechanical characteristics of the material are affected by the inherent residual and thermal stresses during welding with various phase transitions, making it impossible to describe the decreased impact toughness based on fractography results alone.

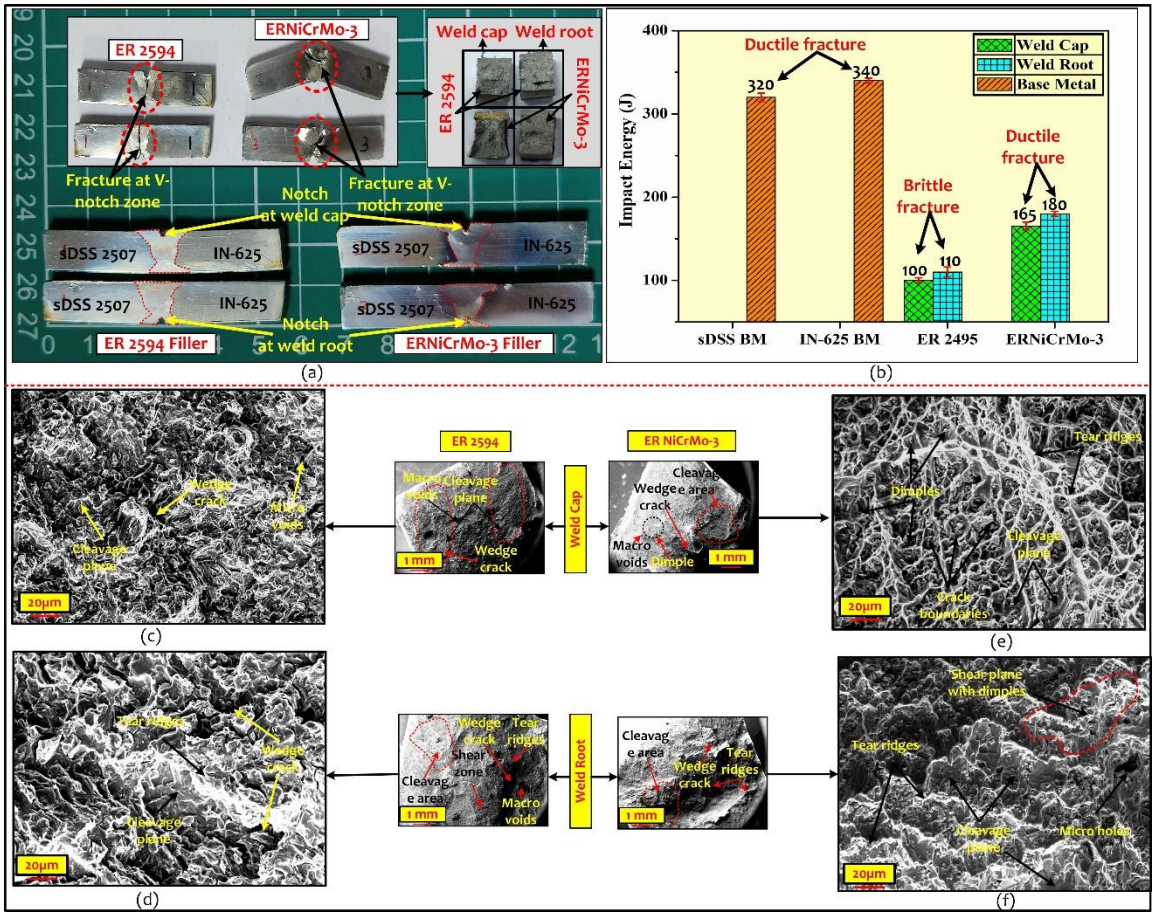

Figure 5.21 : Impact toughness test specimens of the weldment using ER2594 and ERNiCrMo-3 filler: (a) weld cap and root impact specimen before and after the test, and (b) Schematic of base metal and filler weldment's impact test results and failure mode, SEM fractographs of weld cap and weld root for (c and d) ER2594 respectively, and (e and f) ERNiCrMo-3 filler, respectively

The schematic graph of the impact toughness value, shown in Figure 5.22(c), also illustrates the failure mode. In the welded state, the ERNiCrMo-3 filler's impact toughness is enhanced, although it is still significantly inferior to the base metal. Impact toughness for the LHI weldment was 155 ± 3 J and 160 ± 2 J for the cap and root regions, respectively, while it was 185 ± 7 J and 195 ± 3 J for the HHI weldment. Both weldments with ERNiCrMo-3 filler had lower impact toughness due to the intermetallic phases in the interface affecting fracture behavior. Toughness values tend to increase as the cooling rate increases due to changes in heat input. Heat input affects microstructure evolution and impacts toughness value. The Laves phase and Mo concentration in the weld zone give HHI better impact toughness than LHI. As a result of the Laves phase formation, the toughness value decreases. Laves phases with long-

striped morphology and near-grain boundaries strongly participate in fracture formation and propagation, reducing toughness. Supercooling during solidification gave HHI weldment finer grain size and more intensive precipitate precipitation, increasing impact toughness compared to LHI. Figure 5.23 illustrates notch impact testing SEM fractographs of weld metal fracture surfaces. Both weldments have a dendritic and cellular solidification structure, and the SEM image demonstrates that precipitates contained in a dendritic core produce microvoid coalescence. The fractured surface of the all-weld metal indicates a predominant ductile failure, which exhibits dimples, the shear plane with dimple facets, wedge cracked boundaries, and layer debonding as fractographic features (Figure 5.23(a-d)). It is impossible to explain the lower impact toughness based solely on fractography results because the existing residual and thermal stresses influence the material's mechanical properties during welding with different phase transitions.

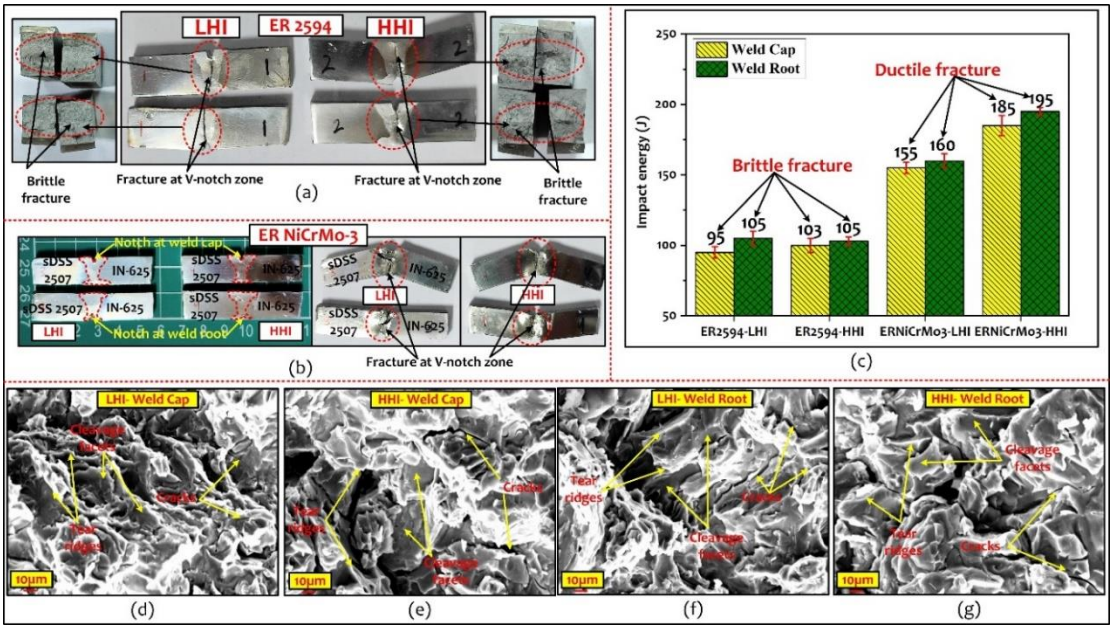

Figure 5.22 : (a and b) Impact toughness test for weld cap and root specimens after LHI and HHI weldment with ER2594 and ERNiCrMo-3 filler, (c) Schematic of LHI and HHI weldment impact test results and failure mode, and (d-g) SEM fractography of weld cap and weld root for LHI and HHI weldment of ER2594 filler, respectively

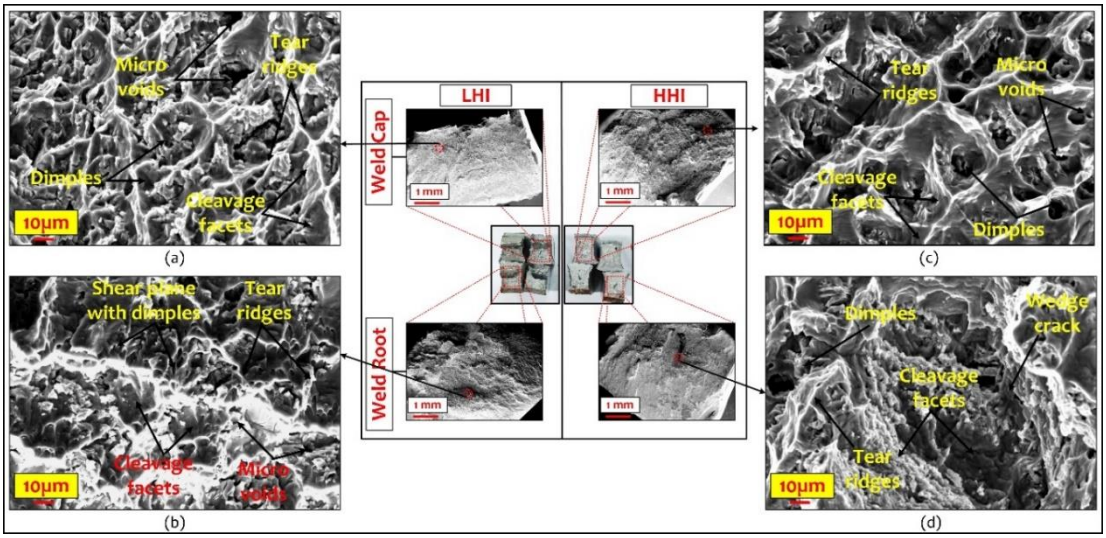

Figure 5.23 : SEM fractographs of (a and b) weld cap and (c and d) weld root for LHI and HHI weldment of ERNiCrMo-3 filler, respectively

5.1.4 RESIDUAL STRESS MEASUREMENT

The most precise experimental method for evaluating residual stresses caused by welding is generally regarded as the deep-hole drilling (DHD) technique. Figure 5.24(a) shows the through-thickness residual stress distribution in the weld zone for both filler weldments. ERNiCrMo-3 and ER2594 had a compressive residual stress of 168 MPa and 33 MPa at the filler pass, respectively, and a tensile residual stress of 591 MPa and 481 MPa near the weld cap at 3 mm. The ER2594 and ERNiCrMo-3 WZ's solidification modes, ferritic or austenitic, were connected to shrinkage and tensile residual stresses. At 3 mm depth, the ER2594 filler exhibited a peak transverse residual stress of 250 MPa, while the ERNiCrMo-3 filler had 560 MPa. At the root pass of the ERNiCrMo-3 filler, compression transverse residual stress reached 88 MPa at 7 mm, which changed to tensile in the backing pass of the weld zone. Although the DHD approach may not provide location-specific data, it does offer realistic and consistent measurements of welding-induced residual stress. Weld zone contraction and expansion are affected by cooling rates, phase transitions in weld joints, and multiple heat cycles during filler deposition (Skouras et al., 2013). Figure 5.24(b) depicts the results of this investigation using the DHD technique to analyze transverse and longitudinal residual stresses in both weldments for ER2594 filler. The study's results showed that along the thickness of the plate, the filler-to-backing pass had the highest tensile residual stress. The highest longitudinal tensile stress observed at 3 mm was 423 MPa for the LHI state and 491 MPa for the HHI state.

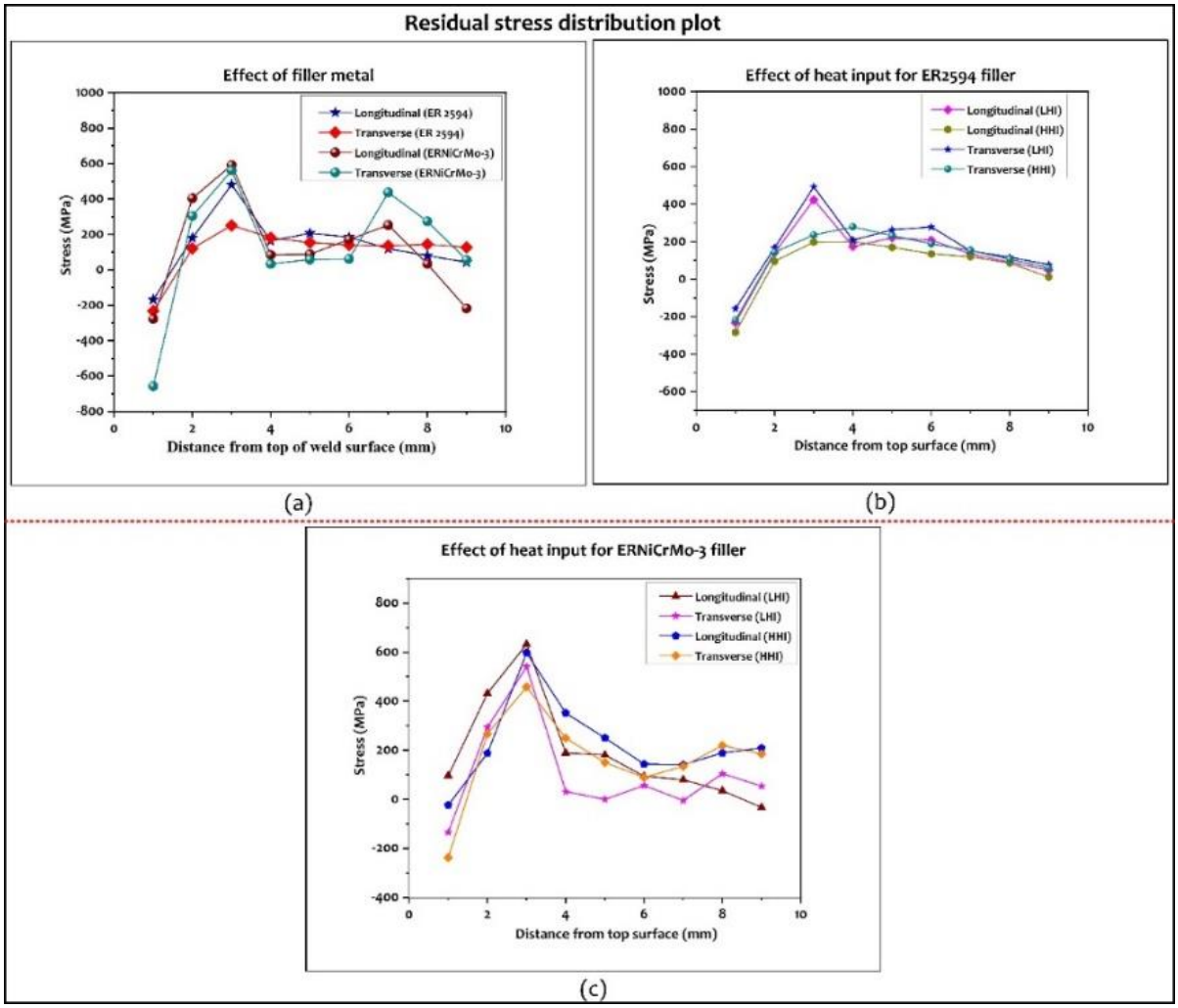

Figure 5.24 : Residual stress distribution plot in weld zone for (a) both filler metal, (b) effect of heat input for ER2594 filler, and (c) effect of heat input for ERNiCrMo-3 filler

Both weldments' filler passes had the maximum residual stress. The weld zone had predominantly tensile transverse residual stresses, with the LHI state's highest level at 198 MPa and the HHI states at 235 MPa at 3 mm. Both the LHI and the HHI joints had substantial

differences in the residual stresses along the thickness of the welded plate, with the HHI weldment showing larger residual stress magnitudes in both the tangential and longitudinal directions. High heat input increased longitudinal and transverse residual stress by 16% and 19%, respectively. Figure 5.24(c) depicts the results of calculated longitudinal and transverse residual stresses in the LHI and HHI states for ERNiCrMo-3 filler. Along the plate's thickness, the filler-to-backing pass had the highest tensile residual stress. At a depth of 3 mm, the highest longitudinal tensile stress of 471 MPa for the LHI state and 583 MPa for the HHI state was measured. In both weldments' filler passes, residual stress was highest. The transverse residual stress was mainly tensile, with a peak value of 301 MPa in the LHI state and 488 MPa in the HHI state at a depth of 3 mm.

5.1.5 TRIBOLOGICAL INVESTIGATIONS

The tribological investigation examines erosion behaviors, aiding material selection, optimizing heat input, and enhancing wear resistance in sDSS 2507/IN-625 DWJs for sub-sea manifold applications.

5.1.5.1 SLURRY EROSION CHARACTERIZATION

Figure 5.25 correlates slurry concentrations with all specimens' cumulative weight loss and erosion rate. The findings of the erosion wear characterization conducted using a slurry pot under different slurry concentrations align with the observed hardness trend in both the base metal and weld zones. It shows that the weight loss significantly increased for all specimens as slurry concentration was increased. In 10 wt.% slurry concentration testing, the sDSS 2507 BM lost 0.245 g, and the IN-625 BM lost 0.285 g (Figure 5.25(a)). Due to work hardening, changes in hardness, and microstructural evolution, IN-625 BM experiences more significant weight loss than sDSS 2507 BM. Work hardening makes particles less likely to cause significant deformations or fractures by increasing material strength and hardness. This reduces particle agglomeration, clustering, and abrasive particle impacts, reducing material removal and weight reduction. The weight loss plots against hardness show that the ER2594-LHI (0.14 g) and ERNiCrMo-3-LHI (0.13 g) weld joints have the lowest erosion wear, while the wear remains in the same range and is higher for the corresponding ER2594-HHI and ERNiCrMo-3-HHI weld joints. Low heat input welding causes more uniform microstructure, smaller grain sizes, and higher mechanical performance. These characteristics improve slurry wear and particle impact resistance, reducing weight loss. Under 30 wt.% slurry concentration testing, the higher slurry concentrations generate significant weight loss in slurry erosion tests due to sand particle density, particle-to-surface contact, particle interactions, and fluid effects. Significant weight loss is seen in IN-625 BM (0.38 g) compared to sDSS 2507 BM (0.30 g) (Figure 5.25(b)). A similar trend was observed in the case of ER2594-LHI and ERNiCrMo-3-LHI, which led to a lower volume loss than HHI weld joints. Therefore, it can be inferred that all specimens' erosion-wear resistance is influenced primarily by their hardness value.

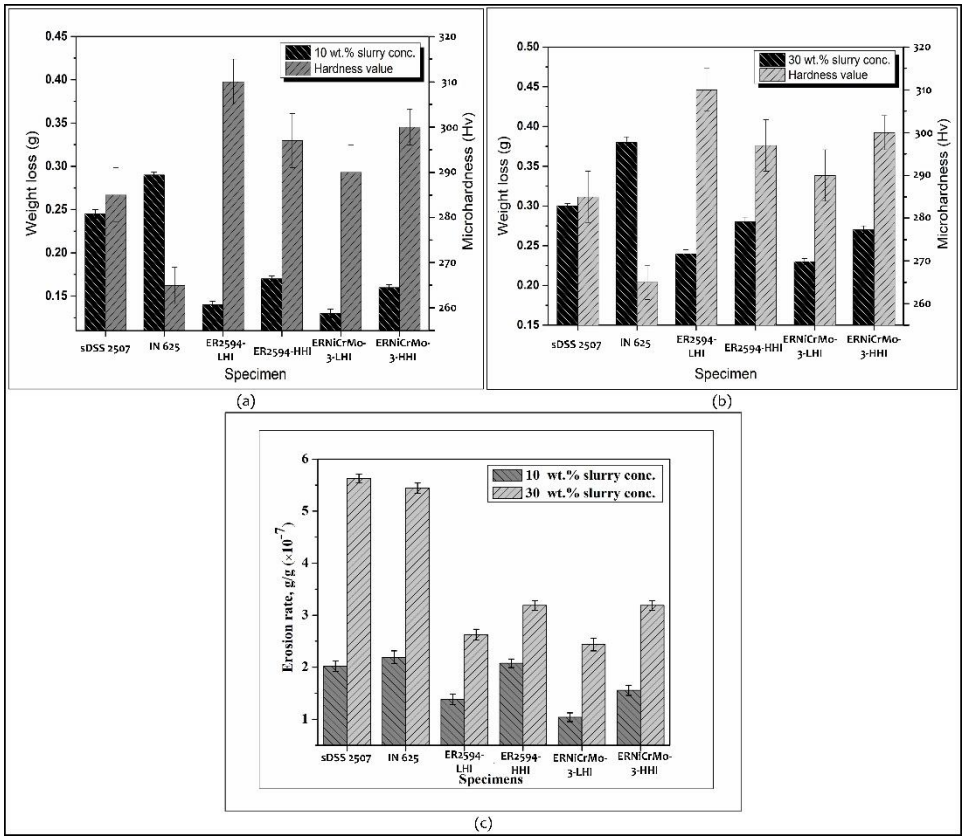

Figure 5.25 : Microhardness and weight loss for the tested specimen (a) 10 wt.% slurry concentration, (b) 30 wt.% slurry concentration, and (c) Variation in erosion rate with varying slurry concentrations for all specimens

Figure 5.25(c) plots the average slurry-erosion rates of all specimens against slurry concentrations. As the slurry concentration in the mixture rises, more particles will strike the surface, increasing erosion wear. Thus, the erosion rate rises with slurry concentration (Desale et al., 2008). Erosion wear rises at a slower rate than the amount of striking sand particles in a solid-liquid mixture does when the slurry concentration rises. It's necessary to understand that the correlation between slurry concentration, weight loss, and erosion rate is unlikely to be linear. This could be caused by particle aggregation, impact energy, or material response. At high slurry concentrations, abrasive particle agglomeration forms more significant masses that produce more deformities and fractures, culminating in higher weight loss. But, since they collide less frequently, larger masses erode at a slower rate. Additionally, the energy delivered to each particle at higher slurry concentrations could decrease, leading to a reduced erosion rate. Still, a higher percentage of particle hits can cause more weight loss. And finally, the eroding material reacts differently depending on the slurry concentration. The material's microstructure, mechanical qualities, or composition may render it more prone to wear or degradation at high slurry concentrations, resulting in more weight loss. Particle rotation makes sharp cutting edges, increases contact points fragments particles, induces chemical interactions, accelerates fatigue and crack propagation, affects slurry velocity, alters surface texture, and is influenced by material microstructure and hardness (Prasad et al., 2004). Despite the higher weight loss, the material might also have a more robust surface or a mechanism that restricts the overall erosion rate. The current experiment found that as slurry concentration increased, the erosion rate considerably increased. Several researchers observed a comparable phenomenon (Dasgupta et al., 1998; Lindgren & Perolainen, 2014; Nguyen et al., 2014). This study discovered that the slurry erosion resistance increased as the hardness of both BM decreased. Due to its hardness and microstructural evolution, BM's slurry erosion rate and cumulative weight loss increased. ER2594-LHI and ERNiCrMo-3-LHI specimens had lower slurry erosion rates than both BM, showing greater resilience to slurry erosion. HHI welded joints for both filler metals exhibit a comparable erosion rate trend to LHI welded joints.

5.1.5.2 *SLURRY EROSION MECHANISM*

SEM analysis of all eroded samples reveals varied material removal methods caused by sand particle sharpness and collision trajectory on different sample surfaces. Thus, impact energy varies, causing sample surface erosion rates to vary. Pit-like damage implies considerable material removal owing to sand particle erosion. In the specimens, craters appear across a number of phases of development, including material loss brought on by fatigue processes initiated by repeated plastic deformation. These craters on the specimen's surface were formed in part due to the impact of sand particles. The specimens' lips around the craters indicate plastic deformation. This material loss takes the form of fragments. Figure 5.30 schematically illustrates the effect of slurry concentration on the erosion mechanism. However, comparing the micrographs shows no substantial difference in erosion mechanism due to slurry concentration. Combinations of micro-cutting and ploughing modes served as the primary method for material removal for both the base metal and the weldments. Deep micro-cutting was also observed, which caused a large amount of material loss by removing material from the surface through shearing action. Figure 5.30(a) shows the volume of material separated out by an edged sand particle. Hutchings and Levy's earlier research has shown that when spheres or other rounded particles strike a surface, the material is dispersed and accumulates where the particle escapes (Hutchings & Winter, 1974; Levy, 1986). This method of material removal is commonly referred to as ploughing (Figure 5.30(b)). Figure 5.30(c) shows that debris is unlikely to remain attached to the crater. Micro-cutting and ploughing are likely to be involved in the erosion process when the particle shape is somewhere between the highly sharp and blunt type. In such instances, shearing action and particle displacement generate a mixed method of material removal. Figure 5.30(d) illustrates a mixed cutting-ploughing mechanism where the material is initially removed through cutting but is later deformed plastically due to the subangular shape of the sand particles. As a result, the initial shearing is likely to be accompanied by plastic deformation. Additionally, the existence of this mode proved to be more beneficial than either pure ploughing or microcutting. Figure 5.31 and Figure 5.32 illustrate the effect of concentration on the erosion mechanism. Nevertheless, a comparison of the micrographs reveals that concentration has no discernible effect on the erosion mechanism. The material was removed by crater formation, deep micro-cutting, ploughing, and mixed cutting-ploughing mode.

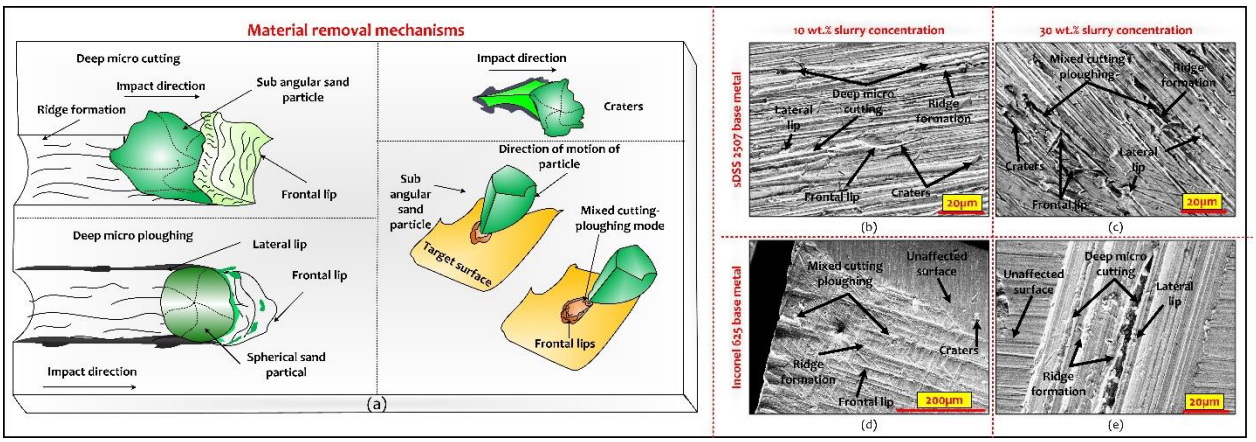

Figure 5.26 : (a) Schematic of ideal material removal processes: micro-cutting, ploughing, craters, and mixed cutting-ploughing mode, SEM image of the eroded surface after erosion tests at 10 and 30 wt.% slurry concentration of (b and c) sDSS 2507 BM and (d and e) IN-625 BM, respectively

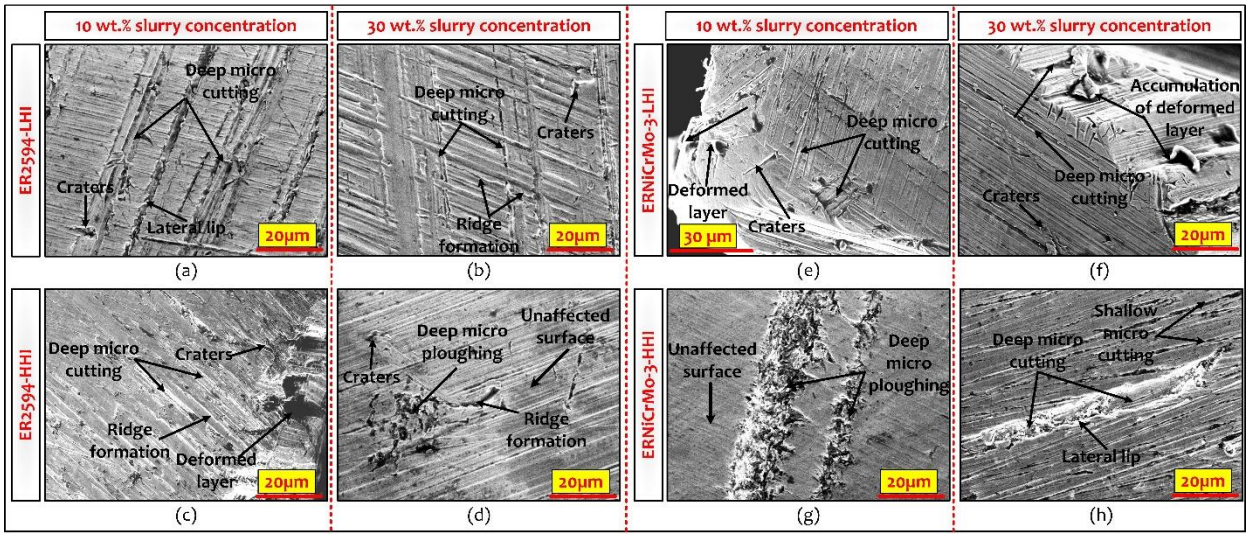

Figure 5.27 : SEM image of the eroded surface after erosion tests at 10 and 30 wt.% slurry concentration of (a-b) ER2594 LHI, (c-d) ER2594 HHI, (e-f) ERNiCrMo-3 LHI, (g-h) ERNiCrMo-3 HHI, respectively

5.1.6 CORROSION INVESTIGATIONS

This study on corrosion-resistant alloys for severe marine conditions is crucial. Structural integrity for the sDSS2507/IN-625 DWJs in severe marine conditions is ensured by addressing the effect of precipitation on corrosion in both the weld and the base metals.

5.1.6.1 COMPLETE IMMERSION TEST

A full immersion test was performed on the specimens, and then visual inspections were carried out to detect corrosion-related surface damage. Fig. 5.28(a) shows the 60-day visual inspection results for all samples in 3.5 wt.% NaCl solutions after continuous immersion corrosion test. Additionally, the scale on the exposed parent metal surface was visually assessed after three days of immersion to identify any changes. Visual inspection reveals that corrosion is relatively minor in all specimens, primarily due to the high corrosion resistance of sDSS 2507 and IN-625 BM. The weight loss analysis and corrosion rates show that pitting corrosion is more likely to occur in sDSS 2507 base metal and overmatching ER2594 filler weldments than in IN-625 base metal and its matching overmatching ERNiCrMo-3 filler weldments. Table 5.7 tabulated the weight loss and corrosion rate results from the complete immersion corrosion weight loss test. Therefore, the plot strongly suggests that IN-625 base metal and its overmatching filler weldments have better corrosion resistance than sDSS 2507 and ER2594. SEM images of all samples following corrosion are shown in Fig. 5.28(b-e). The samples' smooth surfaces with occasional pits or fissures indicate minor deterioration. Their excellent corrosion resistance is highlighted by the overall surface's remarkable smoothness and lack of shedding.

Table 5.7 : Weight loss and **c**orrosion rate results for all specimens in 3.5 wt% NaCl solution

Specimen	*Weight loss (g)*	*Corrosion rate (mm/year)*
IN-625 BM	0.0001	0.000755
sDSS 2507 BM	0.0002	0.00151
ER2594-LHI	0.0002	0.00151
ER2594-HHI	0.0002	0.00151
ERNiCrMo-3-LHI	0.0001	0.000755
ERNiCrMo-3-HHI	0.0001	0.000755

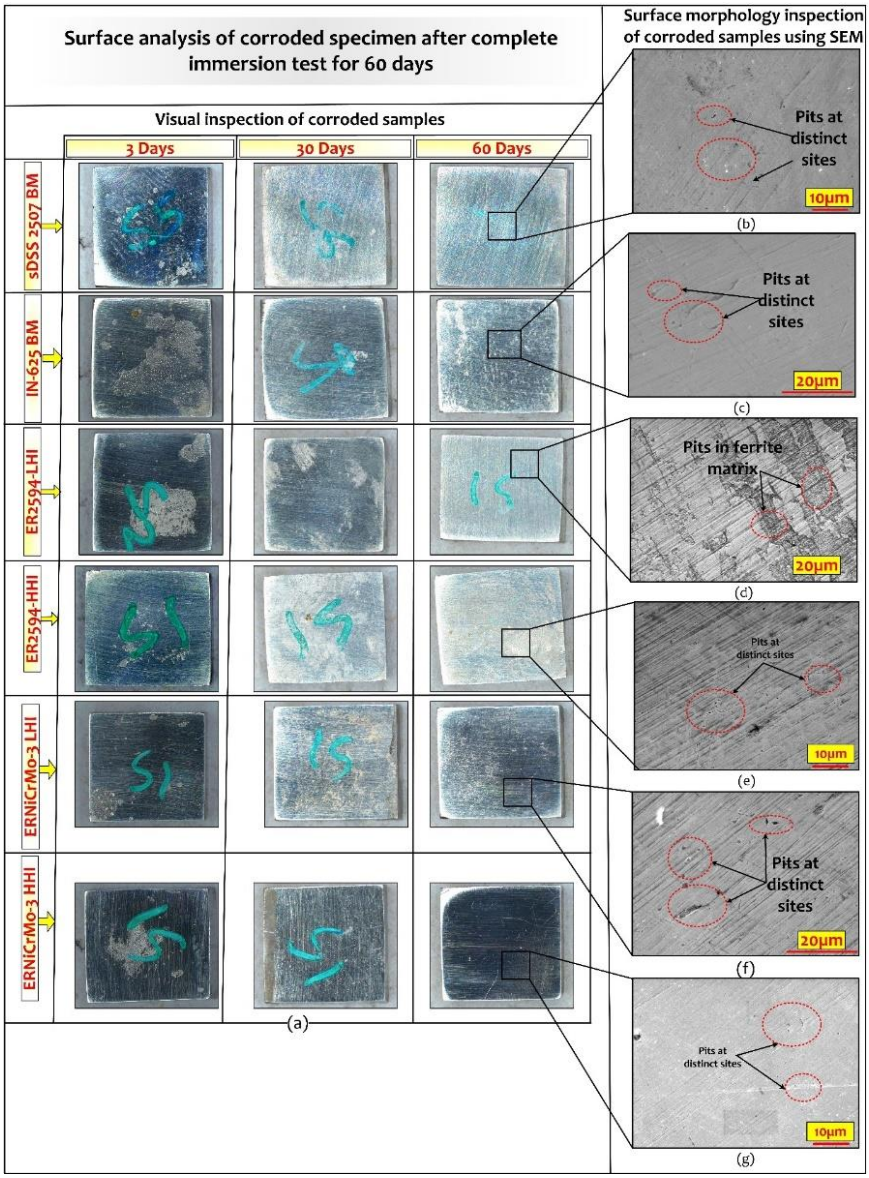

Figure 5.28 : *(a) Visual inspection, and (b-g) surface morphology of all sample surfaces following complete immersion in 3.5 wt.% NaCl for a range of duration periods (3–60 days)*

5.1.6.2 *ELECTROCHEMICAL CORROSION TEST*

The base and weld metals were corrosion-tested in 3.5 wt% NaCl using an Autolab electrochemical workstation. The Tafel plot for all test specimens is shown in Figure 5.29(a-d). A reduced corrosion potential (E_{corr}) indicates that a material is more susceptible to thermodynamic corrosion. Thus, E_{corr} is a more reliable indicator of corrosion resistance. Table 5.8 shows the values of E_{corr} in the 3.5 wt% NaCl solution. A lower E_{corr} (-202.1 mV) was measured for sDSS 2507 BM compared to IN-625 BM (-176.9 mV). The ERNiCrMo-3 weldment's E_{corr} (-169.9 mV for LHI and -124.7 mV for HHI) was significantly lower than the ER2594 weldment's E_{corr}, which showed readings of -199.8 mV for LHI and -154.6 mV for HHI. The ER2594 weldment demonstrated more excellent corrosion resistance than the sDSS 2507 BM, while the ERNiCrMo-3 weldment performed better. According to E_{corr}, the following order is based on corrosion resistance from least noble: sDSS 2507 BM > ER2594-LHI > IN-625 BM > ERNiCrMo-3-LHI > ER2594-HHI > ERNiCrMo-3-HHI. The corrosion rate (mm/year) is rated from high to low, with higher being less corrosion-resistant: sDSS 2507 BM (0.02245) > ER2594-LHI (0.01040) > IN-625 BM (0.00673) > ERNiCrMo-3-LHI (0.002760) > ER2594-HHI (0.002552) > ERNiCrMo-3-HHI (0.00075). An sDSS 2507 BM exhibits the lowest corrosion resistance. ERNiCrMo-3 weldment has the best electrochemical corrosion rate compared to ER2594. Extrapolating the anodic and cathodic branches of the polarization curves to the corrosion

potential yields the corrosion currents (I_{corr}). Higher corrosion rates are indicated by higher corrosion currents (I_{corr}). Repassivation is fast for high-corrosion-resistant alloys like sDSS 2507 and IN-625. In Figure 5.29, nonlinearity in stainless steel Tafel curves may have caused inaccuracies in distinguishing β_a and β_c slopes. The corrosion current is thus rated from high to low, with the higher being less corrosion resistant: sDSS 2507 BM (0.92 µA) > ERNiCrMo-3-HHI (0.70 µA) > ER2594-HHI (0.45 µA) > IN-625 BM (0.29 µA) > ERNiCrMo-3-LHI (0.12 µA) > ER2594-LHI (0.11 µA). This E_{corr} ranking corresponds with the I_{corr} ranking and indicates the sDSS 2507BM as the least corrosion-resistant section of the weld joints.

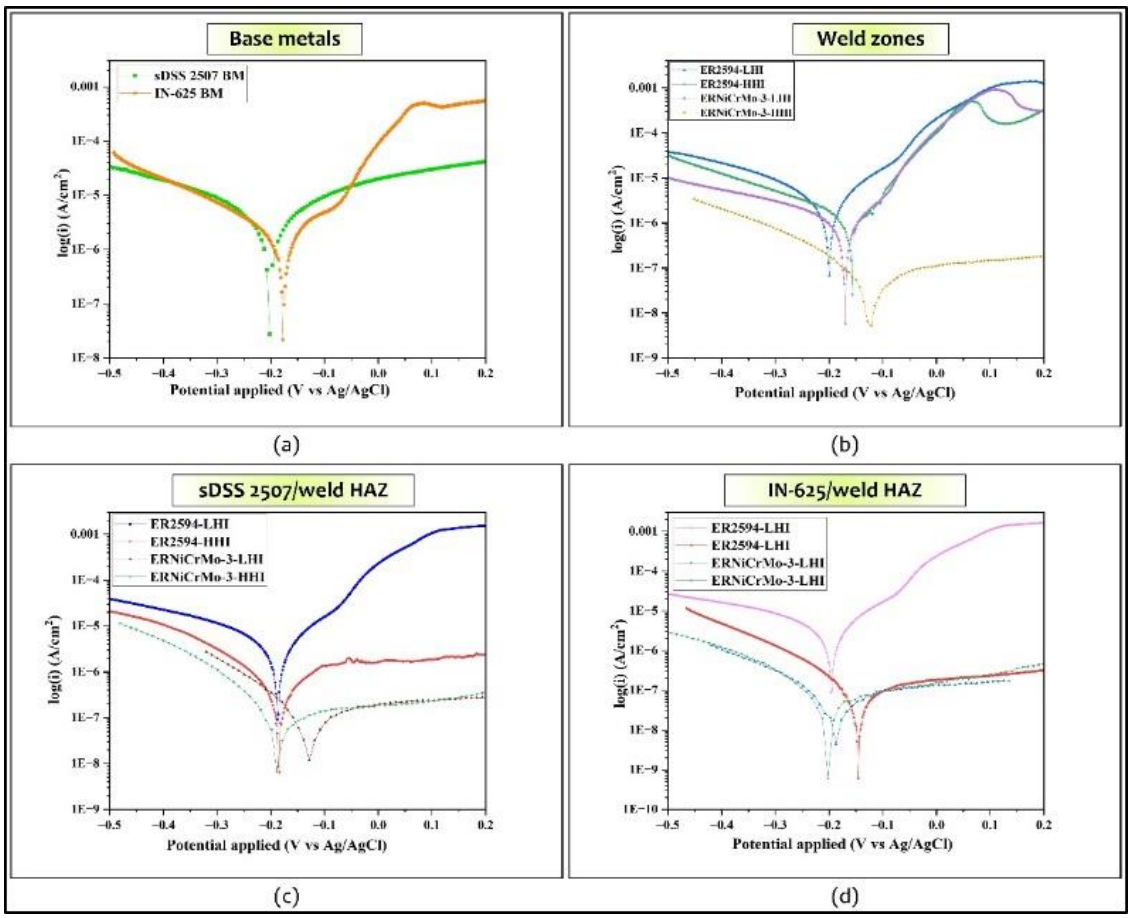

Figure 5.29 : (a-d) Tafel plot of all samples following electrochemical test in 3.5 wt.% NaCl

Electrochemical impedance spectroscopy was also employed to investigate corrosion behavior and charge transfer mechanisms efficiently. The results from potentiodynamic polarization and immersion corrosion experiments aligned with the outcomes of these methods (McCafferty, 2010; Raj & Biswas, 2023). Figure 5.30 shows the Nyquist and Bode plots of EIS fittings for ER2594/ERNiCrMo-3 filler weld joints in various regions with different heat inputs and base metals in 3.5 wt.% NaCl. In the Nyquist diagram, the capacitive arc radius represents the corrosion product's charge transfer resistance; a larger radius indicates higher corrosion resistance (Huang et al., 2021). Nyquist plots for IN-625 BM and sDSS 2507 BM in Figure 5.30(a) display a straight pattern, indicating ion diffusion through the metal-solution contact. Both base metals exhibit a larger capacitive impedance arc radius, suggesting superior corrosion resistance. Figure 5.30(b) shows Nyquist plots of EIS results for weld zones of both filler metals. A larger capacitive arc radius on the ERNiCrMo3-HHI welded joints indicates superior corrosion resistance. Small capacitive semi-circles in the high-frequency zone indicate corrosion product formation, while large semi-circles in the low-frequency range show electric double-layer capacitance. Due to its larger capacitive loop, the ERNiCrMo-3 filler welded joint samples have superior corrosion resistance than the ER2594 filler welded joint. Compared to other welded joints, the ER2594-HHI/ERNiCrMo3-LHI welded sample exhibits increased intermediate and low-frequency impedance (Figure 5.30(b)). Figure 5.30(c-e) presents Nyquist

plots for the HAZ of both base metals. Figure 5.30(c and d) shows the Nyquist plots of both filler specimens in the IN-625 and sDSS 2507 HAZ. These plots show a distinct capacitive arc with large diameters, which indicates the formation of a capacitive layer on the surface and excellent corrosion resistance.

Table 5.8 : Tafel analysis results for base and weld metal in a 3.5 wt% NaCl solution

Specimen	*Ecorr (mV)*	*ICorr (μA)*	*βc (mV/dec)*	*Ba (mV/dec)*	*Corrosion rate (mm/year)*
IN-625 BM	-176.9	0.29	24.5	20.1	0.00673
sDSS 2507 BM	-202.1	0.92	54.3	39.4	0.02245
Weld zones					
ER2594-LHI	-199.8	0.45	58.5	48.1	0.01040
ER2594-HHI	-154.6	0.11	16.1	14.8	0.002552
ERNiCrMo-3-LHI	-169.9	0.12	15.8	21.3	0.002760
ERNiCrMo-3-HHI	-124.7	0.70	171.8	66.5	0.00075
HAZ on sDSS 2507 BM side					
ER2594-LHI	-187.11	1.64	67.42	58.3	0.038188
ER2594-HHI	-184.87	0.217	76.26	55.9	0.00505
ERNiCrMo-3-LHI	-127.9	0.079	209.7	91.1	0.001844
ERNiCrMo-3-HHI	-189.8	0.30	-430.2	158.4	0.008574
HAZ on IN-625 BM side					
ER2594-LHI	-195.4	2.79	93.6	178.8	0.06351
ER2594-HHI	-146.5	0.028	59.1	47.2	0.000649
ERNiCrMo-3-LHI	-189.04	0.053	292.7	121.7	0.001212
ERNiCrMo-3-HHI	-201.6	0.032	96.002	80.9	0.00074582

Bode plots show that currents either lead or lag relative to one another, with positive phase angles showing leading currents and negative phase angles showing capacitive systems. Low-frequency (10^2–10 Hz) represents solution resistance (Huang et al., 2021; Raj & Biswas, 2023). The impedance and phase angle vs. frequency Bode plots for base metals and the ER2594/ ERNiCrMo-3 weld zones are shown in Figure 5.30(f and g). The impedance diagrams for sDSS 2507 and IN-625 BMs in Figure 5.30(f) show a flat high-frequency region and a linear decline at low and medium frequencies. The rise in phase angles with frequency is attributed to the oxide film contribution, and the low-frequency impedance modulus exceeds 10^5 Ω·cm^2. In the Bode plot, both base metals display a maximum phase angle of 60° over a wide frequency range, indicating charge transfer dominance in the high-frequency region. Bode plots reveal amplitude and phase variations with frequency in ER2594 and ERNiCrMo-3 filler weld zones (Figure 5.30(g)). Charge transfer predominates in the high-frequency domain, evident from phase angles reaching 60° at high frequencies. Bode plots show a decline in all weld zone samples at lower frequencies than sDSS 2507 BM and ERNiCrMo3-HHI. Slower reaction kinetics at lower frequencies suggest a thicker coating of corrosion products on weld surfaces. However, the low impedance modulus of the corrosion product layer indicates insufficient protection. Figure 5.31(h and i) presents the phase angle vs. frequency and impedance Bode plots for IN-625 and sDSS 2507 HAZ for both fillers. Similar to the weld zone, the Bode plots exhibit a decline in IN-625/sDSS 2507 HAZ samples at lower frequencies.

Figure 5.31(j) presents the proposed electrical equivalent circuit (EEC) applied to match the experimental data. In the EEC, Q_f stands for the electrical capacity of the corrosion product layer, R_s stands for solution resistance, R_f for corrosion product film resistance, R_{ct} for charge transfer resistance, and CPE for constant phase element at the double layer. The capacitor does not perform optimally in actual electrochemical processes due to electrode geometry inhomogeneity or surface roughness. To simulate the effects of real-world variation in capacitance, the equivalent circuit model included CPE as a non-ideal capacitor capacitance.

The impedance of the CPE is expressed as $Z_{CPE} = [Y_o(j\omega)^n]^{-1}$, where Y_o is the capacitance, j is the imaginary number ($j = \sqrt{j^{-1}}$), ω is the angular speed, and n is the power index number (Eghlimi et al., 2014). The CPE can change its electrical properties to that of an inductor, a resistor, or a capacitor, correspondingly, for the values of n = -1, 0, and 1, respectively (Brytan et al., 2016; Eghlimi et al., 2014). Table 5.9 lists the EIS parameters from equivalent circuit fitting. An oxide film-like capacitive behavior is suggested by the observed n values (0.6–0.99). Experimental data fits the equivalent circuit accurately and generates circuit elements (Harrington & Van Den Driessche, 2011). Figures 5.30 and 5.31 show that fitted and experimental spectra match, indicating little fitting error and high data accuracy. EIS measures double capacitance arc resistance and semicircular arc reaction corrosion products in the high-frequency area and semicircular arc-reflecting electrode processes at the electrode-rust layer interface in the low-frequency region (Dou et al., 2023). In sDSS 2507/IN-625 DWJ for both filler weldments, the oxide film characteristics are assessed using the overall resistance ($R_s + R_f$) or R_{ct} parameter. Superior corrosion resistance is indicated by a higher R_{ct} (Raj & Biswas, 2023). The EIS data and fitting plots indicate that both base metals have higher R_{ct} and R_f values than weld and HAZ specimens, reflecting superior corrosion resistance. Significant differences in R_{ct} values suggest that ERNiCrMo3-HHI exhibits the highest corrosion resistance among the weld zones due to its thicker protective film layer. ER2594-HHI/ ERNiCrMo3-LHI weld metals exhibit poor corrosion resistance, with n values of 0.742 and 0.627, respectively, indicating the corrosion behavior of the oxide film layer. In IN-625 HAZ, ERNiCrMo-3 filler demonstrates better corrosion resistance than ER2594 filler. The corrosion resistance of ER2594 filler weldment (LHI (n=0.868), HHI (n=0.69)) varies significantly compared to ERNiCrMo-3 (LHI (n=0.767), HHI (n=0.89)) for sDSS 2507 HAZ.

The correlation between current density and corrosion resistance of samples obtained at various sites of welded joints appears to be ambiguous, according to the findings of electrochemical investigations. This is evident from analyzing the pit geometries formed in the base and the weld metal. To establish similar surface conditions, every sample was polished to 1200 grit with abrasive sandpaper before the electrochemical test. This investigation used SEM to obtain surface morphology images from several zones, including the base metal. However, following the electrochemical test, the scratches deepen, and a few pits show up on the surface (Figure 5.31(a-b)). Due to the presence of stress concentration, it is hypothesized that the areas where the scratches are located are more prone to corrosion. However, this concept needs further study. Figure 5.31(c–h) shows all weld zones' surface morphologies. The number and size of corrosion pits were assessed after the electrochemical test to assess corrosion. Consistent with the prior explanation, sDSS 2507 BM clearly shows the most severe corrosion, followed by ER2594-LHI.

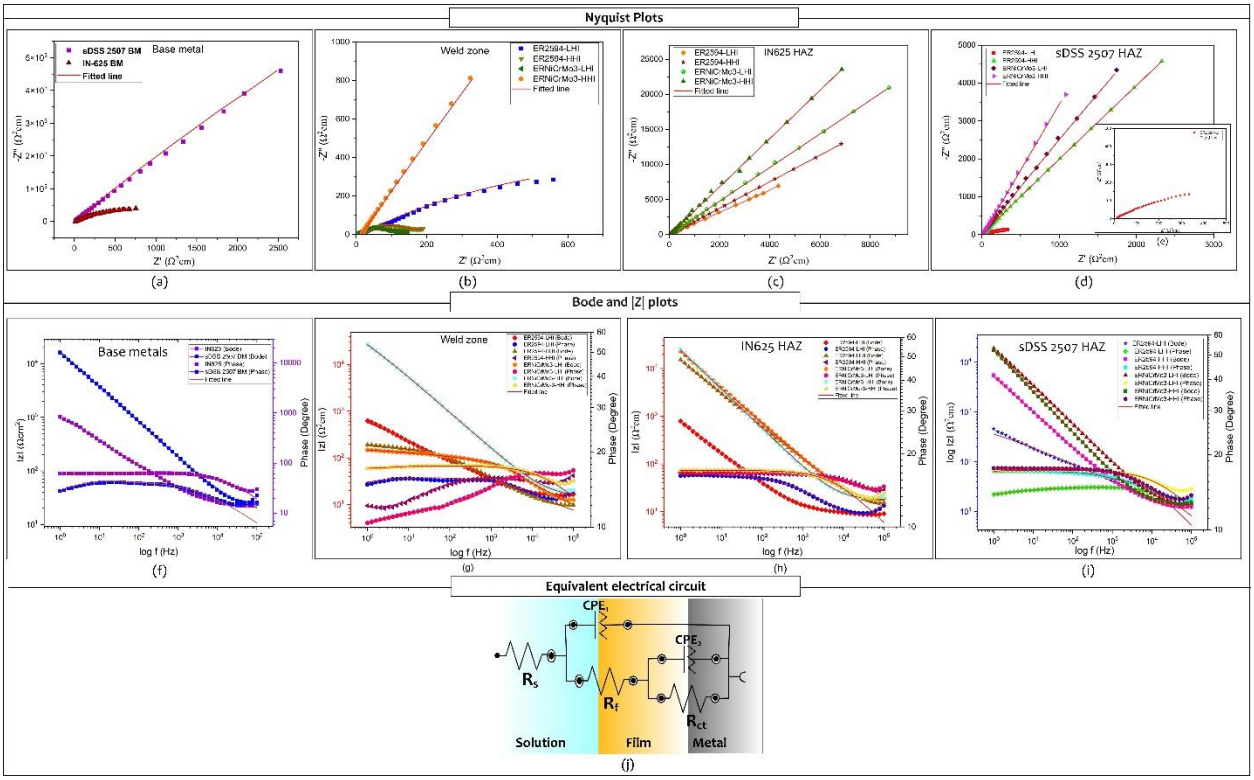

Figure 5.30 : EIS study of base and weld metal: Nyquist plot (a-e); Bode and |Z| plot (f-i), respectively, (j) All samples' EIS test results fitted with an equivalent electrical circuit

Table 5.9 : Equivalent circuit fitting of EIS data of all samples

Specimen	R_s ($\Omega.cm^2$)	CPE_1		R_f ($\Omega.cm^2$)	CPE_2		R_{ct} ($\Omega.cm^2$)
		Y_{01} ($\mu F.cm^{-2} S^{(n-1)}$)	n_1		Y_{02} ($\mu F.cm^{-2} S^{(n-1)}$)	n_2	
sDSS 2507 BM	10.6	283	0.862	654	112	0.902	482
IN-625 BM	11.6	276	0.68	542	236	0.82	106
Weld zone							
ER2594-LHI	21.4	71.6	0.83	110	55.8	0.749	183
ER2594-HHI	5.5	79.4	0.742	104	75.8	0.718	110
ERNiCrMo3-LHI	13.8	281	0.627	112	174	0.824	120
ERNiCrMo3-HHI	14.4	74.4	0.77	74.7	267	0.924	134
HAZ on IN-625 BM side							
ER2594-LHI	11.2	130	0.55	279	261	0.703	110
ER2594-HHI	9.94	192	0.69	210	99.6	0.91	104
ERNiCrMo3-LHI	17.0	234	0.86	316	111	0.748	127
ERNiCrMo3-HHI	17.3	94.2	0.815	429	90.5	0.893	143
HAZ on sDSS 2507 BM side							
ER2594-LHI	15.8	13.8	0.868	132	995	0.636	106
ER2594-HHI	10.5	53	0.69	188	865	0.785	110
ERNiCrMo3-LHI	11.4	126	0.767	131	619	0.862	134
ERNiCrMo3-HHI	13.2	131	0.89	158	859	0.786	123

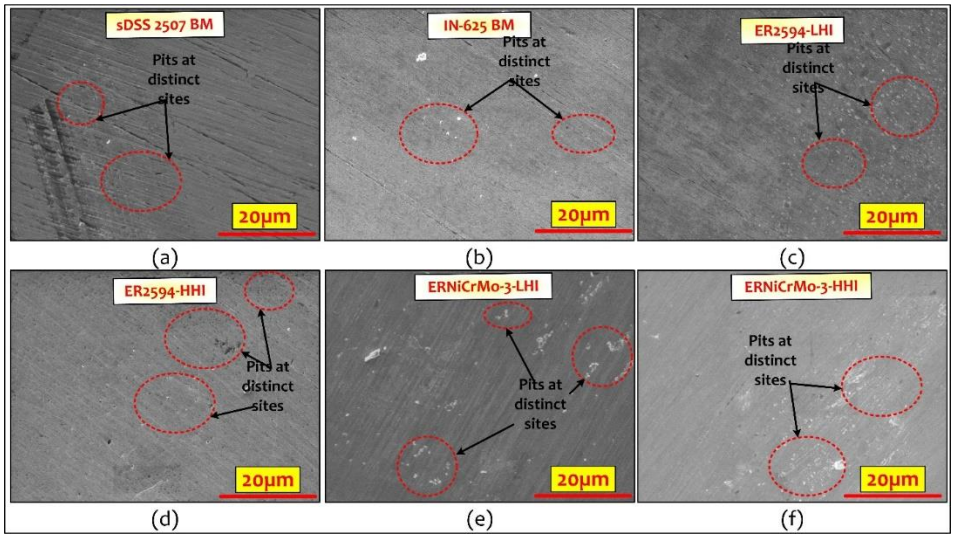

Figure 5.31 : *(a-f) Surface morphology of all sample surfaces following electrochemical test in 3.5 wt.% NaCl*

5.2 DISSIMILAR METAL WELD OF SUPER DUPLEX STAINLESS STEEL AND NITRONIC STEEL

This section extensively explores the relationship between structure and properties in the context of filler metal selection and heat input parameters for weldment. The joint's potential applications in subsea oil and gas drilling production equipment, such as high-pressure tubing and tubing couplers, are highlighted. The analysis includes detailed metallurgical characterization of the base metal, heat-affected zone, and weld zone, along with a comprehensive evaluation of mechanical properties and wear and corrosion behavior.

5.2.1 QUALITATIVE AND QUANTITATIVE WELD JOINT INSPECTION

Before mechanical and microstructural evaluations, macrostructure analysis examined the weld joints for defects. Under a stereo zoom macroscope, the weldments were examined for macrostructural integrity, providing information about the fusion zone and weld interfaces. Pass sequence, fusion width, and depth were examined to determine how the capping pass affected the underlying passes. Inspection revealed that the weld joints were fully penetrating and flawless. The base metals had fully fused at the weld interface in all welds. With ER2594 filler, the cross-sectional macroscope view of specimens under LHI and HHI conditions included the base metal, HAZ, and weld zone. The weld area for LHI and HHI was estimated using Image J software, resulting in 80 mm^2 for LHI and 85 mm^2 for HHI weldment (Figure 5.32(a and b)). Figure 5.32(c and d) shows multi-pass weld macrostructures for ER70S-2 filler at LHI/HHI conditions. Using Image J software, an area of 85 mm^2 was obtained for lower heat input weldment and 90 mm^2 for higher heat input weldment.

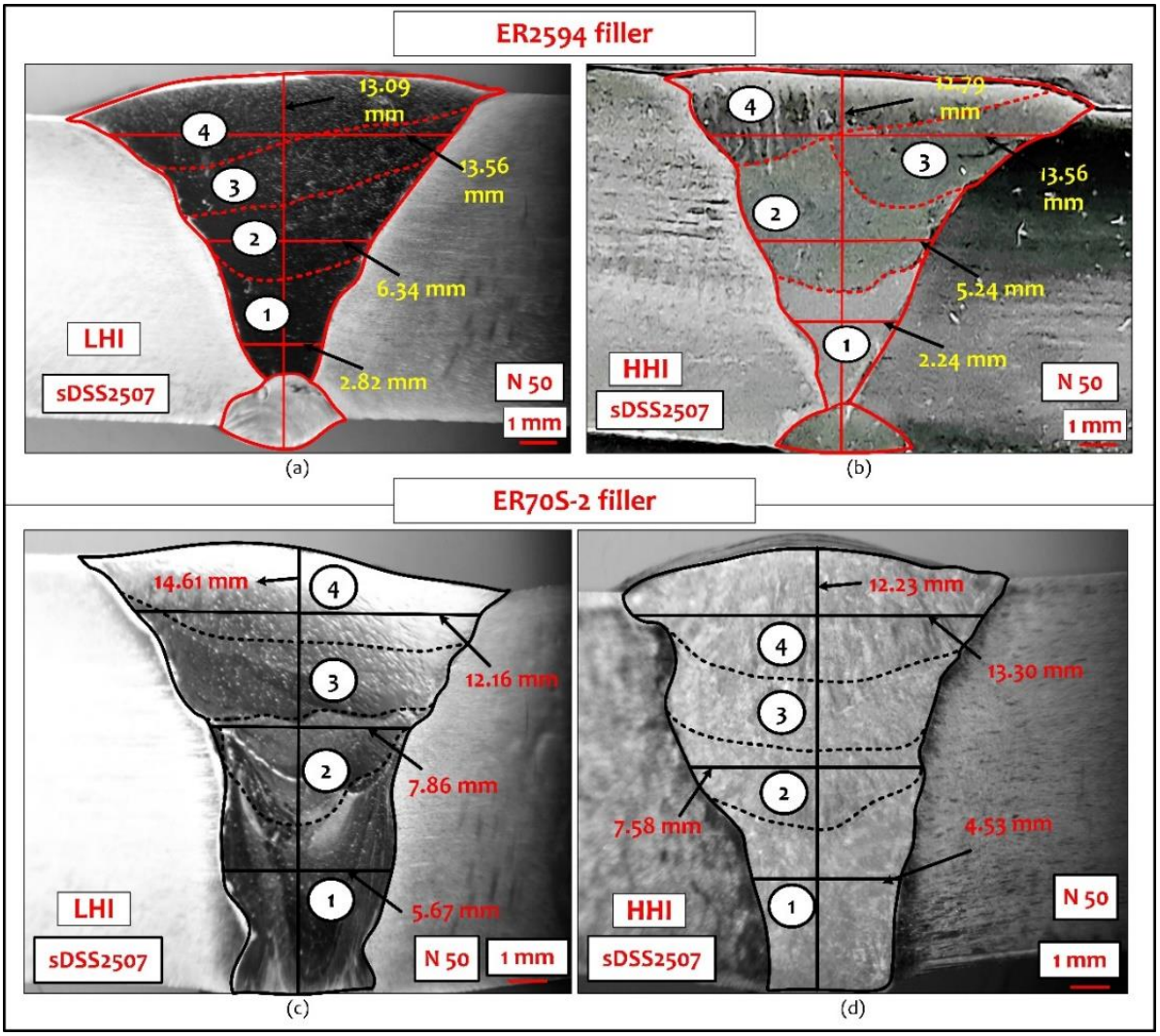

Figure 5.32 : Macrostructure study of LHI and HHI weldments showing its weld and passes for (a and b) ER2594 filler, (c and d) ER70s-2 filler, respectively

5.2.2 MICROSTRUCTURAL CHARACTERIZATION

Microstructural characterization involves assessing the base metal's microstructure, studying the microstructure's evolution at the weld interface, and examining the weld zone for both filler metals. This is crucial for understanding the structure-property relationship influenced by different heat inputs.

5.2.2.1 BASE METALS

The microstructure of the sDSS 2507 base metal, as depicted in Figure 5.33 (a and b), reveals the presence of austenite (γ) within the ferrite (δ) matrix. The XRD pattern in Figure 5.33(g) confirms that only γ and δ phases are present, with no intermetallic phases. Therefore, the ferrite matrix is devoid of intermetallic phases such as secondary austenite or sigma phases. Using ImageJ software, the area fraction of austenite in the ferrite matrix was determined to be 48.6%, and the average grain size of austenite was measured at 25 µm (Figure 5.33(a)). The N50 base metal's microstructure (Figure 5.33(d and e)) consists of equiaxed austenite with twins and carbide precipitates at the grain boundaries. The XRD pattern in Figure 5.33(h) for N50 base metal indicates only the presence of the γ phase without any detrimental phases. The microstructure of N50's austenite exhibits an average grain size of 30 µm. The EDS analysis of the sDSS 2507 and N50 base metals is presented in Figure 5.33(c and f).

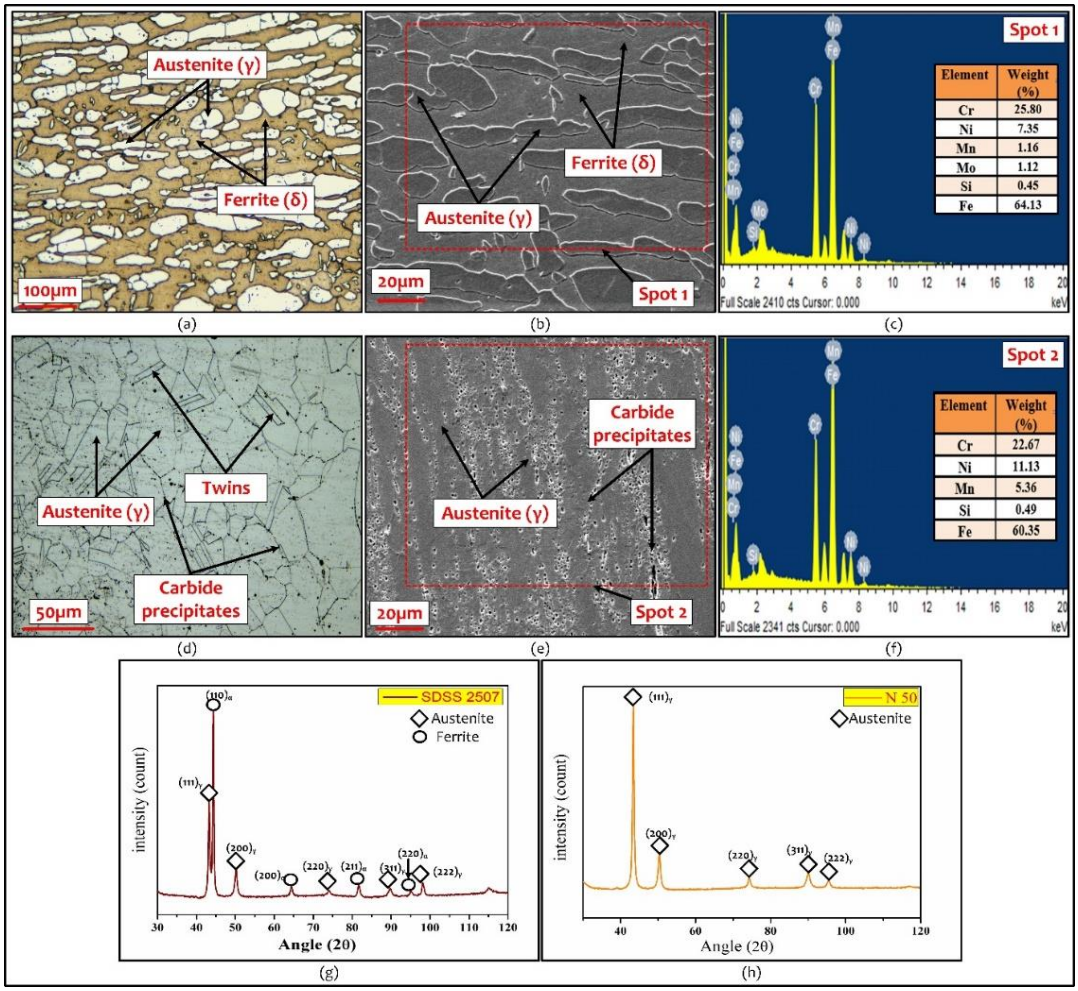

Figure 5.33 : Optical and SE micrograph of base metal (a-b) sDSS 2507, (d-e) N50, respectively, The EDS analysis of base metal (c) sDSS 2507, (f) N50, respectively, and the XRD plot of the (g) sDSS 2507 and (h) N50

5.2.2.2 *WELD INTERFACE*

The microstructural evolution of the HAZ on the sDSS 2507 side, utilizing the super duplex filler ER2594, is illustrated in Figure 5.34(a and b). As known, the microstructure of sDSS 2507 BM consists of equiaxed and homogeneously distributed dual-phase ferrite and austenite grains. Studying the microstructural evolution of the HAZ is complex, depending on thermal factors and chemical composition. Multi-pass welding introduces variations in heating and cooling rates, influencing grain nucleation and growth in the HAZ (Lippold, 2014). (Gunn, 1998) have observed that the HAZ's microstructure is controlled by heat input, interpass, preheat temperature, and the weld coupon's thickness in multi-pass welding. Thermal cycles and higher cooling rates from multi-pass welding affect HAZ microstructure. Figure 5.34(a and b) clearly displays the formation of WA and PTA away from the fusion boundary in the sDSS 2507 HAZ. Narrow HAZ formation is evident on the sDSS 2507 side. The microstructural evolution of the N50 interface and its HAZ region using the super duplex filler ER2594 is presented in Figure 5.34(c and d). The partially mixed zone (PMZ) and HAZ region at the N50 interface show the appearance of columnar dendrites. N50 solidification mode and microstructural changes depend on factors like the welding process, cooling rates, filler elemental composition, and heat input. The width of the HAZ region on the N50 side is more extensive than the super duplex side. SEM images display the WZ and N50 interface, showcasing the formation of WA, PTA, and coarse carbide precipitates in the HAZ. EDS spectra of the N50 interface's austenitic region reveal elemental compositions. The microstructural evolution of the HAZ on the sDSS 2507 side using filler ER 70S-2 is depicted in Figure 5.34(e and f). Microstructure examination reveals the formation of an unmixed zone near the sDSS 2507 interface and WZ, characterized by filler-deficient beaches, peninsulas, islands, and a distinct fusion line between the base metal, HAZ,

and WZ. The banding phenomenon is also observed and attributed to variations in solidification rate, growth rate fluctuations, thermal fluctuations, and microsegregation. It shows the presence of δ-ferrite in the sDSS 2507 HAZ region with ferrite and austenite. Figure 5.34(e) shows the presence of unmixed zone formation consisting of beaches, islands, peninsulas, Type-II boundary, and the banding phenomenon. EDS spectra were used to obtain the elemental composition near the sDSS 2507 fusion boundary. Cr and Ni segregation migration in the HAZ region decreases compared to super duplex filler.

The microstructural evolution of the HAZ region of the N50 side using filler ER 70S-2 is shown in Figure 5.34(g and h). The formation of the fusion boundary line can be seen clearly with the presence of carbide precipitates and austenites in the N50 BM. The formation of filler-deficient beaches along with peninsulas and islands can be seen clearly along with the fusion boundary, as shown in Figure 5.34(g and h). The HAZ region of N50 is wider than sDSS 2507 for the filler ER70S-2. The formation of island and Type II boundaries was notable at the HAZ interface of both BMs with ER70S-2 weld zone, which was not observed using ER2594 filler metal. The Type II boundary is detected parallel with the fusion boundary at the sDSS 2507 and N50 steel sides. (Nelson et al., 2000) noticed that the necessary conditions and dependency for forming Type II boundaries are the allotropical transformation of ferrite to austenite at elevated temperature, WZ's solidification behavior, and the nature of solid-state change in the BM substrate. The occurrence of this type of boundary affects the WZ's composition gradient due to the difference in crystal structure between the BMs, variation in BM dilution, and diffusion mixing of impurities and alloys between the WZ and the stagnant boundary. EDS spectra and line scans performed in the weldment and HAZ disclose the concentration gradients of elements like Cr, Ni, and Mn around the fusion line. (Lu et al., 2011) and (Saedi et al., 2018) have also stated the Type II boundary formation in dissimilar welding of austenitic and ferritic steels.

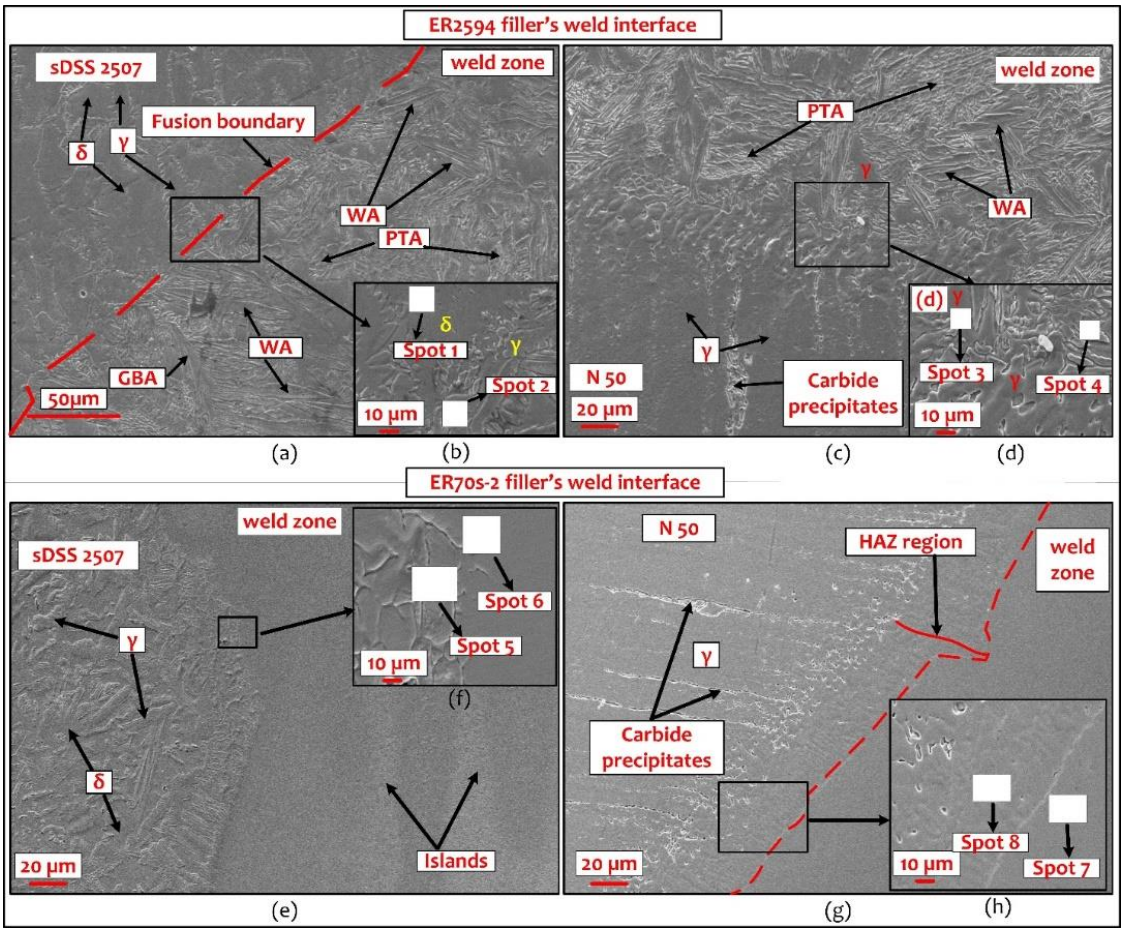

Figure 5.34 : Interface microstructure between the sDSS 2507BM/N50 BM and weld zone for (a-d) ER2594 filler, (e-h) ER70S-2 filler, respectively

Table 5.10 : *EDS spectra of the indicated at weld interfaces spot for both filler metals*

Elements (wt.%)	*1*	*2*	*3*	*4*	*5*	*6*	*7*	*8*
Cr	28.66	27.01	26.28	24.65	15.67	11.43	4.33	17.89
Ni	5.86	9.83	9.59	10.43	4.95	3.08	1.60	7.17
Mo	1.50	0.48	2.07	1.08	----	---	----	----
Mn	----	----	----	----	1.59	1.56	1.94	4.65
Si	0.53	0.21	0.68	0.82	0.73	0.93	0.71	0.48
Fe	63.24	61.56	57.50	61.18	73.78	83.00	82.80	57.84

EDS analysis near the fusion boundary and interface shows Cr and Ni enrichment in the HAZ region (Table 5.10). Elemental line mapping across the interface of both base metals (sDSS 2507 and N50) with super duplex filler ER2594 is conducted to confirm element segregation at the HAZ and WZ interface (Figure 5.35(a and b)). The line mapping displays sharp gradients for elements like Ni, Fe, Cr, Mo, Mn, and Si. Almost equal spike gradients are observed for all elemental compositions like Ni, Fe, Cr, and Mo. The EDS line scan indicates a nearly constant concentration of elements like Cr, Ni, and Mo in both N50 and sDSS 2507 interfaces. The sDSS 2507 base metal and filler ER2594 exhibit similar chemical compositions, while N50 shows minor changes in Cr, Mn, and Ni concentrations due to its lower content of Cr and Ni. The HAZ region's EDS spectra clearly show the variation in Cr, Mn, and Ni segregation in the WZ and near the fusion boundary. The line mapping across the interface of both BMs with filler ER70S-2 is accomplished across the fusion boundary and WZ to confirm the segregation of elements, i.e., shown in Figure 5.36(a and b). The variation in the spike of Cr, Ni, and Mo can be clearly seen, showing the significant change in the spike of the WZ of ER70s -2 and the BM sDSS 2507 and N50. The variation in Fe concentration for both line scans can be seen clearly.

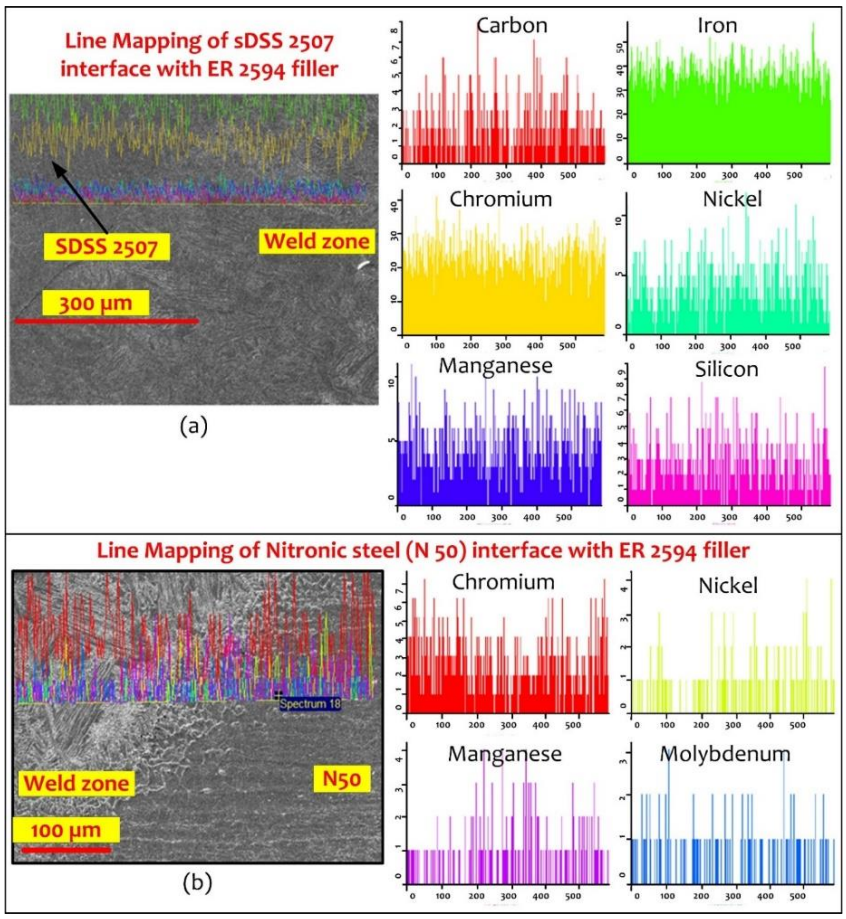

Figure 5.35 : *ER2594 filler line mapping analysis at the (a) sDSS 2507 and (b) N50 interface, respectively*

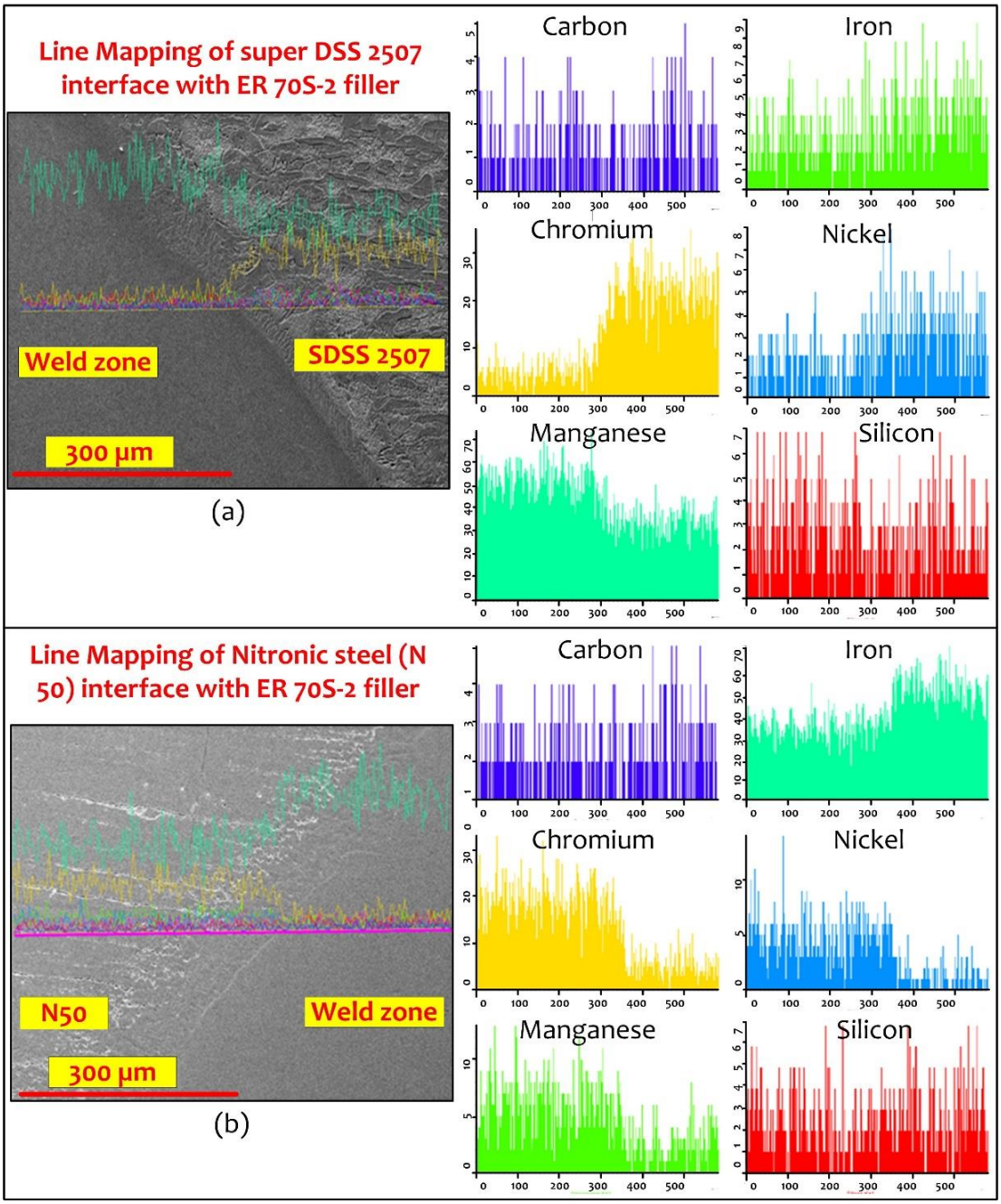

Figure 5.36 : *ER70S-2 filler line mapping analysis at the (a) sDSS 2507 and (b) N50 interface, respectively*

5.2.2.3 *WELD ZONE*

The microstructure of the ER 2594 WZ results in the ferrite phase mixture with reformed austenite into the matrix, as shown in Figure 5.37(a and b). Thermally active reformed austenite was observed in the WZ because of the weld joint's steady cooling and the ferrite's transformation during the cooling process. The heating and cooling cycle in every weld pass causes the sequential precipitation of various morphologies of the austenite in the WZ. Figure 5.37(a and b) shows the schematic diagram showing the microstructural evolution of reformed austenite in the WZ. The precipitation of GBA occurs at existing δ/δ grain boundaries and is favored in the high-temperature range of 1350°C–800°C. As the cooling continues further of the deposited filler metal, the nucleation of WA starts at δ ferrite grain boundaries and grows inside the grains. Figure 5.37(b) shows the straight lathe surface of the WA and merged at the needle-like edge. If time permits more diffusion, the last reformed austenite nucleates at a low-temperature range and grows within the δ ferrite matrix is IGA. The precipitation of IGA occurs in polygonal shapes. It appears in the irregular shape of twinning sub-particles distributed in the WZ. (W. N. Khan & Chhibber, 2021b) and (Sieurin & Sandström, 2006) stated that some of

the primary austenite stays in its original appearance after the continuous heating-cooling cycle is PTA, a plateau-like structure. Its presence in the WZ inhibits grain growth. It also confirms the formation of reformed austenite like GBA, WA, IGA, and PTA. The EDS analysis was performed on the WA and ferrite matrix to conclude the elemental differences in both spots, as tabulated in Table 5.11. The WZ of filler ER 70S-2's microstructure results in the ferrite phase (light white patches) with long martensite laths, as shown in Figure 5.37(c and d). The WZ microstructure shows the occurrence of martensite laths and packets, ferrite patches, and strips adjacent to the boundaries of martensite laths. The EDS analysis was performed on the grain boundary martensite lath and ferrite matrix to conclude the elemental differences in Cr and Ni in both spots.

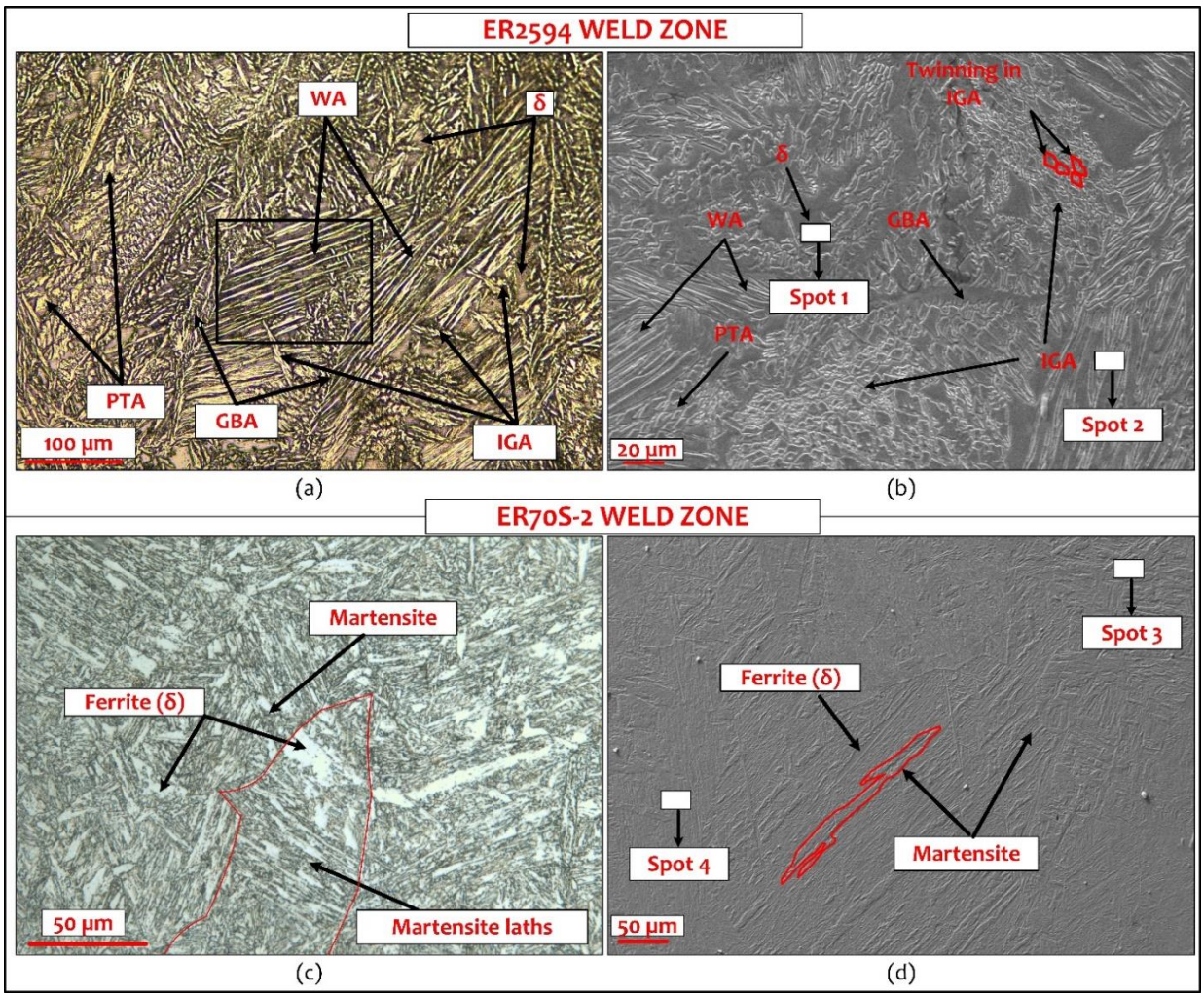

Figure 5.37 : Optical and SEM image of weld zone microstructure for (a and b) ER2594 filler, (c and d) ER70S-2 filler, respectively

Table 5.11 : *EDS spectra of the indicated at weld zones spot for both filler metals*

Elements (wt.%)	*1*	*2*	*3*	*4*
Cr	22.41	22.79	3.32	3.12
Ni	9.76	8.15	1.45	1.03
Mn	2.08	0.36	1.45	1.42
Si	0.30	0.42	0.88	0.90
Fe	52.33	53.57	86.74	86.79

The pseudobinary phase diagram of Fe-Cr-Ni and the Schaeffler diagram both highlight the significance of Cr_{eq}/Ni_{eq} values in influencing the solidification mode and microstructural evolution in the weld zone (Figure 5.38(a)). Schaeffler constitution diagrams, depicted in Figure 5.39, were utilized to ascertain the weld microstructures resulting from different filler metals. Table 4.1 provides the equivalent quantities of Cr_{eq} and Ni_{eq} for both base and filler metals. The compositions associated with each filler metal were located by projecting these values onto the Schaeffler diagram to identify the microstructures of the weld metal. In the case of ER2594 and ER70S-2 filler metals, their weld compositions (circle signs) coincided in the fully ferritic and fully austenitic regions, respectively, with a 30 percent dilution in the weld cross-section area. For ER2594 filler metals with high Cr_{eq}/Ni_{eq} ratios, the initial solid formed during solidification is ferrite, while for ER70S-2 filler metals with low Cr_{eq}/Ni_{eq} ratios, austenite is the first solid to form, presenting a distinction from the sDSS 2507 BM. Although the fully austenitic (FA) mode exhibits the highest resistance to solidification or hot cracking, compositions favoring primary austenite solidification (A and AF) are susceptible to cracking. The primary solidification mode and HAZ depend on the Cr_{eq} and Ni_{eq}. The EDS analysis was performed to get the elemental composition at different spots in the WZ, HAZ region of sDSS 2507 side, and HAZ region of N50 side for both the filler, i.e., ER2594 and ER 70S-2. Schaeffler diagram was used to confirm the microstructure evolution of the HAZ regions and WZ for both fillers, as shown in Figure 5.39(a and b). The corresponding values of Cr_{eq} and Ni_{eq} were calculated using SEM-EDS analysis in the HAZ and WZ, and then the points were plotted in the Schaeffler diagram. The values of Cr_{eq} and Ni_{eq} and the predicted microstructure of these regions for fillers are tabulated in Table 5.12. The diffraction peaks of the WZ for ER 2594 filler reveal mainly two-phase (austenite and ferrite) without indication of secondary phases or precipitation Figure 5.38(c). The peaks of the WZ for ER70S-2 filler show shallow peaks of austenite with the presence of a ferrite matrix (Figure 5.38(c)). (Kangazian & Shamanian, 2017) also observed the same XRD peak for sDSS 2507 BM, whereas (Caplan, 1976) observed the same XRD peak for N50 BM. In contrast, the XRD peak for ER2594 is also observed by (W. N. Khan & Chhibber, 2021a). The evolution of austenite starts at grain boundaries and progresses in the intergranular direction and its transformation results in the ferrite-austenite microstructure. As the cooling cycle occurs, the solidification mode of the ER 2594 and ER70S-2 filler is the fully ferritic and austenitic mode, respectively. Figure 5.39(c and d) shows the prediction of solidification mode according to the filler composition analysis and weld chemistry analysis, respectively. The filler composition analysis shows that the solidification mode of ER70S-2 is a ferrite matrix with martensite bands, whereas martensite formation takes place according to the weld chemistry analysis. Ferrite content indicated in the Schaeffler diagram is in the range of 60%, with solidification in the ferritic mode for both cases.

Table 5.12 : Microstructure prediction of sDSS and N50's HAZ and WZ

Zone	Filler 2594		Filler ER70S-2		Microstructure ER2594	Microstructure ER70S-2
	Cr_{eq}	Ni_{eq}	Cr_{eq}	Ni_{eq}		
sDSS 2507's HAZ	28.50	9.85	17.18	6.84	δ+ϒ	δ+ϒ+M
	27.805	11.03	12.89	4.89	δ+ϒ	δ+M
N50's HAZ	16.765	6.95	4.965	3.09	δ+ϒ+M	M
	12.85	5.06	18.03	9.89	δ+M	δ+ϒ+M
Weld zone	29.07	9.75	4.84	2.63	δ+ϒ	M
	27.82	10.23	4.04	2.89	δ+ϒ	M
[δ: Ferrite, ϒ: Austenite M: Martensitic]						

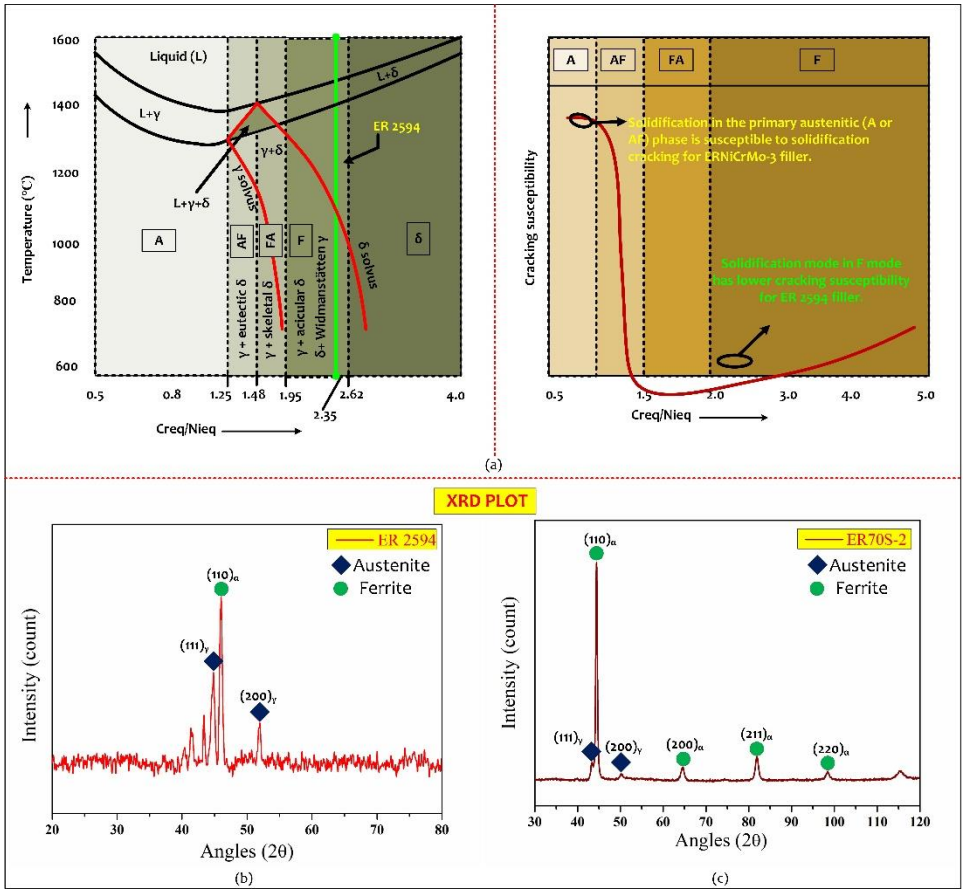

Figure 5.38 : The pseudo-binary diagram shows (a) the relative positions of the filler metals ER2594 and (b and c) both filler weldments' X-ray diffraction (XRD) patterns

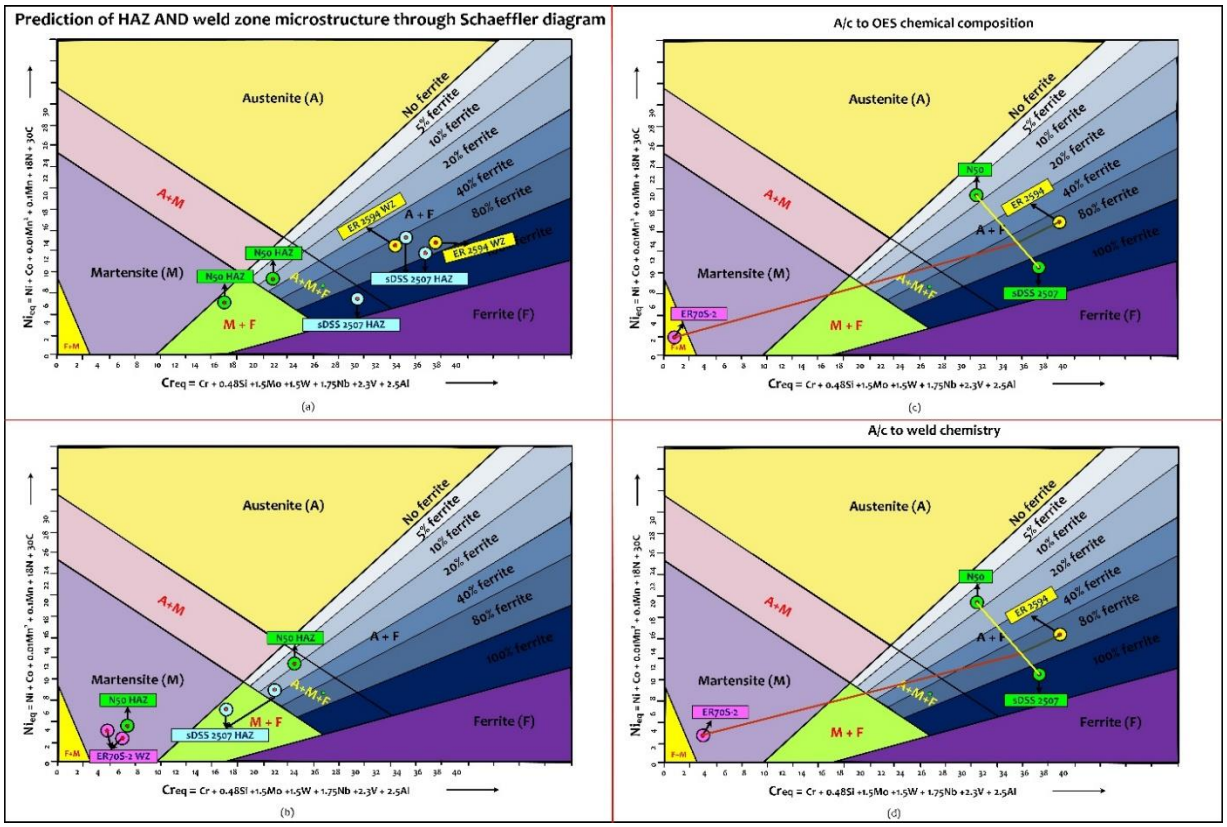

Figure 5.39 : (a and b) Prediction of HAZ and WZ's microstructure of both filler through Schaeffler diagram, and Schaeffler diagram for WZ (c) according to the filler composition, (d) according to the weld chemistry

5.2.2.4 *EFFECT OF HEAT INPUT ON MICROSTRUCTURE EVOLUTION*

To enhance impact toughness, hot cracking resistance, and corrosion resistance, the ferrite fraction in the welded joints plays a crucial role, influenced by thermal exposure and chemical composition. The ferrite content estimation in the ER2594 filler weldments can be theoretically calculated using ferritoscope measurement and verified with the Schaeffler diagram for assessing the weldability of dissimilar joints like sDSS 2507/N50. The Cr_{eq}/Ni_{eq} ratio for ER 2594 filler in LHI and HHI conditions is 3.56 and 3.22, resulting in primary ferrite (F) solidification mode for both conditions in Table 5.13. The Schaeffler diagram predicts ferrite content in the range of 80-90% for LHI and HHI weld zones. Microstructure analysis using optical and SEM micrographs confirms the Schaeffler diagram interpretation. Optimizing ferrite content is crucial for achieving a balanced relationship between mechanical and corrosion properties. The ferrite content measured using a ferritoscope aligns with the Schaeffler diagram prediction. In LHI weldment, the root pass has 29.2% ferrite, while the cap pass has 27.1% ferrite. In HHI weldment, these values are 37.6% and 35.8%, respectively. The difference is attributed to the thermal cycle variation, affecting the transformation of δ to γ. The acceptable ferrite content range for GTAW with ER2594 filler is maintained. Increased heat input leads to higher ferrite content, with notable reformed austenite (WA, GBA, IGA) within the δ-ferrite matrix, indicating enhanced transformation due to prolonged cooling time and improved diffusion of γ-stabilizing elements (N and Ni). The most noteworthy features of the microstructure for both heat input conditions are GBA, WA, IGA, and partially transformed austenite (PTA). The minimum content of austenite should be 30-70% in both root and cap pass to get optimum structural integrity of the weldment with better corrosion properties and improved mechanical properties (Ouali et al., 2019). The results of ferrite content tabulated in Table 5.13 show that the austenite amount increases as heat input increases. At higher heat input, the weld metal is maintained at a high temperature for a longer time, and the cooling rate is slow, which allows more transformation of ferrite to austenite. The thermal cycle involved in root to cap pass causes the subsequent precipitation of several morphologies of the austenite in the weld zone.

The microstructure evolution of the weld zone also shows the formation of the unmixed zone like an island in both heat input conditions, as shown in Figure 5.40(a-c). The UMZ having direct contact with the weld metal forms an island because of the liquidus temperature difference between the filler and base metal. Figure 5.40(b and c) shows the trait of the elemental macrosegregation along the boundaries, causing the banding phenomenon and rate of solidification changes because of the temperature gradient growth and effect on the solidified microstructure. As stated earlier, one of the most important secondary precipitates that can form in the ER2594 weld zone is secondary austenite (γ_2) and sigma phase (σ). The schematic representation of the sequential formation of γ_2 and σ at the δ/γ interfaces is shown in Figure 5.40(d-g), respectively. Essentially, the 50/50 phase balance will not occur if a high cooling rate causes an insufficient transformation from austenite to ferrite. The thermodynamic equilibrium of the primary phase during the effect of welding heat input or more diffusion due to reheating of the specimen could help in the formation of γ_2 in the sDSS 2507 weld zone (Ramirez et al., 2003). The transformation of δ to γ due to reheating by filling passes occurred in the center of the weld zone is called secondary austenite (γ_2). The transformation of γ_2 and σ may form as a result of the eutectoid reaction of $\delta \rightarrow \sigma + \gamma_2$ and $\delta \rightarrow M_{23}C_6 + \gamma_2$ or $\delta + \gamma_1 \rightarrow \delta + \gamma_1 + \gamma_2$. The SEM micrographs confirm the formation of γ_2 in the root pass shown in Figure 5.41(d-e). During the multi-pass welding, the amount of γ_2 reduces in the cap pass compared to the root pass because other filling passes did not reheat the cap pass. The difference in microstructure evolution from root to cap pass is due to differences in the growth rate (R), cooling rate, and temperature gradient (G) of the two subsequent passes. The G/R ratio will increase due to a reduction in the cooling rate due to the application of filling passes and welding heat input effect, leading to an γ structure with columnar dendritic morphology in the cap pass of HHI weldment. Several researchers have observed two different forms of γ_2 (Nowacki & Łukojc, 2006; Ramirez et al., 2003). The first is the intergranular type of γ_2, which usually has a small white needle and island-like morphology nucleates within the δ matrix and is related to Cr_2N or formed at the

δ/γ interfaces. The second is the intragranular type of γ_2, which simply grows off the existing austenite or acicular particles created where the intragranular nitride existed before reheating. Figure 5.41(d and e) shows the fine intergranular γ_2, respectively. The density of the γ_2 is so high that it forms a basketweave structure. Figure 5.40(e) shows both intergranular and intergranular γ_2 formed at the δ/γ interface. The thickness of the γ_2 that grew from the primary γ_1 is uniform all along with the δ/γ interface. The growth of Cr_2N forms at the zone where Ni content is high, and Cr content is low. Many researchers reported that the γ_2 deteriorates the pitting corrosion resistance compared to primary austenite.

Table 5.13 : The average ferrite volume fraction (vol %) of both weldments as per ferritoscope measurement

Specimen	*Cr_{eq}/Ni_{eq}*	*Solidification mode*	*sDSS BM*	*sDSS 2507 HAZ*	*N50 HAZ*	*Weld zone*	
						Root pass	*Cap pass*
ER2594-LHI	3.56	Primary Ferrite	50.9	42.3	9	29.2	27.1
ER2594-HHI	3.22	Primary Ferrite	51.2	45.7	10	37.6	35.8

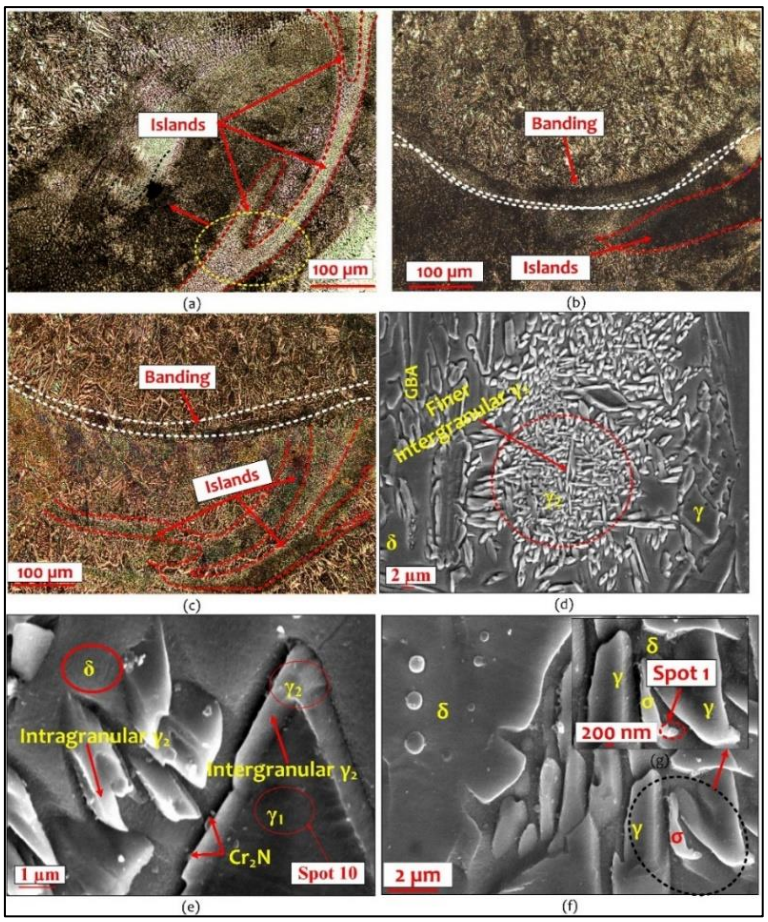

Figure 5.40 : (a-c) The formation of island and banding phenomenon in LHI/HHI weldment, (d) finer intergranular γ_2 in the form of basketweave structure, (e) formation of γ_2 at the δ/γ interface, and (f-g) possible formation of sigma phase at the δ/γ interface, at lower and higher magnification, respectively

The HAZ's microstructure of ER70S-2 LHI/HHI weldment is influenced by filler metal composition, welding parameters, and thermal cycles. At both lower and higher heat inputs, the base metal-weld zone interface exhibits good welded joint quality. However, a wider HAZ is observed at higher heat input conditions, confirmed through image analysis. The calculated

HAZ width increases from 125/80 µm (lower heat input) to 235/162 µm (higher heat input) in super duplex stainless steel/nitronic steel weldments. Grain coarsening and changes in morphology and phase content are noted in the heat-affected zone with increased heat input, aligning with findings from other studies (Y. Yang et al., 2011). The microstructure study reveals no significant grain growth in the sDSS 2507 interface under both heat input conditions. The HAZ exhibits a mix of austenite and ferrite, with a distinct fusion line and type II boundary observed for both heat input conditions. Along the fusion boundary, a subtle transition region (Type II boundary) is observed between the base and weld metal. Several factors prevent the consistent and complete mixing of filler and base metal like welding parameters, thermomechanical differences, nature of the fluid flow, joint design, welding process, and segregation of alloying elements during non-equilibrium solidification results in macrosegregation in dissimilar metal welding (Tasalloti et al., 2017). Macrosegregation occurs because of the incomplete mixing of elements from base and filler metal. Generally, the types of macrosegregation are available in the published works: islands, beaches, and peninsulas (Y. K. Yang & Kou, 2007). The macrosegregation mentioned above is shown in Figure 5.41(a-i) for both heat input conditions near the interface. The formation of the peninsula and the island are initiated from unmixed molten base metal, and its formation is independent of filler composition. The formation of the peninsula and islands parallel to the fusion boundary occurred when the liquidus temperature of weld zone (T_{LW}) is less than the liquidus temperature of base metal (T_{LB}), which also leads to the formation of a filler-deficient beach near the fusion zone. An adverse effect on the weld structural integrity could occur because of macrosegregation, like loss of toughness, stress corrosion cracking, and hydrogen-induced cracking. The investigation of the internal microstructure of the island and peninsula became important in recognizing the correlation between macrosegregation and the weak region of HAZ. The banding phenomenon near sDSS 2507′HAZ of LHI weldment is observed near the sDSS 2507interface region in LHI weldment. The banding phenomenon is the trait of the elemental macrosegregation along the boundaries and sudden change in solidification rate. Other investigators also stated similar results near the interface region (Jula et al., 2018). The type II boundary is oriented parallel to the fusion boundary, which can be seen at the sDSS 2507 and N50 interface. Several researchers also observed the same during the analysis of weld interface and HAZ (Nelson et al., 2000).

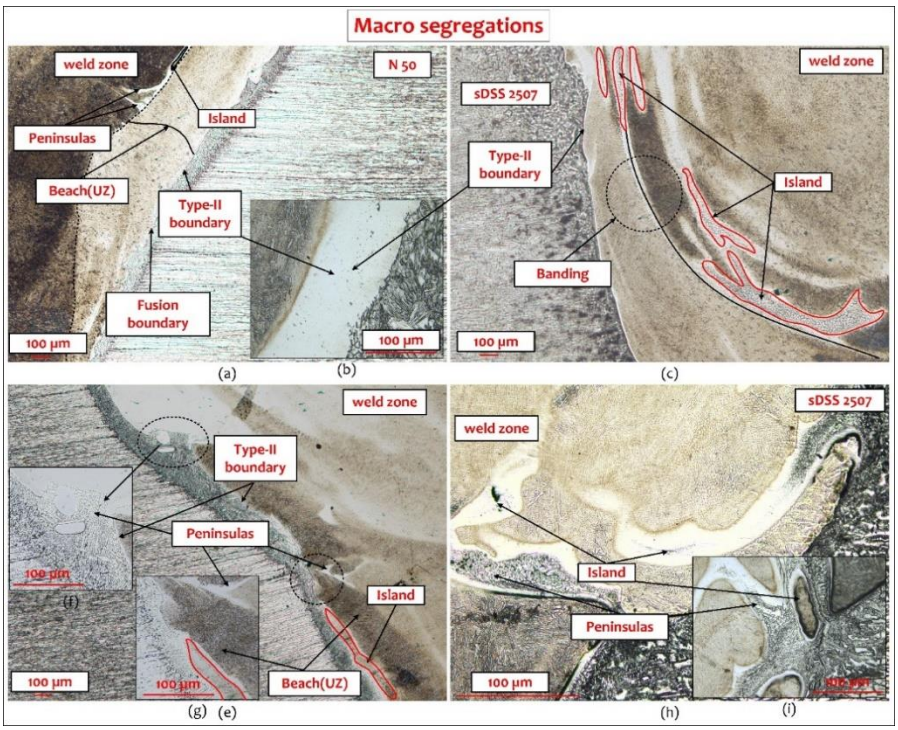

Figure 5.41 : (a-i) Microstructure of the weld zone/nitronic steel interface shows the formation of the UMZ appearing as the peninsula, island, and banding phenomenon, respectively.

5.2.3 MECHANICAL CHARACTERIZATIONS

Microhardness, tensile, and impact tests are used in microstructural characterization to evaluate the effect of filler metal and heat input on the structural integrity of weld joints.

5.2.3.1 *MICROHARDNESS*

The microhardness profiles of the BM, HAZ, and weld zone for both fillers were examined across the transverse direction of the weldment, and the results are presented in Figure 5.42(a). Vickers microhardness testing (model- VHD-1000A) was employed, with the reference point (x=0) set at the weld center for all tested weldments. The sDSS 2507 exhibited an average hardness of 290.17 ± 10 $HV_{0.5}$, while N50 displayed a superior hardness value of approximately 317.86 ± 10 $HV_{0.5}$. The microhardness profile of the WZ in as-welded (AW) condition revealed an average hardness of 287.34 ± 10 $HV_{0.5}$ for filler ER 2594 and 372.36 ± 10 $HV_{0.5}$ for ER70S-2. This difference in hardness was attributed to the presence of soft reformed austenite in the microstructure of ER 2594 filler WZ and the formation of martensite bands or carbide precipitates in ER70S-2 filler WZ. (García-Mateo & Caballero, 2005) observed a similar result for the base and weld metal. The average hardness in the ER70S-2 filler was found to be higher than that of the ER 2594 filler. The average hardness values of sDSS 2507 and ER 2594 filler WZ were comparable, both around 290.17 ± 10 $HV_{0.5}$. In super duplex filler ER 2594, the HAZ on both sides showed comparable average hardness values, i.e., 278.4 ± 10 $HV_{0.5}$ for N50 side HAZ, and 283.49 ± 10 $HV_{0.5}$ for sDSS 2507 side HAZ, indicating minor variations due to grain coarsening and morphology changes in the HAZ region. Similarly, ER 70S-2 filler displayed comparable average hardness values of 373.36 ± 10 $HV_{0.5}$ in sDSS 2507 side HAZ and 369.48 ± 10 $HV_{0.5}$ in N50 side HAZ. Figure 5.42(b) illustrates microhardness variations in the WZ, showing higher average values at the cap (top) than the root (bottom). The non-uniform variations in hardness along the WZ were attributed to changing heat input during multi-pass welding, with average hardness values of about 297.76 ± 10 $HV_{0.5}$ for ER 2594 and 368.48 ± 10 $HV_{0.5}$ for ER70S-2 throughout the WZ.

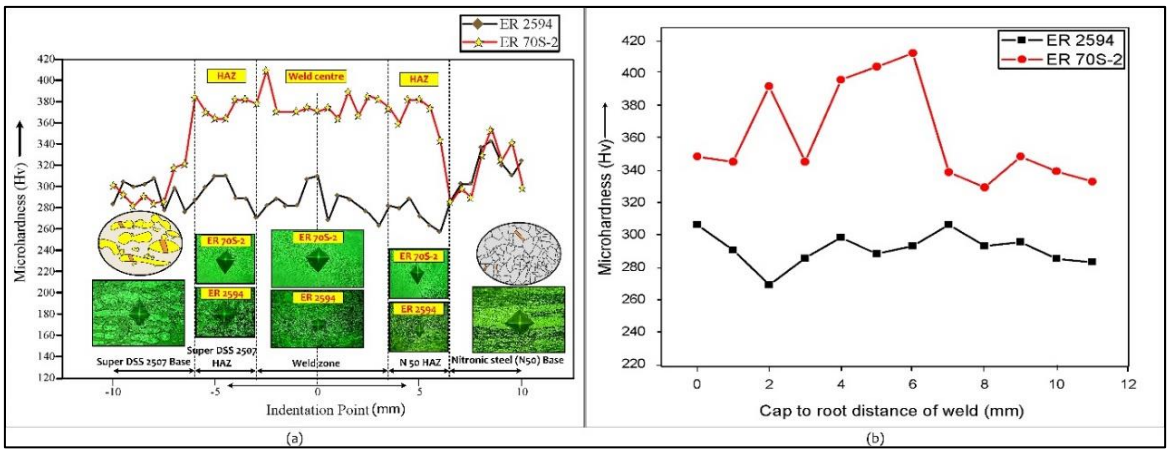

Figure 5.42 : (a) Microhardness profile of the welded joint between SDSS 2507 and N50 across the weld joint, (b) Hardness profile variation across the WZ of filler (ER 2594 and ER 70s-2) from cap to the root

The microhardness results for the ER2594 LHI/HHI weldment reveal minor variations in the hardness values of the HAZ for both heat input conditions, as depicted in Figure 5.43(a and b). As the indentor passes outwards from the weld zone to the HAZ region, microhardness in the sDSS 2507 HAZ side increases from 294 $HV_{0.5}$ to 296 $HV_{0.5}$, and correspondingly, the microhardness in the N50 HAZ side increases from 271 $HV_{0.5}$ to 276 $HV_{0.5}$ for LHI and HHI weldment, respectively. The change in hardness value of LHI and HHI weld zone is 284 $HV_{0.5}$ to 274 $HV_{0.5}$, respectively (Table 5.14). There are many important factors for the decrement in hardness value from LHI to HHI described in microstructure evolution of weld zone that can be ascribed to the difference in cooling rate, austenite to ferrite ratio, lower content of ferrite, presence or absence of precipitation, and coarse grain structure. In addition to the content of the

ferrite phase in the weld zone, several factors could affect the change in hardness value. Hence, it can be concluded that phase ratio, secondary phase formation, and grain size are some of the most important determining factors in the hardness of the weld zone. The average hardness value from cap to root in the weld zone is 332 $HV_{0.5}$ to 290 $HV_{0.5}$, respectively, and similarly, HHI from cap to root in the weld zone is about 305 $HV_{0.5}$ to 301 $HV_{0.5}$, respectively. The progressive reduction in hardness value as the indentor approaches from cap to root is because of variations in cooling rate and changes in heat input. The microhardness profile generally shows that the hardness value indicates no significant variation in base metal, HAZ, and weld zone for both LHI and HHI joints. However, it can also be noted that the heat input increment shows a decrement in the hardness value.

Microhardness in ER70S2-LHI/HHI weldment increases from 370 to 382 $HV_{0.5}$ (LHI) and from 346 to 380 $HV_{0.5}$ (HHI) as the indenter moves from the weld center towards the HAZ, as depicted in Figure 5.43(c and d). As discussed in microstructure evolution, the formation of martensite bands and laths and carbide precipitate, grain coarsening in the microstructure of LHI and HHI weldments evidently reveals that welded specimen with LHI depicts a higher hardness value than HHI in the weld zone. Both weldments' HAZ regions encountered a rise in microhardness because of macrosegregation formation near the fusion boundary. For LHI weldment, the HAZ of sDSS 2507 and N50 shows negligible variation in the hardness value (i.e., 375 $HV_{0.5}$ and 365 $HV_{0.5}$, respectively). Subsequently, the HAZ of sDSS 2507 and N50 for HHI weldment shows significant variation in the hardness (i.e., 370 $HV_{0.5}$ and 340 $HV_{0.5}$, respectively) (Table 5.14). Hereafter, the variation in the hardness value is primarily due to the HAZ's grain coarsening and morphological evolution. As discussed in the microstructure evolution, it is suggested that the higher hardness value is accredited to the lath martensite formation with small ferrite pockets due to the cooling rate effect. The increment in heat input tends to a more significant increment in ferrite content due to a lower cooling rate, which leads to a decrement in martensite formation. So, the weld zone's average hardness decreased with increased heat input because of microstructure evolution from martensite to ferrite. The overall performance of the welded joint does not depreciate because of this change in hardness value, which helps maintain the joint's structural integrity. Figure 5.43(d) shows both weldment hardness values from the cap to root pass of the weld zone. The variation of hardness value from cap to root pass is around 367 $HV_{0.5}$ to 315 $HV_{0.5}$ for lower heat input and 375 $HV_{0.5}$ to 305 $HV_{0.5}$ for higher heat input. This variation in microhardness value near the cap of the weld zone is increased. As the indentor approaches the weld center, it progressively reduces because of changes in heat input and cooling rate variation from the cap to the root of the weld zone. The highest hardness (i.e., 395.6 $HV_{0.5}$) location was found between the narrow zone of the Type-II boundary and interface boundary in the sDSS 2507 HAZ.

Table 5.14 : Effect of heat input on microhardness variation of LHI/HHI weldment of ER70S-2/ER2594 filler

Microhardness properties		
Filler metal	*Weldments*	*Microhardness ($HV_{0.5}$)*
ER70S-2	LHI	340 ± 6
	HHI	380 ± 4
ER2594	LHI	284 ± 5
	HHI	274 ± 4

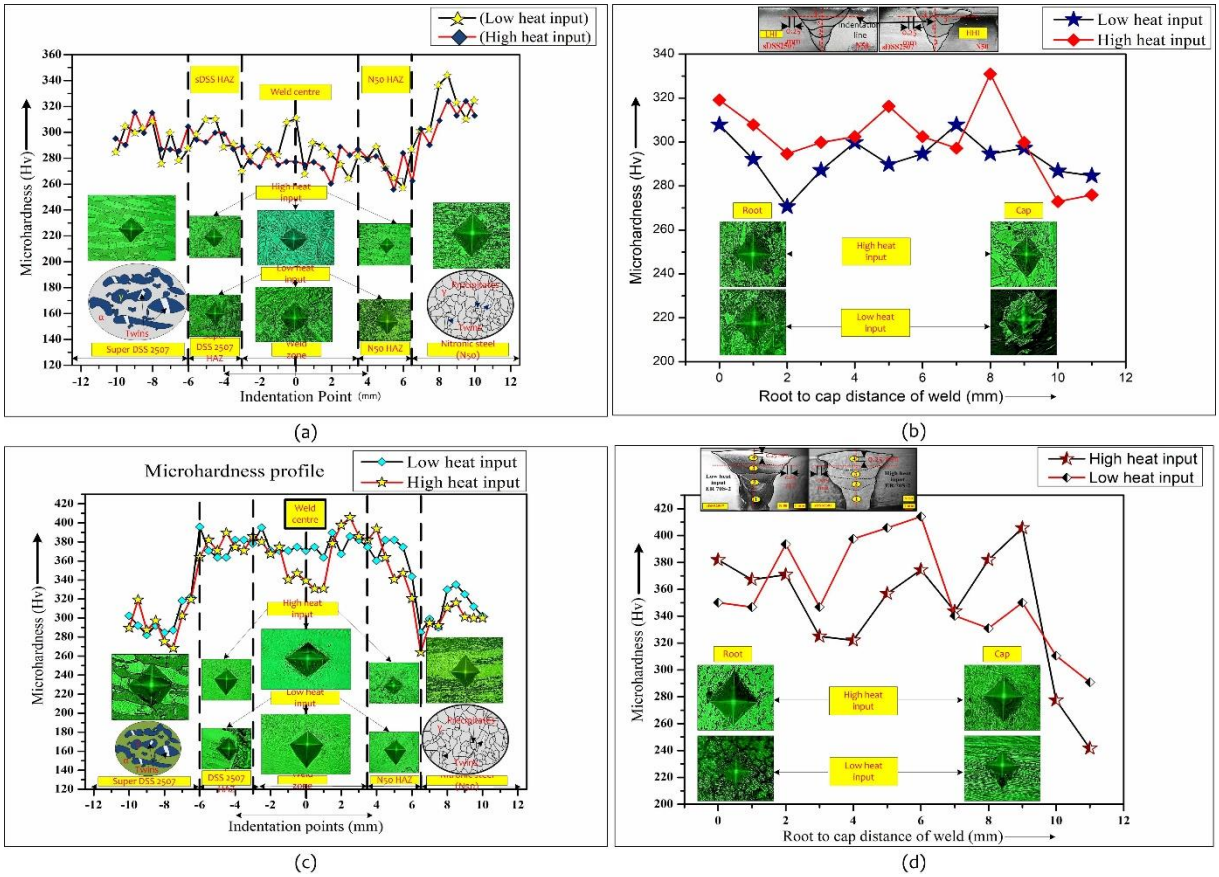

Figure 5.43 : Microhardness profile across the weld joint and hardness profile variation across the weld zone from cap to the root of LHI and HHI weldment for (a-b) ER2594 filler, (c-d) ER70S-2 filler, respectively

5.2.3.2 *TENSILE TEST*

The tensile testing was conducted on the as-welded (AW) specimens of dissimilarly welded joints involving sDSS 2507 and N50 (Figure 5.44(a)). The tensile strength of the base metals (sDSS 2507 and N50) was consistently measured at 830 ± 10 MPa and 910 ± 10 MPa, respectively. The ultimate strength of the AW specimens with ER2594 and ER70S-2 fillers was recorded as 897.32 MPa and 872.15 MPa, respectively. These values were higher than sDSS 2507 but lower than N50. Notably, both AW specimens exhibited failure within the weaker base metal, specifically within the sDSS 2507, at a considerable distance from the fusion line. The use of ER2594 filler resulted in superior tensile strength (897.32 MPa) with mismatches of 1.068 and 0.976 compared to sDSS 2507 and N50, respectively. Conversely, the welded joint with ER70S-2 filler displayed an ultimate strength of 872.15 MPa, with mismatches of 1.0385 and 0.95 with sDSS 2507 and N50 base metals, respectively. Notably, the ER70S-2 filler exhibited nearly 10% better ductility than ER2594. The stress-strain curves and relevant tensile test results are presented in Table 5.15, and the corresponding curve is illustrated in Figure 5.44(b). The weld mismatch was calculated using the formula: Weld mismatch = (Ultimate tensile strength of the welded joint) / (UTS of the as-received base metal) × 100%. The SEM fractographs of both filler's weldments and base metal specimens, observed at high magnification in Figure 5.44(c-f), revealed fractured surfaces with features such as dimples, microvoids, and cleavage facets. The fractured tensile specimen of sDSS 2507 displayed ductile and cleavage facets, dimples, and quasi-cleavage facets, while N50's SEM fractograph exhibited cleavage facets, small and uniform dimples with inclusions, and tearing ridges. Plastic deformation before fracture from different orientations was evident in the base metals, indicating ductile failure modes for both sDSS 2507 and N50. The tested tensile specimen of ER2594 filler weldments exhibited transgranular ductile dimple facets with cleavage facets and macro voids in the SEM fractograph. Similarly, the broken specimens of ER70S-2 filler displayed a more dominant cup-and-cone structure than ER2594, with the SEM fractograph comprising dimple and cleavage facets along with microvoids.

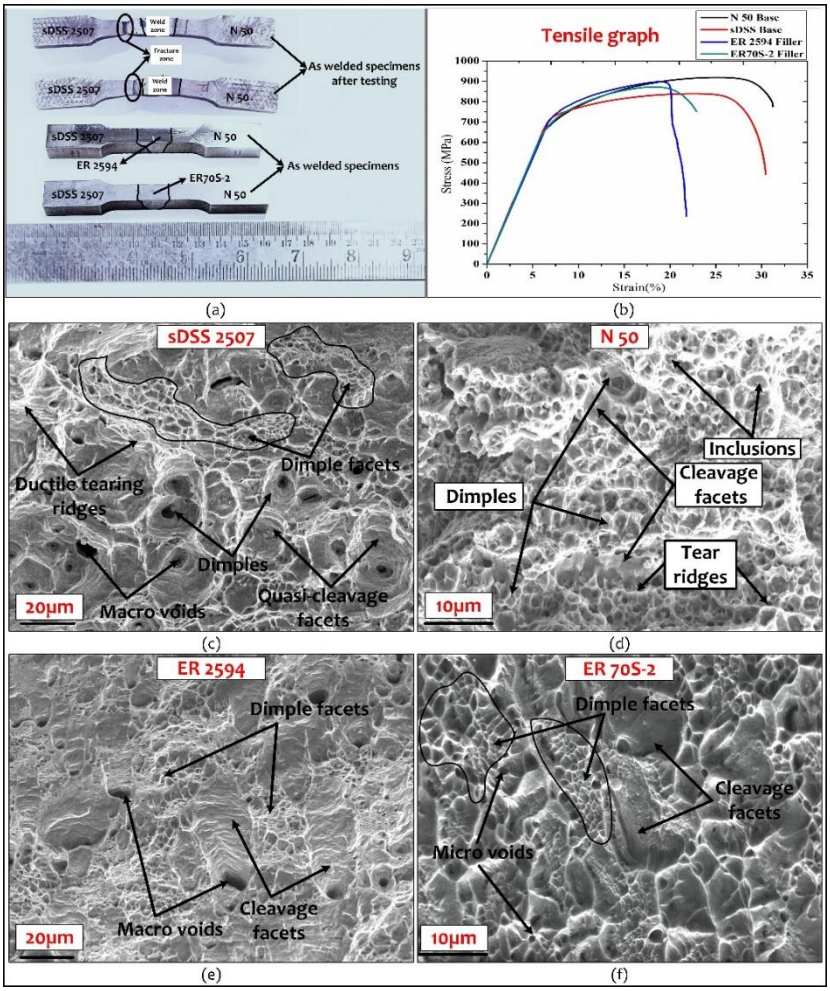

Figure 5.44 : (a) Tensile test specimens before and after fracture in the AW condition, (b) Tensile graph of both BM and filler metal, SEM fractograph of (c) sDSS 2507 BM, (d) N50 BM (c and d) ER 2594 and ER 70S-2 filler, respectively

Table 5.15 : Detailed tensile properties of filler metal with weld mismatch

Material	Tensile Strength (MPa)	Weld mismatch with sDSS 2507 base	Weld mismatch with N50 base	Elongation (%)	Location of the fracture
sDSS 2507	839.826	--------	--------	30.5	--------
N50	919.01	--------	--------	32.24	--------
ER2594	897.32	1.068	0.976	21.8	(sDSS 2507 side)
ER70S-2	872.15	1.0385	0.95	23.56	(sDSS 2507 side)

Transverse tensile tests on welded joints using ER 2594 filler under LHI and HHI conditions revealed comparable average strengths of 895 ± 4 MPa and 900 ± 5 MPa (Figure 5.45(a)). Weld mismatch values were 1.070 and 1.075 for LHI with sDSS 2507 and N50 base metals and 0.97 and 0.98 for HHI (Table 5.16). Due to the increased ductility and tensile strength in the HAZ and weld metal, LHI fractured at sDSS 2507 base metal. HHI weldments fractured at the weld zone but displayed higher tensile strength than sDSS 2507 base metal. Minor variations in tensile strength between LHI and HHI weldments suggest fractures under heterogeneous and local deformation conditions. Fractographic analysis revealed the presence of microvoids, dimples, ductile tearing ridges, and quasi-cleavage facets. Hardness studies aligned with weld strength, indicating lower hardness in the weld than both base metals. Higher γ_2 precipitate particles and increased WA in the weld zone decreased ductility in HHI weldments (Figure 5.45(c and d)). At room temperature, transverse tensile tests were conducted on sDSS 2507/N50 BM and welded joints using ER70S-2 filler at different heat inputs (Figure

5.45(b)). The tensile strengths of the welded joints were 870 ± 4 MPa for LHI and 835 ± 6 MPa for HHI weldment. The weld mismatch, calculated as the ultimate tensile strength ratio of the weld metal with the base metal, showed superior tensile strength for LHI (872.15 MPa) and a mismatch of 0.948 and 1.0392 with sDSS 2507 and N50. HHI weldment had lower tensile strength (839.2 MPa) and a mismatch of 0.912 and 1 with sDSS 2507 and N50 BM (Table 5.16). All specimen failures occurred at the weaker sDSS 2507 BM. Microhardness results correlated with tensile test results, indicating higher hardness in the weldment than the base metal. Fractography revealed the presence of microvoids, dimples, ductile tearing ridges, and cleavage facets on fractured surfaces, indicating ductile mode failure. The HHI weldment exhibited coarser dimples, suggesting differences in surface morphology due to varying cooling rates. Coarse grain formation in HHI resulted in slower cooling rates and larger dimples, while faster cooling in LHI led to finer and shallower dimples, indicating superior ductility and tensile strength (Figure 5.45(e and f)).

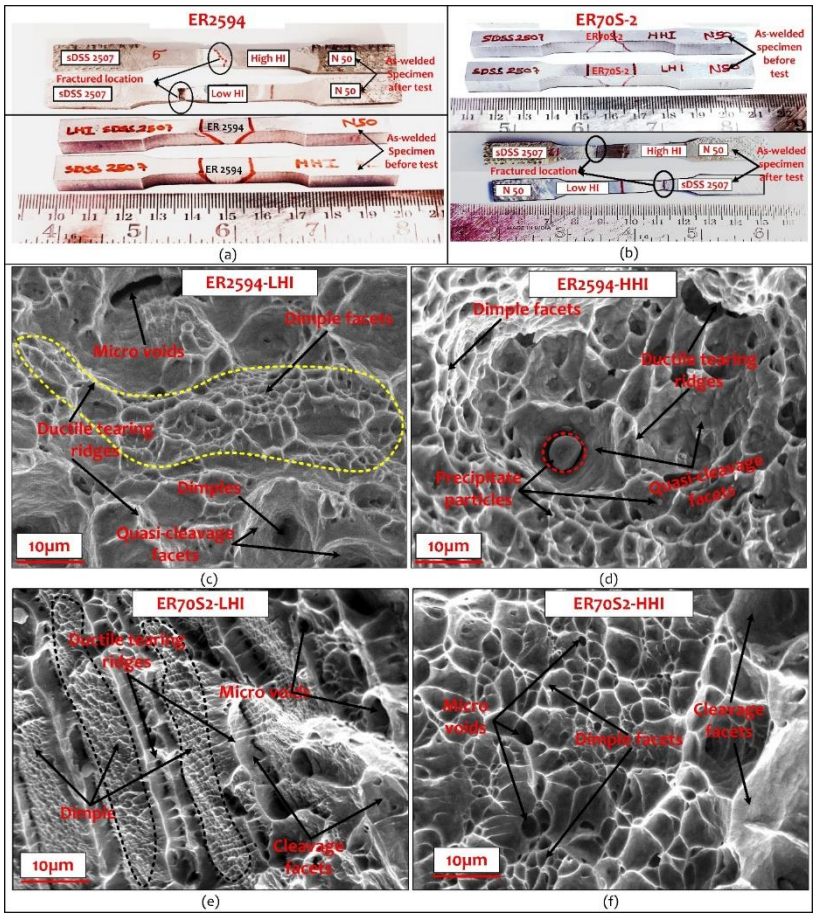

Figure 5.45 : (a and b) Tensile test specimens before and after fracture in the LHI/HHI condition for ER2594 and ER70S-2 filler, respectively, SEM fractograph of LHI/HHI weldment for (c-d) ER2594 filler, (e-f) ER 70S-2 filler, respectively

Table 5.16 : Comprehensive tensile properties with weld mismatch of ER2594/ER70S2 weldment of LHI and HHI conditions

Filler metals	*Weldments*	*Tensile properties*			*Location of the fracture*
		Tensile Strength (MPa)	*Percentage elongation (%)*	*0.2% Yield Strength*	
ER70S-2	LHI	872.15	23.66	640.16	sDSS 2507 BM side
	HHI	839.2	22.87	676.78	sDSS 2507 BM side
ER2594	LHI	898.6	21.80	692.73	sDSS 2507 BM side
	HHI	901.76	18.65	700.14	At weld centre

5.2.3.3 IMPACT TEST

The Charpy impact test (CIT) was conducted to assess the impact behavior of the base metals (sDSS 2507 and N50) and weldments of sDSS 2507 and N50 using fillers ER2594 and ER70S-2 under sudden impact loads. Specimens from both base metals and weld zones were prepared for the CIT, and the results are displayed in Figure 5.46(a). Notably, the sDSS 2507 and N50 base metals and the weldment with filler ER2594 exhibited V-notch deformation, while the ER70S-2 weldment fractured at the V-notch zone (Figure 5.46(a)). The average CIT value for sDSS 2507 BM and ER2594 filler metal was 320 ± 6 J and 165 ± 5 J, respectively. The sDSS 2507 impact specimen displayed ductile fracture with parabolic dimples and tearing edges in the SEM micrograph (Figure 5.46(b)). Similar observations were reported for the sDSS 2507 BM by (Pilhagen et al., 2014) and (Zhang et al., 2016). The N50 impact specimen showed typical ductile fracture failures, with an average impact value of 220±5 J. The SEM fractograph revealed dimples, microvoids, and cleavage facets at the fracture surface (Figure 5.46(c)). The ER2594 weldment impact specimen exhibited ductile fracture with features such as microvoids, inclusion particles, ductile tearing ridges, and cleavage facets (Figure 5.46(d)). The ER70S-2 impact specimen displayed a quasi-brittle fracture with an average impact toughness of approximately 110±8 J. The SEM fractograph showed a predominantly brittle fracture surface with areas of ductile features, including microvoids, tear ridges, inclusion particles, dimples, and dimple facets (Figure 5.46(e)). The presence of inclusion particles hindered dislocation movement, reducing the weldment's ductility and toughness. Overall, the ER2594 filler exhibited superior impact toughness compared to the ER70S-2 filler.

The impact toughness test was conducted on the sDSS 2507/N50 BM and LHI/HHI weldment for ER70S-2 and ER2594 filler (Figure 5.47(a)). The specimens from base metals showed significant plastic deformation before fracture, while the weld centers exhibited complete fracture, indicating a quasi-brittle fracture mode for ER70S2-LHI/HHI welded joint. Notched specimens at the weld center had lower impact energy absorption due to fracture at the V-notch zone. The ER70S-2 weldment had average impact toughness values of 110±8 J and 142±5 J for lower and higher heat input, respectively (Table 5.17). The HHI weldment exhibited higher impact toughness, attributed to the presence of martensite in the weld zone. LHI weldment resulted in the formation of low-carbon lath martensite, leading to higher hardness and lower toughness. Fractography revealed ductile fractures in the base metals and weld zones, while the weld zones showed predominantly brittle fractures with microvoids, precipitate particles, dimples, and cleavage facets (Figure 5.47(b-c)). Moreover, the average CIT test value of ER2594 weldment with LHI and HHI is around 165±5 J and 145±3 J, respectively. The impact toughness of the weldments shows a decreasing trend with increasing heat input due to HHI weldment experiencing a slower cooling rate. The decreasing trend in the CIT test results with heat input can be correlated with microstructure evolution. The LHI weldment exhibits a higher impact toughness than HHI, which can be explained by several factors linked with microstructure evolution. Firstly, the LHI specimen experienced the lowest heat input with a higher cooling rate. Secondly, the adequate amount of phase transformation from ferrite to reformed austenite could improve the toughness of the weldment, and it subsequently increases the impact energy (Vahman et al., 2020). Another critical factor that influences the impact toughness is the existence of secondary phases like secondary austenite and sigma phases (Yousefieh et al., 2011). Figure 5.47(d-e) shows the SEM fractograph of both heat input conditions. It commonly consists of microvoids, ductile facets, dimples, ductile tearing ridges, and inclusion particles. The SEM fractograph of LHI weldment also demonstrates extensive ductile fracture mode due to the fracture surface taking on a “whipped cream” type appearance, as shown in (Figure 5.47(d)).

Table 5.17 : Comprehensive impact energy with fracture type of ER2594/ER70S2 weldment of LHI and HHI conditions

Impact toughness			
Filler metal	*Weldments*	*Impact energy (J)*	*Fracture type*
ER70S-2	LHI	110 ± 8 J	Ductile
	HHI	142 ± 5 J	Ductile/brittle
ER2594	LHI	165 ± 5	Ductile
	HHI	145 ± 3	Ductile

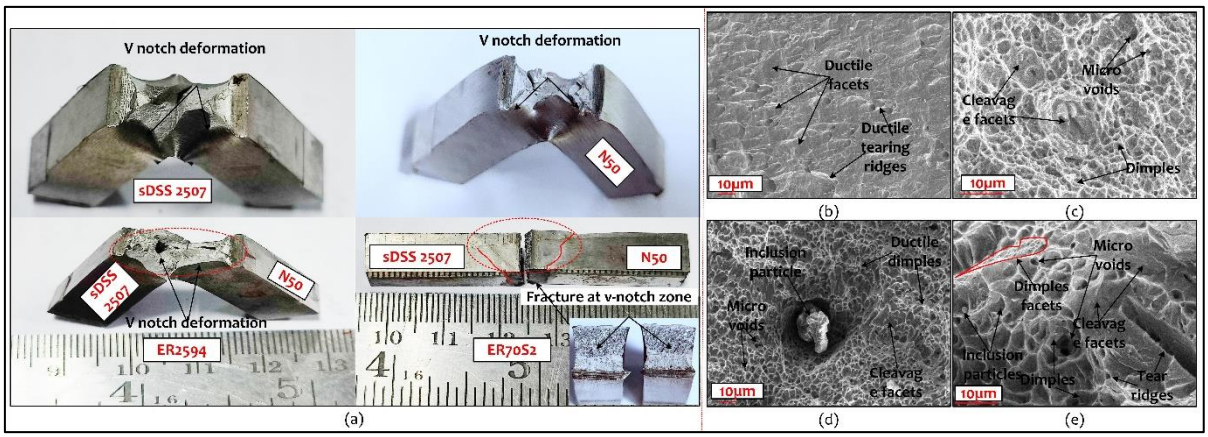

Figure 5.46 : Impact toughness test specimens of the weldment using ER2594 and ER70S-2 filler: (a) base and weld impact specimen after the test, and SEM impact fractographs of (b and c) sDSS 2507 and N50 BM, and (d and e) ER2594 and ER70S-2 filler, respectively

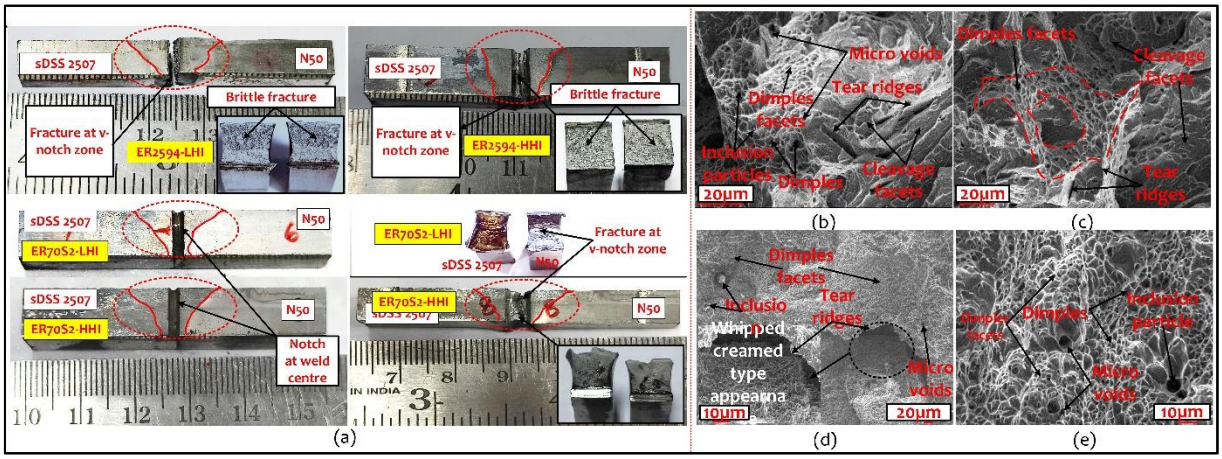

Figure 5.47 : Impact toughness test specimens of the LHI/HHI weldment using ER2594 and ER70S-2 filler: (a) base and weld impact specimen after the test, SEM impact fractographs of the LHI/HHI weldment using (b and c) ER2594 filler, and (d and e) ER70S-2 filler, respectively

5.2.4 TRIBOLOGICAL INVESTIGATIONS

This study is crucial for selecting optimal welding parameters, fillers selection, and optimizing tubing and coupler assembly design for sDSS 2507/N50 DWJs, providing insights into wear behavior to enhance performance and durability.

5.2.4.1 *MICROHARDNESS AND WEAR CHARACTERIZATION*

The tribological behavior of the surface is directly related to its mechanical properties. The sample's significant initial hardness first predominates while friction is present. High hardness diminishes wear debris between friction subgroups and increases the surface's plastic deformation resistance. The wear resistance of the material is directly correlated with hardness.

The hardness value of the sDSS 2507 and N50 BM is 290 ± 4 $HV_{0.5}$ and 315 ± 6 $HV_{0.5}$, respectively. Even though strain hardening increased the microhardness of both base metals, sDSS 2507 surpassed N50 in work hardening because it had more dislocation movement planes. Dislocations move more readily in sDSS 2507's FCC crystal lattice, minimizing deformation and work hardening. The LHI and HHI weld zones of ER 2594 have average hardness values of 285 ± 5 $HV_{0.5}$ and 274 ± 7 $HV_{0.5}$, respectively. ER2594 filler weldment hardness changes due to microstructural variations. Increasing work hardening and hardness are the results of sliding friction. Hardness increases with phase changes like ferrite to austenite. The test may diminish hardness due to grain growth and higher grain sizes. The hardness drop from LHI to HHI is caused by cooling rate, γ to δ ratio, ferrite content, precipitation, and coarse grain structure. Depending on the size and distribution of the components that precipitate, the hardness can be increased or decreased. In comparison, the ER70S2 weld zone has a higher average hardness of 365 ± 4 $HV_{0.5}$ for the LHI and 350 ± 7 $HV_{0.5}$ for the HHI. Martensite bands and laths, carbide precipitate, grain coarsening, and martensite to ferrite transformation increased LHI and HHI weld zone average hardness. Pin-on-disc wear testing increased the microhardness of ER70S-2 filler weldments, whereas it decreased for ER2594 filler weldments. The mean weight loss and average hardness values for all specimens are compared and depicted in Figure 5.48.

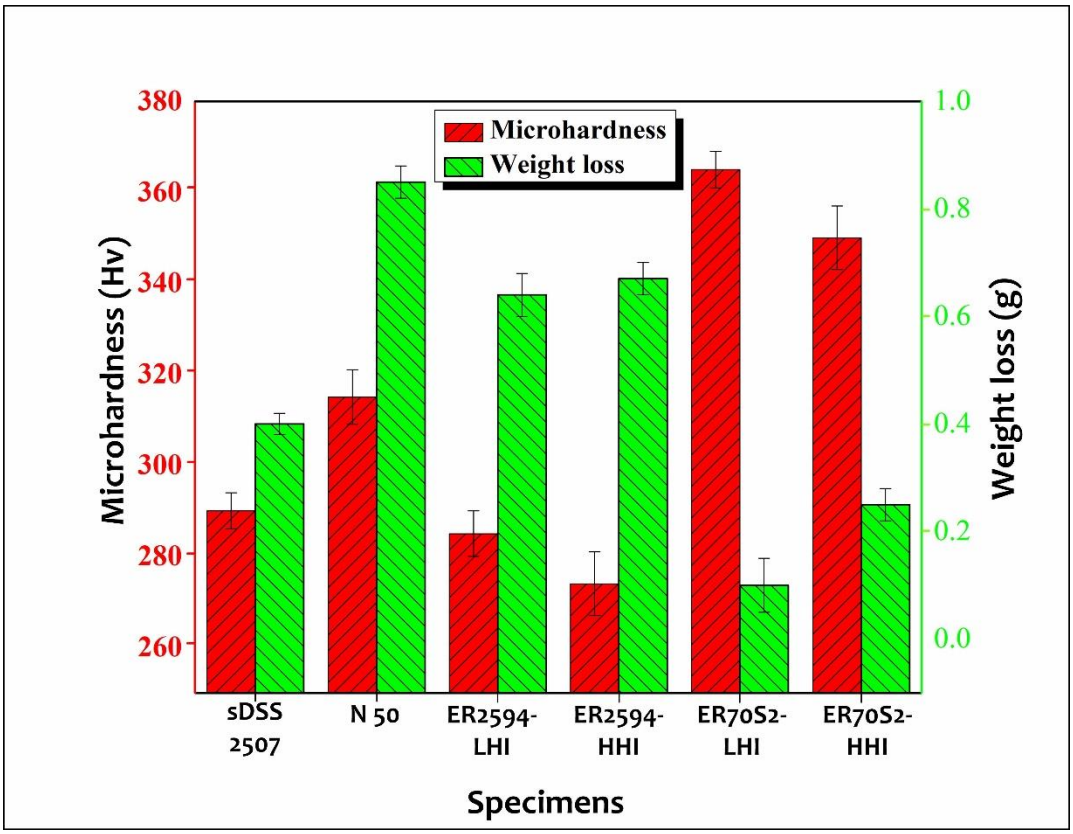

Figure 5.48 : Microhardness and weight loss owing to wear of all base metal and weld zone

The pin-on-disk tribometer test findings followed a similar pattern to the hardness values for the weld zone. Progressive sliding distances of 500 to 3000 meters were applied to the pins of each specimen. The pins extracted from sDSS 2507BM, N50BM, ER2594-LHI, and ER70S2-LHI were investigated under the same testing parameters, and their mean weight losses were 0.40 g, 0.85 g, 0.65 g, and 0.10 g, respectively (Figure 5.49). Table 5.18 lists the wear performance parameters for all specimens, and a comparative plot of these parameters (Figure 5.49(a-d)) indicates that the ER70S2-LHI specimen had the lowest volume loss (12.83 mm^3) and the N50 BM exhibited the greatest (112.65 mm^3). The volume loss seen in the N50 BM sample is 88% greater than that observed in the ER70S2-LHI weldment sample with the lowest volume loss. The LHI and HHI weld zones using ER2594 filler had approximately equal volume loss results of 87.33 mm^3 and 87.90 mm^3. The ER70S-2 filler weldments demonstrate superior

performance compared to the ER2594 filler weldments, with a volume loss reduction of 85% and 60% for the LHI and HHI weldment conditions, respectively. This consistency in weight loss can be attributed to the identical chemical compositions and microstructural evolution observed in both weld zones. These results show that ER2594-filled LHI and HHI weld zones contribute to the same wear parameters as the sDSS BM. N50 BM exhibits lower wear performance parameters than other specimens despite wear lying within acceptable performance limits. However, despite minor wear performance parameter variations, both fillers' weld zones fulfill acceptable performance criteria. The wear data, given as material loss in micrometers, followed a similar pattern. The corresponding wear graphs (in μm) obtained versus the sliding distance (in m) show that the ER70S2-LHI weldment had the least material loss due to wear (Figure 5.50(a)). However, the wear of ER2594-LHI and ER2594-HHI weldment was identical and higher than sDSS 2507BM. Sliding over shorter distances resulted in less wear at first, but the result rapidly prevailed over the exponential increase in wear for longer sliding distances. The pin's wear rate is directly correlated with the friction force applied to it. Measurement of friction force and wear in μm demonstrated a similar influence of microstructure evolution and microhardness on the specimens (Figure 5.50(b)). Notably, the N50 BM specimen experienced the most significant friction force magnitude, while the ER70S2-LHI specimen experienced the least.

The gradual removal of material from surfaces in contact is known as wear. Changes to the affected material's dimensions are the first visible sign of this process, followed by noticeable variations in the material's geometry as the stages progress. Thus, the component's dimensions change as the contacting surface loses material. Increased contacting surface dimensions increase moving part clearance. Thus, material loss is caused by altering the contacting surface size and geometry. As the sliding distance increased, the pin specimen's weight loss confirmed progressive wear. As the pin slid over longer distances, an increase in the material's weight loss was observed. The metal's hard surface initially resisted material removal, resulting in minimal weight loss. The hard outermost layer was gradually worn when the pin slid over 1000 and 1500 m, causing significant weight loss. Weight loss increased pin wear face diameter and geometry as sliding distance increased. When the pin and disc's contact surface area changed, material removal was accelerated, and weight loss significantly increased—especially at an extended sliding distance of 3,000 m. Following the abovementioned pattern, Figure 5.50(c)) depicts the weight loss as a function of sliding distance. Figure 5.50(d)shows the evidence of progressive wear in the form of a wear track and pin face profile. As the pin surface moved against the disc, it experienced a substantial change in appearance and geometry. When pins were subjected to extended sliding distance, wear tracks became more prominent in the images.

Table 5.18 : Wear performance factors for base metals and all weld zones

Specimens	*Volume loss (mm^3)*	*Wear rate ($\times10^{-3}$ mm^3/m)*	*Wear coefficient ($\times10^{-4}$)*	*Specific wear coefficient ($\times10^{-4}$)*
sDSS BM	55.29	18.43	17.81	6.14
N50 BM	112.65	37.55	39.43	12.51
ER2594-LHI	87.33	29.11	27.65	9.70
ER2594-HHI	87.90	29.3	26.76	9.76
ER70S2-LHI	12.83	4.28	5.20	1.42
ER70S2-HHI	35.87	11.96	13.95	3.98

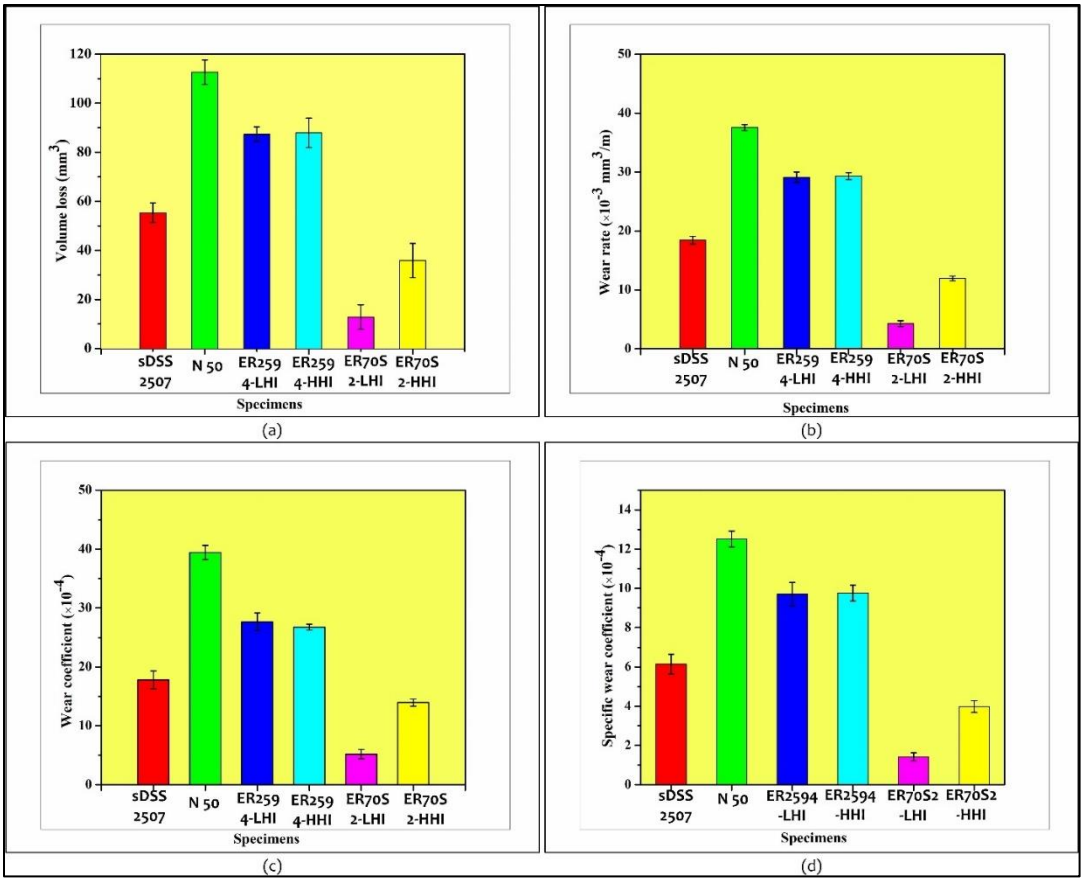

Figure 5.49 : Wear parameters: (a) volume loss, (b) wear rate, (c) wear coefficient, (d) specific wear coefficient

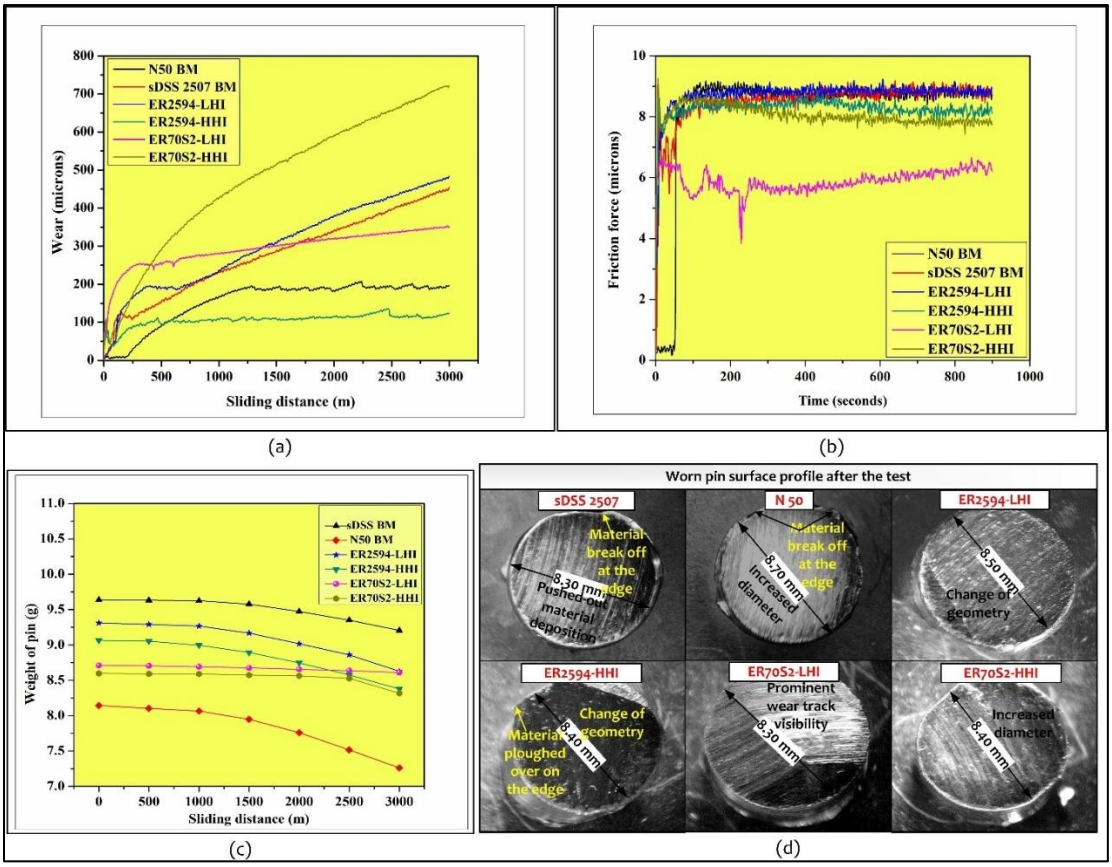

Figure 5.50 : (a) Wear rate versus sliding distance (m) plot for all specimens, (b) coefficient of friction operating on all specimens, (c) Progressive weight loss with changing sliding distance for all specimens, (d) Macrograph of worn pin surface of all base metals and weld zones after the test

5.2.4.2 *WEAR MECHANISM*

A stereomicroscope and SEM were employed to analyze the pins' wear mechanism. The results revealed that the pins experience material break-off at the edge, resulting in an increased diameter, distorting the pin's circular geometry. This break-off occurred in all pins removed from base metals and ER2594 weld zones except ER70S-2'weld zones (Figure 5.51(a-d)). The material appeared to have been removed by the ploughing mechanism because it seemed like it had been pushed outward from the center of the pin toward the pin's edge. The cracks grew wider and were easier to observe when the sliding distance was increased to 3,000 m. After investigating the worn surface with SEM, it was discovered that the wear occurred in several different modes, as depicted in (Figure 5.52(a-d)). A thorough investigation of the surface deterioration and material removal provided details on the wear mechanism. The increase in sliding speed is seen to result in severe plastic deformation, which in turn causes groves in the sliding direction associated with the local stress, causing abrasive wear with more extensive damage on the BM sample, where a ploughing mechanism is primarily caused by debris, also spalling and flaking are observed in both BM (Figure 5.52(a-b)). Adhesive wear was evidenced by tracks' scratches, grooves, and furrows. The narrow longitudinal tracks that are visible on the worn surface indicate that the boundary of adhesive wear is linked to material loss and surface deterioration caused by abrasive wear. These tracks represent unequal metal loss from the surface due to misorientation between adjacent materials. It can be concluded from the samples' surface deterioration, such as pits, cracks, and flaking, that fatigue wear separates the chips from the surface. Pits or material spalling can eventually arise from these cracks, originating on the surface or within the subsurface. The friction coefficient and weight loss often determine surface deterioration. Revolution marks and debris that fall from the surface are more frequently linked to adhesive or abrasive wear. N50 BM demonstrated severe abrasion-induced wear damage despite its high hardness. Wear debris formation reduces asperities contact and can swiftly generate a high quantity of wear debris, getting surface contact closer. Deep scratches are caused by hard asperities ploughing the surface. Damaged debris can abrade both surfaces as a third body. (Davanageri et al., 2016; Hashemi & Halvaee, 2014; Paula et al., 2021) have indicated that the presence of hard particles or debris that glide over the surface and remove material along their route is usually what causes deep grooves like those seen in Figure 5.52(b). Deep parallel grooves with wear debris are formed on the surface due to significant plastic deformation caused by increased sliding distance during wear. High-stress concentrations may result in cracks that spread perpendicular to the direction of sliding at high sliding speeds. These findings suggest that abrasion occurred via a three-body wear mechanism, resulting in significant material loss. Examination of the worn surfaces of all specimens revealed that material removal occurred in a mixed mode characterized by surface abrasion, plastic deformation, fatigue, and adhesion.

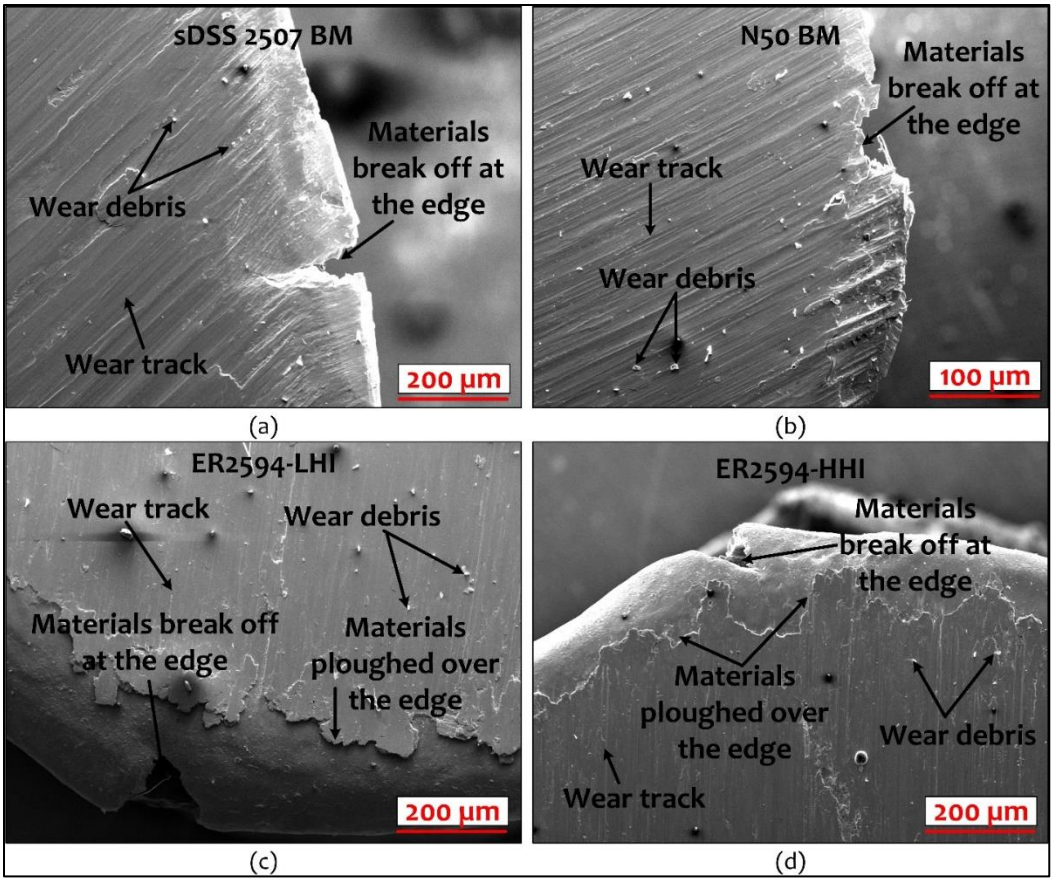

Figure 5.51 : Material break-off at the worn pin's edge from (a and b) sDSS 2507 and N50 BM, respectively, and (c and d) ER2594 weld zones

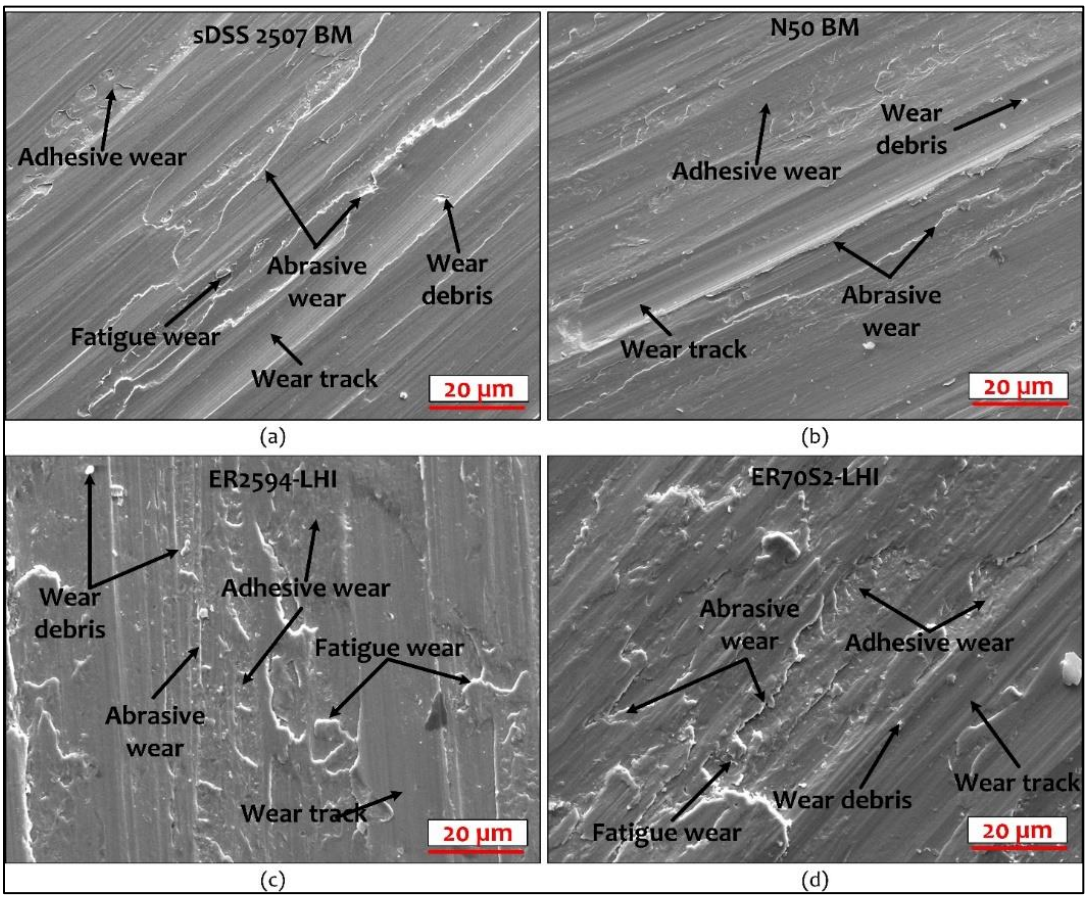

Figure 5.52 : SEM image of worn surfaces of base metals and both filler weld zones

5.2.5 CORROSION INVESTIGATIONS

This study highlights complex interactions between alloy composition, microstructure, and corrosion resistance to enhance performance, offering significant insights for tubing-couple assembly design in deep-water environments.

5.2.5.1 COMPLETE IMMERSION TEST

Figure 5.53 depicts the average weight changes and corrosion rates of base and weld metals after 60 days of exposure in a 3.5 wt.% NaCl solution. In Figure 5.53(a), the % weight change during complete immersion corrosion is evident, showing substantial weight reduction for ER70S2-LHI and similar loss for ER70S2-HHI. In contrast, BMs and ER2594 filler weldments exhibit noticeably lower weight loss than ER70S-2 filler weldments. Figure 5.53(b) presents corrosion rates after complete corrosion tests for all specimens. Both base metals show minimal weight loss, indicating robust corrosion resistance attributed to their chemical composition and balanced ferrite–austenite microstructures, particularly in the case of sDSS 2507 BM. Compared to sDSS 2507 BM (0.002 g and 0.0015 mm/y), N50 BM had the lowest weight loss and corrosion rate (0.001 g and 0.00075 mm/y). Conversely, ER70S2-LHI and HHI weldments experienced substantial weight loss and faster corrosion (0.028 g and 0.19 mm/y, and 0.30 g and 0.22 mm/y, respectively). Weight loss and corrosion rates were equal for sDSS 2507 BM and ER2594 filler weldments but higher for ER70S-2. Compared to ER70S-2 filler weldments, ER2594-LHI and HHI weldments displayed weight loss and corrosion rates of 0.002 g and 0.0015 mm/y, respectively. The results show that weld heat input reduces welded joint corrosion sensitivity and rates. Compared to ER70S-2 filler weldment, ER2594 filler weldment have significantly lower corrosion rates. For sDSS 2507/N50 DWJ, corrosion rate order is ER70S2-HHI > ER70S2-LHI > ER2594-HHI > ER2594-LHI > sDSS 2507 BM > N50 BM.

Visual inspections were conducted on base and weld metal samples during sixty days of complete immersion in 3.5% NaCl solutions (Figure 5.54). After 3, 30, and 60 days, variations in the surface scale of corroded samples were observed. Macro-examination reveals that scale production in ER70S2 filler weldment increases over time, exhibiting thicker, dark brown scales under complete immersion compared to both base metals and ER2594 weldment specimens (Figure 5.54(a)). After 60 days, ER70S2-LHI and HHI weldment exhibit substantial rust layers with thin, dense yellowish-brown inner layers and porous black outer layers. In contrast, there is no rust deposit on either base metals or ER2594 filler weldments. After removing the rust layer, SEM was employed to examine the surfaces of the corroded samples (Figure 5.54(b)). Both sDSS 2507 and N50 BM exhibited nearly identical corrosion patterns in complete immersion tests (Figure 5.54(b)).

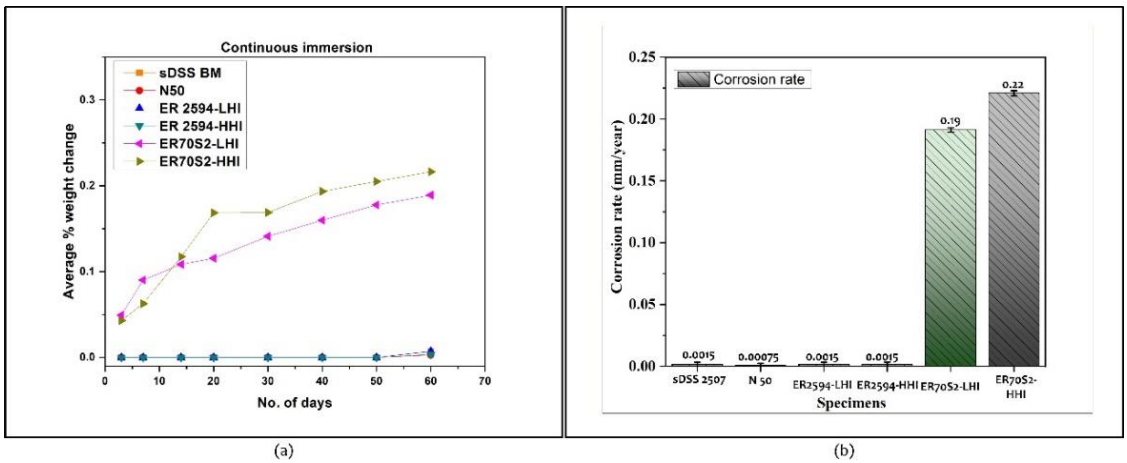

Figure 5.53 : (a and b) Average % weight change and corrosion rates assessed for all specimens during complete immersion

The microscopic pits observed in sDSS 2507 BM and N50 BM can be attributed to the balanced presence of δ and γ phases, along with elevated levels of ferrite-forming elements like Cr, Mo, and Si, contributing to increased pitting resistance. Notably, the presence of neighboring γ grains acted as a barrier, preventing the expansion of pits. The weight loss study further supports that both sDSS 2507 and N50 BM display enhanced corrosion resistance despite experiencing general corrosion. The corroded surface of ER2594-LHI and HHI weldments displays significant intergranular corrosion, primarily in the δ phase. It is characterized by the dissolution of WA/δ and PTA/δ interfaces within the δ-matrix, attributed to an unstable passive film and shear-assisted diffusional changes. Ferrite exhibits lower nobility in ER2594 weld metals due to its susceptibility to intergranular corrosion. The pitting corrosion resistance of ferrite reduces due to Cr-depleted zones, particularly from secondary phases like Cr_2N. Lower PREN and clustering of Cr_2N result in the formation of pits in the δ-matrix or boundaries between δ and reformed austenite. Among the microstructural components, the δ matrix exhibits the highest level of corrosion severity, followed by IGA, PTA, and WA. The SEM micrograph analyses align with the findings from Table 5.19, indicating that IGA exhibits reduced resistance to pitting corrosion compared to GBA and WA, which is attributed to its lower PREN. The EDS spectrum analysis of corroded ER2594 filler weldments under both conditions shows that passivation has occurred because of the presence of oxygen, Cr, Mo, Ni, and Fe on the surface. Higher Cr and Ni levels in ER2594 form a protective passivation layer, which improves corrosion resistance (Table 5.19). The increased pitting potential in ER2594 weldments is due to the higher Cr, Mo, and Ni content, resulting in a higher Cr_{eq}/Ni_{eq} ratio. Secondary phase precipitates reduce pitting potential in ER2594 weldments compared to sDSS 2507 BM. Figure 5.54(b) also illustrates intergranular corrosion on the ER70S-2 weldment. Pits with sizes ranging up to 12-16 µm are visible after the complete immersion test, as depicted in Figure 5.54(a and c). Within the martensite laths, the Cr content is approximately 7.0 wt.%. Depletion of Cr (<7%) at the martensite/ferrite interfaces can result in the formation of a weak passive film. This film becomes a preferred site for pit nucleation in a chloride solution due to its susceptibility to chloride ion penetration. Cr-depletion at the martensite/ferrite interface reduces pitting corrosion resistance.

Table 5.19 : EDS spectra result of the mentioned spots in Figure 5.54

Complete immersion test								
Elements (wt.%)	*1*	*2*	*3*	*4*	*5*	*6*	*7*	*8*
Cr	25.0	21.68	26.11	25.07	23.02	25.86	7.45	7.68
Ni	6.86	13.29	7.55	8.70	8.30	6.98	2.80	1.74
Fe	57.3	56.17	57.8	53.4	58.45	59.5	82.41	84.5
Mo	2.86	----	2.86	4.25	2.35	2.46	----	----
Mn	1..46	4.81	0.33	1.09	0.86	1.23	1.77	2.17
Si	1.04	1.31	1.67	0.78	0.64	0.49	0.99	0.24
O	4.10	1.86	2.49	5.19	3.97	2.17	3.56	2.89
Cl	1.39	0.88	1.02	1.52	2.41	1.30	1.02	0.78

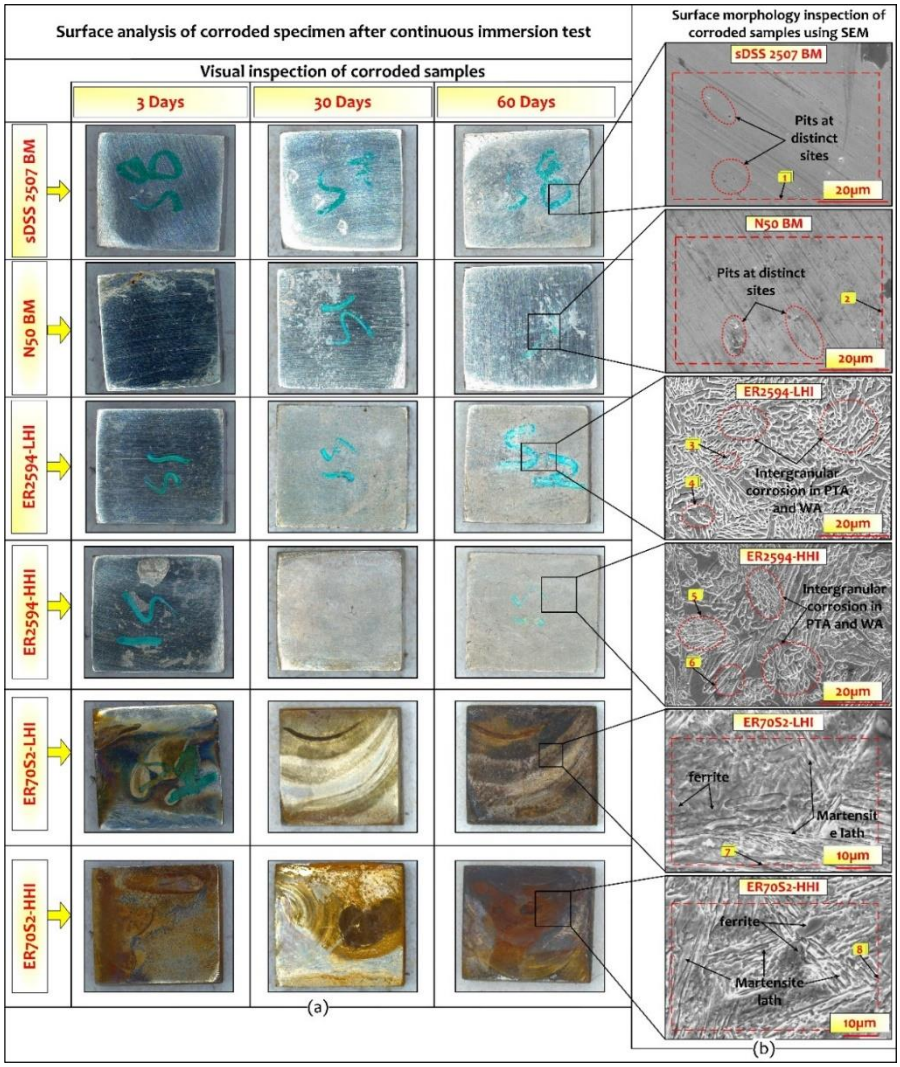

Figure 5.54: (a) Visual inspection, (b) SEM surface morphology inspection of all corroded sample surfaces

5.2.5.2 *ELECTROCHEMICAL CORROSION TEST*

Rapid passivation in highly corrosion-resistant alloys like sDSS 2507 and N50 steel may introduce nonlinearity in Tafel curves, potentially affecting the accuracy of anodic (β_a) and cathodic (β_c) Tafel constant determination (waris nawaz Khan et al., 2023). It is important to note that the HAZ region may influence the calculation of corrosion current density (Icorr) in weld zone specimens. Tafel plots for corrosion potential (E_{corr}), I_{corr}, and corrosion rate (CR) are presented in Figure 5.55 and Table 5.20. E_{corr} values indicate corrosion resistance, while I_{corr} values reflect corrosion rates. The analysis reveals active degradation in all samples, underscoring E_{corr} as a reliable corrosion resistance indicator (S. Wang et al., 2011). According to the E_{corr} values in Figure 5.55(a), the sDSS 2507 BM exhibits a lower corrosion potential (-202.1 mV) than the N50 BM (-152.3 mV). ER2594-LHI and HHI weld zones have higher E_{corr} values (-184.5 mV and -214.1 mV) compared to ER70S2-LHI and HHI (-398.9 mV and -424.5 mV) (Figure 5.55(b)). For the weld interface on the sDSS 2507 BM side, ER2594-LHI and HHI demonstrate superior E_{corr} values (-53.3 mV and -145.4 mV) than ER70S2-LHI and HHI (-295.5 mV and -485.4 mV), respectively. Compared to both BMs, the sDSS 2507 weld interface of ER2594 filler exhibits superior corrosion resistance. The weld interface on the N50 BM side shows E_{corr} values in Fig. 9(d) as -46.80 mV and -226.45 mV for ER2594-LHI and HHI, respectively, and -429.7 mV and -462.6 mV for ER70S2-LHI and HHI. The susceptibility to both localized and uniform corrosion is higher in ER70S2-WZ and N50/sDSS 2507 interfaces of ER70S2 filler weldments compared to ER2594. This is due to the formation of more effective galvanic couples. A shift in corrosion potential towards ER2594-WZ indicates improved corrosion resistance. The superior resistance in ER2594-filler weld zones is attributed to the formation of chromium-rich films.

Microstructure evolution and hardness influence corrosion rates, with martensite laths in ER70S2 filler weldments leading to lower corrosion resistance. E_{corr} is ranked from most corrosion resistant to least corrosion resistant in this order: ER70S2-HHI weld interface for BMs > N50 weld interface (ER70S2-LHI) > ER70S2-LHI/HHI (weld zone) > SDSS 2507 weld interface (ER70S2-LHI) > N50 weld interface (ER2594-HHI) > ER2594-HHI (weld zone) > sDSS 2507 BM > ER2594-LHI (weld zone) > N50 BM > SDSS 2507 weld interface (ER2594-LHI/HHI) > N50 weld interface (ER2594-LHI).

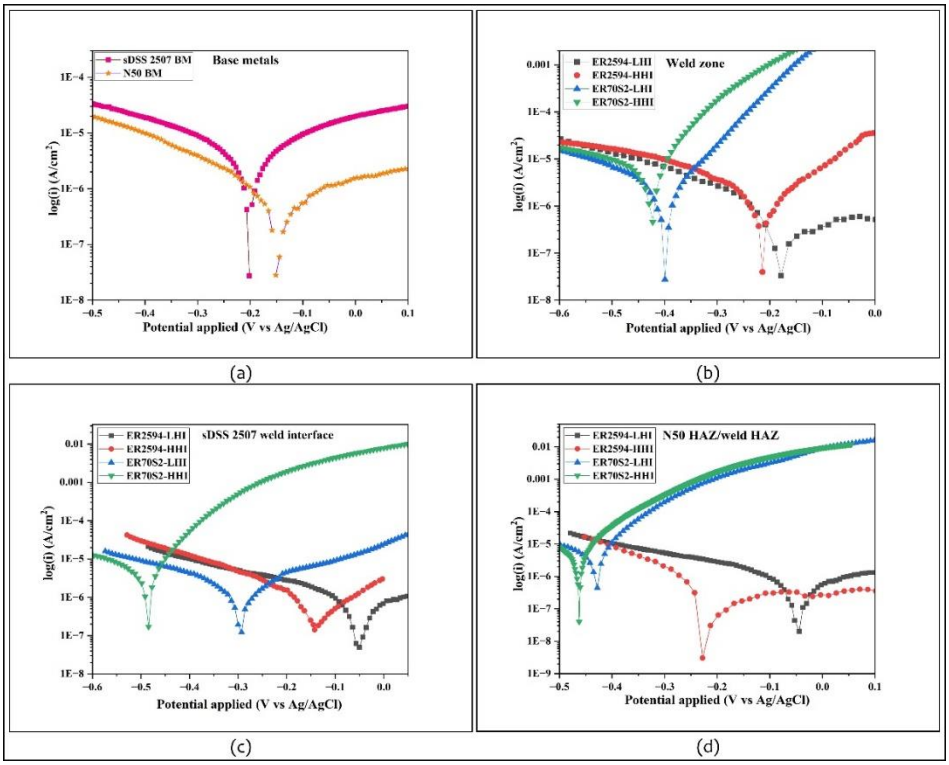

Figure 5.55 : (a-d)Tafel plot of all specimens after electrochemical test in 3.5 wt.% NaCl

Table 5.20 : Tafel plot analysis for all specimens under 3.5 wt.% NaCl solution

Specimen	I_{Corr} (μA)	βc (-mV/dec)	β_a (mV/dec)	E_{corr} (mV)	*Corrosion rate (mm/year)*
sDSS 2507 BM	0.92	39.4	54.3	-202.1	0.0224
N50 BM	0.24	127.5	81.9	-152.3	0.0056
Weld zones					
ER2594-LHI	0.20	292.9	62.6	-184.5	0.0034
ER2594-HHI	0.47	181.1	148.7	-214.1	0.0047
ER70S2-LHI	0.98	60.12	79.18	-398.9	0.0230
ER70S2-HHI	3.96	59.2	138.06	-424.5	0.0920
sDSS 2507 HAZ					
ER2594-LHI	0.74	363.2	156.4	-53.30	0.0011
ER2594-HHI	0.41	284.4	70.53	-145.5	0.0172
ER70S2-LHI	5.11	879.3	429.6	-295.5	0.1190
ER70S2-HHI	15.07	128.7	-488.7	-485.4	0.3503
N50 HAZ					
ER2594-LHI	0.28	74.9	52.5	-46.80	0.0033
ER2594-HHI	0.17	45.72	25.9	-226.45	0.0210
ER70S2-LHI	12.1	100.1	-1.07	-429.7	0.2813
ER70S2-HHI	0.98	20.63	31.43	-462.6	0.3084

Nyquist plots for N50 BM and sDSS 2507 BM in Figure 5.56(a) display a straight pattern, indicating ion diffusion through the metal-solution contact. Both base metals exhibit a larger capacitive impedance arc radius, suggesting superior corrosion resistance. Figure 5.56(b-c) shows Nyquist plots of EIS results for weld zones of both filler metals. A larger capacitive arc radius on the ER2594-LHI/HHI weldment indicates superior corrosion resistance. Due to its larger capacitive loop, the ER2594 filler weldment samples have superior corrosion resistance than the ER70S2 filler weldment. Compared to other weldments, the ER2594-LHI welded sample exhibits increased intermediate and low-frequency impedance (Figure 5.56(b)). Nyquist plots of ER70S2-HHI specimens display a single semi-circle at high frequencies, signifying a single time constant and suggesting the lowest corrosion resistance among all specimens (inset image Figure 5.56(c)). Figure 5.56(d-g) presents Nyquist plots for the HAZ of both base metals. Figure 5.59(d and e) shows the Nyquist plots of the ER2594 filler specimens in the sDSS 2507 and N50 HAZ. These plots show a distinct capacitive arc with large diameters, which indicates the formation of a capacitive layer on the surface and excellent corrosion resistance. In contrast, the ER70S2-HHI specimens' Nyquist plots for both HAZ display a single semi-circle at high frequencies, suggesting that this specimen has the lowest corrosion resistance (Figure 5.56(d and e)).

The impedance and phase angle vs. frequency Bode plots for base metals and the ER2594/ER70S2 weld zones are shown in Figure 5.56(h and i). The impedance diagrams for sDSS 2507 and N50 BMs in Figure 5.56(h) show a flat high-frequency region and a linear decline at low and medium frequencies. In the Bode plot, both base metals display a maximum phase angle of 60° over a wide frequency range, indicating charge transfer dominance in the high-frequency region. Bode plots reveal amplitude and phase variations with frequency in ER2594 and ER70S-2 filler weld zones (Figure 5.56(i)). Charge transfer predominates in the low-frequency domain, evident from phase angles reaching 60° at intermediate frequencies. Bode plots show a decline in all weld zone samples at lower frequencies than sDSS 2507 BM. Single peaks in ER70S2-LHI/HHI plots indicate charge transference control at intermediate frequencies with a single time constant. Figure 5.56(j-k) presents the phase angle vs. frequency and impedance Bode plots for sDSS 2507 and N50 HAZ for both fillers. Similar to the weld zone, the Bode plots exhibit a decline in sDSS 2507 HAZ samples at lower frequencies. However, N50 HAZ plots of the ER70S-2 filler show single peaks representing a larger corrosion product layer on the surface, leading to reduced corrosion resistance. These single peaks indicate charge transference control at intermediate frequencies with a single time constant. Figure 5.56(l) presents the proposed EEC applied to match the experimental data. Table 5.21 lists the EIS parameters from equivalent circuit fitting. The EIS data and fitting plots indicate that both base metals have higher R_{ct} and R_f values than weld zone and HAZ specimens, reflecting superior corrosion resistance. Significant differences in R_{ct} values suggest that ER2594-LHI exhibits the highest corrosion resistance among the weld zones due to its thicker protective film layer. ER70S2 LHI/HHI weld metals exhibit poor corrosion resistance, with n values of 0.6 and 0.75, respectively, indicating the corrosion behavior of the oxide film layer. In N50 HAZ, ER2594 filler demonstrates better corrosion resistance than ER70S-2 filler. The corrosion resistance of ER2594 filler weldment (LHI (n=0.810), HHI (n=0.792)) varies significantly compared to ER70S2 (LHI (n=0.785), HHI (n=0.778)) for sDSS 2507 HAZ.

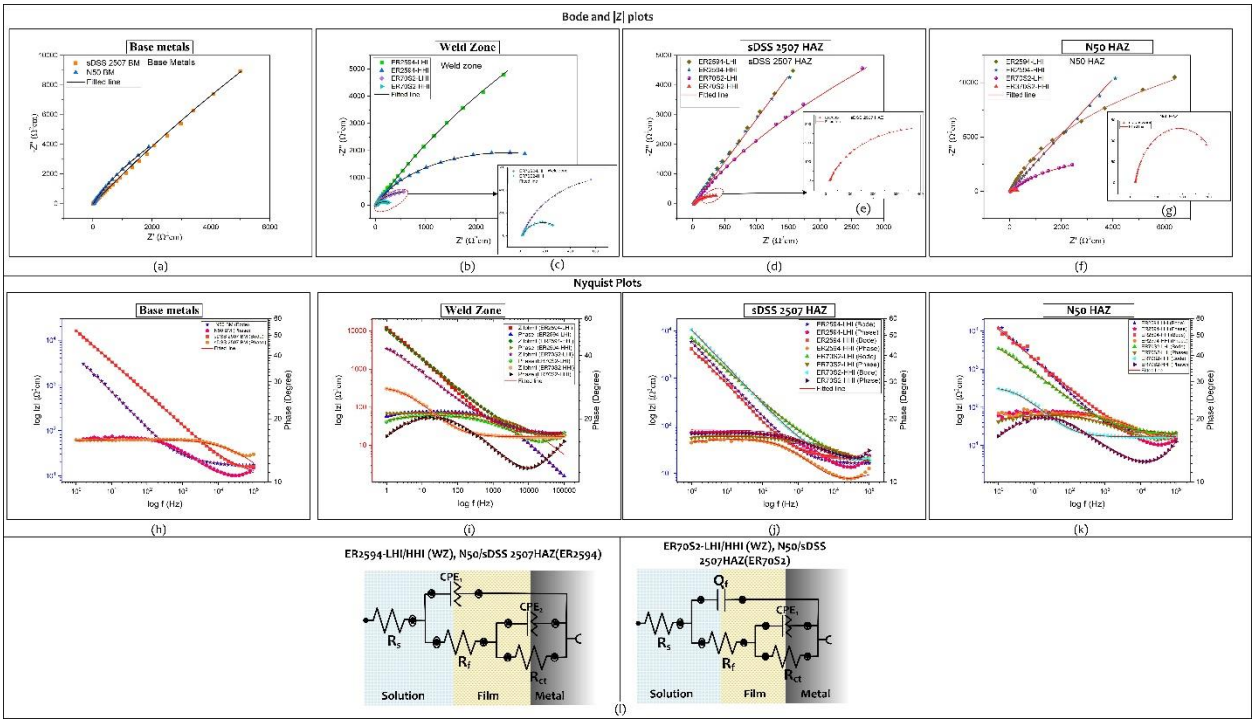

Figure 5.56: EIS spectrum analysis of BM, WZ, and HAZ: Nyquist plot (a-g); Bode and |Z| plot (h-k), respectively, (l) Fitting EIS test results with an equivalent electrical circuit for all samples

Table 5.21 : Equivalent circuit fitting of EIS data of all samples

Specimen	R_s ($\Omega.cm^2$)	CPE_1		R_f ($\Omega.cm^2$)	CPE_2		R_{ct} ($\Omega.cm^2$)	Q_f (μF)
		Y_{01} ($\mu F.cm^{-2} S^{(n-1)}$)	n_1		Y_{02} ($\mu F.cm^{-2} S^{(n-1)}$)	n_2		
sDSS 2507 BM	9.12	17.6	0.821	64.3	10.3	0.892	478	----
N50 BM	10.6	51.8	0.739	86.2	42.2	0.828	560	----
Weld zones								
ER2594-LHI	19.9	40.6	0.795	16.2	15	0.878	279	----
ER2594-HHI	16.7	41.2	0.769	18.8	9.06	0.898	237	----
ER70S2-LHI	17.7	456	0.627	2.40	----	----	46.3	43.6
ER70S2-HHI	18.1	402	0.725	9.56	----	-----	33.8	42.1
N50 weld interface								
ER2594-LHI	8.74	38.9	0.764	19.2	11.6	0.902	286	----
ER2594-HHI	9.68	42.9	0.772	24.3	13.8	0.878	274	----
ER70S2-LHI	10.6	60.5	0.72	14.1	----	----	9.13	74.1
ER70S2-HHI	17.9	84.2	0.675	16.6	----	----	10.89	63.9
Sdss 2507 WELD INTERFACE								
ER2594-LHI	12.8	62.8	0.810	4.28	12.3	0.865	----	3.6
ER2594-HHI	11.6	79.6	0.792	5.63	10.5	0.843	----	1.9
ER70S2-LHI	9.56	402	0.785	18.1	----	----	310	42.9
ER70S2-HHI	8.23	342	0.778	309	----	----	330	58.4
Note: R_s is solution resistance, R_f is film resistance, R_{ct} is charge transfer resistance, Q_f is capacitance, and CPE_1 and CPE_2 are constant phase elements. n_1 and n_2 are corrosion product layers and steel surface fitting accuracy.								

Electrochemical studies show that current density and corrosion resistance in different regions of welded joints are unclear. A thorough analysis of the corrosion morphology of both filler weldments on the welded joint surface was conducted using SEM analysis. Figure 5.57 shows the microscopic morphologies of welded joints (BM, WZ, and weld interfaces) after corrosion scale removal. Figure 5.57(a-d) displays corroded weld zones of ER2594 and ER70S2 fillers. The results indicate that in ER2594 weldments, ferrite is more prone to intergranular corrosion attacks than austenite, attributed to its lower PREN value (Figure 5.57(a-b)). Conversely, the martensite lath-ferrite interface in ER70S2 filler promotes intergranular corrosion (Figure 5.57(c-d)). Compared to ER2594, ER70S2 weldments exhibit more severe intergranular corrosion. Figure 5.57(e-g) shows intergranular corrosion in the ferrite matrix at the N50 HAZ for ER2594 filler. The narrow width of the weld interface makes it challenging to comprehend corrosion behavior in N50 HAZ. SEM images of corroded samples in the N50 HAZ for ER70S2 filler reveal island formation with a significant impact on pitting corrosion (Figure 5.57(h)). The N50 HAZ region has a higher corrosion potential due to the development of carbide precipitates (Figure 5.57(i and j)). However, localized corrosion in the sDSS 2507 HAZ for ER2594 filler weldments has caused pits, which may affect corrosion resistance (Figure 5.60(k-l)). Similar pitting is seen in the sDSS 2507 HAZ region for ER70S2 filler at the weld interface and in the HAZ region (Figure 5.57(m and n)), primarily resulting from galvanic coupling due to potential differences. N50 BM shows a non-uniform corrosion pattern with pitting at distinct phases, indicating lower susceptibility to pitting corrosion (Figure 5.57(h)). In contrast, sDSS 2507 BM exhibits localized corrosion, leading to pitting at different phases, which is easily controlled due to the balanced phase ratio and essential alloying elements, including Cr, Mo, Ni, and Si (Figure 5.57(k)).

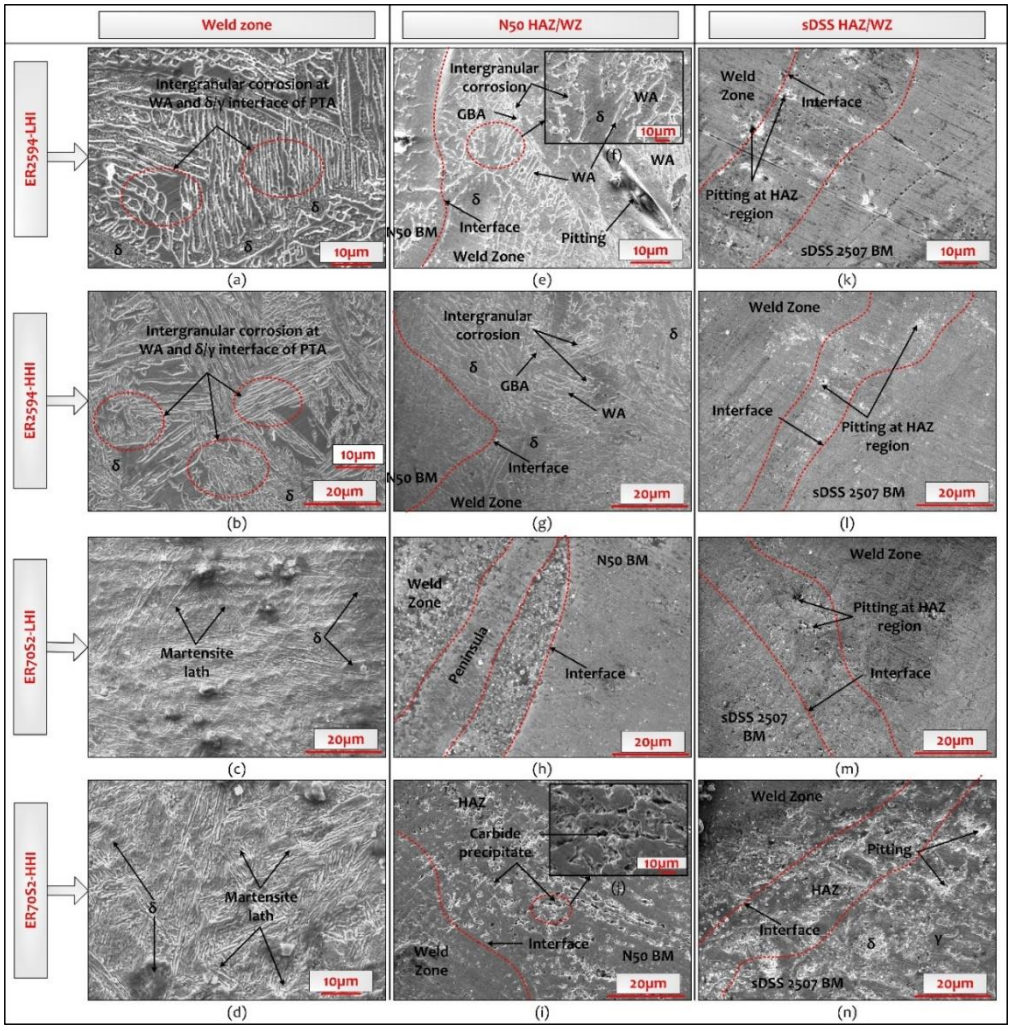

Figure 5.57 : Typical corrosion surface morphology after electrochemical studies (a-d) weld zone, (e-j) N50/WZ, (i-l) sDSS 2507/WZ

5.2.5.3 CORROSION PRODUCT ANALYSIS AND MECHANISM

The corrosion behavior in weld joints with various fillers in underwater marine applications is complex and can result in galvanic corrosion due to differing compositions and microstructures in the welding zones (WZ, HAZ, and BM) (Bai et al., 2017). Seawater triggers the formation of a permeable corrosion product layer when aggressive ion attacks commence. The loose and porous nature of this layer accelerates corrosion through facilitated oxygen diffusion, particularly in microstructurally distinct regions like the HAZ. As immersion progresses, variations in corrosion product layer thickness and protective characteristics become evident. Certain sections exhibit a loose structure that facilitates oxygen diffusion, while denser areas act as a physical barrier to slow down corrosion. Over time, the structure of the corrosion product layer changes, significantly impacting the corrosion mode (Gong et al., 2021). Thus, understanding the rust layer's composition is essential for assessing the corrosion product layer's effect on sDSS 2507/N50 DWJ structural integrity. In Figure 5.58, the corrosion product morphologies of samples immersed in a complete environment reveal insights into rust phase characteristics. Surface attributes, including distinct morphology and compactness, provide valuable information about the corrosion process. Weight loss analysis and visual inspection confirm that base metals and ER2594 filler exhibit minimal rust and weight loss compared to ER70S2 filler weldment. Over an extended immersion period, these corrosion specimens demonstrate lower corrosion rates and superior corrosion resistance than ER70S2 filler. Figure 5.58(a and b) illustrates corrosion product morphology after 60 days in 3.5 wt.% NaCl. The SEM image shows that ER70S2-LHI/HHI weldments feature an open porous structure lacking compactness, compromising the protective properties of the matrix as segments of the corrosion scales break and detach. This observation indicates lower corrosion resistance and higher corrosion rates for these specimens, aligning with weight loss results. The initial corrosion products display globular and lamellar forms on their surface, attributed to cloud-like β-FeO(OH) formation in response to localized high Cl^- concentrations. As γ-FeO(OH) develops, its morphologies become more compact. Needles or whiskers typical of α-FeO(OH) appear around the periphery of γ-FeO(OH). Over time, the corrosion product morphology transitions to a combination of globular γ-FeO(OH) and α-FeO(OH) needles/whiskers, with the latter resulting from the transformation of the former. This transition contributes to an increase in the compactness of the corrosion product. The surface morphology remains consistent in the final corrosion stage, featuring exfoliated structures likely corresponding to magnetite (Fe_3O_4 or Fe_2O_3) on the innermost surface. FeO(OH) characterizes the outermost surface, while Fe_3O_4 is primarily found on the innermost surface. Changes in the average corrosion rate are directly reflected in the evolution of the corrosion products. Figure 5.58(a and b) illustrates the primary surface corrosion products, including goethite needles (α-FeO(OH)), cloud-like (β-FeO(OH)), solid globular-like magnetite particles (Fe_3O_4 or Fe_2O_3), and lepidocrocite mineral morphology (γ-FeO(OH)). The EDS spectra results for various corrosion products are presented in Table 5.22, revealing Cl^-, O, Na, and Fe as the primary elements in varying concentrations for each morphology. EDS analysis indicates a higher concentration of Cl^- in the inner rust layer compared to the outer layer. The data also highlights that the outer corrosion products have a higher oxygen content, while the distribution of Fe follows the opposite trend (Table 5.22). Previous studies have reported higher Cl^- concentrations in regions with loose and fractured structures (Gong et al., 2021; Gong, Wu, Xie, et al., 2020; Nishimura et al., 2000; Yu et al., 2018). Wide cracks in corrosion product layers facilitate the quicker passage of chloride and oxygen ions, accelerating the corrosion process.

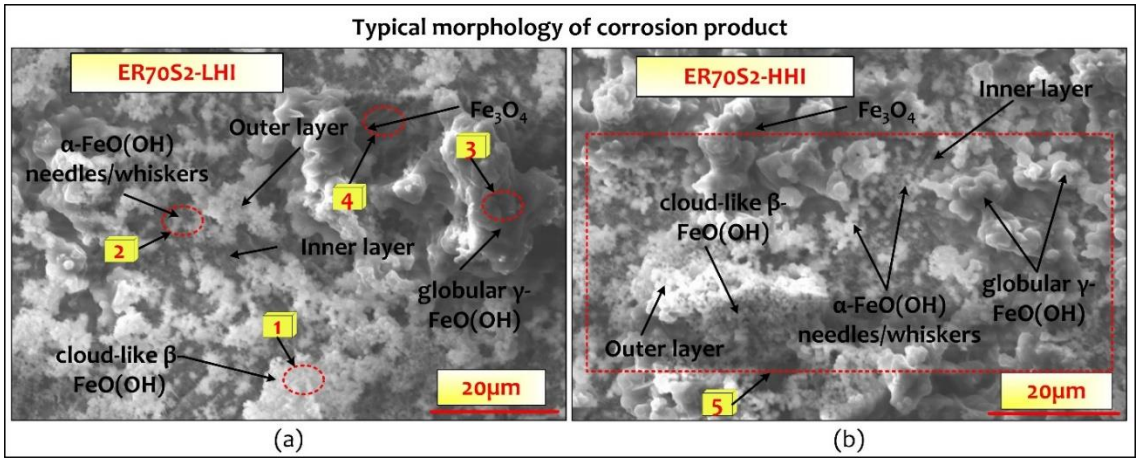

Figure 5.58 : (a-b) Typical morphology of corrosion product formed in ER70S-2 filler weldments after continuous immersion corrosion test

Table 5.22 : EDS spectra result of different corrosion product morphology in Figure 5.58

Elements (wt.%)	*Spot 1*	*Spot 2*	*Spot 3*	*Spot 4*	*Spot 5*
O	27.49	17.54	35.72	9.46	20.84
Na	13.72	26.81	7.39	24.62	25.89
Cl	14.83	34.46	6.90	36.12	26.52
Fe	43.97	21.19	49.99	29.8	20.62

Weight-loss analysis and electrochemical measurements may show discrepancies due to differences in cathodic and anodic reactions, potentially causing overestimating corrosion rates. The electrochemical activities of rust layers before and after exposure can differ, impacting corrosion rate estimations. The rust layer, initially loose and composed of γ-FeO(OH) with a small amount of β-FeO(OH) during the initial immersion, undergoes changes over the long term. The thicker inner layer that develops contains a significant amount of β-FeO(OH). Both β-FeO(OH) and γ-FeO(OH) exhibit high reduction reactivity, with β-FeO(OH) playing a major role in accelerating the corrosion rate when coexisting with γ-FeO(OH). Oxygen and ferric products are the predominant oxidizing type in aerated corrosive media. In transport-limited oxygen supply conditions, a galvanic coupling between iron (anodic site) and ferric product (cathodic site) occurs, facilitating electron transfer. The initial rust composition of γ-FeO(OH), combined with a loose rust layer, favors the transport of dissolved oxygen. In the initial phases of sDSS 2507/N50 DWJ corrosion, the electrochemical reactions (equation 5.1) to (equation 5.5) can be depicted as follows (Chen et al., 2005; EVANS, 1965; Gong, Wu, & Liu, 2020; Ma et al., 2009):

Anodic reaction: $Fe \rightarrow Fe^{2+} + 2e^{-}$ (5.1)

$Fe^{2+} \rightarrow Fe^{3+} + e^{-}$ (5.2)

Cathodic reaction: $O_2 + 2H_2O + 2e^{-} \rightarrow 4OH^{-}$ (5.3)

After prolonged immersion, rust primarily comprises γ-FeO(OH), β-FeO(OH), and Fe_3O_4, while the dense inner layer limits oxygen diffusion, depleting dissolved oxygen.

$8\,\beta - FeO(OH) + Fe^{2+} + 2e^{-} \rightarrow 3Fe_3O_4 + 4\,H_2O$ (5.4)

The corrosion process initiates with the formation of $Fe(OH)_2$, which evolves into more stable phases such as lepidocrocite, goethite, Fe_3O_4, and α-Fe_2O_3 (Tanaka et al., 2014). Dissolved oxygen, along with γ-FeO(OH), plays a role in the rust layer's oxidation (D. D. N. Singh et al., 2008). The reduction process of γ-FeO(OH) is involved in the corrosion mechanism:

$8\,\beta{-}FeO(OH) + Fe2{+}{+} + 2e{-}{\rightarrow}3Fe3O4 + 4\,H2O$ (5.5)

Steel corrosion in immersion zones follows an oxygen-absorbing mechanism, primarily influenced by the rust layer due to the stable marine environment (Bai et al., 2017). Equations (5.1) to (5.5) summarize the oxygen-absorbing corrosion mechanism for sDSS 2507/N50 DWJs during complete immersion (Figure 5.59). After a few days of complete immersion, stable corrosion was observed during the immersion stage. During the first stage of a wet surface, unhindered oxygen diffusion contributes to activation-controlled corrosion. Subsequently, after a few more days of complete immersion, a rapid corrosion stage was reached. During this stage, dissolved Fe ions underwent hydrolysis and oxidation, resulting in the formation of various corrosion products, including γ-FeO(OH), Fe_2O_3, Fe_3O_4, β-FeO(OH), and α-FeO(OH). Although surface defects or inclusions can cause potential variations, the uniform corrosion reactions inhibit significant pitting corrosion on the steel surface. Notably, γ-FeO(OH) can crystallize from β-FeOOH and transform into α-FeOOH/Fe_3O_4 as the corrosion progresses. The corrosion product layers become compact and thick in the subsequent stage, inhibiting the anodic process. This inhibition is attributed to the synergistic effect of anti-corrosion elements and the stability of γ-FeO(OH) and Fe_3O_4 products. However, the generation of corrosion products limits the activation-controlled phase, and as corrosion progresses, the rust layer impedes oxygen diffusion, shifting the corrosion process to oxygen diffusion control.

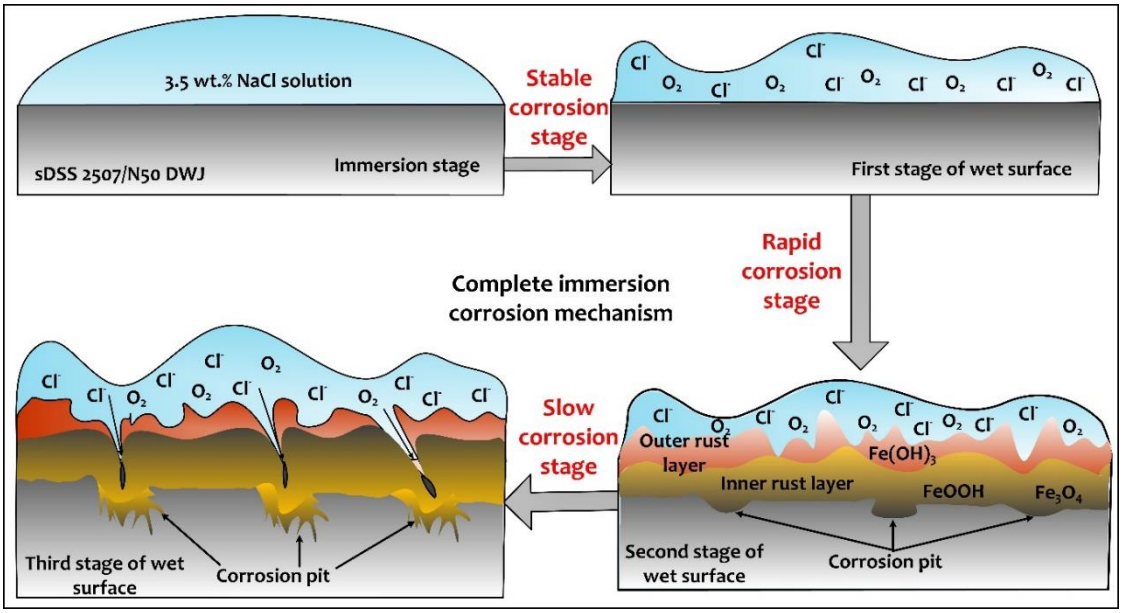

Figure 5.59 : Schematic of the corrosion mechanism under complete immersion conditions

5.3 DISSIMILAR METAL WELD OF SUPER DUPLEX STAINLESS STEEL AND PIPELINE STEEL

This section thoroughly investigates the relationship between structural integrity and heat input parameters in sDSS 2507/X-70 weldments. The study highlights the joint's potential application in the splash zone of risers used in hydrocarbon drilling. It includes an in-depth analysis of the base metal, heat-affected zone, weld zone, mechanical properties, abrasive slurry wear, and corrosion performance.

5.3.1 QUALITATIVE AND QUANTITATIVE WELD JOINT INSPECTION

The QUASMO SZB-45L stereo zoom microscopes were utilized to measure fusion characteristics, including appearance, depth, and weld bead width in the sDSS 2507/X-70 DWJs. In Figure 5.63, the macrograph illustrates a well-fused joint with complete penetration, a narrow weld bead, an absence of undercuts or underfills, no noticeable pores, excessive root-side penetration, and excessive convexity. The macrostructure reveals a narrower HAZ on the sDSS 2507 side due to its lower thermal conductivity (15 W/m K vs. 80 W/m K). Each of the four

welding passes is depicted in the macrograph. For ER2594-LHI weldments, capping and backing pass widths were measured at 16.83 mm and 5.25 mm, respectively, compared to 14.28 mm and 4.55 mm for ER2594-HHI weldments. The fusion zone size was 110 ± 2 mm^2 for ER2594-LHI weldments and 100 ± 3 mm^2 for ER2594-HHI weldments (Figure 5.60(a and b)). The cap region groove opening after filling passes for ER309L-LHI and ER309L-HHI weldments measured 10.23 mm and 11.84 mm, respectively. Utilizing Image J software based on the macrograph in Figure 5.60(c and d), the weld zone area for ER309L-LHI and ER309L-HHI was determined to be 65 ± 3 mm^2 and 80 ± 2 mm^2, respectively.

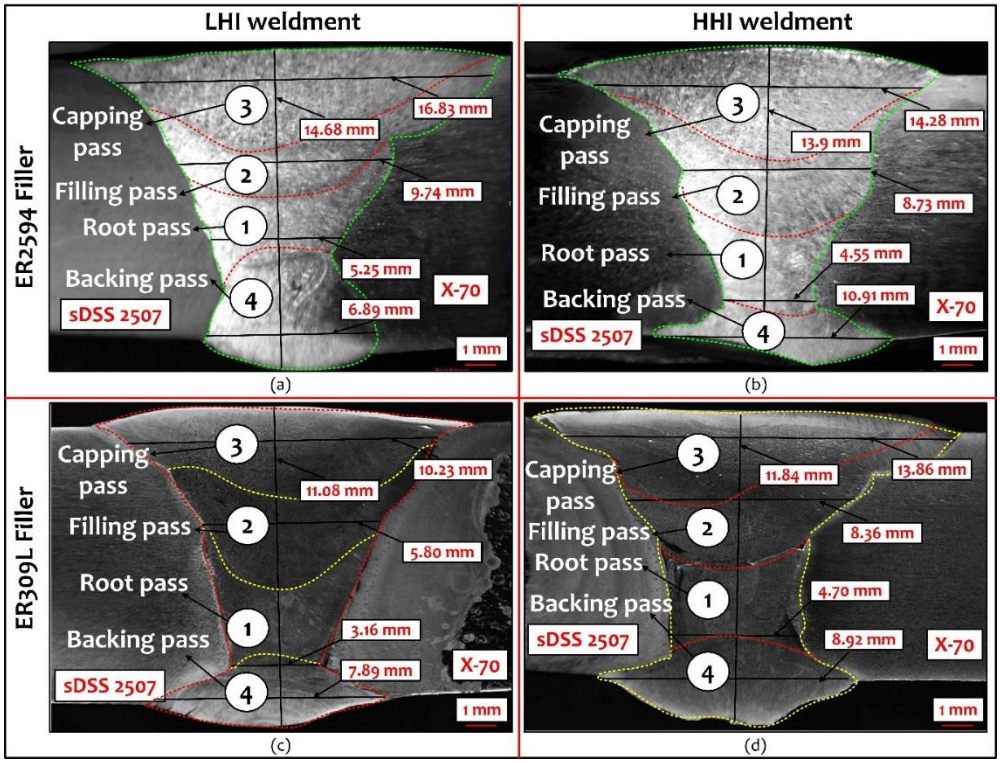

Figure 5.60 : Weldments with macrostructures showing the weld zones and passes for LHI and HHI parameters using (a and b) ER2594 filler and (c and d) ER 309 L filler, respectively

5.3.2 MICROSTRUCTURAL CHARACTERIZATION

The microstructure analysis includes the base metal's microstructure, the weld interface, and both filler metals' weld zones. This is crucial to understanding structure-property relationships, especially under different heat inputs.

5.3.2.1 *BASE METAL*

Figure 5.61 depicts the mechanical characterization and microstructures of the sDSS 2507 and X-70 base metal (BM). Along the rolling direction, austenite (γ) islets are elongated in the ferrite (δ) matrix of sDSS 2507 BM (Figure 5.61(a and b)). The ferrite measurement analysis performed in Image J showed that the sDSS 2507 microstructure is composed roughly of equal parts ferrite (52.3%) and austenite (47.7%). EDS spectra analysis validated the presence of increased elements Fe, Cr, Ni, Mn, and Mo (Figure 5.61(c)). The microstructure of the X70 steel is shown in Figure 5.61(d and e), and it is composed mainly of fine ferrites such as acicular ferrite (AF), bainitic ferrite (BF), and polygonal ferrite (PF). The microstructure shows that martensite-austenite (M-A) components are evenly distributed in the ferrite matrix. Figure 5.61(f) displays the EDS spectra of X-70 BM. The research focused on the base metal plates' microhardness, toughness, and tensile strength. Using ImageJ software, sDSS and X-70 BM had average grain sizes of 144 µm and 5 µm, respectively. Figure 5.61(g and h) shows that the distribution of grain sizes in both base metals was not uniform, with different-sized grains being dispersed irregularly.

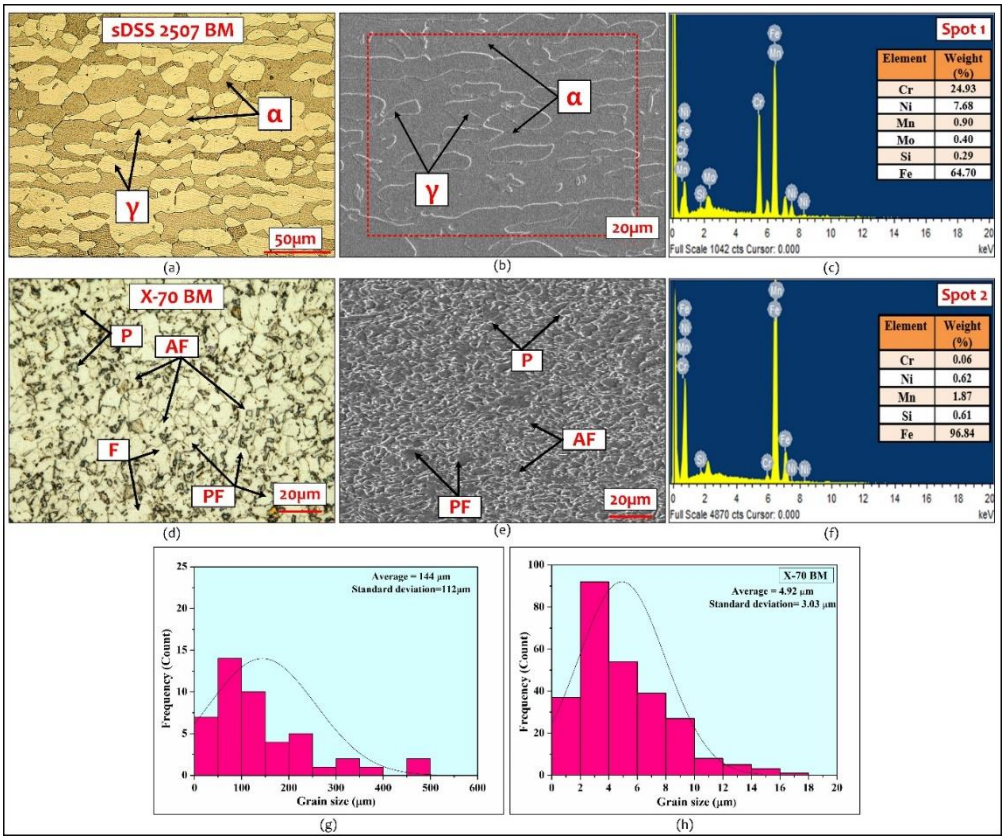

Figure 5.61 : Base metal microstructure (a-b) sDSS 2507, (d-e) X-70, respectively, EDS examination of the (c) sDSS 2507, (f) X-70, and (g and h) sDSS 2507 and X-70 BM tensile and XRD plots, respectively, (i and j) Normal grain size distribution in sDSS 2507 and X-70 BM, respectively

5.3.2.2 *CHARACTERIZATION AND IDENTIFICATION OF SUBZONES AND X-70 HAZ*

Controlling the HAZ microstructure in multi-pass welding involves careful consideration of coupon thickness, heat input, preheat, and interpass temperature. Weld interface formation could be challenging to predict with a V-groove and matching filler metal. Due to its dependence on temperature and chemical conditions, the HAZ region's microstructural evolution study is more complicated than that of the WZ and BM. The HAZ region's grain nucleation and growth depend on heating and cooling rates. Both base metals' physical characteristics and experimental conditions also influence the X-70 HAZ's size and nature. Researchers examined the X-70 BM's weld interface response to welding heat input. Microstructure changed continually from the weld zones to the X-70 BM. As shown in Figure 5.62(a), distinct zones, including the inter-critical (ICHAZ), fine grain (FGHAZ), and coarse grain (CGHAZ), are formed due to the X-70 HAZ experiencing varying peak temperatures during the weld thermal cycle. Figure 5.62(b–e) shows the optical image of the LHI state X-70 HAZ and weld interface. The X-70 HAZ undergoes metallurgical modifications due to partial melting during welding. The austenite grains acted as a barrier, preventing bainite production from occurring outside their boundaries. Figure 5.63(a and b) shows that the FGHAZ microstructure comprised primarily PF and PAGBs with low quantities of AF, BF, and M-A constituents. The CGHAZ austenite grain size increases when precipitation dissolves at high temperatures. The CGHAZ developed coarse prior austenite grain boundaries (PAGBs) because of the growth of M-A constituents and bainitic ferrite (BF) lath blocks. Continuous cooling in the HAZ results in the formation of M/A components and a minor fraction of granular BF. The CGHAZ's high temperature coarsened grain boundaries, dissolving matrix precipitates, and reduced grain boundary pinning boosted PAGB development. The FGHAZ formed near the CGHAZ at temperatures just above Ac_3, away from the X-70 weld interface (Figure 5.63(c and d)). Figure 5.63(e and f) depicts the additional parts of the X-70 HAZ that comprise the ICHAZ. The ICHAZ had more precipitation due to temperatures below Ac_1 and above 750 °C, while the FGHAZ had a peak temperature that was higher or comparable to Ac_3.

The microstructure and precipitate percentage changed depending on the FGHAZ/peak ICHAZ's temperature. The ICHAZ zone was narrower than the CGHAZ or FGHAZ, rendering distinguishing challenging. The base metal is over-tempering when the temperature is below Ac_1 and above 725 °C. The base metal matrix softens more with over-tempering, lowering hardness. Table 5.23 shows the EDS spectra analysis of spots and precipitates in the X-70 HAZ for both weldments. Because of more PAGs, the CGHAZ in the X-70 had a higher martensite starting temperature (M_s) and more robust M-A components. The M-A component's proportion and volume increased as the PAG size increased. The X-70 HAZ's toughness, especially near the PAGBs, is affected by this increase in M-A constituents. As the heat input increased, recrystallization and slower cooling caused the CGHAZ to exhibit larger grain sizes. The average grain size for LHI and HHI weldment was 65 µm and 70 µm, respectively (Figure 5.64(a and b)). The FGHAZ exhibited a limited grain size gradient due to quick cooling and dynamic recrystallization, with typical LHI and HHI weldment grain sizes of 25 µm and 31 µm, respectively (Figure 5.64(b and e)). The ICHAZ's typical grain size was identical to the X-70 base metals. However, with less heat input, the cooling process was sped up, and the grain size was reduced, averaging 8 µm in LHI and 10 µm in HHI (Figure 5.64(c and f)).

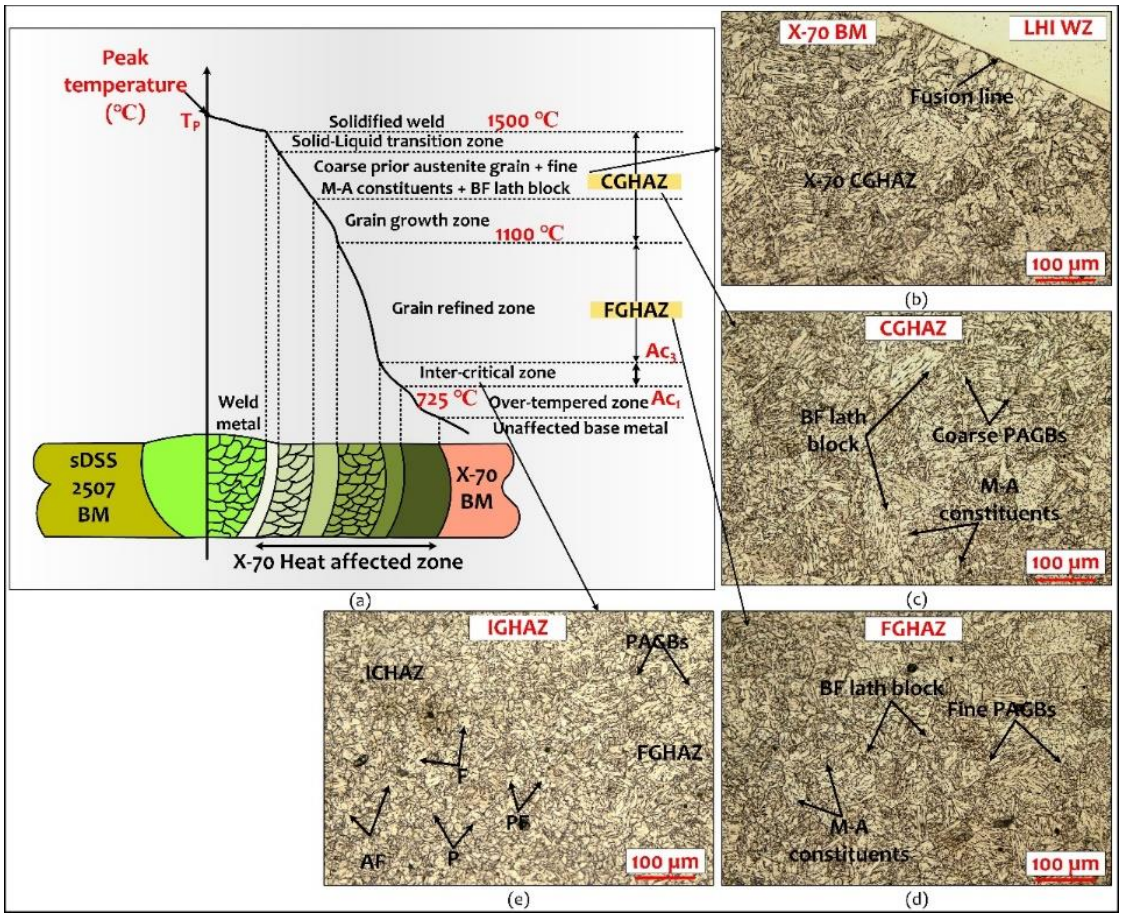

Figure 5.62 : (a) Schematic of the X-70 HAZ's relationship to temperature (Joo et al., 2012), (b) LHI weld interface optical microscope image, (c) CGHAZ, (d) FGHAZ, (e) ICHAZ

Table 5.23 : Results of EDS spectroscopy on the places depicted in Figure 5.62

Elements (wt.%)	1	2	3	4	5	6	7	8
Cr	0.12	0.26	0.42	0.16	0.08	0.32	0.08	0.18
Mn	1.98	1.84	1.81	1.75	1.87	1.56	1.78	2.11
Ni	0.15	0.52	0.72	0.28	0.38	0.27	0.24	0.40
Si	0.46	0.60	0.59	0.46	0.39	0.40	0.55	0.36
Fe	97.29	96.78	96.46	97.41	97.38	97.45	97.35	96.95

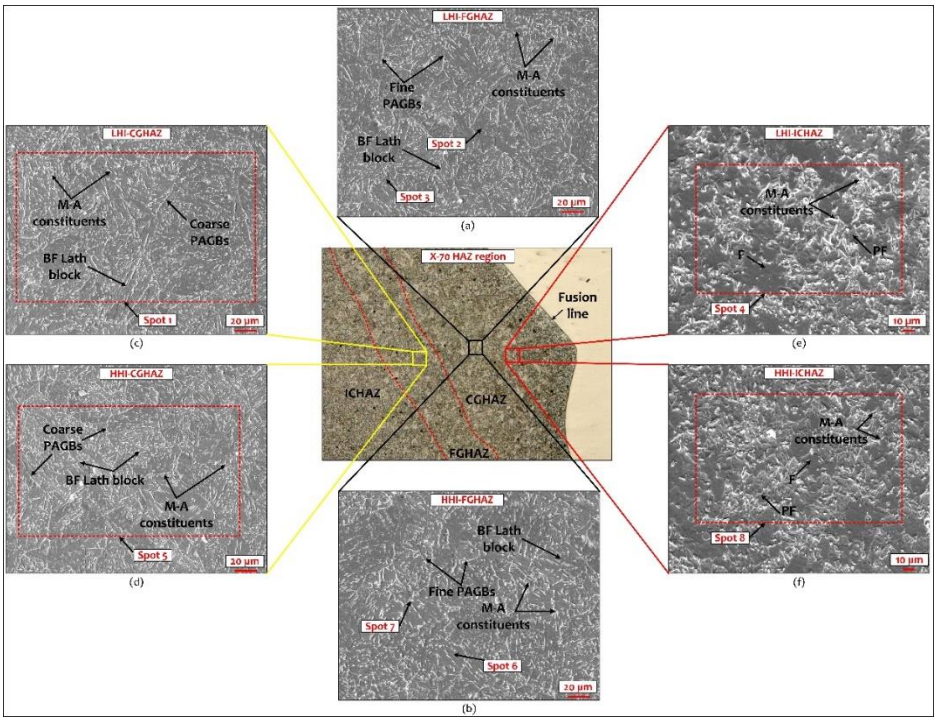

Figure 5.63 : LHI and HHI's X-70 HAZ zones (a, b) FGHAZ (c,d) CGHAZ (e, f) IGHAZ

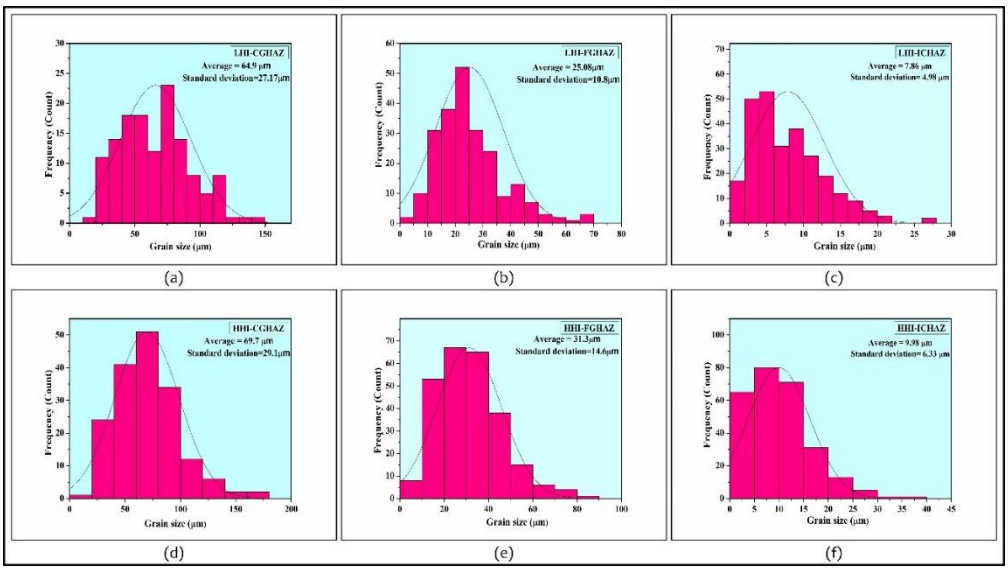

Figure 5.64 : Normal distribution of grain size in X-70 HAZ regions of (a-c) LHI weldment (d-f) HHI weldment, respectively

5.3.2.3 *WELD INTERFACE*

The X-70 weld interface's microstructural examination showed macro segregation and Type II boundaries for ER2594/ER309L filler metals in Figures 5.65(a and c) and 5.66(c-h), respectively. After welding in both weldments, X-70 weld interfaces had BF mixed with M/A components and carbide precipitation. The distribution of alloying elements inside the weld pool may be uneven due to macro segregation and Type II boundaries that might form during welding at the X-70 weld interface. These concerns can impair weld quality, mechanical characteristics, and cracking susceptibility. Macro segregation can be caused by thermophysical variations between the materials being welded, joint design, welding process, and heat and fluid flow during welding. Non-uniform element distribution is typical in dissimilar metal welding's base-filler metal interface and HAZ. Filler-deficient structures like islands and peninsulas can occur when base and filler metal elements are not entirely fused during welding.

Moreover, concentration gradients at the X-70 weld interface caused by generating a partially mixed zone (PMZ) can result in significant segregation and degradation of mechanical performance. Due to its increased thermal conductivity (45W/mK vs. 15W/mK), the X-70 HAZ shows a larger width than the sDSS 2507 HAZ. Ensure proper base and filler metal mixing during welding to reduce these defects and enhance joint strength. High temperatures generated during the welding process cause ferrite to change into austenite, which causes the formation of Type II boundaries. This process can affect the weld metal's solidification behavior, creating non-uniform microstructures and impurities at the weld interface. The formation of a boundary parallel to the fusion boundary and a few microns away is considered to be influenced by various factors, including the solidification behavior and crystal structures variations of the weld zone, dilution levels of BM, impurities element transfer into a stagnant boundary, the allotropic transformation of δ to γ at higher temperatures and diffusional alloy mixing, which modifies the composition gradient of the weld metal.

One of the essential factors in controlling the phase transformation in the sDSS HAZ is the cooling rate after welding. The cooling rate after welding varies on heat input, interpass temperature, preheating temperature, plate or tube thickness, and material thermophysical characteristics (H. Sen Wang, 2005). According to (H. Sen Wang, 2005), heat input is a critical factor that significantly affects the cooling rate. Slow cooling enhances δ to γ conversion and a better phase balance with high heat inputs. However, High heat inputs also coarsen ferrite grains and precipitate brittle secondary phases. During rapid cooling, inadequate heat inputs generate high ferrite concentrations and substantial Cr-rich nitride precipitation. In multi-pass welding, the precipitating mechanism divides austenite into two types: primary austenite and secondary austenite (γ_2). Solidification of molten metals within ferritic dendrites and the following solid-state phase transition of δ into γ contribute to forming the primary austenite (Muthupandi et al., 2003). The increased heat input influenced the development of fine IGA and GBA. Three types of austenite arise from ferrite: GBA, WA, and IGA. GBA, WA, and IGA were formed when the molten pool's temperature was below the ferrite solution line. At first, GBA formation was aided by high interface energy and sufficient chemical elements at the ferrite grain boundary (W. N. Khan et al., 2021). As temperature decreased, nucleation sites at δ/γ boundary decreased. Thus, near the δ/γ interface, the WA nucleated and expanded towards the ferrite. IGA was produced when austenite developed inside ferrite (Eghlimi et al., 2014). Most of the γ_2 was precipitated in the weld root, and the HAZ was caused by the subsequent weld pass being reheated.

Additionally, with the coexistence of the γ and δ, it is anticipated that most of the austenite will melt after reheating to the dual-phase region. However, partially transformed austenite (PTA) could be seen as a plateau structure, showing that an insignificant amount of austenite remained in the ferrite after transformation. The remaining partially transformed austenite inhibited Cr and Mo segregation and ferrite grain growth at the solidus temperature (Eghlimi et al., 2014). Figures 5.65(b and d) and 5.66(a and d) show the sDSS 2507 HAZ microstructure for LHI and HHI weldment. However, the HAZ of the sDSS 2507 often features an austenite grain distribution within the ferrite matrix. The HAZ of the sDSS is split into two regions: the HTHAZ close to the fusion line and the LTHAZ farther from the fusion line. The weldments' LTHAZ and HTHAZ regions have a network of γ grains within the ferrite matrix, but the HTHAZ completely transforms to ferritic. HTHAZ's peak temperature was above 1000 °C, while LTHAZ's was 950–650 °C. The LTHAZ microstructures are identical to the sDSS 2507BM and contain any intermetallic phases. Thus, most experiments are carried out at the HTHAZ due to structural changes that reduce toughness and corrosion resistance (Zhang et al., 2018). Due to multi-pass welding, the HTHAZ may experience γ_2 precipitation. With heating and cooling, the HAZ in sDSS 2507 undertakes numerous transformations, including γ to δ and δ to γ, resulting in grain growth and coarsening. Optical images show WA, PTA, GBA, and IGA nucleation in the sDSS 2507 HAZ (Figure 5.65(b and c)). The epitaxial growth between the sDSS 2507 BM/LHI and the HHI weld zone has been observed due to consistent chemical composition across the interface **(**(Figure 5.65(b-point 2)).

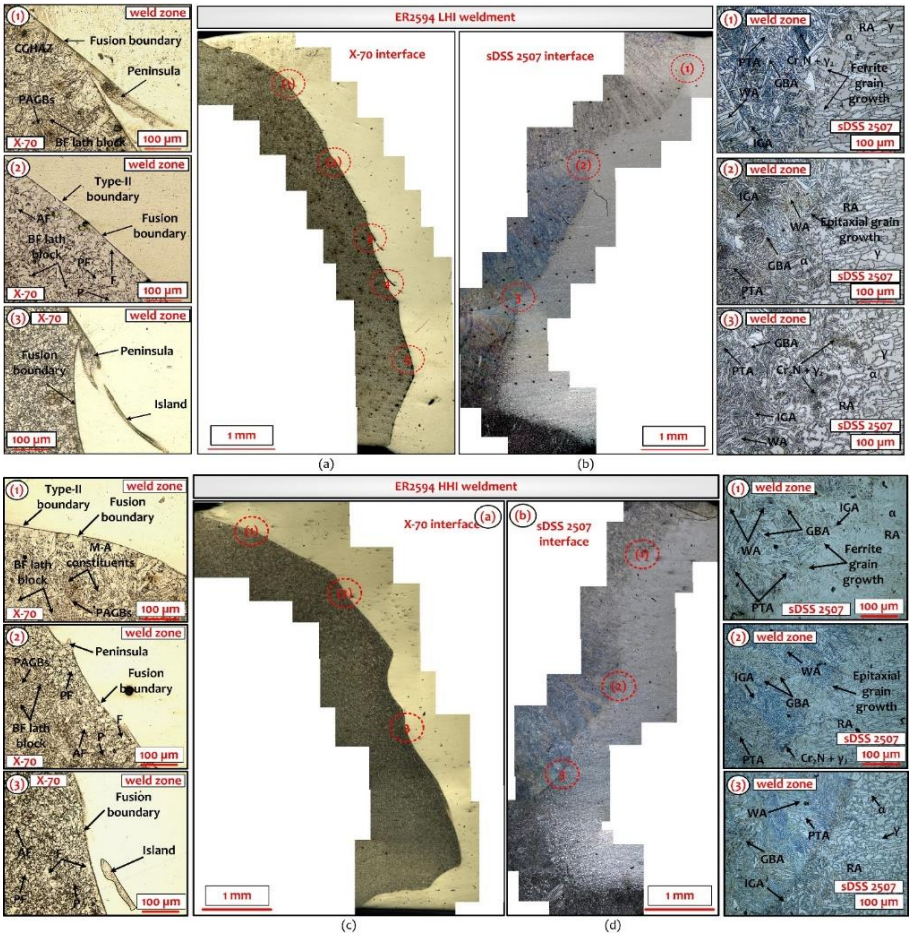

Figure 5.65 : Weld interface characterization of X-70 and sDSS 2507 BM for ER2594 (a and b) LHI weldment, (c and d) HHI weldment

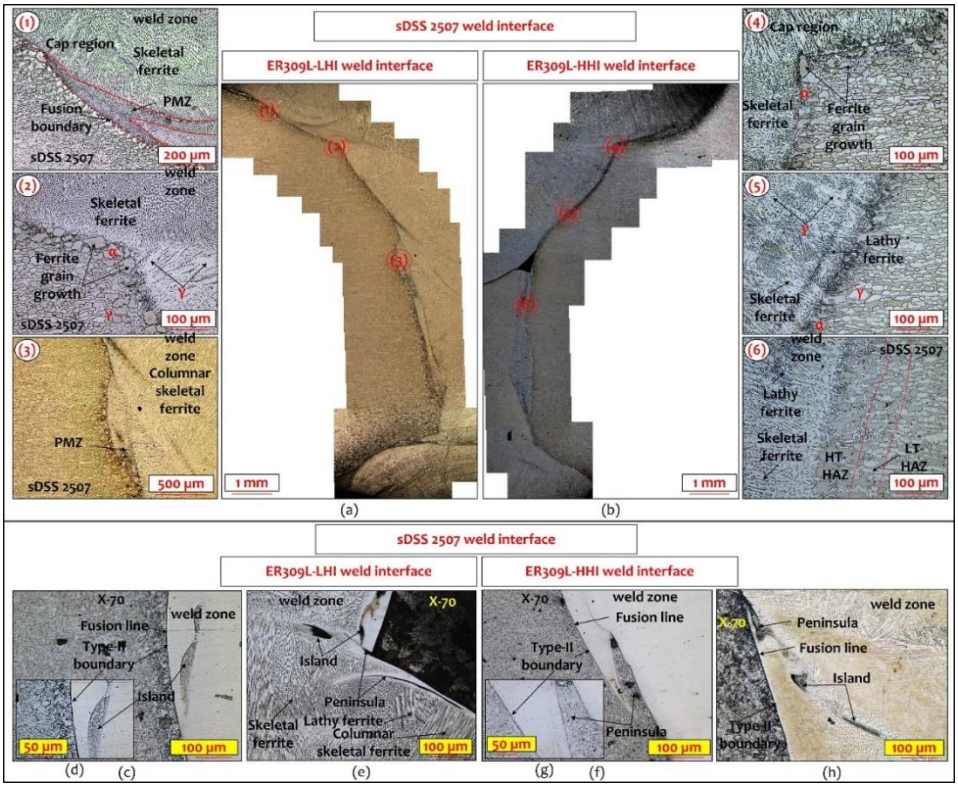

Figure 5.66 : Weld interface characterization for ER309L filler of LHI/HHI weldment at (a and b) sDSS 2504 HAZ side, (c-h) X-70 HAZ side

Line mapping and EDS spectra examined element mobility across weld interfaces in ER2594-LHI and HHI weldments (Figure 5.67). Figure 5.67(a and e) demonstrates the microstructural evolution and EDS spectra site of the sDSS 2507 BM to WZ interface for both weldments. According to EDS analysis, the sDSS 2507 BM's Cr, Ni, Fe, and Si composition variation was almost identical to that of LHI and HHI WZ (Table 5.24). Line mapping investigation validates the insignificant element composition disparity adjacent to the interface (Figure 5.67(b and f)). The elemental composition of the sDSS 2507 BM, LHI, and HHI weld interfaces shows a smooth transition in the EDS spectra results. The EDS spectra and line scan illustrate the elemental composition of the X-70 weld interface and peninsula, along with the ER2594-LHI and HHI weldments' EDS spectra (Figure 5.67(c and g)). X70 BM had a greater concentration of Fe than sDSS 2507 BM due to its lower Ni and Cr content (Figure 5.67(d and h)). Several peaks were seen in the HAZ of the dissimilar weld, indicating that the chemical components, including Cr, Ni, Fe, Mn, and Si, were not uniformly distributed. The peninsula and island regions near the weld interface show a significant reduction in Cr, Ni, Fe, and Mn concentrations (Table 5.24). The peninsula or island between Type II and fusion boundaries allows super duplex carbon diffusion and carbide dissolution. The X70 HAZ's low Cr and Fe levels make it more prone to corrosion failure, while the Mn content drops as one passes through the WZ and into the sDSS2507 HAZ. Due to low Ni and Cr levels on the X70 side, corrosion remains challenging despite the sDSS2507 weld zone and HAZ's corrosion and pitting resistance.

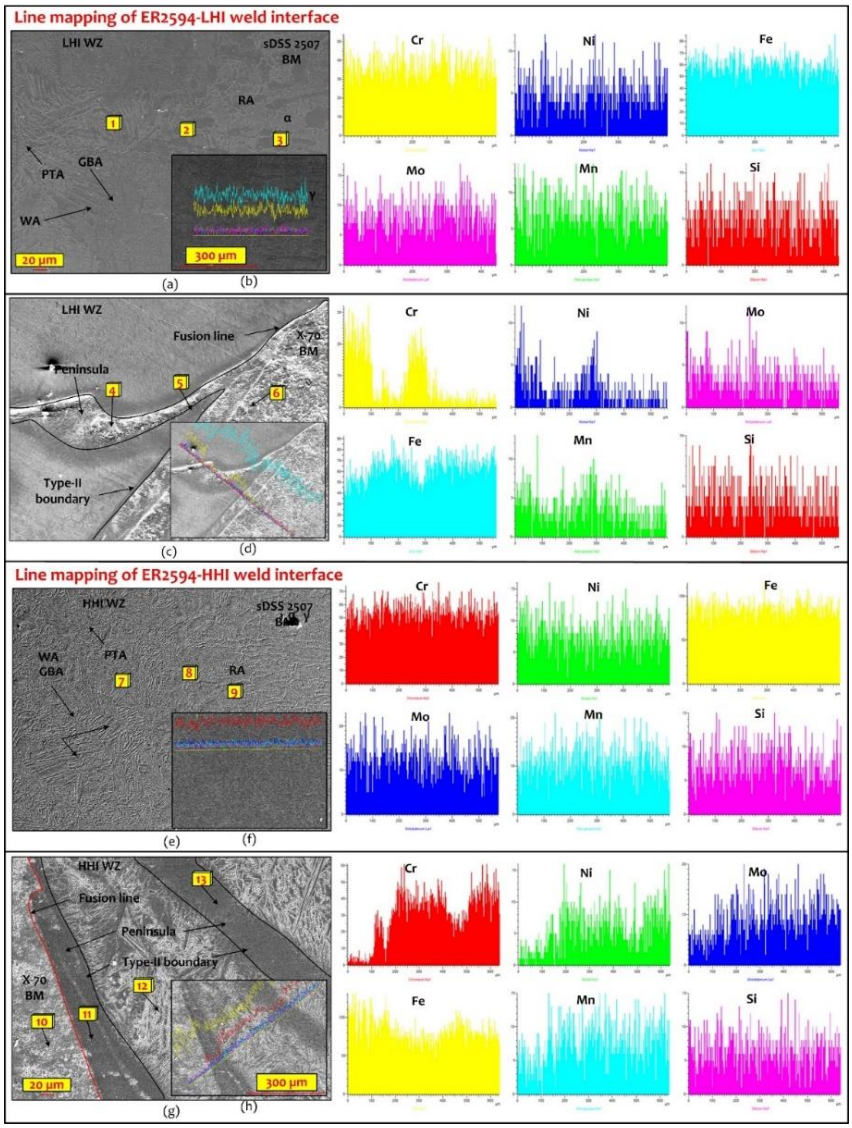

Figure 5.67 : Line mapping study of (a-d) ER2594-LHI weld interface at sDSS 2507 BM and X-70 BM, (e-h) ER2594-HHI weld interface at sDSS 2507 BM and X-70 BM, respectively

Table 5.24 : EDS study of the spot mentioned in LHI/HHI weldments at both BM weld interfaces for ER2594 filler

	LHI interface (sDSS 2507 BM)			*LHI interface (X-70 BM)*			*HHI interface (sDSS 2507 BM)*			*HHI interface (X-70 BM)*			
Elements (wt.%)	*1*	*2*	*3*	*4*	*5*	*6*	*7*	*8*	*9*	*10*	*11*	*12*	*13*
Cr	27.13	28.4	27.1	1.7	5.9	0.4	27.1	28.1	27	0.38	12.1	24.7	13.9
Ni	6.47	5.97	6.93	0.5	2.35	0.2	6.03	5.5	5.8	0.17	4.1	8.1	4.1
Fe	64.4	63.2	64.4	95.4	90	97.2	64.7	64.5	64	97.2	81	65.1	79.6
Mn	0.99	0.82	1.12	1.6	1.36	1.78	1.09	0.89	1.19	1.7	1.17	1.4	1.5
Si	0.94	1.55	0.48	0.65	0.3	0.4	1.15	0.92	1.27	0.5	0.8	0.7	0.7

Line mapping and EDS spectra of ER309L filler show the primary constituent element's mobility across weld interfaces in Figure 5.68. Both weldments' interface microstructural evolution and EDS spectrum position for the sDSS 2507 weld interface are depicted in Figure 5.71(a and e), respectively. EDS analysis showed that the sDSS2507 BM and ER 309L WZ have comparable Cr, Ni, Fe, and Si contents. Line mapping analysis confirms the minor element composition variation near the interface (Figure 5.68(b and f)). The EDS spectra (Table 5.25 and 5.26) demonstrate a relatively smooth variation in the marginal element composition of the sDSS 2507BM interface. The elemental composition variation along the X-70 weld interface and peninsula was corroborated by the EDS spectra and line scan in (Figure 5.68(c and g)). Findings showed that X70 BM, with its low Ni and Cr content, had a higher Fe concentration than the sDSS 2507 BM ((Figure 5.68(d and h)). Carbon (C) and iron (Fe) significantly affect the combined dissimilar welded joint. Cr, Ni, Fe, and Mn reduced considerably in the island and peninsula regions at the weld interface. Carbon diffusion and carbide dissolution from the sDSS 2507 side may occur in the peninsula or island on the X70 side between the type II boundary and the fusion boundary. In multi-pass welding, the HAZ is especially vulnerable to the thermal cycle. Carbide dissociation and precipitation in this region can significantly affect weld mechanical behavior. The X70's HAZ is prone to corrosion failure due to the low concentration of Cr and Fe. sDSS 2507 weld zone and HAZ's nickel concentration are sufficient for corrosion and pitting resistance. However, corrosion is a significant concern on the X70 side because of the low Ni and Cr concentrations.

Table 5.25 : EDS study of the spot mentioned in LHI weldments at both BM weld interfaces for ER309L filler

	ER309L-LHI interface (sDSS 2507 BM)			*ER309L-LHI interface (X-70 BM)*			
Elements (wt.%)	*1*	*2*	*3*	*4*	*5*	*6*	*7*
Cr	25.36	23.65	25.01	10.62	21.32	3.97	0.15
Ni	10.89	11.35	8.63	5.56	8.15	1.06	0.68
Fe	61.53	62.7	64.72	8.13	68.89	92.89	96.71
Mn	1.76	1.51	1.06	1.82	1.01	1.57	1.89
Si	0.46	0.79	0.58	0.62	0.63	0.51	0.57

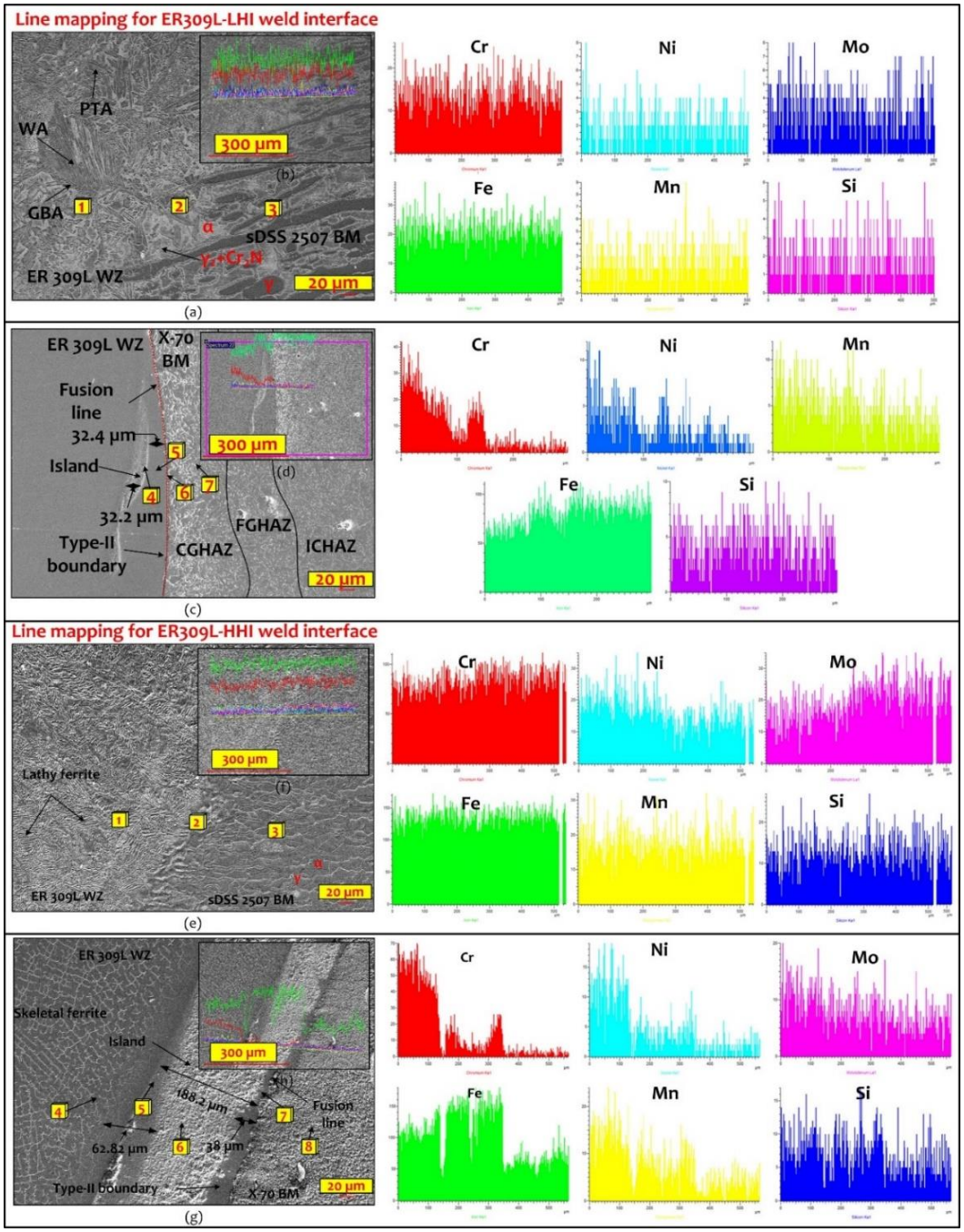

Figure 5.68 : Line mapping study of (a-d) ER309L-LHI weld interface at sDSS 2507 BM and X-70 BM, (e-h) ER309L-HHI weld interface at sDSS 2507 BM and X-70 BM, respectively

Table 5.26 : EDS study of the spot mentioned in HHI weldments at both BM weld interfaces for ER309L filler

	ER309L-HHI interface (sDSS 2507 BM)			*ER309L-HHI interface (X-70 BM)*				
Elements (wt.%)	*1*	*2*	*3*	*4*	*5*	*6*	*7*	*8*
Cr	25.73	23.86	25.10	21.67	4.20	1.40	7.73	0.21
Ni	11.03	11.72	8.93	10.41	2.07	0.91	4.60	0.47
Fe	60.96	61.96	64.19	65.74	91.51	95.12	84.96	97.05
Mn	1.83	1.57	1.08	1.35	1.90	1.95	2.07	1.68
Si	0.45	0.89	0.69	0.83	0.32	0.62	0.64	0.59

EPMA analysis was utilized to quantify elemental composition and generate element maps at the sDSS 2507 and X-70 weld interface to study microstructure anomalies and element distribution. Both BMs' HAZs demonstrated a significant disparity in elemental composition. Figure 5.69(a and b) shows the EPMA diffusion outcomes for C, Fe, Si, Ni, Cr, Mn, and Mo at the sDSS 2507 and X-70 interfaces with ER2594 filler. Figure 5.69(a) depicts the sDSS 2507 BM interface's elemental distribution. Due to the identical chemical composition of the sDSS 2507 BM and ER 2594 filler, elements like C, Si, and Fe do not exhibit any noticeable diffusion during solidification. However, there is a slight variation in Cr, Ni, and Mo across the weld interface. The result also reveals that the weld zone's Mn concentration was higher than that of sDSS 2507 BM. The X-70 weld interface's elemental composition map for both weldments indicates that Cr, Ni, and Mo are scarcely present (Figure 5.69(b)). These elemental compositions exhibit an apparent diffusion that appears to pass the fusion boundary and reach the weld zone. Carbon activity may increase in this region due to Cr's high elemental composition gradient. At the X-70 weld interfaces, C segregation with a C-rich zone was observed. Figure 5.69(c and d) shows elemental distribution results for C, Fe, Si, Ni, Cr, Mn, and Mo at the sDSS 2507 and X-70 interfaces with ER309L filler. The elemental composition map for the X-70 weld interface indicates low Cr, Ni, and Mo content, with C segregation (Figure 5.69(c)). These elemental compositions extend beyond the fusion boundary into the weld zone, and the notable chromium gradient indicates a potential increase in carbon activity within this region. Figure 5.69(d) shows the elements' distribution at the sDSS 2507 BM interface, where components like C, Si, and Fe do not migrate during solidification due to the nearly identical chemical composition of sDSS 2507 BM and ER309 filler. However, variations in Cr, Ni, and Mo diffusion near the weld interface are observable.

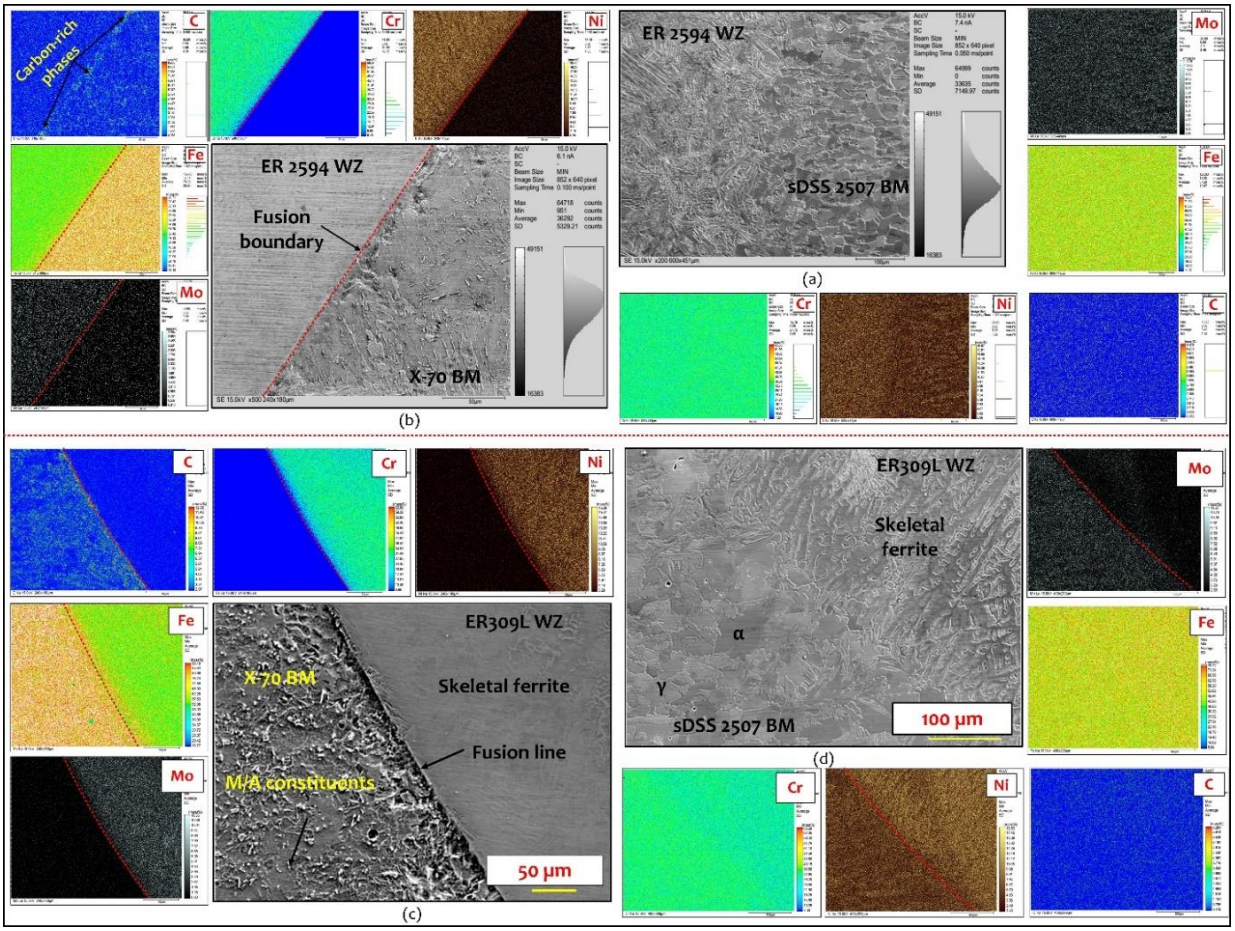

Figure 5.69 : EPMA study showing element distribution at the sDSS 2507 and X-70 weld interface for (a and b) ER2594 filler and (c and d) ER309L filler, respectively

5.3.2.4 *WELD ZONE*

The solidification mode and microstructural evolution in the weld zone are affected by the Cr_{eq} and Ni_{eq} levels, as indicated by the Fe-Cr-Ni pseudo-binary phase diagram and the Schaeffler diagram (Figure 5.70 and 5.71). The Schaeffler diagram was used to determine the weld metal microstructure by plotting the tie line center between the base metals and locating the spot corresponding to each heat input's composition. The X-70 BM had Cr_{eq} and Ni_{eq} values of 0.55% and 2.31%, respectively; the sDSS 2507 BM had 29.5% and 8.58%, while the Filler ER2594 had 30.8% and 12.56%. Ferritic solidification in ER2594-LHI weldments is less susceptible to solidification cracking than ferritic-austenitic (FA) solidification in HHI weldments. For ER2594-LHI and HHI weldment, the Cr_{eq}/Ni_{eq} ratios of welded joints are 2.3 and 1.78, respectively (Figure 5.70(a)). Solid-phase transformations proceed from reformed to reformed austenite after primary ferrite solidification. Due to its higher Ni_{eq} value, the ER2594-HHI weldment shifted up on the Schaeffler diagram. The Schaeffler diagram shows 80% ferrite in ER2594-LHI and 35% in HHI weldment (Figure 5.71(a and b)). Significant amounts of austenite can still be produced at interfaces before solidification completion. Finally, this causes a shift in crystallography at the X70 BM interface and results in Type II boundaries forming transverse to the fusion boundary. The ER309L filler metal has a ferritic-austenitic (FA) solidification process that begins with ferrite. There may be significant austenite formation at the interface due to additional peritectic/eutectic transformations before the solidification is complete. The ER309L filler's weld compositions are located in the FA zone, considering a 30% dilution from the weld cross-sectional area. The Cr_{eq}/Ni_{eq} ratios of weld joints are 1.81 and 1.76, respectively, under both heat input conditions. As Figure 5.71(b) indicates, both weldments are situated correctly on the Schaeffler diagram. ER309L-LHI and HHI weldments with FA solidification are very resistant to solidification cracking. Due to having a substantially higher Ni_{eq} value than the ER309L-LHI weldment, the HHI weldment's position on the Schaeffler diagram shifted upwards. The Schaeffler diagram shows 35% and 25% ferrite content for ER309L-LHI and HHI weldments (Figure 5.71(a and b)). The solidification of ER309L filler as a primary ferrite resulted in skeletal ferrite and lathy morphology reminiscent of FA-type solidification.

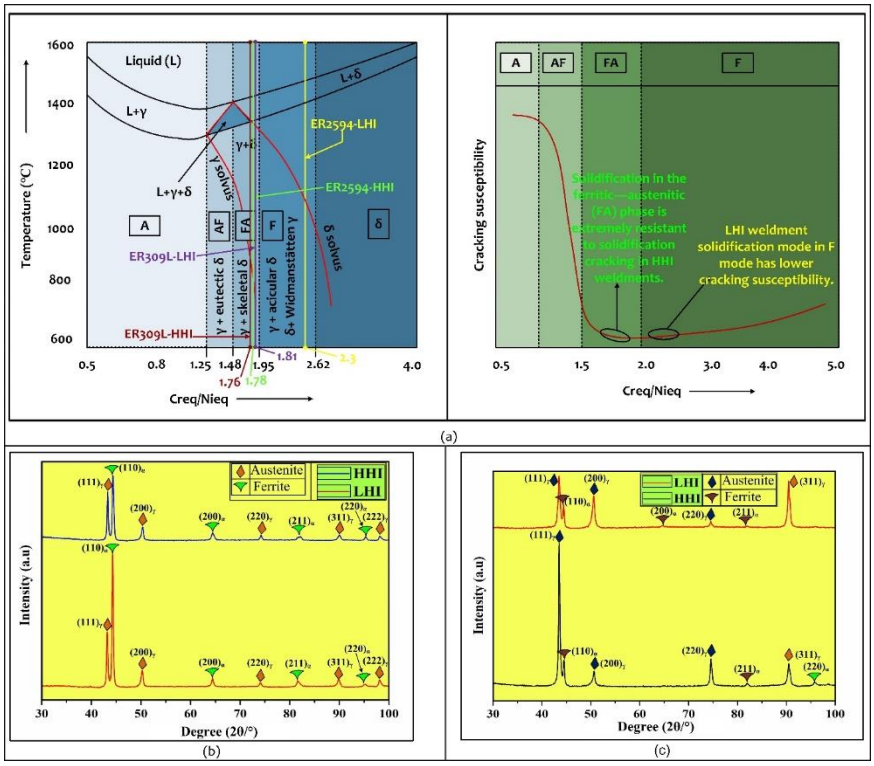

Figure 5.70 : (a) Pseudo-binary diagram demonstrating the solidification mode, and LHI/HHI weld zone XRD patterns for (b) ER2594 filler and (c) ER309L filler, respectively

Figure 5.70(b and c) shows the effect of heat input on the XRD patterns of both ER2594/ER309L weldments. Both the α and γ phases are conformable to the phases observed in Figure 5.70(b and c), and the α phase's diffraction pattern is like the peaks on JCPDS Card No. 00-06-0694, while the γ phase resembles the peaks on JCPDS Card No. 00-033-0397. The (111), (200), and (220) planes of austenite are represented by the peak intensities at 43.47°, 50.67°, and 74.68°, respectively. The majority of the γ and δ precipitation typically occurred on closely packed planes $(111)_{\gamma}$ and $(110)_{\delta}$. Due to their low composition and small size, the BM and ER2594/ER309L filler weldments mainly consisted of ferrite and austenite phases, with no intermetallic phases like Cr_2N, sigma (σ), or χ phase. According to their respective intensities, the XRD peaks of γ and δ can be used to determine their relative content. A relative phase transition with a larger peak intensity indicates one phase's stronger presence (Zhang et al., 2018).

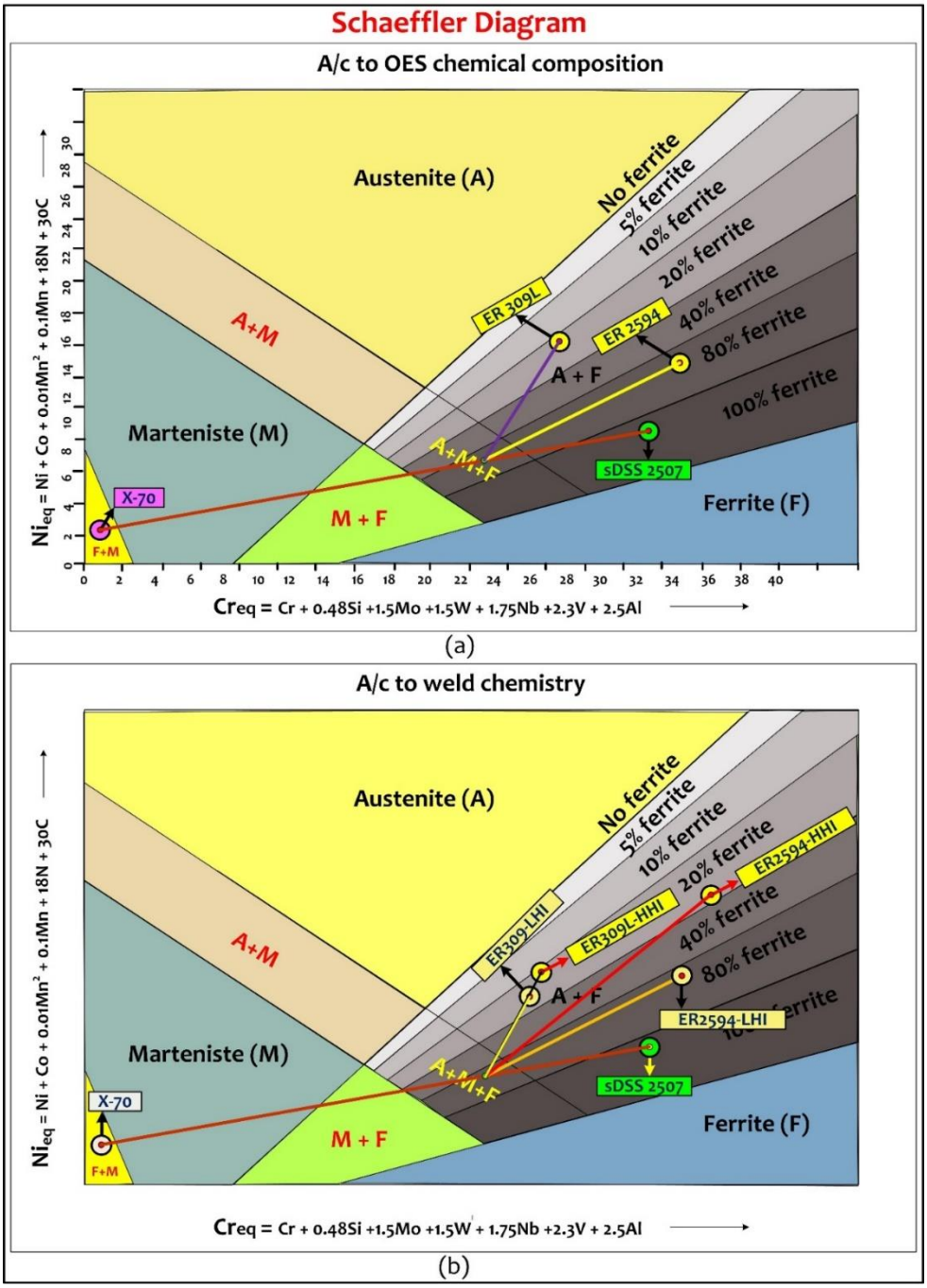

Figure 5.71 : (a and b) Schaeffler constitution diagrams based on chemical composition and weld chemistry for ER2594 and ER309L filler, respectively

SEM images of the ER2594-LHI and HHI weld zone's various regions are shown in Figure 5.72. In both LHI and HHI states, duplex microstructure, such as GBA, WA, and IGA, dominates the cap and filler pass of the weld zone microstructure (Figure 5.72(a, b, g, and i)). The root and backing pass microstructure also shows typical duplex characteristics such as PTA, chromium nitride (Cr_2N), and γ_2 precipitation in the ferrite matrix (Figure 5.72). Skeletal ferrite structure dominates the root pass of the HHI weld zone (Figure 5.72(j and k)) and becomes duplex microstructure in the backing pass (Figure 5.72(l and m)). The skeletal ferrite's thin, dendritic structure contrasts with the lathy ferrite's blocky, asymmetrical structure (Figure 5.72(k)). Higher concentrations of Cr and Ni, which substantially impact the development of various ferrite morphologies, were identified according to the SEM/EDS analysis, shown in Figure 5.72 and tabulated in Table 5.27. However, the SEM revealed an extensive amount of γ_2 with Cr_2N precipitation in the weld joint's root and backing pass. The two varieties of the γ_2 can be distinguished based on the locations of the precipitation: intragranular and intergranular γ_2. Intergranular γ_2 is a kind of γ_2 that forms at δ/γ interfaces or is connected with Cr_2N and appears as tiny white needles or island-like structures inside the matrix (Figure 5.72(d and f)). The second form of γ_2 is intragranular, and it forms in regions where austenite or acicular particles originated after reheating. In Figure 5.72(e), fine intergranular γ_2 forms a basketweave structure due to their high density. In areas with high Ni and low Cr concentrations, Cr_2N tends to grow. EPMA analysis was also done to understand alloying element micro-segregation in the ER2594 weld zone. A typical BSE image of the root pass weld zone, which consists of skeletal ferrite and γ, is displayed in Figure 5.72. The elemental maps showed significant C, Cr, Ni, Si, and Fe segregation (Figure 5.73). After welding, certain elements had distinct distributions: C, Si, and Mn were more abundant in skeletal ferrite, whereas Cr, Ni, and Fe were more abundant in austenite. The skeletal ferrite zone of the weld showed Fe depletion from 55 wt% to 25%. According to observations, the duplex microstructure is formed by ferrite and austenite stabilizer partitioning during weld solidification (Gunn, 1998).

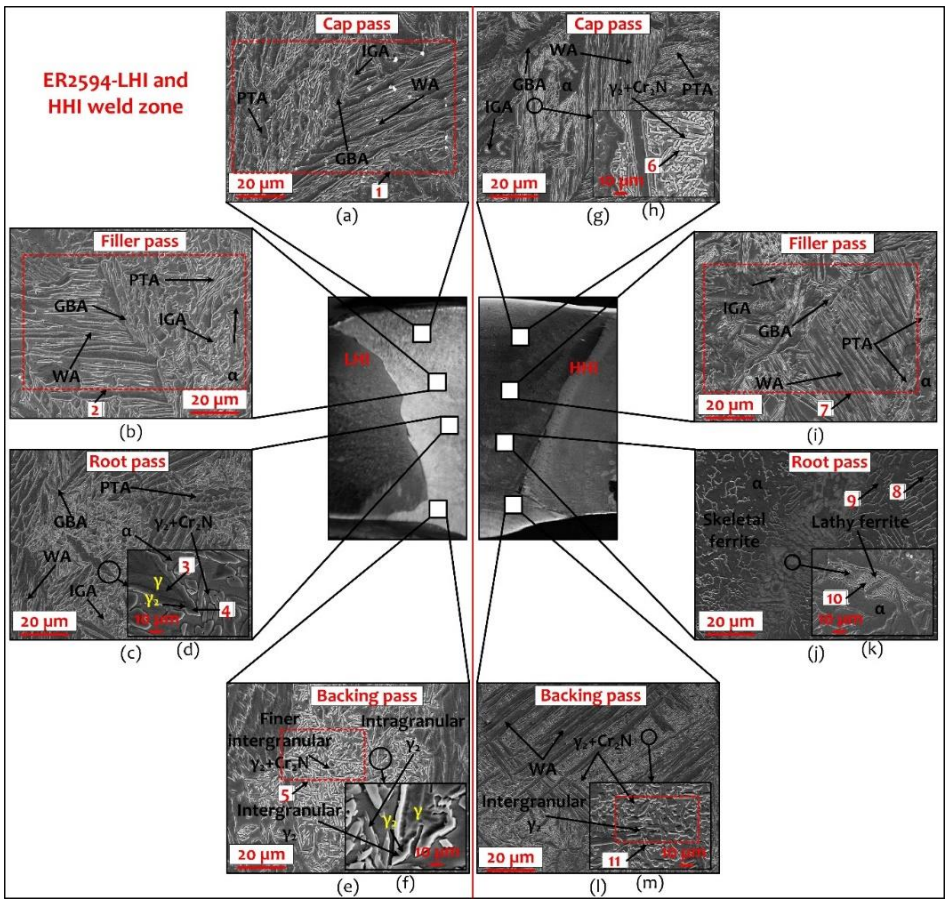

Figure 5.72 : SEM image of LHI state: cap pass (a), filler pass (b), root pass (c and d), backing pass (e and f), SEM image of HHI state: cap pass (g and h), filler pass (i) root pass (j and k), and backing pass (l and m)

Table 5.27 : Results from EDS spectra for the spots mentioned in Figure 5.72

	ER2594-LHI weldment EDS spot spectra					*ER2594-HHI weldment EDS spot spectra*					
Elements (wt.%)	*1*	*2*	*3*	*4*	*5*	*6*	*7*	*8*	*9*	*10*	*11*
Cr	24.1	23.36	22.90	20.80	25.41	25.91	28.56	26.24	20.72	23.74	24.4
Ni	7.98	7.62	8.02	9.80	7.85	7.99	5.96	5.36	10.63	8.03	8.45
Fe	66.1	67.05	66.65	67.08	65.01	64.41	63.14	65.36	66.53	65.70	64.9
Mn	0.87	0.45	0.78	1.06	0.35	0.98	0.31	1.23	1.63	0.74	0.37
Mo	0.41	0.61	0.64	0.41	0.70	0.09	1.47	1.25	0.09	0.90	0.81
Si	0.56	0.90	1.01	0.86	0.69	0.88	0.56	0.57	0.40	0.88	1.00

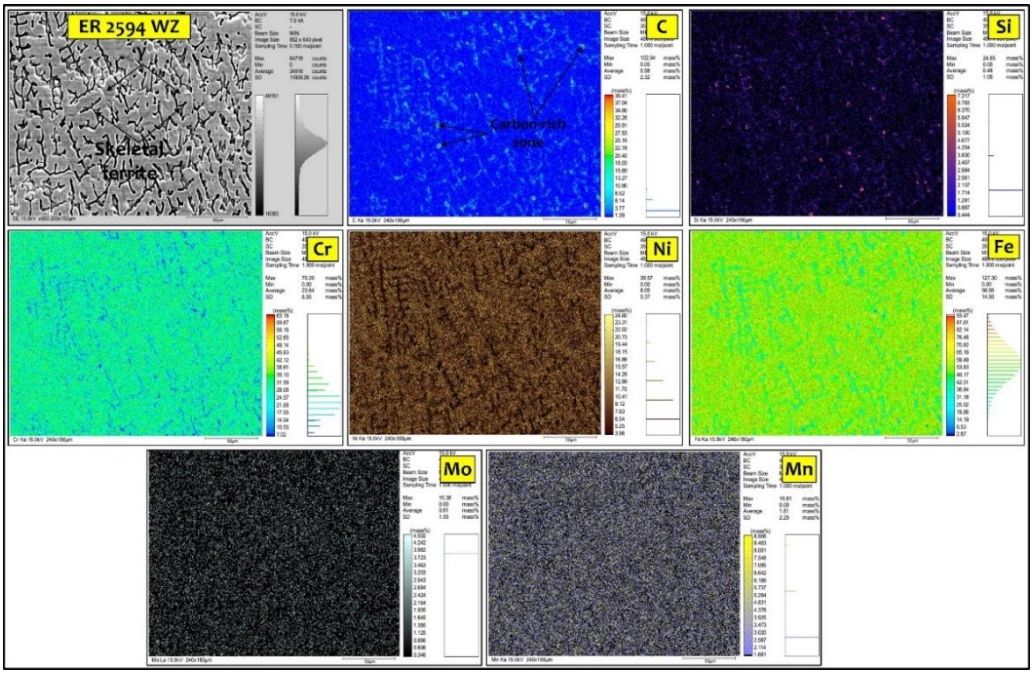

Figure 5.73 : EPMA study showing element distribution across the ER2594 weld zone

Figure 5.74 depicts the microstructure evolution of the ER309L WZ for both weldments during several passes. The 309L filler wire exhibits a skeletal and lathy ferrite structure that is perpendicular to the fusion line and solidifies as the primary delta ferrite (Kellai et al., 2018). Lathy and skeletal ferrite dominate the weld zone microstructure in both LHI and HHI states. Specific structural traits can be seen in these ferrite morphologies (Figure 5.74(a, f)). Skeletal ferrite has a thin, dendritic structure with distinctly discernible dendrites (Figure 5.74(b,c, and g)), contrasting to lathy ferrite's blocky, uneven structure. The ferrite appears lathy because of instability at the δ/γ interface during the transformation process, which is regulated by diffusion during cooling. Interdendritic ferrite microstructure, which is present in the 309L filler and is situated between the primary and secondary dendrite arms, enhances the weld joint's impact toughness and aids in preventing cracking during solidification. The root area exhibits columnar skeletal ferrite and lathy ferrite structure, while the cap and filler pass exhibit both lathy and skeletal ferrite (Figure 5.74(d and h)). The SEM/EDS analysis, shown in Figure 5.74 and tabulated in Table 5.28, indicated the presence of a higher amount of Cr and Si, which significantly impact the formation of delta ferrite. The EDS results for the weld zone also reveal that the austenite region is Ni-rich, and the ferrite region is Cr-rich. Inoue et al. (Inoue et al., 2000) found that the Cr/Ni ratio increases total skeletal and lathy ferrite content. As seen in Figure 5.74(i, e), a skeletal ferrite structure results from reduced welding heat input and increased cooling rate. However, as welding heat input increases, the cooling rate reduces, allowing ferrite dendrites to grow, forming a continuous structure like lathy ferrite (Figure 5.74(e, h)).

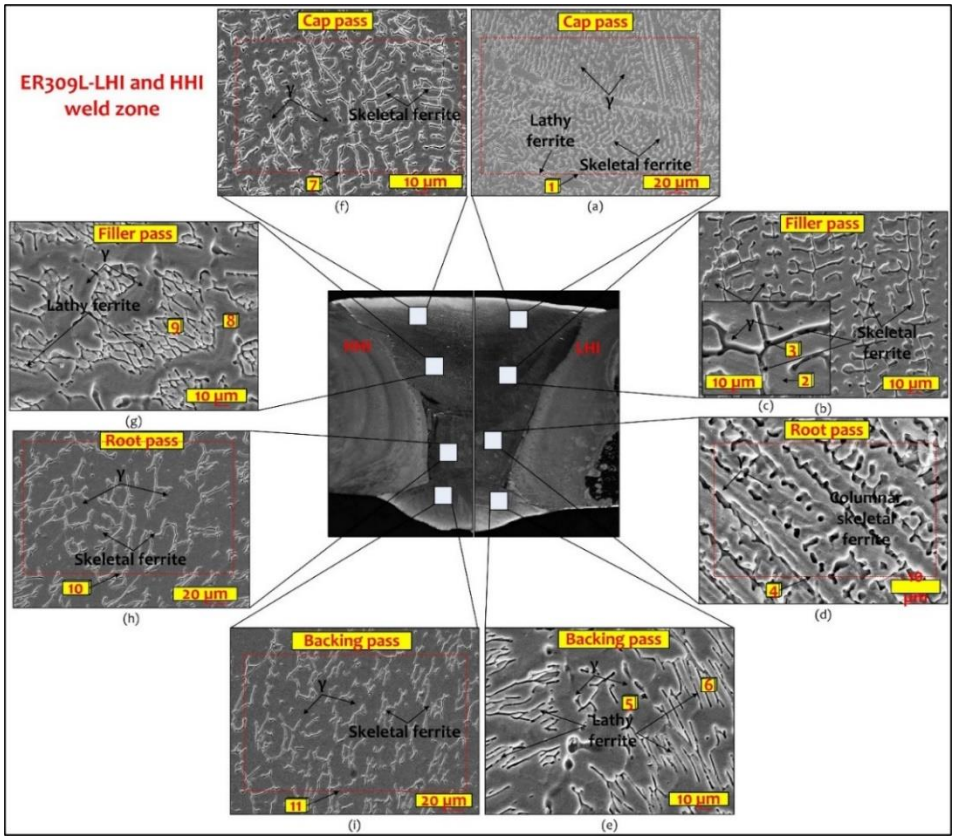

Figure 5.74 : SEM micrograph of the WZ showing (a, f) cap, (b, c, and g) filler, (d, h) root and (e, i) backing pass in LHI and HHI weldment, respectively

Table 5.28 : Results from EDS spectra for the spots mentioned in Figure 5.74

	ER309L-LHI interface EDS spot spectra						ER309L-HHI interface EDS spot spectra				
Element (wt.%)	1	2	3	4	5	6	7	8	9	10	11
Cr	22.8	21.7	22.5	23.7	21.1	21.1	23.5	22.7	21.5	23.7	23.7
Ni	13.8	13.8	12.9	13.0	11.6	10.4	11.6	13.0	10.6	8.03	12.8
Fe	60.6	61.6	62.0	61.1	64.89	65.71	62.11	61.65	65.17	66.60	61.79
Mn	1.88	1.95	1.80	1.24	1.45	1.75	2.11	1.62	1.72	0.74	0.85
Si	0.79	0.82	0.77	0.84	0.90	1.00	0.61	1.02	0.99	0.88	0.79

5.3.3 MECHANICAL CHARACTERIZATIONS

Microstructural characterization includes using microhardness, tensile, and impact testing to assess how heat input affects the structural integrity of weld joints.

5.3.3.1 MICROHARDNESS

Figures 5.75 and 5.76 illustrate BM, HAZ, and WZ microhardness maps and profile variations for sDSS 2507/X-70 weldments. The weldment's hardness fluctuation was quantified using a hardness map. A closer look at the microhardness profile and map of ER2594 weldments reveals that the sDSS 2507 BM has higher hardness than the X-70 BM (Figures 5.75(a) and 5.76(a and b)). Microhardness readings for the sDSS 2507 and X-70 BM were 283 ± 5 $HV_{0.5}$ and 230 ± 6 $HV_{0.5,}$ respectively. For both BMs (W. N. Khan & Chhibber, 2021a), comparable outcomes were noted. For the sDSS 2507 HAZ, there are marginal differences in hardness value (275 ± 6 $HV_{0.5}$ for ER2594-LHI and 285±4 $HV_{0.5}$ for ER2594-HHI weldment). Hardness values in the X-70 HAZ showed a modest difference, from 250 ± 6 $HV_{0.5}$ for ER2594-LHI weldment to 275 ± 4 $HV_{0.5}$ for ER2594-HHI weldment. In the X-70 HAZ, carbon diffusion from the X-70 BM side, unmixed zone, and alloying element diffusion into the weldment contributed to an increase in microhardness. Different heat input peak hardnesses result from variations in interface

concentration gradients. Several studies have found a martensitic band near the Type-II boundary and weld interface (Sadeghian et al., 2014; Saedi et al., 2018). Weld zone hardness values changed from 190 to 320 $HV_{0.5}$, with ER2594-LHI weldment averaging 275 ± 7 $HV_{0.5}$ and ER2594-HHI weldment averaging 285 ± 5 $HV_{0.5}$. Microhardness tests exhibit negligible variations in the hardness of the weld zone for both weldments. The microhardness profile demonstrates that weld zone hardness varies from the cap to the backing pass for both heat input weldments. The map displays ER2594-LHI and HHI weldments' distinguished microhardness distribution. The cap pass of ER2594-LHI and HHI weldments (280 ± 3 $HV_{0.5}$ and 315 ± 6 $HV_{0.5}$, respectively) and the filler pass (270 ± 4 $HV_{0.5}$ and 285 ± 5 $HV_{0.5}$, respectively) both show a substantial variation in the microhardness value. The microhardness scatters of 30 $HV_{0.5}$ in both weld zones match the microstructural disparities reported in cap passes. This hardness variation does not influence the weld joint's structural integrity. It's also clear that heat input enhances hardness. Other researchers found comparable results (W. N. Khan & Chhibber, 2021b; Saedi et al., 2018).

Slight variations in hardness value (240 ± 5 $HV_{0.5}$ for ER309L-LHI and 270 ± 4 $HV_{0.5}$ for ER309L-HHI weldment) are observed for the sDSS 2507 HAZ (Figures 5.75(b) and 5.76(c and d)). The hardness value of the X-70 HAZ, which is 220 ± 6 $HV_{0.5}$ for ER309L-LHI weldment and 260 ± 4 $HV_{0.5}$ for ER309L-HHI weldment, shows modest variation. The ER309L-LHI and HHI weldments have non-uniform hardness distributions, and the X-70 HAZ/ER309L weld interface has considerable hardness variations. In the filler pass of the ER309L-HHI weldment, the region with the maximum hardness (i.e., 287.1 $HV_{0.5}$) was located between the PMZ and Type-II boundary near the X-70 weld interface (Figure 5.75(b) and 5.76(d)). This effect could result from the interface producing hard constituents (martensite/carbides). Some other investigations have reported a martensitic band perhaps formed adjacent to the Type-II boundary and UMZ interface (J. Dupont & Kusko, 2007; Sadeghian et al., 2014; Saedi et al., 2018). Weld zone hardness values varied from 190 to 290 $HV_{0.5}$, with ER309L-LHI weldment averaging 205 ± 6 $HV_{0.5}$ and ER309L-HHI weldment averaging 225 ± 4 $HV_{0.5}$. Microhardness tests demonstrate minor variations in WZ hardness for both heat input weldments. Although the F-A solidification mode is common for both WZ, the microhardness values in the weld zone are heterogeneous due to the different chemical compositions, morphologies, and microstructure distributions of the weldments. The microhardness profile shows that the WZ's hardness changes from the cap to the backing pass for both heat input weldments (Figure 5.75(b)). The microhardness range of 30-45 $HV_{0.5}$ in the weld zone is consistent with the microstructural heterogeneity observed in both weldments' cap and backing pass. The scatter in the 10-35 $HV_{0.5}$ values may be caused by multi-pass welding with simultaneous heating and cooling, along with differing heat input in each pass. During their investigation, several authors observed similar results (W. N. Khan & Chhibber, 2021b, 2021a; Saedi et al., 2018).

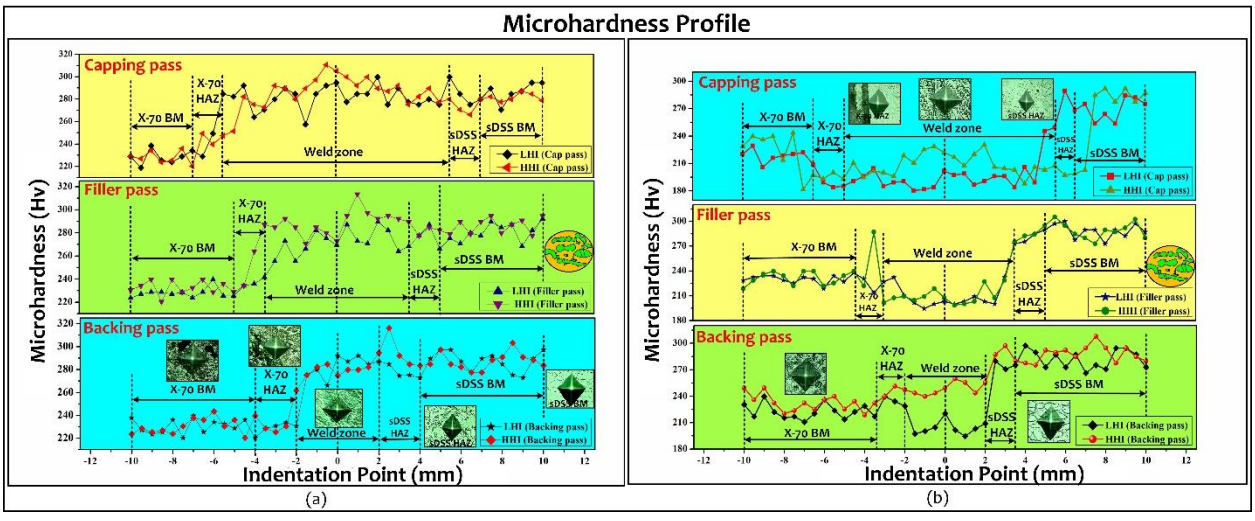

Figure 5.75 : Comparative microhardness profile for capping, filler, and backing pass of (a) ER2594-LHI/HHI weldment and (b) ER309L-LHI/HHI weldment, respectively

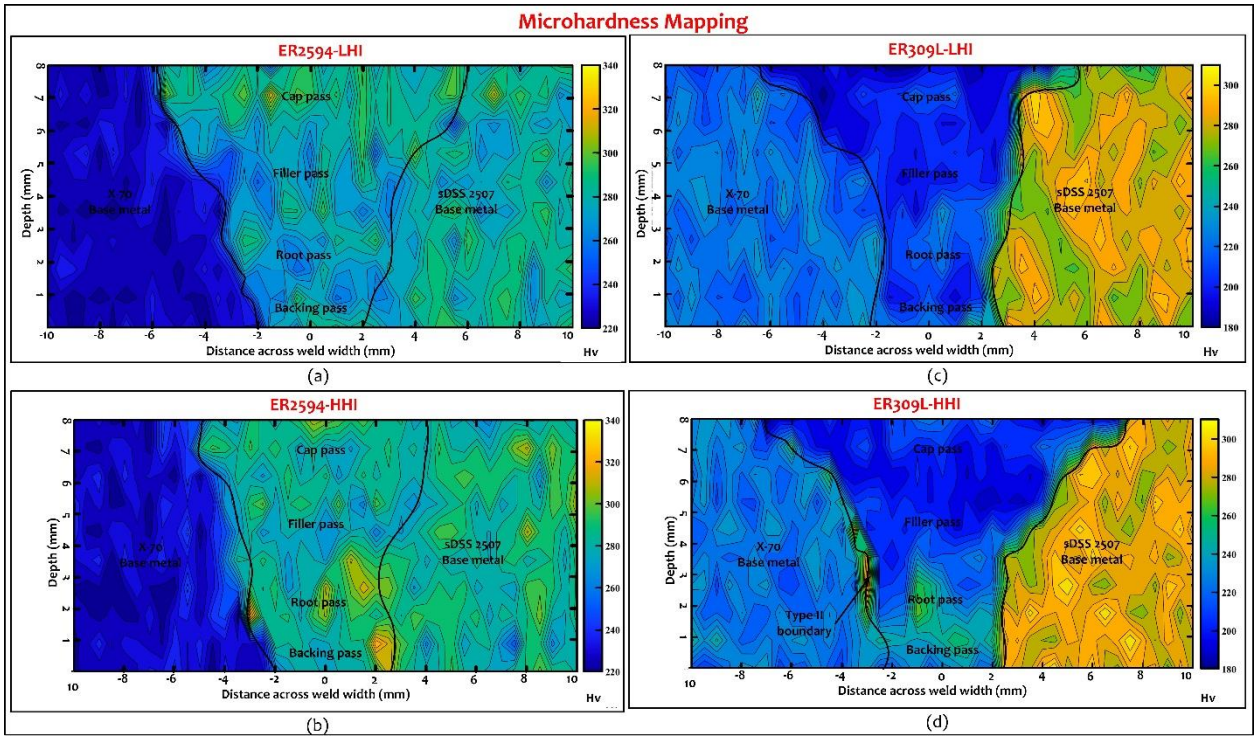

Figure 5.76 : Microhardness mapping of (a and b) ER2594-LHI/HHI weldment, (c and d) ER309L-LHI/HHI weldment, respectively

5.3.3.2 *TENSILE TEST*

Tensile tests were conducted on sDSS 2507/X-70 DWJs with ER2594/ER309L filler under LHI and HHI conditions. It was noted that the sDSS 2507 and X-70 BM have ultimate tensile strength (UTS) of 1000 ± 5 MPa and 615 ± 2 MPa, respectively. Both BM satisfied ASTM A312/A790 and A1024/A1024M tensile requirements. The UTS of the ER2594-LHI and ER2594-HHI weldments were 600 ± 3 MPa and 610 ± 5 MPa, respectively. LHI and HHI weldment elongation percentages were 22% and 18%, respectively. The ER309L-LHI and HHI-ed samples' tensile strength and percentage elongation were measured to be 609.4 MPa and 25.3%, and 601.7 MPa and 30.8%, respectively. The tensile test clearly demonstrated that the specimen broke from failed at the weaker X70 BM side in both filler weldments, as illustrated in Figure 5.77(a). Table 5.29 and Figure 5.77(c) list and show all specimens tested under each condition's UTS, weld mismatch, YS, and % elongation. Since ductility was reduced due to the welding process's rapid cooling and heating, the specimens' percentage elongation was less than the base metal. The area reduction averaged over 50%, indicating that the tensile specimen underwent significant plastic deformation before fracture. As heat input increases, the UTS and YS of tensile samples reduce. This is consistent with observed values for hardness and cooling rate. Higher heat input and slower cooling both increase grain size in the WZ. Figure 5.77(b) shows all specimens' engineering stress-strain plots after tensile testing. Weld mismatch was calculated using WM's UTS ratio with BM. It can provide an appropriate justification for the failure location caused by the tensile load. To accept the results of tensile tests, ASME BPVC Section IX states: "If the fracture occurs in the BM outside the weld zone or HAZ, the testing shall be approved as meeting requirements, providing the strength is not more than 5% below the minimum required tensile strength of BM. Consequently, this criterion allowed specimens to proceed to the tensile test".

Fractography analysis was done on broken tensile specimens to determine their failure mode. Using FESEM at high magnifications, Figure 5.78 shows the fractography of the BM and both filler weldments. Neck formation was visible in the top view of both base metals' broken tensile specimens. The cup-cone fracture is a unique ductile fracture characteristic in uniaxial tension with necking caused by local plastic deformation at the ultimate stress point. Both base metals' fractured surfaces revealed large-density fine dimples, cleavage facets, microvoids, and tear ridges in the SE image (Figure 5.78(a and b)). Analysis of both ER309L-LHI/HHI

weldment's fractured specimens by SEM revealed a predominantly ductile failure mode, as demonstrated by the presence of microvoids, dimples, ductile tear ridges, and with cleavage facets in the fractography (Figure 5.78(c and d)). Both weldments' elongation results from interdendritic ferrites, favoring the ductile tearing mode. Many tearing ridges show early weld tearing has caused failure. However, ductile tearing would have predominated the failure mechanism as the tensile load increased. Both ER2594-LHI/HHI weldments have fractured surfaces with dimples, microvoids, cleavage facets, dimple facets, and tear ridges. A cup and cone configuration predominates in the fractured tensile samples of both weldments. Both weldments' cracked surfaces are featured in transgranular ductile dimples. Grain coarsening and the appearance of microvoids are caused by multipass welding's tendency to heat the weld zone. The weld joints become ductile due to the coalescence of these microvoids, which also causes ductile tearing (Figure 5.78(e and f)). Differences in cooling rates between weldments produced by differing heat input conditions lead to surface morphological variations, such as the size of dimples, cracks, etc.

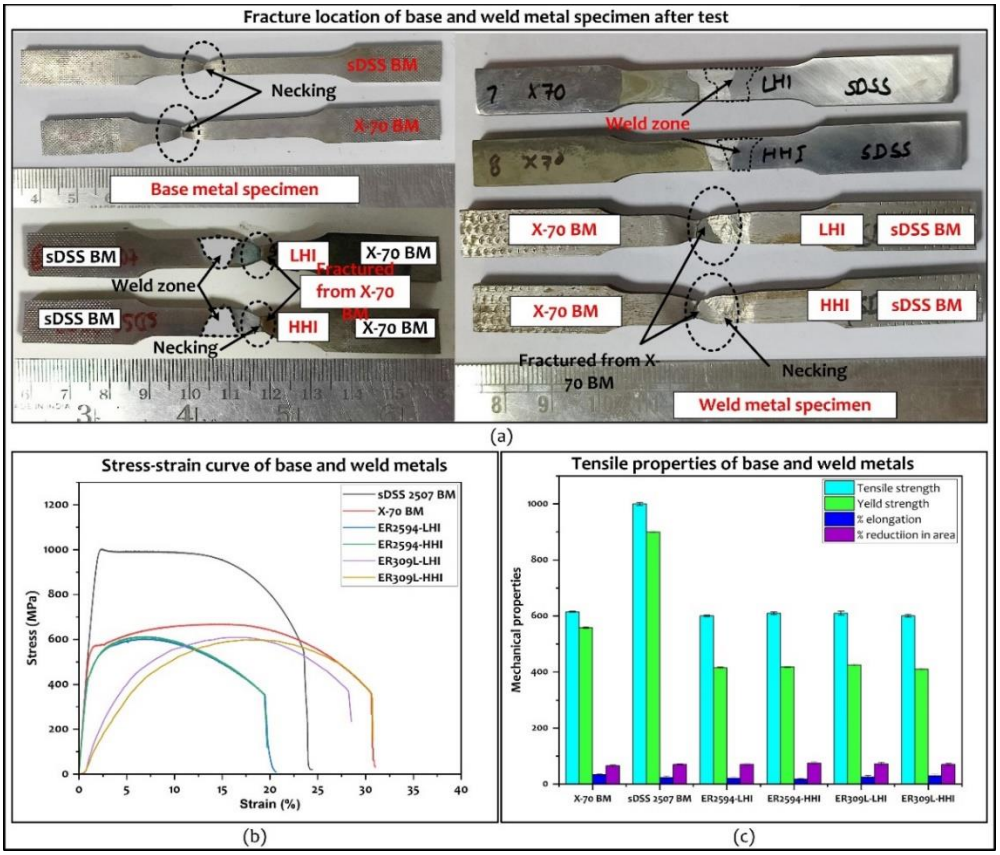

Figure 5.77 : (a) Fractured location of base and weld metals specimens after test, (b) Stress-strain curve of base and weld metal, (c) Tensile properties of base and weld metal

Table 5.29 : Detailed tensile properties of BM and weld metals with weld mismatch

Specimens	Tensile properties			*Weld mismatch with X-70 BM*	*Weld mismatch with sDSS 2507 BM*	*Failure location*
	UTS (MPa)	strain (%)	YS (0.2% offset) (MPa)			
X-70 BM	617.2	35.6	556.4	--------	--------	--------
sDSS 2507 BM	996.3	26.5	896.2	--------	--------	--------
ER2594-LHI	602.4	21.2	413.3	0.976	0.605	X-70 BM side
ER2594-HHI	612.5	18.4	420.5	0.992	0.615	X-70 BM side
ER309L-LHI	609.4	25.3	425.3	0.98	0.61	X-70 BM side
ER309L-HHI	601.7	30.8	410.5	0.97	0.60	X-70 BM side

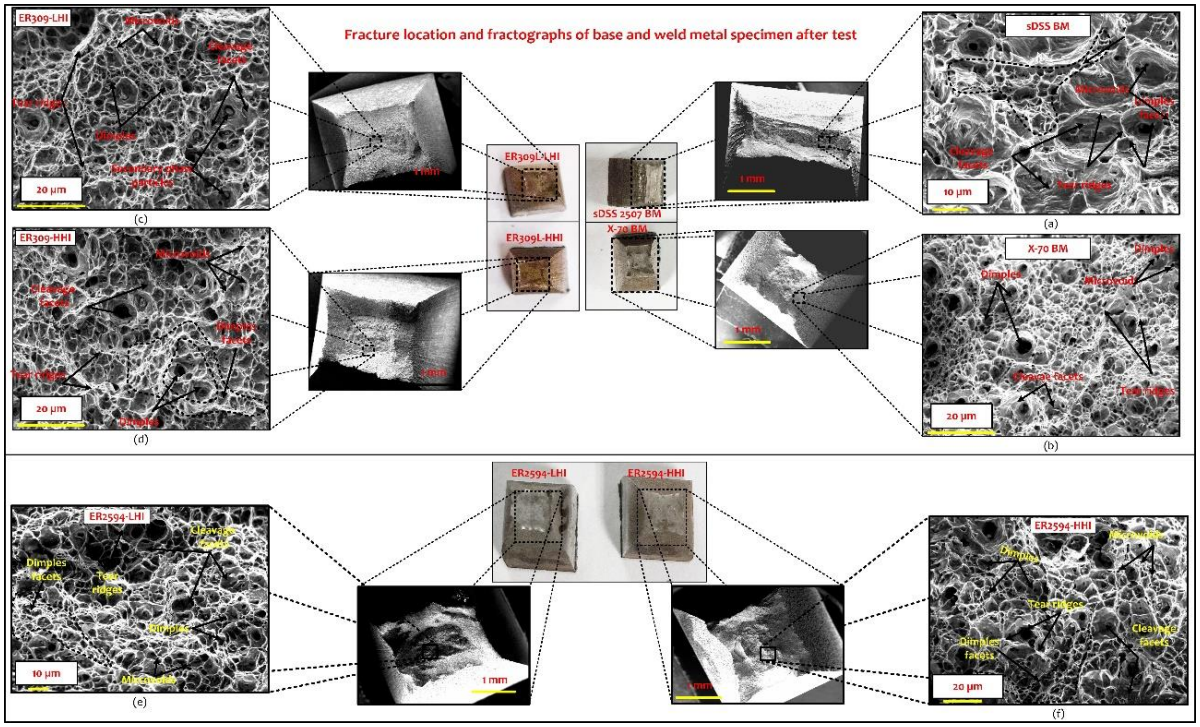

Figure 5.78 : Fracture tensile sample's fractograph for (a and b) sDSS 2507 BM and X-70 BM, (c and d) ER309LHI/HHI weldment, (e and f) ER2594-LHI/HHI weldment, respectively

5.3.3.3 *IMPACT TEST*

The Charpy V-notch test was carried out on weld specimens to measure their resistance to impact energy at room temperature, per the standard specification for both filler weldments. The specimen was made using WCEDM, and the V-notch has been fabricated on base metal and includes weld cap and root for both filler weldments (Figure 5.79(a)). Figure 5.79(b) shows the fracture mode and impact toughness value's schematic graph. Both filler metal weldments have experienced enough plastic deformation before fracture and ductile mode after the test, as shown in Figure 5.79(a and b). With respect to average impact toughness, ER2594-LHI weldments (200 ± 7 J, 210 ± 4 J) and ER2594-HHI weldments (210 ± 5 J, 220 ± 8 J) are inferior to the sDSS 2507 BM (320 ± 3 J), and the X-70 BM (300 ± 6 J). The notched specimen for both filler weldments shows that fracture at the V-notch zone absorbs less impact energy, indicating the quasi-mode of ductile fracture. Heat input affects microstructure evolution in the WZ, resulting in higher impact energy for ER2594-HHI weldments than ER2594-LHI. Improvements in weld toughness can be attributed to an increase in cooling rate due to heat input variation. The impact toughness result for the cap and root sections of the ER309L-LHI weldment was 195 ± 5 J and 185 ± 2 J, respectively, compared to 180 ± 4 J and 200 ± 3 J for the ER309L-HHI weldment. Both weldments' ferrite skeletal microstructure reduces solidification and liquation cracking and increases impact strength. The microstructure phases also resemble tempering-related changes in such ways because multipass welding involves a heating and cooling cycle. ER309L-HHI appears to have greater impact toughness than ER309L-LHI due to the impact of heat input on microstructure evolution within the weld zone. Increased cooling rate brought on by heat input variations is responsible for weld toughness improvements. For marine application requirements and to lower the chance of weld metal's brittle fracture, the EN ISO 13628-5:2009 and DNVGL-OS-B101 require for 47 J and 27 J, respectively.

Fractured samples were examined with an SEM to characterize the failure mechanism. Figure 5.79(c-f) shows images of the weld root and cap of the ER309L-LHI's and HHI's fracture surfaces. The all-weld metal fractured surface exhibits dimples, microvoids, and ductile tearing ridges with the least amount of cleavage facets, indicating ductile failure. Uniformly distributed dimples of various sizes were observed in all the fractographs. Secondary phase particles and shear dimples are visible at higher magnification. Charpy test results corroborated the fracture surface appearance. Furthermore, the fractured specimens of the ER309L-HHI weldments

showed dimples oriented in the failure direction, corroborating the plastic deformation (Figure 5.79(e-f)). The fractured surface image of the sDSS 2507/X-70 weldment is represented in Figure 5.80(a and b). Plastic deformation before fracture indicated ductile failure in both base metals. The sDSS 2507 and X-70 BM exhibited ductile fracture with microvoids, cleavage facets, and parabolic dimples at the fractured region (Figure 5.80(a and b)). The ER2594 weldment fractured surface shows a shear plane with dimple facets, dimples, tear ridges, and cracked boundaries, indicating ductile failure (Figure 5.80(c-f)). In addition, a fractography analysis of broken ER2594-HHI weldments confirmed the plastic deformation depicted in Figure 5.80(e and f) by observing dimples that pointed toward the direction of failure. The dimples were discovered to be uniformly dispersed and of varied sizes. The fracture surface develops dimples during ductile fracture. The stretched-out dimples strengthen the toughness of the ER2594-HHI weldment. A material's decreased toughness can't be fully explained by looking only at its fracture surface. Additional factors, such as residual stress and thermal stresses from welding and phase transformations, also impact its mechanical properties.

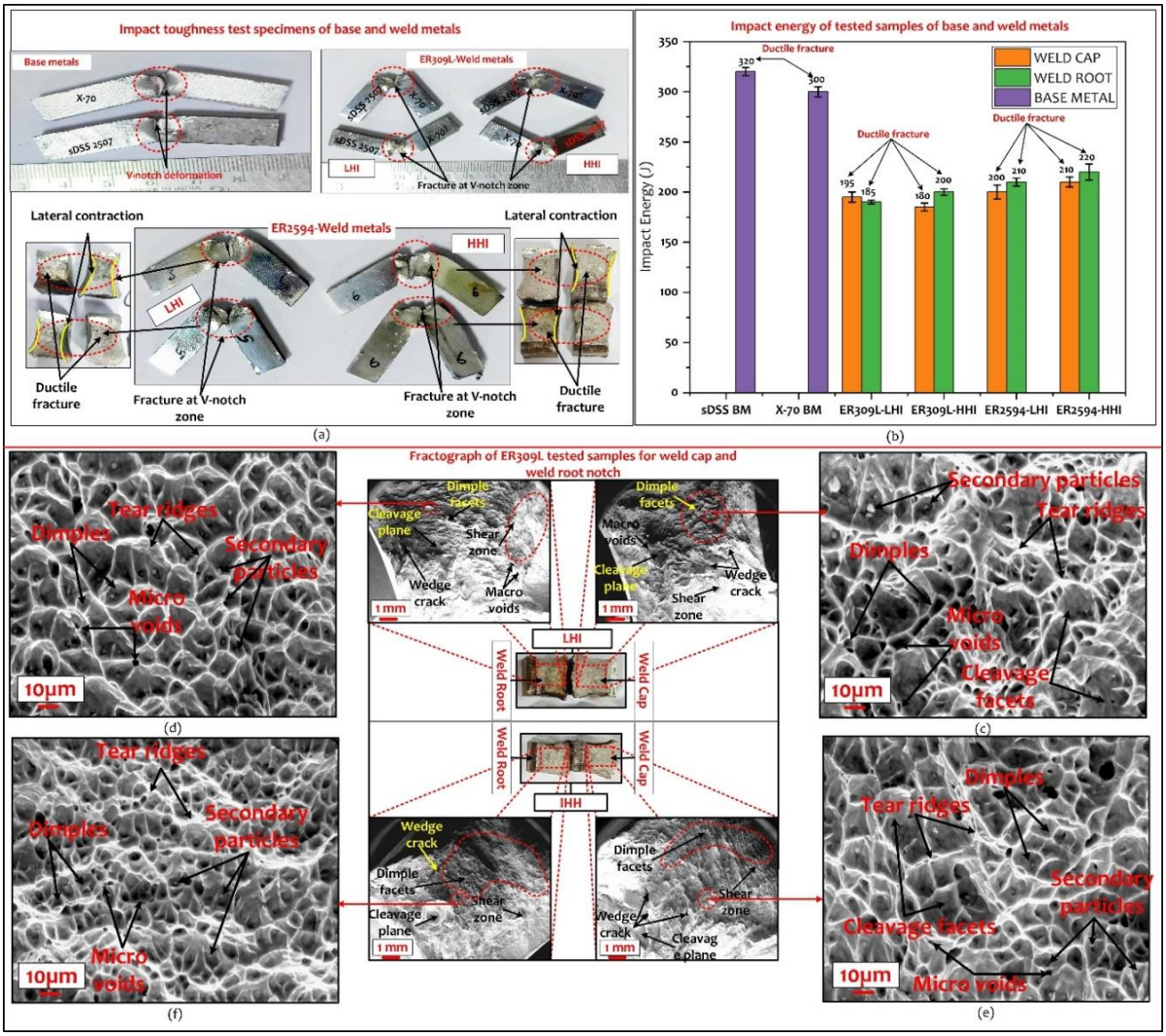

Figure 5.79 : (a) Impact toughness test specimens of base and both weld metals, (b) Impact test result and failure modes of base and weld metals, fractograph for weld cap and root for (c and d) ER309L-LHI, (e and f) ER309L-HHI, respectively

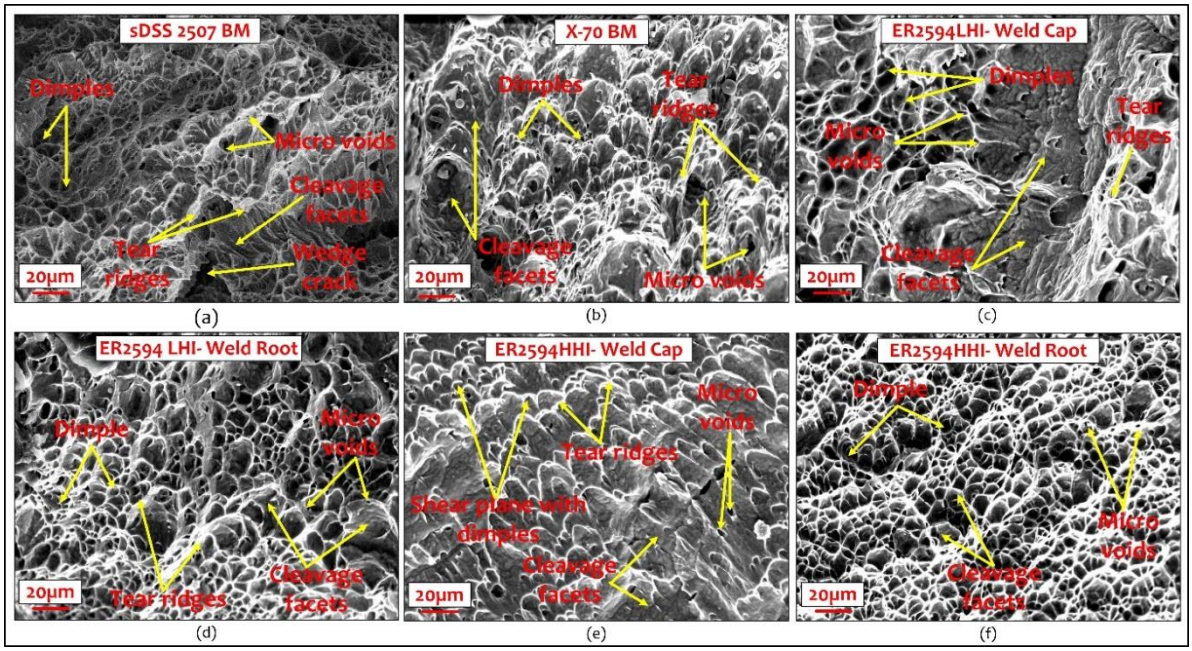

Figure 5.80 : SEM fractography of ER2594 fractured sample of (a and b) sDSS and X-70 BM, (c and d) LHI weld cap and root, and (e and f) HHI weld cap and root, respectively

5.3.4 RESIDUAL STRESS MEASUREMENT

Subsurface residual stress in the weld zone has been investigated using the DHD method, and the residual stresses in the longitudinal and transverse directions for both fillers have been calculated (Figure 5.81). The results showed that the residual stress was predominantly tensile in nature and distributed throughout the thickness of the ER2594 filler. The highest longitudinal tensile stress was recorded at 241 MPa, with the highest level at the surface of the weld and the lowest at the root. The transverse residual stress was predominantly tensile, with a maximum value of 156 MPa at a depth of 5 mm. Tensile residual stresses in ER2594 weldments occur from volume changes during phase transformation, solidification contraction, and constrained cooling, while compressive stresses result from constrained expansion during solidification and localized volume expansion during phase transformation. In the ER309L filler, the maximum tensile residual stress measured 175 MPa near the weld cap, while the highest compressive residual stress measured 46 MPa close to the weld root. However, thermal expansion and contraction increase as heat input increases, causing increased stress in the weld zone and putting the weld cap in tension and the weld root in compression. The transverse residual stresses were mainly in tension throughout the weld zone, attaining 139 MPa at 4 mm. The residual stress is higher in the longitudinal than the transverse direction due to the intricate thermal cycle experienced by the weld metal during welding. The longitudinal direction shows slower heat dissipation, resulting in a reduced cooling rate. This slower cooling allows for more effective relaxation of thermal stresses, leading to elevated residual stresses in the longitudinal direction compared to the transverse direction, where cooling is comparatively quicker. Although the DHD approach may not provide location-specific data, it does offer realistic and consistent measurements of welding-induced residual stress. Different weld zones may contract at different rates throughout the cooling process due to thermal gradients, dissimilar materials, and phase transitions in dissimilar weld joints. This may lead to internal stresses and pose significant structural issues (Skouras et al., 2013)

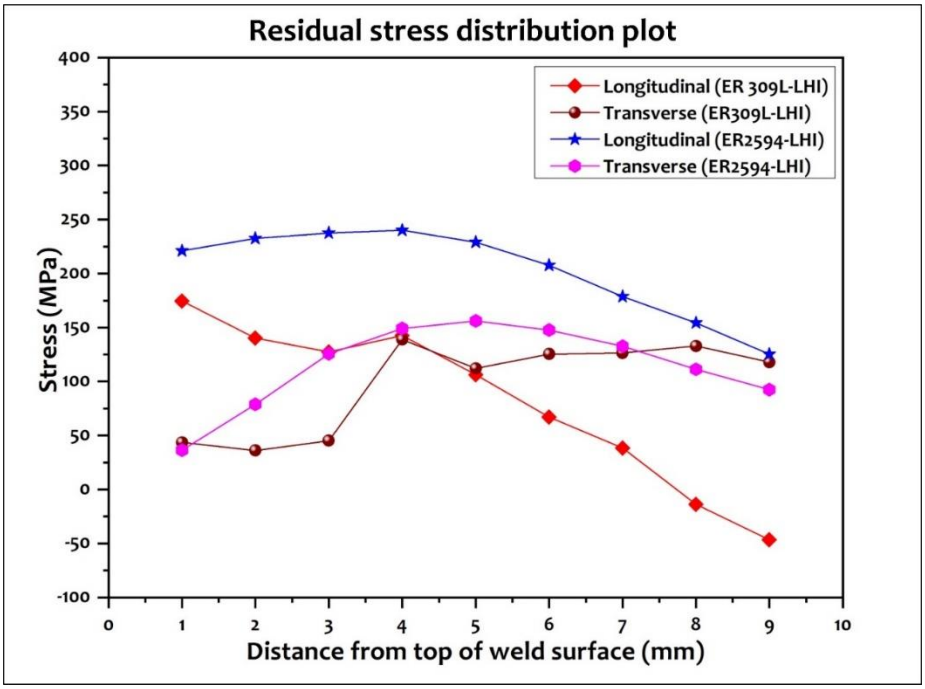

Figure 5.81 : Residual stress distribution plot for ER2594-LHI and ER309L-LHI weld zone

5.3.5 TRIBOLOGICAL INVESTIGATIONS

This study benefits the comprehension of slurry erosion characterization and wear mechanisms, offering valuable insights for material design, filler metal selection, and optimal welding parameters in the context of hydrocarbon drilling riser applications.

5.3.5.1 SLURRY EROSION CHARACTERIZATION

The correlation between slurry concentrations and cumulative weight loss for each specimen is shown in Figures 5.82(a and b), indicating a substantial increase in weight loss with increased slurry concentrations for all specimens. Initially, all specimens displayed a higher rate of weight loss, which gradually decreased over the test duration. The specimens underwent work hardening due to continuous particle impingement or the gradual disintegration of sand particles during the test, which slowed down the weight loss over time (Lindgren & Perolainen, 2014). The erosive wear characterization results obtained from a slurry pot at different concentrations align with the observed hardness trend in both the weld zones and base metal. It is apparent that with increased slurry concentration, all specimens experienced a notable rise in weight loss. Microhardness increased after erosion testing for both base metals, indicating strain hardening. In 10 wt.% slurry concentration tests, X-70 and sDSS 2507 BMs lost 0.38 and 0.30 g, respectively (Figure 5.82(a)). The combination of work hardening, variations in hardness, and microstructure attributes contributed to a more pronounced reduction in weight loss for X-70 BM compared to sDSS 2507 BM. An increase in slurry concentration resulted in a 17% increase in weight loss for sDSS 2507 BM and a 36% increase for X-70 BM. The higher work hardening capability of sDSS 2507 BM, attributed to a more significant number of dislocation movement planes, contributed to this difference. The crystal lattice of FCC structures provides more planes for dislocations to move through, facilitating easier deformation and increased work hardening (Hwang et al., 2011). This reduces particle aggregation, clustering, and abrasive particle impacts, thereby minimizing material removal and weight reduction. The graph shows that erosive wear is most significant in the ER2594-LHI (0.20 g) and ER309L-LHI (0.31 g) weldments. In contrast, the wear on the corresponding ER2594-HHI (0.16 g) and ER309L-HHI (0.25 g) weldments remains within a similar range. Higher slurry concentrations cause significant weight loss in slurry erosion experiments under 30 wt.% due to sand particle density, particle-to-surface contact, particle interactions, and fluid effects. The weight loss is notably higher in X-70 BM (0.52 g) compared to sDSS 2507 BM (0.35 g) (Figure 5.82(b)). ER309L-LHI (0.42 g) and ER2594-LHI (0.25 g) weldments exhibited a more substantial volume loss than their HHI

weldments. ER309L-LHI lost 55% more weight than ER2594-LHI in response to increased slurry concentration, while ER309L-HHI lost 56% more weight than ER2594-HHI. Therefore, the hardness value is a critical factor in determining a specimen's resistance to erosion wear. Notably, ER309L-LHI and HHI specimens had a more substantial impact than sDSS 2507 BM. The increase in hardness can be attributed to the strain hardening of the target surface caused by repeated impacts from solid and liquid particles. Several factors, including chemical composition, testing parameters, material characteristics, and surface features, contribute to the observed hardness after the erosion test. ER309L-LHI and ER2594-LHI specimens experienced less weight loss compared to X-70 BM. The slurry concentration influenced erosion, decreasing collision efficiency as it became more concentrated despite the increasing cumulative weight loss.

Figure 5.82(c) shows the average slurry-erosion rates of all specimens at different concentrations. Erosive wear increases with slurry concentration because more particles collide. Accordingly, the erosion rate increases with increasing slurry concentration (Desale et al., 2008). Erosion wear increases more slowly as slurry concentration rises despite the increase in the number of sand particles contacting the solid-liquid mixture. The correlation between slurry concentration, weight loss, and erosion rate is complex. This complexity is influenced by elements like material response, impact energy, and particle aggregation. Abrasive particle agglomeration at higher slurry concentrations leads to greater masses, deformities, and fractures, resulting in increased weight loss. However, larger masses disintegrate more slowly due to less frequent collisions. Higher slurry concentrations may decrease the energy imparted to each particle, potentially lowering the erosion rate. However, increased particle collisions can also lead to higher weight loss. Wear and degradation are influenced by slurry concentration, with microstructure, mechanical properties, and composition playing key roles, contributing to an increase in weight loss. Rotating particles generate sharp cutting edges, enhance contact points and fragment particles, induce chemical reactions, accelerate fatigue and crack propagation, alter slurry velocity, and modify surface texture (Prasad et al., 2004). Despite experiencing higher weight loss, the material may possess a more robust surface or a mechanism that limits erosion. The current study reveals a substantial increase in erosion rate with rising slurry concentration (Figure 5.82(c)). This aligns with a corresponding increase in weight loss across all specimens, suggesting an augmented impact of sand particles on the specimens with higher slurry concentration. Several researchers observed a comparable phenomenon (Dasgupta et al., 1998; Lindgren & Perolainen, 2014; Nguyen et al., 2014). The results indicate an inverse relationship between slurry erosion resistance and X70 BM hardness. This is attributed to the lower hardness and microstructural characteristics of X-70 base metal, resulting in higher average slurry erosion rates and cumulative weight loss. Nevertheless, the ER309L-LHI and ER2594-LHI specimens exhibited less severe slurry erosion rates compared to X-70 BM, indicating enhanced resistance to slurry erosion. Slurry concentration enhances sDSS 2507 and X-70 BM erosion by 1.8 and 1.4 times. ER2594-LHI and ER309L-LHI specimens were more resistant to slurry erosion than both BM. The erosion rate of ER2594-HHI and ER309L-HHI increases 1.14 and 1.32 times with slurry concentration. The erosion rate trend of HHI weldments for both filler metals is similar to that of LHI weldments.

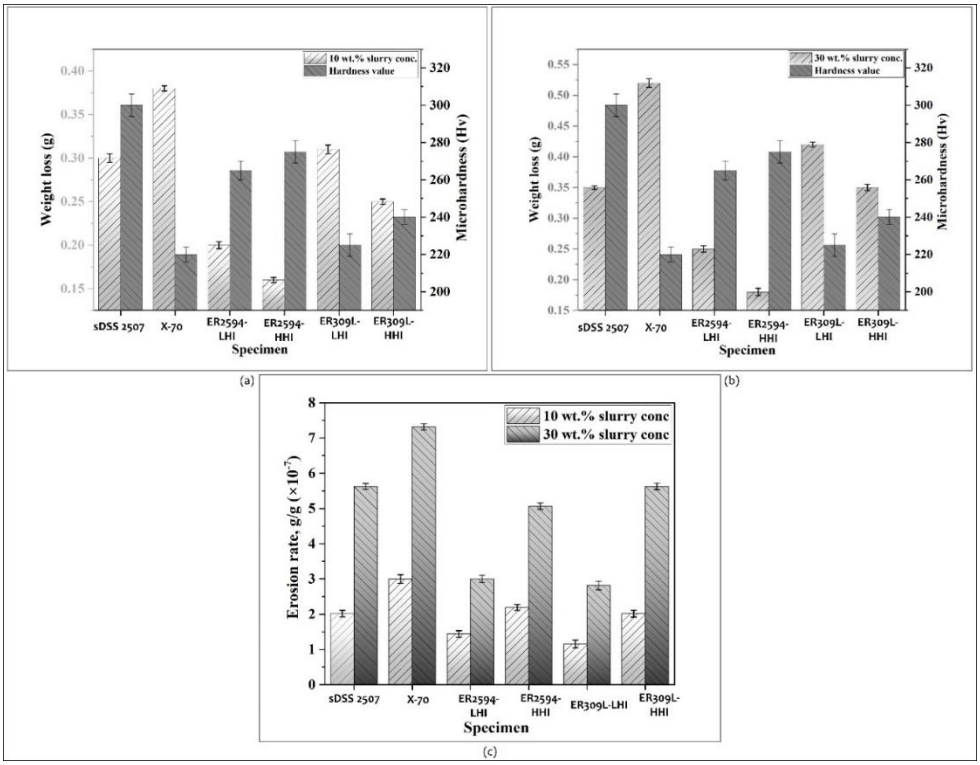

Figure 5.82 : Microhardness and weight loss for the tested specimen (a) 10 wt.% slurry concentration, (b) 30 wt.% slurry concentration, and (c) Variation in erosion rate with varying slurry concentrations for all specimens

5.3.5.2 *SLURRY EROSION MECHANISM*

SEM analysis of all eroded samples was performed to demonstrate material removal mechanisms. Figures 5.83 and 5.84 show the mechanisms accountable for the slurry erosion of all specimens. Figure 5.83(a) displays the schematic representation of the mechanisms responsible for the slurry erosion of both base and weld metals. Sand particles impacting the surfaces of the base metal samples induced the formation of craters through fatigue mechanisms, facilitated by the deep penetration of erodent particles and repeated plastic deformation. Repeated collisions from entering erodent particles removed the penetrated particles from the material surface, leading to the formation of craters and lateral lips (Figures 5.83(b-e)). Subsequently, incoming particles erode these lateral lips. Furthermore, the constant impact of the slurry on the material's surface results in the formation of a work-hardened layer. Numerous studies have reported weight loss in connection with crater formation (Alam & Farhat, 2018; Shivamurthy et al., 2009). The SEM micrographs of the eroded surfaces of ER2594-LHI samples are presented in Figures 5.84(a through d). The micrographs depict deep micro-cutting, microploughing, and plastic deformation at different locations on the sample surface under both 10 and 30 wt.% slurry concentrations (Figures 5.84(a and b)). Additionally, the formation of a bright, hardened, deformed layer is evident (Figure 5.84(a)). The micrograph also shows sand particles embedment near the ploughing path under 30 wt.% slurry concentration (Figures 5.84(c and d)). ER2594-HHI samples had deeper pit-like indentations because sand particles hit the surface at a normal angle. The zone with significant surface deformation, characterized by deep micro-cutting and plastic deformation under 30 wt.% slurry concentration, along with changes in hardness and microstructure evolution, may contribute to the observed variations in the wear rate on the ER2594 filler's eroded surface. The lower hardness observed in HHI samples could be a contributing factor to the occurrence of deep micro ploughing caused by sand particles (Figures 5.84(e-g)). ER309L-LHI samples also exhibit comparable material removal mechanisms, such as deep micro-cutting, lateral and frontal lips formation, and ridge formation, at 10 and 30 wt.% slurry concentrations (Figures 5.84(h and i)). At 10 wt.% slurry concentrations, the SEM images of ER309L-HHI samples show that irregular-shaped sand particles induce deep micro-cutting, deep micro-ploughing, and the formation of narrow craters (Figure 5.84(j)). At 30 wt.% slurry concentrations, the SEM images of ER309L-

HHI samples reveal that the low hardness of HHI samples causes increased surface material deformation during sand particle impact. This results in deep micro-ploughing, frontal and lateral lip development, sand particle embedding, and ridge formation (Figures 5.84(k and l)). Similar features are observed in ER309L-LHI samples, with increased impact energy of sand particles leading to deeper craters and more pronounced deformation.

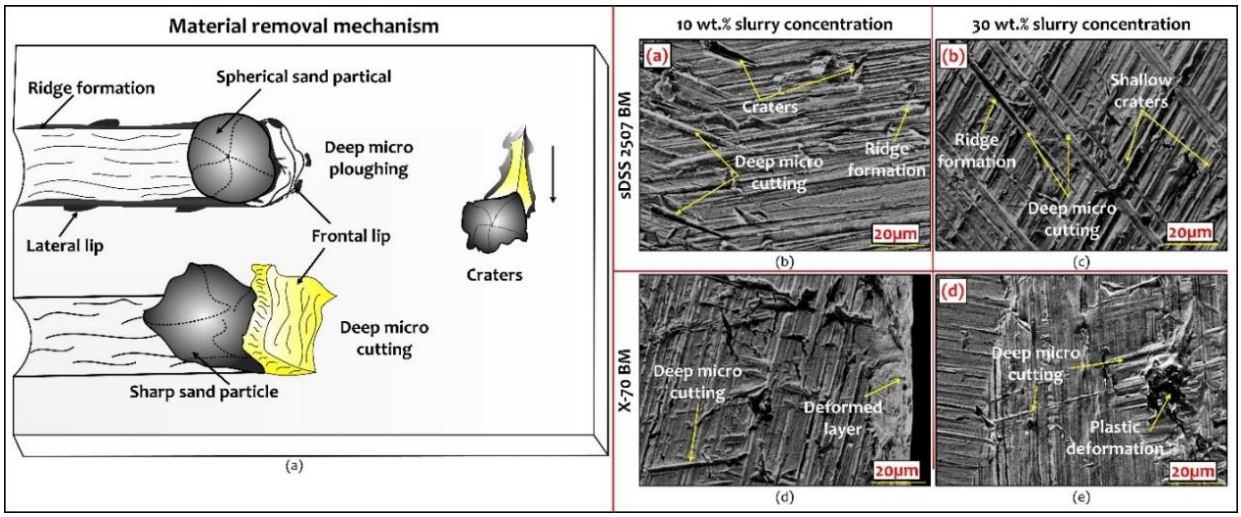

Figure 5.83 : (a) Material removal mechanism schematic for all specimens, SEM image of the eroded surface after erosion tests of (b and c) sDSS 2507 BM and (d and e) X-70 BM at 10 and 30 wt.% slurry concentration, respectively

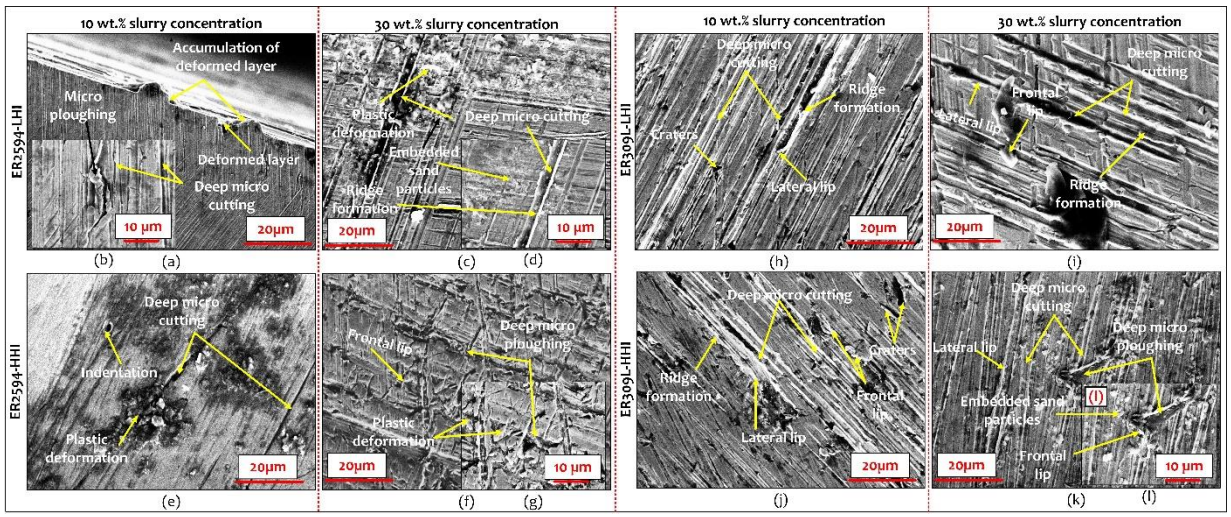

Figure 5.84 : SEM image of the eroded surface after erosion tests of ER2594-LHI (a-d) and ER2594-HHI (e-g) and ER309L-LHI (h and i) and ER309L-HHI (j-l) at 10 and 30 wt.% slurry concentration

5.3.6 CORROSION INVESTIGATIONS

This study delves into the corrosion behavior and compares corrosion mechanisms in dry/wet cycling and immersion conditions, aiming to maintain the structural integrity of the sDSS 2507/IN-625 DWJ. The presented outcomes offer valuable insights for the offshore industry, particularly for structures operating in severe corrosive conditions.

5.3.6.1 COMPLETE IMMERSION TEST

After 60 days of exposure to a 3.5 wt.% NaCl solution, Figure 5.85 shows the average percentage weight changes and corrosion rates of base and weld metals. Figure 5.85(a and b) shows the average % weight change of complete and dry/wet cyclic corrosion specimens. As time progresses, X-70 BM undergoes a substantial weight reduction, while the average weight changes of sDSS 2507 and ER2594 filler weldments are noticeably lesser than ER309L filler

weldments. Figure 5.85(c and d) shows the corrosion rates from weight loss tests for all specimens in both corrosion tests. sDSS 2507 BM shows nearly no corrosion weight loss during the immersion corrosion process, indicating its strong resistance to corrosion in the harsh chlorine environment of the 3.5 wt.% NaCl solution. sDSS 2507 BM had the lowest weight loss and corrosion rate (0.003 g and 0.0015 mm/y for dry/wet cyclic immersion and 0.002 g and 0.002 mm/y for complete immersion). In contrast, X-70 BM lost significant weight and corroded faster (0.23 g and 0.59 mm/y for dry/wet cyclic and 0.11 g and 0.32 mm/y by complete immersion). ER2594 filler weldments had weight loss and corrosion rates similar to sDSS 2507 BM, but ER309L had much higher values. In comparison to ER309L-HHI (0.03 g and 0.33 mm/y, 0.04 g and 0.0037 mm/y), the weight loss and corrosion rate for ER309L-LHI were 0.04 g and 0.30 mm/y, and 0.03 g and 0.23 mm/y for dry/wet cyclic and complete immersion, respectively. In contrast, in ER2594-HHI (0.0004 g and 0.0055 mm/y, 0.0004 g and 0.0053 mm/y), these values in ER2594-LHI were 0.0003 g and 0.0047 mm/y, 0.00025 g and 0.0037 mm/y. These findings imply that weld heat input influences sensitivity in welded joints compared to the base metal, resulting in lower corrosion rates. Corrosion rates are significantly lower in ER2594 filler weldments than in ER309L filler weldments, and the corrosion rate order for sDSS 2507/X-70 DWJ is X70 BM > ER309L-HHI > ER309L-LHI > ER2594-HHI > ER2594-LHI > sDSS 2507 BM.

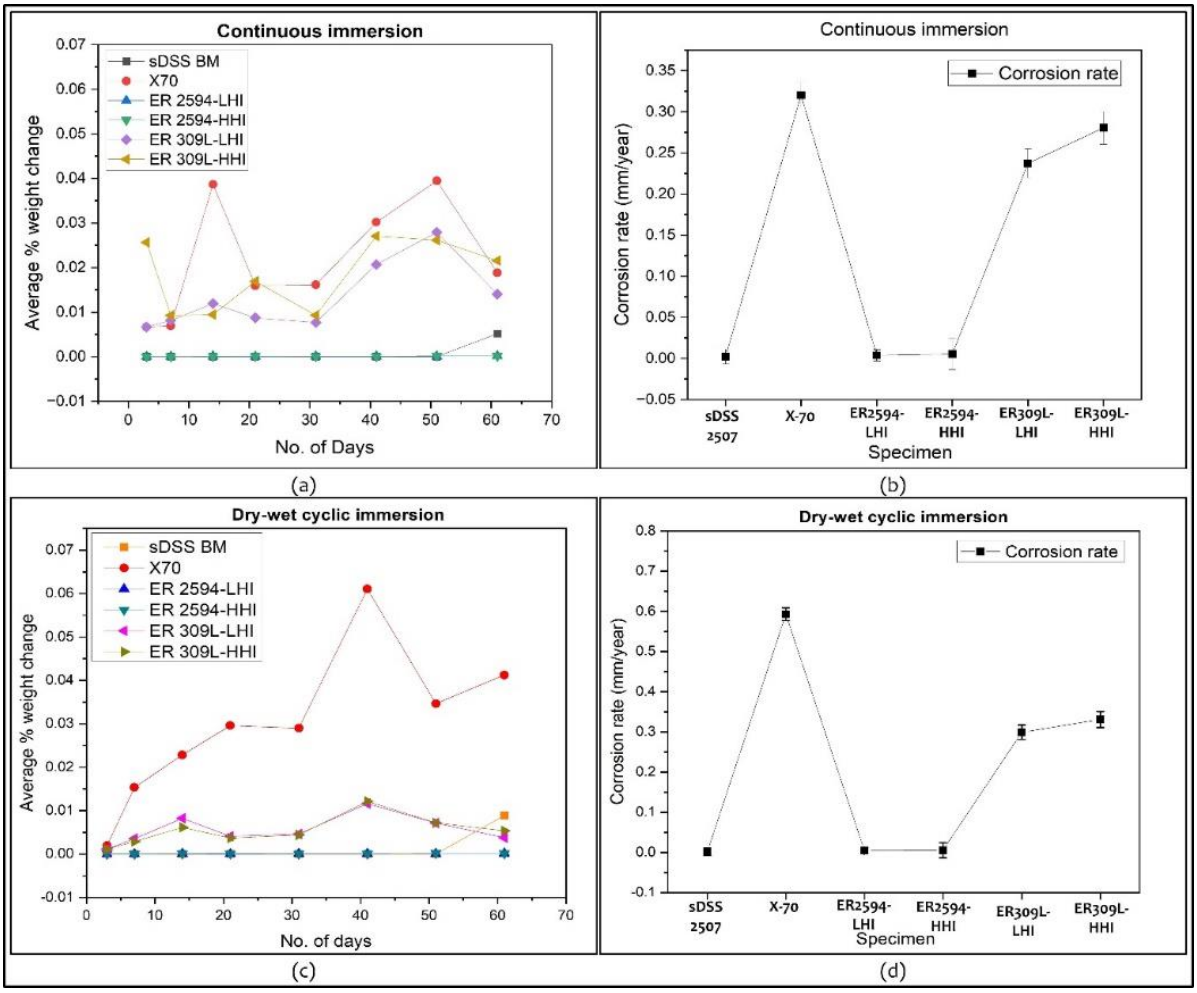

Figure 5.85 : Average % weight change and corrosion rate for all specimens in 3.5 wt.% NaCl solution for 60 days (a and b) complete immersion, (c and d) dry/wet cycle immersion

Figures 5.86 and 5.87 show base and weld metal samples visually investigated in 3.5 wt.% NaCl solutions for 60 days under complete immersion and dry/wet cycle conditions. Scale changes on the exposed parent metal surface were monitored by frequently assessing immersion corrosion tests at different intervals (3 days, 30 days, and 60 days). Macro-examination shows that scale production in X-70 BM increases over time, with thicker, dark

brown scales in both testing conditions than in other BM and WM specimens. In Figures 5.86(a) and 5.90(a), X-70 BM samples show thick rust layers in dry/wet cyclic corrosion after three days, with porous black outside and thin, dense tawny inside layers. However, sDSS 2507 BM has no rust layer in either testing condition. Complete immersion corrosion generates a thin coating of easily removed black solid on weld metal surfaces, with most corrosion products pale grey and orange-yellow. SEM observations were carried out on the sample surfaces after the rust layer was removed (Figures 5.86(b) and 5.90(b)). In dry/wet cycle and complete immersion tests, sDSS 2507 and X70 BM exhibited distinct corrosion morphologies. Figures 5.86(b-i) and 5.90(b-i) show few microscopic pits in sDSS 2507 BM. Balanced ferrite and austenite phases and an increased proportion of ferrite former elements like Cr, Mo, and Si enhance pitting resistance. Pitting at distinct phases offered sDSS 2507 BM superior corrosion resistance despite general corrosion. The presence of austenitic grains on adjacent sides prevented these pits from expanding. However, X-70 BM's surface topography, which had several peaks and valleys, mirrored the lunar surface (Figure 5.86(b-ii) and 5.87(b-ii)). The X-70 steel surface exhibited extensive coverage and many corrosion pits, but no localized corrosion was observed. The non-uniform corrosion pattern of X-70 BM suggests significant pitting corrosion, aligning well with weight loss analysis results.

The corroded surface of the weld metals employing ER2594 filler is shown in Figures 5.86(b-iii & iv) and 5.87(b-iii & iv). Significant intergranular corrosion, primarily in the ferrite phase, was seen in the microstructure of the ER2594 weldments at different heat inputs. The dissolution of WA/δ and PTA/δ interfaces was observed in the δ-ferrite matrix due to an unstable passive film and shear-assisted diffusional change (Figures 5.86(c-i)). This highlights the ferrite phase's preferential sensitivity to intergranular corrosion attacks in ER2594 weld metals, demonstrating its inferior nobility compared to austenite. The ferrite phase's Cr-depleted zones from secondary phases, especially Cr_2N, reduce pitting corrosion resistance. Lower PREN and clustered Cr_2N cause pits in ferrite or borders between ferrite and reformed austenite. The ferrite matrix exhibits the highest level of corrosion severity, followed by IGA and WA. The passive film is stabilized and continuous by fine-grained IGA with a greater PREN, which prevents pit propagation. Furthermore, in certain places, pitting affects the δ/γ interfacial regions. As shown in Figure 5.87(b-iii and iv), IGA precipitates in ferrite grains may prevent corrosion pit propagation. In both testing conditions, the corroded surface of the ER309L weldment shows intergranular corrosion (Figures 5.86(b-v & vi) and 5.87(b-v & vi). As seen in Figure 5.86(c-ii), ER309L weldments exhibit a large amount of intergranular corrosion compared to ER2594 weldments. Lace-like pit coverings occur more frequently in the skeletal ferrite nests than austenite in the weld matrix.

The corroded samples underwent elemental line mapping and EDS spectrum analysis. The EDS spectrum examination of corroded ER2594 filler weldments under both conditions shows that passivation has occurred because of the presence of oxygen, Fe, Cr, Ni, and Mo on the surface (Figure 5.86(c-i)). Higher Cr and Ni levels in ER2594 form a protective passivation layer, which improves corrosion resistance (Table 5.30). The line scanning of the ER309L weldment (Figure 5.86(c-iii)) shows a Cr-poor region near the pit site. The presence of a high oxygen concentration (27%) further supports this finding. X-70 BM exhibits the lowest pitting potential, whereas sDSS 2507 and ER2594 filler weldments have the highest pitting potential, followed by ER309L filler weldments. The increased pitting potential in ER2594 weldments is due to the higher Cr, Mo, and Ni content, resulting in a higher Cr_{eq}/Ni_{eq} ratio. Secondary phase precipitates reduce pitting potential in both weld joints compared to sDSS 2507 BM.

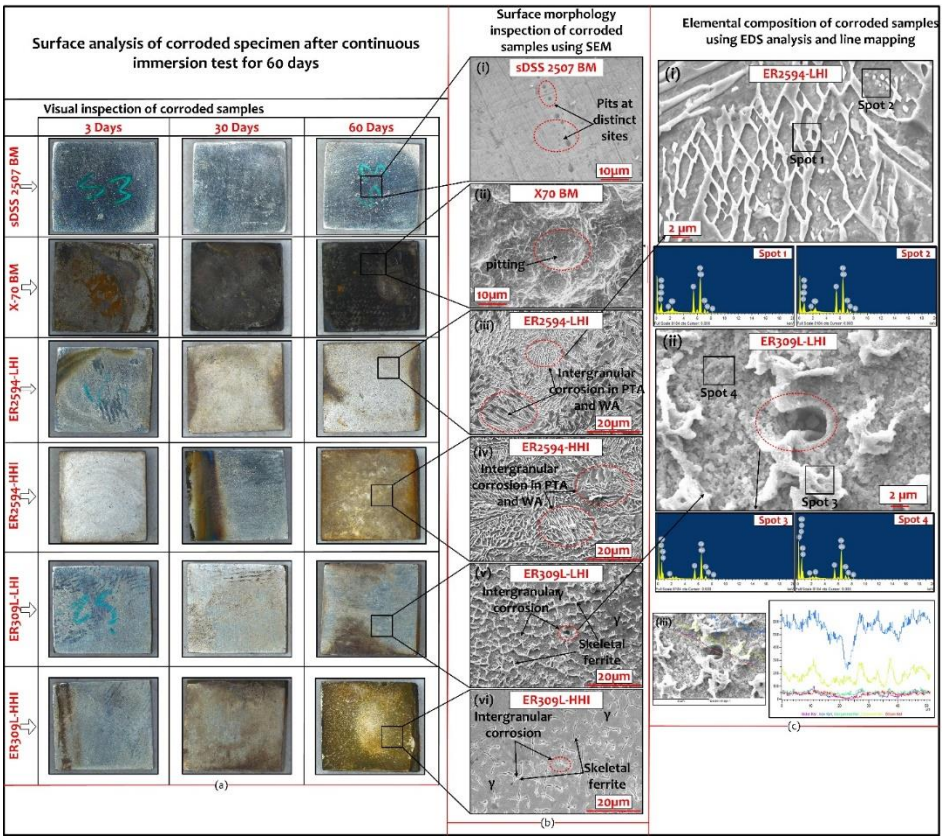

Figure 5.86 : (a) Visual inspection, (b) SEM surface morphology inspection, (c) EDS and line mapping analysis of corroded sample surfaces in complete immersion test for 60 days

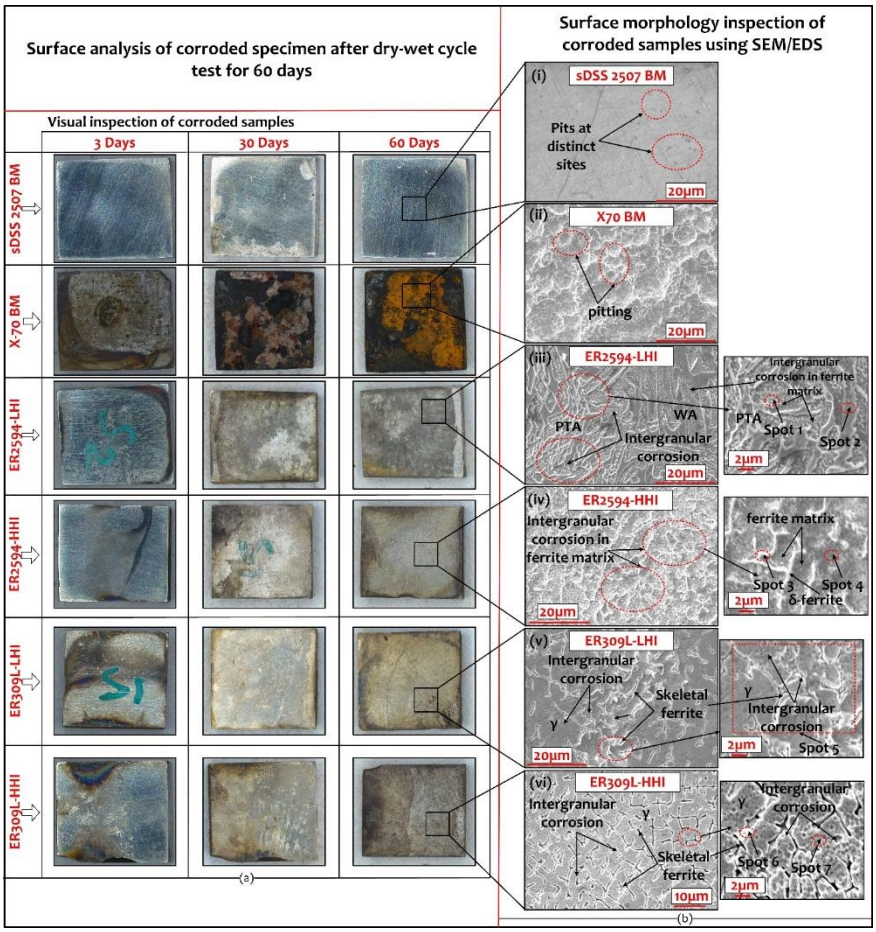

Figure 5.87 : (a) Visual inspection, (b) SEM surface morphology inspection of all corroded sample surfaces in dry/wet cyclic immersion test for 60 days

Table 5.30 : EDS spectra result of mentioned spots in Figures 5.86 and 5.87

	Complete immersion test				*Dry/wet cyclic immersion test*						
Elements (wt.%)	*1*	*2*	*3*	*4*	*1*	*2*	*3*	*4*	*5*	*6*	*7*
Cr	26.5	25.4	17.1	11.4	22.6	24.9	24.1	22.5	22.1	19.0	22.4
Ni	5.45	7.83	6.21	5.74	11.78	10.9	8.28	10.46	7.95	7.21	6.57
Fe	58.61	58.8	53.9	53.1	55.1	53.2	61.1	59.1	61.7	52.1	62.6
Mo	2.82	2.68	----	----	2.56	3.92	----	----	-----	----	----
Mn	1.02	1.19	1.08	1.02	1.30	----	1.45	1.67	1.52	1.08	1.35
Si	0.56	0.49	0.60	0.45	0.54	0.56	0.63	0.78	0.46	1.20	0.72
O	3.94	2.33	8.96	27.27	4.23	5.12	3.74	4.51	3.84	15.90	4.02
Cl	1.09	1.15	12.11	1.04	1.79	1.35	0.80	0.95	2.42	3.58	2.28

5.3.6.2 ELECTROCHEMICAL CORROSION TEST

The E_{corr} values in Figure 5.88(a) show that the corrosion potential of the X70 BM (-406.87 mV) is lower compared to that of the sDSS 2507 BM (-202.1 mV). Referring to Figure 5.88(b), ER2594-LHI and HHI had higher E_{corr} values (-131.34 mV and -193.54 mV) than ER309L-LHI and HHI (-269.62 mV and -196.29 mV). ER2594-LHI and HHI have superior E_{corr} values for the fusion line and weld interface on the sDSS 2507 BM side (-78.401 mV and -222.42 mV) than ER309-LHI and HHI (-308.76 mV and -242.85 mV) (Figure 5.88(c)). Compared with sDSS 2507 BM, the HAZ of ER2594-LHI exhibits superior corrosion resistance. For both filler metal weldments, Figure 5.88(d) shows low E_{corr} values for the weld interface on the X70 BM side (-351.02 mV and -359.90 mV for ER2594-LHI and HHI, and -384.77 mV and -380.10 mV for ER309-LHI and HHI, respectively). According to the results (Table 5.31), the corrosion resistance of the weld joints is lowest at the X70 BM side weld interface. Therefore, E_{corr} is sorted from highest to lowest, with higher values indicating less corrosion resistance: X-70 BM > X-70 BM side HAZ (for both filler weldments) > sDSS 2507 side HAZ (for ER309-LHI weldment) > ER309L-LHI (WZ) > sDSS 2507 BM > ER309L-HHI (WZ) > ER2594 (both weld zones) > sDSS 2507 BM side HAZ for ER2594-LHI. These results showed that X-70 BM and X-70 HAZ for both filler weldments are highly susceptible to both localized and uniform corrosion. Notably, the X70 to ER2594 weld joints resulted in improved corrosion resistance, as demonstrated by a shift in corrosion potential toward more superior values. Corrosion was more severe at the X-70 weld interface with ER309 than in those filled with ER2594 due to the more effective galvanic couples formation. Low-temperature carbon steel microstructures, such as annealed bainite and tempered martensite, are associated with reduced corrosion resistance and increased hardness (Vargas et al., 2021). However, corrosion rates are affected by microstructure transformations. Weld zones for both fillers had better corrosion resistance, especially for ER2594, in which chromium-rich films developed. ER2594 filler metal has more chromium than ER309L, which stabilizes the passive film in stainless steels.

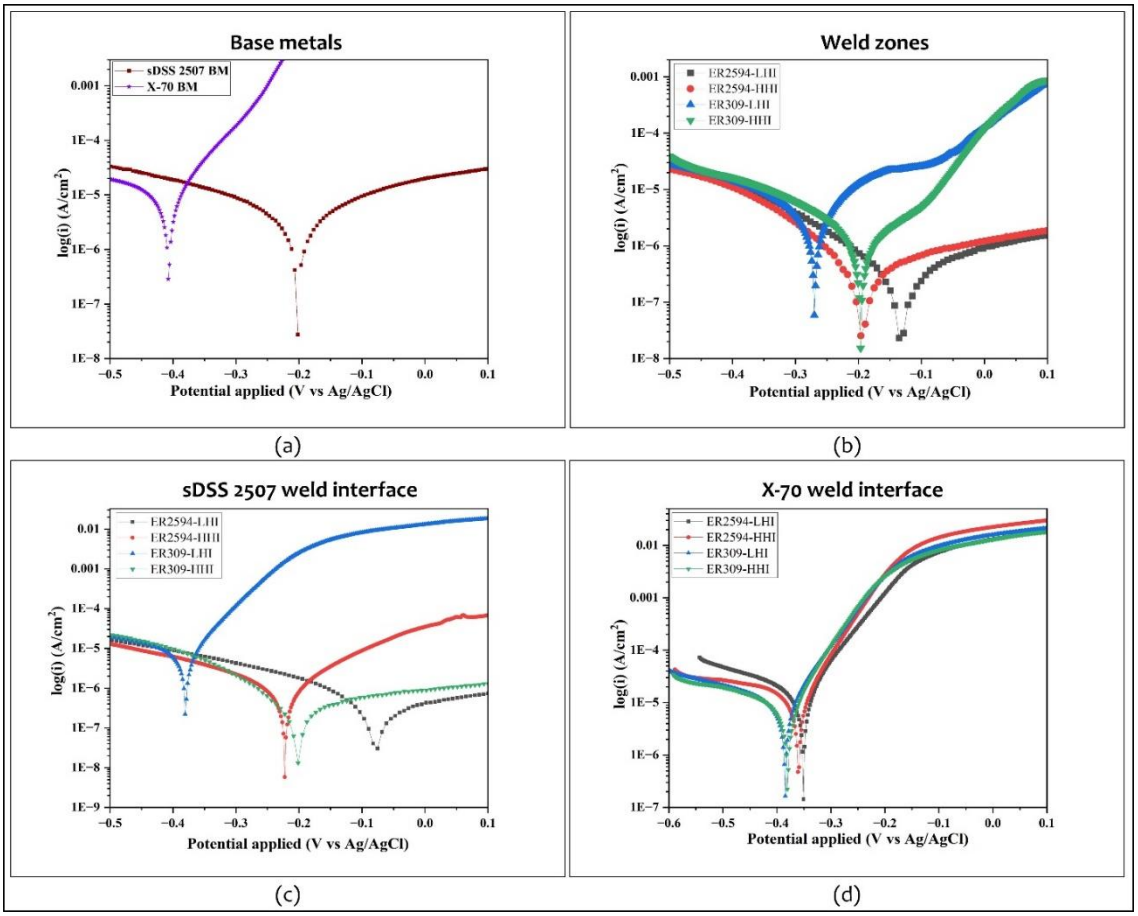

Figure 5.88 : Tafel plot of sDSS 2507/X-70 DWJ following electrochemical test in 3.5 wt.% NaCl

Table 5.31 : Tafel analysis results for sDSS 2507/X-70 DWJ in a 3.5 wt% NaCl solution

Specimen	E_{corr} *(mV)*	I_{Corr} *(μA)*	β_c *(-mV/dec)*	β_a *(mV/dec)*	*Corrosion rate (mm/year)*
X-70 BM	-406.87	5.32	48.5	80.6	0.12375
sDSS 2507 BM	-202.1	0.92	54.3	39.4	0.02245
Weld zones					
ER2594-LHI	-131.34	0.151	89.850	57.830	0.00350
ER2594-HHI	-193.54	0.182	128.09	87.123	0.00420
ER309L-LHI	-269.62	4.526	123.73	240.95	0.10519
ER309L-HHI	-196.29	3.437	492.38	233.15	0.07989
sDSS 2507 HAZ					
ER2594-LHI	-78.401	0.294	-724.60	262.4	0.00346
ER2594-HHI	-222.42	0.493	42.140	42.88	0.00683
ER309L-LHI	-308.76	1.865	120.65	71.65	0.09650
ER309L-HHI	-202.85	1.438	410.23	134.7	0.06010
X-70 HAZ					
ER2594-LHI	-351.02	1.738	119.51	-1.161	0.1160
ER2594-HHI	-359.90	3.778	58.360	142.3	0.23053
ER309L-LHI	-384.77	4.992	44.319	73.09	0.87810
ER309L-HHI	-380.10	6.9103	113.20	2.309	0.40391

Nyquist and Bode plots show the fitting outcomes of EIS for the BM and various regions of ER2594/ER309l filler weld joints at varying heat inputs in a 3.5 wt% NaCl solution (Figure 5.89). The capacitive arc radius represents the corrosion product's charge transfer resistance between the electrode and solution in a Nyquist diagram. A larger radius indicates increased resistance to corrosion (Huang et al., 2021). In Figure 5.89(a), X-70 BM and sDSS 2507 BM Nyquist plots show distinct patterns. X-70 BM's semicircular pattern indicates insufficient oxide layer-solution charge transfer. However, sDSS 2507 BM shows a straight pattern, which could indicate that ions are diffusing via the contact between the metal and the solution. sDSS 2507 BM has a greater capacitive impedance arc radius than X-70 BM, indicating better corrosion resistance. In Figure 5.89(b-d), Nyquist plots show EIS findings for weld zones and HAZs. The impedance data displays a depressed capacitive loop, indicating the presence of double-layer capacitance and charge transfer resistance in the weld zones and sDSS 2507 HAZ for both filler weldments. Higher corrosion resistance is indicated by the larger loops observed in HHI samples in the weld zone. The welded sample ER2594-HHI had higher intermediate and low-frequency impedance than ER309L-HHI (Figure 5.89(b)). All specimens in the sDSS 2507 HAZ Nyquist diagram have an apparent capacitive arc with varying arc diameters for both filler weldments, indicating the formation of a capacitive layer on the surface (Figure 5.89(c)). In contrast, a single semi-circle is apparent in the Nyquist plots of X-70 HAZ with both filler specimens, suggesting the presence of a single time constant at high frequencies (Fig. 5.89(d)). A small capacitive semicircular arc near the end of the high-frequency region suggests the production of corrosion products. A large semicircular arc in the low-frequency range indicates electric double-layer capacitance (Dou et al., 2023). Due to its larger capacitive loop, the ER2594-HHI sample shows better corrosion resistance in X-70 HAZ. Additionally, the welded sample ER309L-LHI exhibits a larger capacitive loop diameter than ER2594-LHI.

Figure 5.89(e-h) shows both BMs' and ER2594/ER309L filler weldments impedance and phase angle vs frequency Bode plot. Figure 5.89(e) shows the total impedance diagram of sDSS 2507 BM, which has a flat high-frequency area and a linear decline at low and medium frequencies. Low-frequency impedance modulus exceeds 10^5 Ω·cm^2, and phase angles rise with frequency, owing to oxide film contribution (Huang et al., 2021). In the Bode plot, the sDSS BM has a maximum phase angle of 60°, while the X-70 BM has 40° over a broad frequency range, indicating that charge transfer dominates in the low-frequency region. X-70 BM's single time constant and small phase angle suggest a stable corrosion mechanism. The Bode plot shows consistent amplitude and phase variations with frequency for both filler weld zone and sDSS 2507 HAZ samples. The phase approaches zero at high frequencies and is approximately constant (Figure 5.89(f)). The ER2594 and ER309L filler weld joints exhibit comparable trends for their respective weldments. The prevalence of charge transfer in the low-frequency domain is indicated by phase angles close to 60° at intermediate frequencies. Compared to sDSS 2507 BM at low frequencies, bode plots decline for all weld zone and HAZ samples (Figure 5.89(g-h)). In contrast to sDSS 2507 BM, ER2594 filler weld metals exhibit a Z module that is substantially lower than ER309L filler weld metals. A single peak in X-70 HAZ Bode plots (Figure 5.89(h)) demonstrates intermediate frequency charge transference control with one time constant. The reaction kinetics slow down as the maximum phase angle moves towards lower frequencies because the corrosion product layer on X-70 HAZ surfaces thickens. Nevertheless, the corrosion product layer does not provide enough protection, as indicated by the low impedance modulus.

Figure 5.89(i) presents and investigates an equivalent circuit for comprehensive EIS data evaluation using NOVA 2.1.5 software. The EIS parameters listed in Table 5.32 are obtained by fitting in the equivalent circuit; observed n values (0.6–0.99) suggest non-ideal capacitive characteristics resembling an oxide film. Fitting experimental data to the equivalent circuit verifies its validity and generates circuit elements (Harrington & Van Den Driessche, 2011). Figure 5.89(a) and Table 5.32 show that sDSS 2507 BM has superior corrosion resistance than X-70 BM due to its highest R_{ct} and R_f. ER2594-HHI has the maximum corrosion resistance in X-70 HAZ, while ER309L-LHI has the lowest R_{ct}. ER2594-HHI has a higher protective corrosion product layer than other weldments. The n parameter represents surface corrosion by

evaluating the corrosion behavior of the oxide film layer in the weld zone and sDSS 2507 HAZ. ER309L LHI and HHI weld metals have n values of 0.704 and 0.742, while ER2594 has 0.604 and 0.786, respectively. These findings show the ER2594-HHI weld zone's improved corrosion resistance over others. Similarly, ER2594 filler weldment (LHI (n=0.764), HHI (n=0.741)) outperforms ER309L (LHI (n=0.641), HHI (n=0.710)) for sDSS 2507 HAZ corrosion resistance. Both EIS test results and polarization data trends are comparable.

Table 5.32 : Equivalent circuit fitting of EIS data of all samples

Specimen	R_s ($\Omega.cm^2$)	CPE_1		R_f ($\Omega.cm^2$)	CPE_2		R_{ct} ($\Omega.cm^2$)	Q_f (μF)
		Q_1 ($\mu F.cm^{-2} S^{(n-1)}$)	n_1		Q_2 ($\mu F.cm^{-2} S^{(n-1)}$)	n_2		
X-70 BM	14.5	867	0.764	2.98	---	---	124	71.7
sDSS 2507 BM	9.82	18.3	0.862	65.4	11.20	0.902	482	----
Weld zones								
ER2594-LHI	14.2	191	0.604	70.7	---	---	---	3.98
ER2594-HHI	11.2	38.4	0.786	19.1	---	---	---	5.84
ER309L-LHI	13.3	100	0.704	43	---	---	---	4.65
ER309L-HHI	9.78	48.1	0.742	24.3	---	---	---	3.43
sDSS 2507 HAZ								
ER2594-LHI	12.9	44.3	0.764	60	---	---	---	2.59
ER2594-HHI	11.8	32.4	0.741	28.3	---	---	---	1.65
ER309L-LHI	14.6	44.9	0.641	622				0.864
ER309L-HHI	15.0	24.4	0.71	74.4	---	---	---	1.67
X-70 HAZ								
ER2594-LHI	14.2	560	0.702	3.12	---	---	41.5	8.03
ER2594-HHI	13.0	896	0.771	4.88	---	---	92.5	8.67
ER309L-LHI	14.8	680	0.618	4.54	---	---	33.4	5.21
ER309L-HHI	12.7	327	0.88	5.16	---	---	46.6	8.40

Note: R_s is solution resistance, R_f represents corrosion product film resistance, R_{ct} is charge transfer resistance, Q_f is capacitance, CPE_1 and CPE_2 constant phase elements, and n_1 and n_2 fitting accuracies for the corrosion product layer and steel surface.

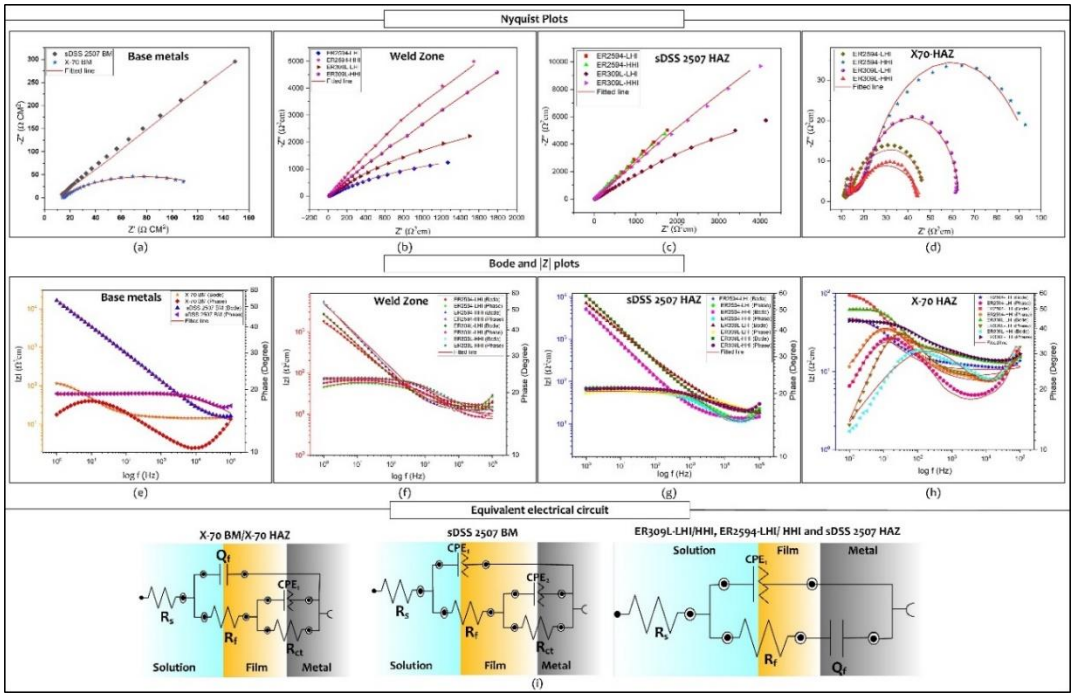

Figure 5.89 : EIS spectrum analysis of BM, WZ, and HAZ: Nyquist plot (a-d); Bode and |Z| plot (e-h), respectively, (i) Fitting EIS test results with an equivalent electrical circuit for all samples

Electrochemical studies show that current density and corrosion resistance in different regions of welded joints are unclear. A thorough analysis of the corrosion morphology of both filler weldments on the welded joint surface was conducted using SEM analysis. Figure 5.90 shows the microscopic morphologies of welded joints (BM, WZ, and weld interfaces) after corrosion scale removal. sDSS 2507 BM showed better thermodynamic stability than X-70 BM, as indicated by its higher E_{corr} values. The appropriate phase ratio and important alloying components such as Cr, Mo, Ni, and Si are responsible for the general local corrosion shown in sDSS 2507 BM, which exhibits pitting at distinct phases (Figure 5.90(e)). However, X-70 BM showed a non-uniform corrosion pattern with many corrosion pits and wide coverage, indicating high pitting corrosion (Figure 5.90(i)). The difference in E_{corr} values shows distinct corrosion behaviors of the two materials. Figures 5.90(a-d) illustrate the ER2594 and ER309L filler-corroded weld zone. According to the results, ferrite is less noble than austenite and is more vulnerable to intergranular corrosion attacks in ER2594 weldments (Figures 5.90(a-b)). In contrast, austenite matrix-skeletal ferrite contacts initiate intergranular corrosion in ER309L filler (Figures 5.90(c-d)). Intergranular corrosion is higher in ER309L weldments than in ER2594. Figures 5.94(e-h) show indications of small pits in the ferrite matrix and localized corrosion at the sDSS 2507 weld interface of both filler weldments. The weld interface width is too small to understand corrosion behavior in sDSS 2507. Meanwhile, the X-70 weld interface for both filler weldments demonstrated significant localized corrosion, resulting in large semicircular pits with shallow morphology, potentially affecting corrosion resistance (Figures 5.90(i-l)).

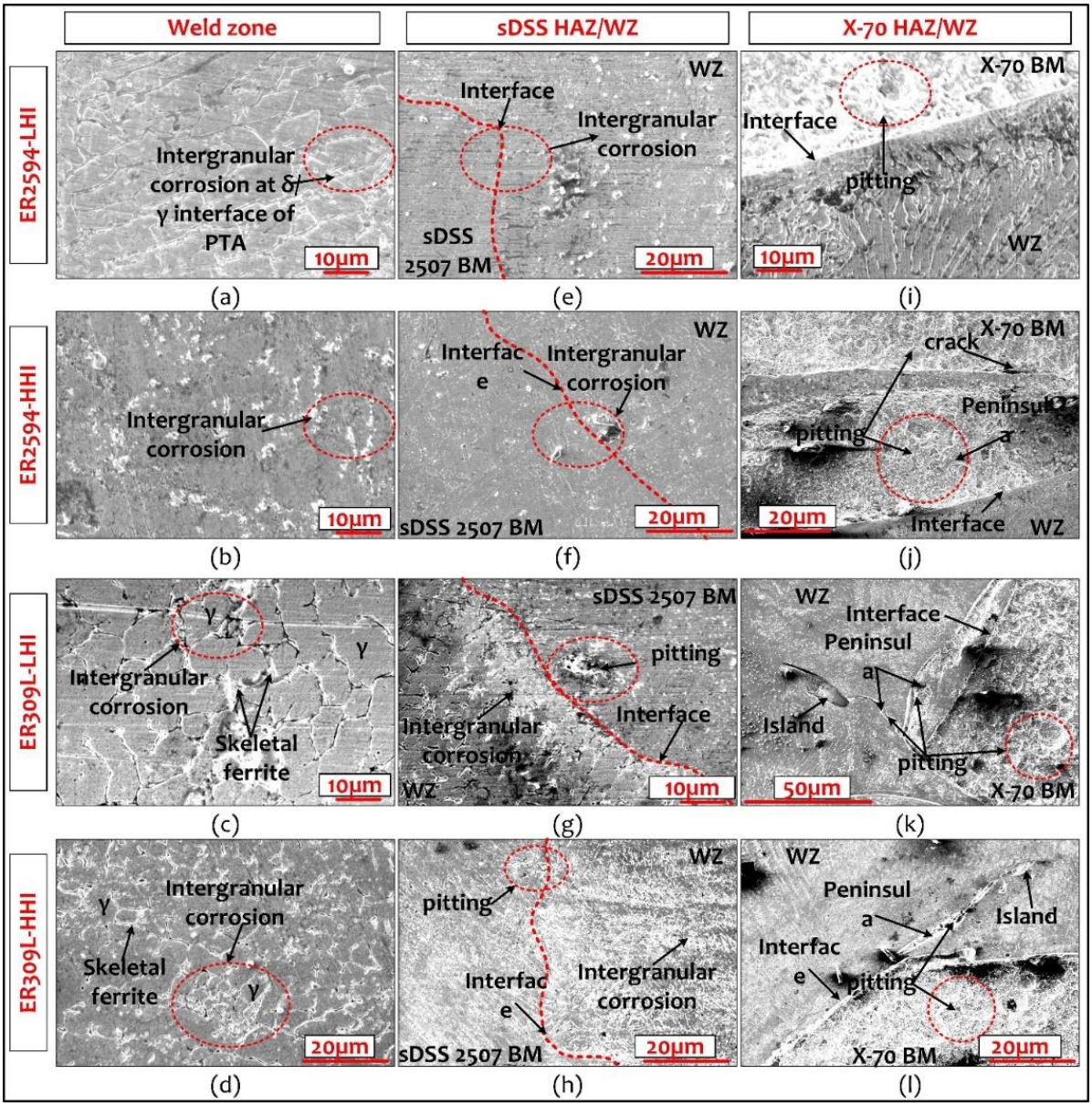

Figure 5.90 : Typical corrosion surface morphology after electrochemical studies (a-d) weld zone, (e-h) sDSS 2507/WZ, (i-l) X-70/WZ

5.3.6.3 *CORROSION PRODUCT ANALYSIS*

Oxygen absorption is the corrosion mechanism under conditions of complete immersion. Initial corrosion occurs in two phases due to surface irregularities; electrochemical corrosion continues even after a thin rust layer has formed in the second stage (Gong, Wu, & Liu, 2020). Evaluating the protective action of the rust layer in maintaining sDSS 2507/X-70 DWJs requires a comprehension of the rust layer's composition. The corrosion product layer formed during the dry/wet cycle is much thicker than complete immersion. This occurs because the rust layer is subjected to a cyclical drying–wetting–drying cycle. During wetting, the rust layer acts as a strong oxidant, which promotes the reduction of Fe^{3+} to Fe^{2+}. During the drying process, oxidation by air results in the re-oxidation of Fe^{2+} to Fe^{3+}, and the above process is repeated to promote the thickening of the corrosion product layer (Gong, Wu, Xie, et al., 2020; Yu et al., 2018). Analyses of corrosion product micro morphologies on base and weld metals under dry/wet cyclic environments are shown in Figure 5.91. Demonstrating corrosion product morphology showed the link between rust phase and SEM morphology. The dry/wet cycling testing damaged the sample surface, exposing a multi-layered corrosion product structure. The outer layer was uneven and rough, whereas the inner layer was dense and adhered to the sample surface with visible cracks (Figure 5.91(a)). The corrosion process was accelerated because these cracks allowed the electrolyte to penetrate the steel surface. (Suzuki et al., 1980)

demonstrated that the corrosion product on the surface of unalloyed steel often consists of two layers: an outer layer with loose crystalline α-FeOOH and γ-FeOOH and an inner layer composed primarily of dense amorphous FeOOH with some crystalline Fe_3O_4. In contrast to X-70 BM, ER2594 and ER309L have different corrosion products. In Figure 5.91(a), large plate-like structures (β-FeOOH, A) are the dominant structure, with three other phases featuring distinct morphologies: thin laminas (bird nest) and lepidocrocite mineral morphology (γ-FeOOH, B), and goethite needles (α-FeOOH, C). Figure 5.91(b) shows ER2594 filler weldment with solid globular-like magnetite particles (Fe_3O_4, D). Figure 5.91(c) shows typical α-FeOOH morphology in ER309L weldments, with "cloud-like" structures and whiskers (E), deviating significantly from (γ-FeOOH, A and C). Table 5.33 presents the results of the EDS spectra for various corrosion products (A-E). The particles' main constituents are Cl^-, O_2, Na, and Fe, with different concentrations for each morphology. EDS examination shows that the inner rust layer has more chloride ions (Cl^-) than the outer rust layer. The EDS data show that the outer corrosion products have more oxygen, and the Fe distribution is the opposite (Table 5.33). Previous research has demonstrated that loose and cracked zones contain considerable Cl^- (Gong et al., 2021; Gong, Wu, Xie, et al., 2020; Nishimura et al., 2000; Yu et al., 2018). The corrosion process is accelerated by wide cracks in corrosion product scales, which allow chloride and oxygen ions to pass through. Corrosion resistance is significantly influenced by the protective layer on the weldments' surface. Stable, dense corrosion products resist electrolyte penetration, extending sDSS 2507/X-70 DWJ's service life.

Table 5.33 : EDS spectra result of different corrosion product morphology in Figure 5.91

Elements (wt.%)	*Spot 1*	*Spot 2*	*Spot 3*	*Spot 4*	*Spot 5*	*Spot 6*
O	16.46	8.38	15.28	31.89	32.40	41.15
Na	31.85	26.72	32.30	16.75	9.88	7.28
Fe	13.32	26.78	11.54	34.23	49.15	46.57
Cl	38.37	38.12	40.89	17.13	8.56	5.00

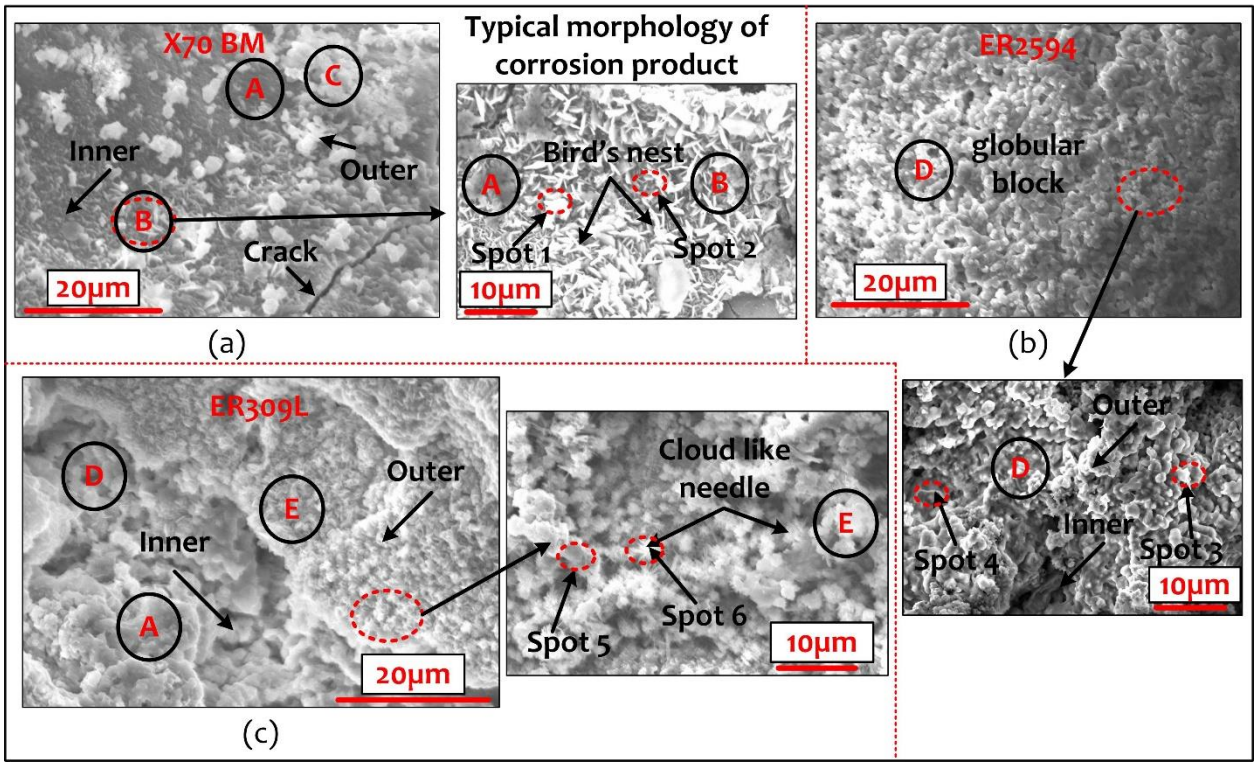

Figure 5.91 : (a-c) Typical morphology of corrosion product formed after corrosion

5.3.6.4 *CORROSION MECHANISM*

The corrosion mechanism of dry/wet cyclic conditions differs from complete immersion conditions due to periodic changes in the dry/wet cycles. The electrochemical process of steel corrosion under dry/wet cycle conditions involves simultaneous oxidation and reduction processes (Xu et al., 2022). Anode reaction dissolution forms ferrous ions on steel surfaces, which oxidize to form rust during dry/wet cycles. Reactions occur at each phase of electrolyte layer growth during the electrochemical corrosion process under dry/wet cycles (Gong, Wu, & Liu, 2020; Gong, Wu, Xie, et al., 2020; Yu et al., 2018). The inner rust layer electrolyte evaporation is weaker than that of the outer. After multiple dry/wet cycles, chloride ions accumulate in the inner rust layer and steel surface. The hydrolysis of Fe^{2+} and Fe^{3+} corrosion products leads to an acidic interface. The presence of this environment facilitates the production of ferrous hydroxy chloride, which acts as a precursor to the final β-FeOOH phase. Under dry/wet cyclic conditions, β-FeOOH is prevalent in the inner rust layer due to high chloride ion concentration and low pH. After being exposed to steel corrosion for an extended time, the γ-FeOOH can transform as goethite by dissolving into amorphous iron oxyhydroxide. The unstable γ-FeOOH and β-FeOOH can be converted to Fe_3O_4 by interacting with Fe^{2+}, leading to magnetite in rust layers (Figure 5.92). Under wet–dry cycle exposure, the most prevalent corrosion products were γ-FeOOH and Fe_3O_4, while during complete immersion corrosion, the principal corrosion products found with increasing exposure duration were α-FeOOH, γ-FeOOH, Fe_3O_4, and Fe_2O_3. In the initial phases of sDSS 2507/X-70 DWJ corrosion, the electrochemical reactions (5.6) to (5.12) can be depicted as follows (Chen et al., 2005; EVANS, 1965; Gong, Wu, & Liu, 2020; Ma et al., 2009):

Anodic reaction conversion (wet stages): $\mathrm{Fe} \rightarrow Fe^{2+} + 2e^{-}, Fe^{2+} \rightarrow Fe^{3+} + e^{-}$ (5.6)

Cathodic reaction conversion (wet stages): $O_2 + 2H_2O + 2e^{-} \rightarrow 4OH^{-}$ (5.7)

Combined reaction conversion: $Fe^{3+} + Cl^{-} + OH^{-} \rightarrow FeOCl + H^{+}$ (5.8)

Anodic reaction conversion (dry stages): $Fe_3O_4 \rightarrow \gamma - Fe_2O_4 + e^{-}$ (5.9)

Cathodic reaction conversion (dry stages):

$8\beta - FeOOH + Fe^{2+} + 2e^{-} \rightarrow 3Fe_3O_4 + 4H_2O$ (5.10)

Combined reaction conversion:

$Fe^{3+} + Cl^{-} + OH^{-} \rightarrow FeOCl + H^{+}$ (5.11)

$FeOCl + OH^{-} \rightarrow \beta - FeOOH + Cl^{-}$ (5.12)

The corrosion product initially formed $Fe(OH)_2$, which underwent oxidation to form the less stable $Fe(OH)_3$. Afterward, the initial corrosion products were transformed into lepidocrocite (γ-FeOOH), goethite (α-FeOOH), Fe_3O_4, and α-Fe_2O_3 (Tanaka et al., 2014). Apart from dissolved oxygen, γ- FeOOH was the oxidant in the rust layer (D. D. N. Singh et al., 2008). The γ-FeOOH reduction process is as follows:

$\gamma - FeOOH + H^{+} + 2e^{-} \rightarrow \gamma - Fe.OH.OH$ (5.13)

Through dry/wet cycling, γ-FeOOH is regenerated from γ-Fe.OH.OH after drying, allowing for another cycle after rust wetting (Han et al., 2014). The corrosion rate was indirectly controlled by the thickness of the electrolyte layer, which influenced the rate of oxygen transfer to the steel surface (de la Fuente et al., 2016; Xu et al., 2022). In short, X-70 steel develops pits by corrosive fluids containing chloride ions and concentration cells that form as a result of alternate dry/wet cycles. Under the chloride ion-containing thin electrolyte layer, initial pits will rapidly develop due to the "autocatalytic effect," resulting in visible pits (Figures 5.86 and 5.87). Three stages of rust formation—wetting of the dry surface, wet surface, and surface drying-out—were proposed by Strattmann et al. (Stratmann, 1990) for dry/wet cycles (Figure 5.92(a)). In the first stage, a thin layer of liquid with no rust formed on the metal surface. The liquid layer grows thinner as the solution slowly evaporates, which impacts the metal's cathodic reaction rate by increasing Cl^{-} concentration, increasing film conductivity, stimulating corrosion, and accelerating O_2 diffusion beneath the thin liquid layer. The rapid corrosion stage (second stage) through electrochemical corrosion evaluates the composition and thickness of the rust layer on the metal surface. The initial thin rust layer does not prevent O_2, Cl^{-} ions, or other corrosive chemicals from reaching the metal surface. A portion of Cl^{-} penetrates the rust

layer, while the remaining Cl^- reaches the metal surface and speeds up corrosion (Gong et al., 2021). EDS analysis revealed Cl^- deposition in the rust layer, linked to β-FeOOH formation (Figure 5.92 and Table 5.32). Equations 5.6, 5.7, and 5.10 provide an overview of the oxygen-absorbing corrosion mechanism that causes sDSS 2507/X-70 DWJs corrosion during complete immersion (Figure 5.92(b)). The formation of a rust layer primarily affects base metals (BMs) and weldments in this stable corrosion environment. As a result, the immersion zone's steel substrate exhibits no evidence of pitting corrosion. Initial corrosion oxygen transport to the sDSS 2507/X-70 DWJs surface is unrestricted, showing activation control. Nevertheless, the protective potential of corrosion products generated during the initial seven days is minimal. A rust layer builds up on the steel surface as corrosion deepens and produces more corrosion products. This inhibits oxygen diffusion together with the water layer, which causes the corrosion process to switch from activation control to oxygen diffusion control.

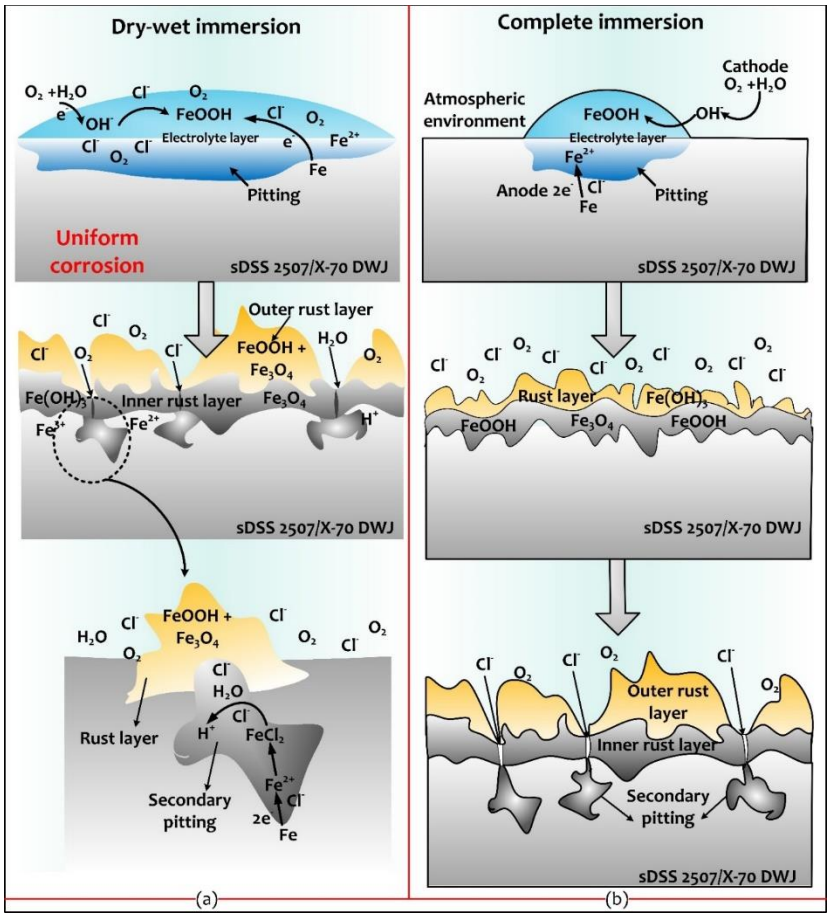

Figure 5.92: (a and b) Schematic of the corrosion mechanism under dry/wet and complete immersion conditions, respectively

SUMMARY OF CHAPTER 5:

This chapter extensively presents the findings of the experimental investigation conducted in the study, encompassing the effect of filler metal selection and heat input on the structural-property relationship. The comprehensive investigation involves evaluating microstructure, mechanical characteristics, residual stress measurement, and investigating wear and corrosion behavior in all dissimilar weld joints. The primary goal is to achieve enhanced structural integrity for various marine applications.

....